



# TECHNICAL REPORTS

## 33



Continuous Measurements of Greenhouse Gases  
and Atmospheric Oxygen in the Namib Desert

by  
Eric J. Morgan



## Technical Reports - Max-Planck-Institut für Biogeochemie 33, 2015

Max-Planck-Institut für Biogeochemie  
P.O.Box 10 01 64  
07701 Jena/Germany  
phone: +49 3641 576-0  
fax: + 49 3641 577300  
<http://www.bgc-jena.mpg.de>

# Continuous Measurements of Greenhouse Gases and Atmospheric Oxygen in the Namib Desert

Dissertation  
in fulfillment of the requirements for the degree “Dr. rer. nat.”  
of the Faculty of Mathematics and Natural Sciences  
at Kiel University

submitted by  
Eric J. Morgan  
Kiel, 2015

First Referee: Prof. Dr. Arne Körtzinger

Second Referee: Prof. Dr. Martin Heimann

Date of oral examination: August 10<sup>th</sup>, 2015

Approved for publication: August 10<sup>th</sup>, 2015

Signed: \_\_\_\_\_

Prof. Dr. Wolfgang J. Duschl, Dean

# Contents

<b>Contents</b>	<b>ii</b>
<b>List of Figures</b>	<b>v</b>
<b>List of Tables</b>	<b>vii</b>
<b>Abstract</b>	<b>viii</b>
<b>Zusammenfassung</b>	<b>x</b>
<b>Acknowledgments</b>	<b>xii</b>
<b>Declaration</b>	<b>xv</b>
<b>1 Introduction</b>	<b>1</b>
1.1 Motivation . . . . .	1
1.2 Carbon Dioxide . . . . .	3
1.3 Methane . . . . .	3
1.4 Nitrous Oxide . . . . .	3
1.5 Carbon Monoxide . . . . .	4
1.6 Atmospheric Oxygen . . . . .	4
1.7 Southern Africa . . . . .	5
1.8 Biomass Burning . . . . .	7
1.9 The African Haze Layer . . . . .	8
1.10 The Benguela Current Region . . . . .	9
1.11 The Namib Desert . . . . .	10
1.12 Gobabeb . . . . .	10
<b>2 The Representativeness of Observations at NDAO</b>	<b>12</b>
2.1 Introduction . . . . .	12
2.1.1 The Hadley Circulation . . . . .	12
2.1.2 Regional Circulation . . . . .	13
2.1.3 Mesoscale Circulation . . . . .	16
2.1.4 NOAA NMB Surface Flask Record . . . . .	17
2.2 Methods . . . . .	17
2.2.1 Atmospheric Transport Modeling . . . . .	18
2.2.2 Flask Data Treatment . . . . .	19
2.3 Results and Discussion . . . . .	20
2.3.1 Back-Trajectories . . . . .	20
2.3.2 Footprints . . . . .	22
2.3.3 Comparison of Back-Trajectories with in situ Meteorology . . . . .	22

2.3.4	The NMB Flask Record, Compared to Other Marine Background Sites	22
2.4	Summary and Conclusions	25
<b>3</b>	<b>Station Design and Performance</b>	<b>27</b>
3.1	Introduction	27
3.2	Methods	27
3.2.1	Overview	27
3.2.2	Response Times	29
3.2.3	Leak and Fractionation Tests	29
3.2.4	Carbon Dioxide and Methane Measurements	30
3.2.5	Nitrous Oxide and Carbon Monoxide Measurements	30
3.2.6	Atmospheric Oxygen Measurements	31
3.2.7	Meteorological Measurements	31
3.2.8	Flask Sampling	32
3.2.9	Sensor Stability	32
3.2.10	Drying and Water Correction	33
3.2.11	Calibrations and System Performance Evaluation	34
3.2.12	Drift Correction of the OA-ICOS Analyzer	35
3.2.13	Performance Goals	36
3.3	Results and Discussion	36
3.3.1	General Performance of the Measurement System	36
3.3.2	Response Times	37
3.3.3	Leak and Fractionation Tests	38
3.3.4	Stability of the CRDS	38
3.3.5	Stability of the OA-ICOS	41
3.3.6	Stability of the DFCA	41
3.3.7	Water Correction of the CRDS	42
3.3.8	Water Correction of the OA-ICOS	44
3.3.9	Calibrations	45
3.3.10	Target Measurements	45
3.3.11	Drift Correction of the OA-ICOS	48
3.3.12	External Validation	48
3.4	Summary and Conclusions	50
<b>4</b>	<b>The NDAO Time Series</b>	<b>52</b>
4.1	Introduction	52
4.2	Methods	52
4.2.1	Data Treatment	52
4.2.2	Singular Spectrum Analysis	53
4.3	Results and Discussion	53
4.3.1	Variability of Basic Meteorological Parameters	53
4.3.2	The Local Wind System	56
4.3.3	Diurnal Variability of the Main Measurands	59
4.3.4	Seasonal Cycles	62
4.3.5	Annual Growth Rates	63
4.4	Summary and Conclusions	64
<b>5</b>	<b>Seasonally Occurring Anomalies of CO<sub>2</sub>, CH<sub>4</sub>, and CO, Induced by Biomass Burning and Variability in Atmospheric Transport</b>	<b>65</b>
5.1	Introduction	65

5.1.1	Enhancement Ratios . . . . .	66
5.1.2	O <sub>2</sub> and CO <sub>2</sub> Molar Exchange Ratios . . . . .	66
5.2	Methods . . . . .	67
5.2.1	Determination of Slopes . . . . .	67
5.2.2	Back-Trajectory Classification . . . . .	67
5.2.3	Remote Sensing Data . . . . .	68
5.3	Results and Discussion . . . . .	68
5.3.1	Seasonal Divergences from the Marine Background . . . . .	68
5.3.2	Pathways of Polluted Air Masses . . . . .	69
5.3.3	Stoichiometry: Enhancement and Molar Exchange Ratios . . . . .	69
5.4	Summary and Conclusions . . . . .	73
<b>6</b>	<b>Top-Down Estimates of Greenhouse Gas Emissions from the Lüderitz and Walvis Bay Upwelling Cells</b> . . . . .	<b>74</b>
6.1	Introduction . . . . .	74
6.2	Methods . . . . .	78
6.2.1	Remote Sensing Data . . . . .	78
6.2.2	Identification of Upwelling Events and Selection of Atmospheric Anomalies . . . . .	79
6.2.3	Top-Down Air–Sea Flux Estimates . . . . .	79
6.2.4	Determination of Spatially Integrated Annual Flux Rates . . . . .	80
6.2.5	FS <i>Meteor</i> Cruise M99 . . . . .	80
6.2.6	Shipboard Air–Sea Flux Density Estimates . . . . .	81
6.3	Results and Discussion . . . . .	82
6.3.1	Chlorophyll <i>a</i> and SST . . . . .	82
6.3.2	Dissolved Gas Concentrations and Air–Sea Fluxes During M99 . . . . .	83
6.3.3	Atmospheric Anomalies Due to Upwelling Events . . . . .	83
6.3.4	Estimated Flux Densities . . . . .	86
6.3.5	Comparison of Top-Down Flux Density Estimates with M99 Shipboard Determinations . . . . .	88
6.3.6	Spatially Integrated Annual Fluxes . . . . .	88
6.3.7	Stoichiometry . . . . .	90
6.4	Summary and Conclusions . . . . .	94
<b>7</b>	<b>Summary and Outlook</b> . . . . .	<b>96</b>
7.1	Summary . . . . .	96
7.2	Outlook . . . . .	97
	<b>Appendices</b> . . . . .	<b>99</b>
<b>A</b>	<b>Supplementary Figures</b> . . . . .	<b>100</b>
<b>B</b>	<b>Supplementary Tables</b> . . . . .	<b>138</b>
	<b>Bibliography</b> . . . . .	<b>146</b>

# List of Figures

1.1	Köppen-Geiger Climate Zones of Southern Africa . . . . .	6
1.2	Biomass Burning in Southern Africa . . . . .	8
2.1	Barometric Pressure and Water Vapor at NDAO . . . . .	13
2.2	Climatology of Major Circulation Modes . . . . .	14
2.3	Wind and Pressure Fields over Southern Africa . . . . .	15
2.4	NOAA Flask Site . . . . .	18
2.5	Marine Background Flask Sites . . . . .	19
2.6	Aggregated Back Trajectories . . . . .	20
2.7	Horizontal and Vertical Length Scales of Back-Trajectories . . . . .	21
2.8	Average 10-day Footprint . . . . .	22
2.9	Wind Sector and Back-Trajectories . . . . .	23
2.10	Climatology of Selected Flask Sampling Sites . . . . .	25
3.1	System Leak Tests . . . . .	39
3.2	Fractionation Test . . . . .	40
3.3	CRDS and OA-ICOS Stability Test . . . . .	41
3.4	Allan Deviation of CRDS and OA-ICOS . . . . .	42
3.5	Allan Deviation of the DFCA . . . . .	43
3.6	Water Correction Functions . . . . .	44
3.7	Target Measurements . . . . .	46
3.8	Measurement Uncertainty . . . . .	47
3.9	OA-ICOS Drift Correction . . . . .	49
3.10	CO Storage Artifact . . . . .	50
3.11	NMB Flask and NDAO in situ Time Series . . . . .	51
4.1	The NDAO Time Series . . . . .	54
4.2	The NDAO Meteorological Time Series . . . . .	55
4.3	PBL Height at NDAO . . . . .	56
4.4	Average Diurnal Cycle of Temperature, Radiation, and PBL Height . . . . .	57
4.5	NDAO Wind Direction . . . . .	58
4.6	Diurnal Variability of Wind Direction . . . . .	59
4.7	Example of a PMW/SB Diurnal Cycle . . . . .	60
4.8	Example of the Effect of MPW on the Diurnal Cycle of CO <sub>2</sub> and O <sub>2</sub> . . . . .	61
4.9	Exchange Ratio by Wind Sector . . . . .	62
5.1	Annual Cycle of Fire and Terrestrial Biosphere Activity . . . . .	69
5.2	NDAO Compared with the CPT Background . . . . .	70
5.3	Median Day of Burning . . . . .	71
5.4	Response of Enhancement and Exchange Ratios to Biomass Burning . . . . .	72



6.1	Conceptual Diagram of the Influences on Air–Sea Fluxes During Upwelling . . . .	76
6.2	An Upwelling Event . . . . .	84
6.3	NDAO Measurands During Upwelling Event . . . . .	85
6.4	M99 Flux Comparisons . . . . .	89
6.5	N <sub>2</sub> O and O <sub>2</sub> Variability in the Atmosphere and Surface Water . . . . .	91
6.6	CO <sub>2</sub> and O <sub>2</sub> Variability in the Atmosphere and Surface Water . . . . .	92
6.7	CH <sub>4</sub> , CO <sub>2</sub> , and O <sub>2</sub> Variability During Upwelling Events . . . . .	94
A.1	Elevation Transect of Southwestern Africa . . . . .	100
A.2	NDVI for Southern Africa . . . . .	101
A.3	Seasonality of Back-Trajectories . . . . .	102
A.4	Seasonality of Footprints . . . . .	103
A.5	NMB Flask Time Series . . . . .	104
A.6	Specifications of Large Cryotraps . . . . .	105
A.7	Specifications of Small Cryotraps . . . . .	106
A.8	Diagram of the Measurement System . . . . .	107
A.9	Tank-Related Artifacts . . . . .	108
A.10	NDAO in situ and MPI-BGC Flask Compatibility . . . . .	109
A.11	Scales of Atmospheric Transport . . . . .	110
A.12	Visualization of Wind Sectors . . . . .	111
A.13	CO <sub>2</sub> Time Series Deconstruction . . . . .	112
A.14	$\delta(\text{O}_2/\text{N}_2)$ Time Series Deconstruction . . . . .	113
A.15	N <sub>2</sub> O Time Series Deconstruction . . . . .	114
A.16	CH <sub>4</sub> Time Series Deconstruction . . . . .	115
A.17	CO Time Series Deconstruction . . . . .	116
A.18	Average Diurnal Cycle of CO <sub>2</sub> by Month . . . . .	117
A.19	Average Diurnal Cycle of $\delta(\text{O}_2/\text{N}_2)$ by Month . . . . .	118
A.20	Average Diurnal Cycle of CH <sub>4</sub> by Month . . . . .	119
A.21	Average Diurnal Cycle of CO by Month . . . . .	120
A.22	Average Diurnal Cycle of N <sub>2</sub> O by Month . . . . .	121
A.23	CO <sub>2</sub> and O <sub>2</sub> Over a PMW/SB Cycle . . . . .	122
A.24	CO <sub>2</sub> and O <sub>2</sub> Over a MPW Cycle . . . . .	123
A.25	Exchange Ratio of Monthly Average Diurnal Cycles . . . . .	124
A.26	Example of the Effect of MPW on the Diurnal Cycle of CH <sub>4</sub> and CO . . . . .	125
A.27	Seasonal Cycle and Emissions of SF <sub>6</sub> . . . . .	126
A.28	Pathways of Polluted Air Masses . . . . .	127
A.29	Correlation Slopes of Selected Air Masses . . . . .	128
A.30	Criteria for Sea Surface Area Affected by Upwelling . . . . .	129
A.31	Upwelling Events . . . . .	130
A.32	Seasonal Averages of SST . . . . .	131
A.33	Underway Measurements of Air–Sea Fluxes and Dissolved Concentrations During M99 . . . . .	132
A.34	Flux Density Maps for M99 . . . . .	133
A.35	Back-Trajectories During M99 . . . . .	134
A.36	Time Series of Atmospheric CO <sub>2</sub> and CH <sub>4</sub> During M99 . . . . .	135
A.37	Back-trajectories of Upwelling Events . . . . .	135
A.38	SST During an Upwelling Event . . . . .	136
A.39	NDAO Measurands During an Upwelling Event . . . . .	137

# List of Tables

3.1	Measurement Scales . . . . .	28
3.2	GAW Recommendations for Measurement Compatibility . . . . .	36
3.3	Total System Leak Rates . . . . .	37
3.4	Measurement Compatibility . . . . .	48
4.1	Seasonal Cycles and Growth Rates of NDAO Measurands . . . . .	63
6.1	Average Top-Down Flux Densities . . . . .	86
6.2	Estimated Total Net Annual Fluxes of the Lüderitz and Walvis Bay Upwelling Cells . . . . .	88
B.1	Flask Sampling Site Locations . . . . .	138
B.2	Variability of NDAO Measurands at Proximal Flask Sites . . . . .	139
B.3	Variability of Additional Measurands at Proximal Flask Sites . . . . .	140
B.4	Part List . . . . .	141
B.5	Measurand Total System Residence ( $\tau_{calc}$ ) and Response ( $\tau_{app}$ ) Times . . . . .	142
B.6	Comparison of Fit Parameters . . . . .	143
B.7	Target Bias . . . . .	144
B.8	Definition of Wind Sectors . . . . .	145
B.9	Growth Rates of Selected Measurands for the Period October 2012–December 2013	145

# Abstract

A new, near-coastal background site was established for observations of greenhouse gases (GHGs) and atmospheric oxygen in the central Namib Desert near Gobabeb, Namibia. The location of the site was chosen to provide observations in a data-poor region in the global sampling network for GHGs. Semi-automated, continuous measurements of carbon dioxide, methane, nitrous oxide, carbon monoxide, atmospheric oxygen, and basic meteorology are made at a height of 21 m a.g.l., 50 km from the coast at the northern border of the Namib Sand Sea. Atmospheric oxygen is measured with a differential fuel cell analyzer. Carbon dioxide and methane are measured with an early-model cavity ring-down spectrometer; nitrous oxide and carbon monoxide are measured with an off-axis integrated cavity output spectrometer. Instrument-specific water corrections are employed for both instruments in lieu of drying.

The representativity of the site was assessed within the context of atmospheric transport. During austral summer, strong equatorward winds are present as a result of the Hadley circulation. This brings marine boundary layer air inland to Gobabeb. In austral winter, the descending branch of the southern Hadley cell is at the same latitude as NDAO, which encourages the establishment of anticyclonic conditions over southern Africa. The variability of air mass history during this time of year is quite high, alternating between marine and terrestrial air masses, as well as air that was recently in contact with the surface and air that had descended from heights greater than 2 km. NOAA flask samples taken at Gobabeb from 1996 to the present appeared to respond to these seasonal patterns in atmospheric dynamics, when compared to other marine background sites at the same latitude as NDAO.

Two years of data are presented from the observatory. Diurnal variability was noted at times for all species, particularly for atmospheric oxygen. Through stoichiometry and phasing, this was attributed primarily to the local wind system, which features a prominent sea breeze, and daily boundary layer oscillations. Large anomalies in carbon monoxide and methane were observed in the time series on a synoptic time scale, during the ascending portion of the seasonal cycle. These were attributed to an alternation between polluted air masses from the continental interior and marine boundary layer air. The continental air masses were progressively influenced by biomass burning as the fire season developed. The concentration of fire activity close to the station increased throughout the year, peaking in September, a fact reflected in the enhancement ratio of  $\text{CH}_4$  to CO. During such synoptic events the molar exchange ratio of  $\text{O}_2$  to  $\text{CO}_2$  also supported this interpretation.

Finally, the NDAO time series was used to make top-down estimates of air-sea fluxes of the main measurands from the Lüderitz and Walvis Bay upwelling cells in the Benguela Current region, during upwelling events. Flux densities were evaluated using shipboard measurements within the study area, showing good agreement with the top-down estimates. Average flux densities for  $\text{CO}_2$  were  $0.45 \pm 0.4 \mu\text{mol m}^{-2} \text{sec}^{-1}$ ,  $-3.9 \pm 2.6 \mu\text{mol m}^{-2} \text{sec}^{-1}$  for  $\text{O}_2$ ,  $6.0 \pm 5.0 \text{nmol m}^{-2} \text{sec}^{-1}$  for  $\text{CH}_4$ ,  $0.5 \pm 0.4 \text{nmol m}^{-2} \text{sec}^{-1}$  for  $\text{N}_2\text{O}$ , and  $2.7 \pm 1.7 \text{nmol m}^{-2} \text{sec}^{-1}$  for CO.  $\text{N}_2\text{O}$  fluxes were fairly low, in accord with previous work, suggesting that

the evasion of this gas from the Benguela is smaller than in other upwelling systems. Conversely, methane release was very high for the marine environment, which adds to mounting evidence of a large sedimentary source of methane in the Walvis Bay area. Carbon dioxide and oxygen fluxes were substantial and probably not accounted for in current budgets.

# Zusammenfassung

Zur Beobachtungen von Treibhausgasen (THG) und Luftsauerstoff wurde eine neue, küstennahe Stelle zur Hintergrundmessung in der zentralen Namib Wüste in der Nähe von Gobabeb, Namibia etabliert. Die Lage des Standortes wurde gewählt, um Erfassungen in einem datenarmen Bereich des globalen Messnetzwerks für THG zu ermöglichen. Halbautomatische, kontinuierliche Messungen von Kohlendioxid, Methan, Distickstoffmonoxid, Kohlenmonoxid, Luftsauerstoff und grundlegender Meteorologie werden in einer Höhe von 21 m über Grund und 50 km von der Küste entfernt an der nördlichen Grenze der Namib Sand Sea gemacht. Der Luftsauerstoff wird mit einer differentiellen Brennstoffzellmessung ermittelt. Kohlendioxid und Methan werden mit einem älteren Cavity Ring-Down Spektrometer gemessen; Distickstoffmonoxid und Kohlenmonoxid mit einem Off-Axis Hohlraumintegrierten Output-Spektrometer. Für beide Instrumente werden entsprechend der Austrocknung gerätespezifische Wasserkorrekturen durchgeführt.

Die Repräsentativität des Ortes wurde im Rahmen des atmosphärischen Transports beurteilt. Im Südsommer herrschen als Folge der Hadley Zirkulation äquatorwärts starke Winde. Dies bringt Luft der marinen Grenzschicht ins Landesinnere nach Gobabeb. In Südwinter ist der absteigende Ausläufer der südlichen Hadley Zelle auf demselben Breitengrad wie NDAO, was antizyklonale Bedingungen über Südafrika begünstigt. Die Variabilität der Luftmassen ist während dieser Zeit des Jahres recht hoch, bedingt durch den Wechsel zwischen marinen und terrestrischen Luftmassen, sowie Luft, die vor kurzem in Kontakt mit der Oberfläche war und Luft, die aus einer Höhe von mehr als 2 km herabgestiegen ist. NOAA-Kolbenproben bei Gobabeb von 1996 bis heute scheinen bei Vergleich mit anderen marinen Stellen zur Hintergrundmessung auf dem gleichen Breitengrad wie NDAO auf diese saisonalen Muster der atmosphärischen Dynamik reagiert zu haben.

In dem Observatorium liegen Daten aus zwei Jahren vor. Diurnale Variabilität wurde manchmal für alle Arten festgestellt, insbesondere für Luftsauerstoff. Durch Stöchiometrie und Phasing wurde dies in erster Linie auf das lokale Windsystem zurückgeführt, das sich durch eine starke Meeresbrise und tägliche Schwingungen der Grenzschicht auszeichnet. Im ansteigenden Teil des Jahreszyklus wurden in der Zeitreihe auf einer synoptischen Zeitskala starke Anomalien in Kohlenmonoxid und Methan beobachtet. Diese wurden auf eine Wechselfolge von verschmutzten Luftmassen aus dem Landesinneren und Meeresschichtluft zurückgeführt. Die kontinentalen Luftmassen wurden zunehmend durch die Verbrennung von Biomasse beeinflusst, während die Brandsaison beginnt. Die Konzentration von Brandaktivitäten in der Nähe der Station erhöhte sich im Laufe des Jahres und erreichte seinen Höhepunkt im September, was sich in der Enhancement Ratio von  $\text{CH}_4$  zu CO widerspiegelt. Während solcher synoptischer Ereignisse wurde diese Interpretation auch durch das molare Umtauschverhältnis von  $\text{O}_2$  zu  $\text{CO}_2$  unterstützt.

Schließlich wurde die NDAO-Zeitreihe verwendet, um Top-Down Schätzungen der Luft-See Strömungen der wichtigsten Messgrößen in den Auftriebszellen der Lüderitz und Walvischbucht in der Benguela Strömungsregion unter Umständen des Auftriebs zu machen.

Mit Bordmessungen wurden im Untersuchungsgebiet Flussdichten gemessen, welche gute Übereinstimmung mit den Top-Down Schätzungen zeigen. Durchschnittliche Flussdichten für  $\text{CO}_2$  waren  $0.45 \pm 0.4 \mu\text{mol m}^{-2} \text{sec}^{-1}$ ,  $-3.9 \pm 2.6 \mu\text{mol m}^{-2} \text{sec}^{-1}$  für  $\text{O}_2$ ,  $6.0 \pm 5.0 \text{nmol m}^{-2} \text{sec}^{-1}$  für  $\text{CH}_4$ ,  $0.5 \pm 0.4 \text{nmol m}^{-2} \text{sec}^{-1}$  für  $\text{N}_2\text{O}$ , und  $2.7 \pm 1.7 \text{nmol m}^{-2} \text{sec}^{-1}$  für  $\text{CO}$ .  $\text{N}_2\text{O}$ -Strömungen waren in Übereinstimmung mit früheren Arbeiten eher niedrig, was darauf hindeutet, dass die Migration dieses Gases aus dem Benguela kleiner ist, als in anderen Auftriebssystemen. Umgekehrt war Methanfreisetzung in der marinen Umwelt sehr hoch, was die Hinweise auf ein großes sedimentäres Vorkommen von Methan in der Gegend Walfisnbucht weiter verdichtet. Die Strömungen von Kohlendioxid und Sauerstoff waren signifikant und werden in laufenden Haushaltsplänen vermutlich nicht berücksichtigt.

# Acknowledgments

Gobabeb Training and Research Centre sees a lot of turnover but everyone I have worked or visited with there has been both wonderfully helpful and good company. A great many people assisted with the running of the station over the 2+ years I was involved. I thank Gillian Maggs-Kölling, Theo Wassenaar, Mary Seely, Machel Boch, and the Gobabeb community for their support and hospitality. I also thank Walter Holch, for his technical assistance and advice, and Josef Gariseb, Jeffrey Khurisab, Richardt Swartboi, and Samuel Gowaseb for their hard work during the construction of the station. I particularly wish to thank and acknowledge Robert Logan, Anna Day, Jessica Sack, Titus Shuuya, and Tayler Chicoine, who did the lion's share of maintenance at NDAO.

I would like to express my appreciation and gratitude to the crew, Master, and principle scientist, Detlef Quadfasel, of the FS *Meteor* for their assistance and generosity in allowing our group to make measurements over several cruises. Express Services, Ltd. of Walvis Bay were very helpful in clearing a shipment of flasks through customs in the nick of time, after lengthy delays. Damian Arévalo-Martínez, Hermann Bange, and Tobias Steinhoff of GEOMAR provided some valuable data from M99.

I thank Casper Labuschagne and Ernst-Günther Brunke for hosting me in South Africa for a fruitful two-month research stay. Ralph Keeling was a similarly hospitable host during my time at Scripps and provided some important guidance at a key moment.

At MPI-BGC, Anna Görner was of great assistance to me during my first year in Germany. Christian König oversaw the transportation of a variety of odd shipments to far-flung places. Andreas Kramer was also very helpful in coordinating the original shipment of our laboratory and storage containers to Namibia. Dietrich Feist fixed a faulty GRUB boot loader on my work computer on the eve before I embarked on a three-month trip to Africa, for which I will be eternally grateful. I would also like to acknowledge the efforts and expertise of Armin Jordan, Willi Brand, Michael Hielscher, Bert Steinberg, Johannes Schwarz, and Jürgen Richter in preparing and analyzing flask samples and gas cylinders.

Bruce Vaughn, Ed Dlugokencky, Paul Novelli, and Tom Conway of NOAA ESRL kindly provided data from the NMB flask sampling site.

Rona Thompson (formerly of MPI-BGC) and Uwe Schultz of the TAG group built the original laboratory that later became NDAO. Uwe and Steffen Schmidt provided a great deal of technical assistance in the installation and maintenance of the station. Jörg Reith of MPI-BGC provided assistance as an electrician during the construction of the laboratory. Reimo Leppert gave valuable technical support in the field on our last trip to Gobabeb. I would particularly like to acknowledge Thomas Seifert, who participated in the *Meteor* cruises, accompanied me on every trip to Namibia, and coded the software for the measurement system. He was always incredibly helpful and supportive and without him this work wouldn't have been possible.

I would like to thank my committee, Arne Körtzinger, Ralph Keeling, Martin Heimann, and Jošt Lavrič, for their expertise and guidance. Special thanks are due to my supervisor,

Jošt Lavrič for taking me on as a student and helping me through the process.

Finally, I would like to acknowledge my wife, Julia McMillan, for her assistance in proof-reading this thesis, and for her inexhaustible love and support.



A portion of this dissertation has been published as a separate manuscript:

- E. J. Morgan , J. V. Lavric , T. Seifert, T. Chicoine, A. Day, J. Gomez, R. Logan, J. Sack, T. Shuuya, E. G. Uushona, K. Vincent, U. Schultz, E.-G. Brunke, C. Labuschagne, R. L. Thompson, S. Schmidt, A. C. Manning, and M. Heimann. Continuous measurements of greenhouse gases and atmospheric oxygen at the Namib Desert Atmospheric Observatory. *Atmos. Meas. Tech.*, 8, 2233-2250, 2015.
- Data analysis and preparation of the manuscript was done by E. Morgan. J. Lavric and T. Seifert assisted E. Morgan with station maintenance, installation, and instrument testing. J. Lavric, M. Heimann, R. Thompson, and A. Manning provided feedback on the manuscript. U. Schultz and S. Schmidt, T. Chicoine, A. Day, J. Gomez, R. Logan, J. Sack, T. Shuuya, E.G. Uushona, and K. Vincent provided technical support while in the field. C. Labuschagne and E.-G. Brunke participated in the interlaboratory comparison. Where otherwise not indicated, all other work was performed by E. Morgan.

# Declaration

Hiermit erkläre ich an Eides statt, dass ich die vorliegende Arbeit unter Einhaltung der Regeln guter wissenschaftlicher Praxis der *Deutschen Forschungsgemeinschaft* selbständig erarbeitet und verfasst und keine anderen als die angegebenen Quellen und Hilfsmittel verwendet habe.

Ich versichere, dass diese Arbeit in der vorgelegten oder einer ähnlichen Fassung noch nicht an anderer Stelle zur Erlangung des Doktorgrades eingereicht worden ist.

I hereby declare, under penalty of perjury, that the work in this dissertation is in full compliance with the Rules of Good Scientific Practice by the Deutsche Forschungsgemeinschaft, and that the work was conducted independently, and that all sources, aids, and assistance have been fully disclosed.

I also declare that this work has not been submitted elsewhere for the purposes of obtaining a doctoral degree.

Signed: \_\_\_\_\_

Eric Morgan  
Jena, June 2015

*For S, Z, and RSM*

# 1

## Introduction

### 1.1 Motivation

Naturally occurring trace constituents of the atmosphere, such as carbon dioxide, methane, and nitrous oxide, can have a profound and complex interrelationship with the planet’s geological and biological surface processes. It has been well-established by considerable scientific inquiry, for instance, that changes in the background abundance of these greenhouse gases (GHGs) affect the earth’s climate system by altering the planetary energy balance of the planet [Forster et al., 2007]. These three species are also significant actors in atmospheric chemistry and composition, and serve as tracers of biogeochemical processes.

A well-distributed global atmospheric sampling network for these gases and related tracers is a necessity for studying their role in Earth system science. Expanding the existing network will further our understanding of global biogeochemical cycles, particularly the uncertainties in terrestrial sources and sinks in the carbon cycle [Bakwin et al., 2004, Cihlar et al., 2002]. Furthermore, remote sensing of trace gases from satellites shows significant bias and uncertainty; such measurements require validation and ground-truthing. All modeling efforts also ultimately depend on in situ measurements. Stationary, long-term time series are particularly crucial for studies of global change, as multi-decadal records are necessary to capture and document significant trends. Records of the dry air mole fractions of these trace gases can also be used to verify anthropogenic emissions, create top-down estimates of fluxes, study regional biogeochemical cycling and surface-atmospheric processes, and compare inter-regional differences in GHG abundance [Nisbet and Weiss, 2010]. Finally, measurements of trace gases also inform on atmospheric mixing and transport, on pollution events, and on regional budgets of species that influence the composition of the atmosphere, as well as on a number of biogeochemical and surface-atmosphere processes.

The continent of Africa is underrepresented in the global network for ground-based measurements of many trace gases, despite its size: currently there are only a handful of operational atmospheric observatories in Africa. Besides the measurement stations at the Cape Verde Islands, Izaña, and the Seychelles, on the continent proper there are measurement sites for GHGs in Kenya (Mt. Kenya), in South Africa—at Cape Point and two additional measurement sites close to the Cape—and a flask sampling site in Algeria (at Assekrem). As of the time of writing a new observatory for continuous observations of GHGs and other trace gases is in development at Mt. Karisimbi, Rwanda. Additionally, there have been quite a few eddy covariance flux measurement sites in operation at various times throughout southern Africa [Kutsch et al., 2011, Merbold et al., 2009, Sjöström et al., 2013]. This means that estimates of the magnitude of fluxes of important gases are still uncertain, and accordingly sensitive to the addition of even a single station to the network [Gloor et al., 2000, Rayner et al., 1996]. Continuous measurements of  $\text{N}_2\text{O}$  are particularly rare [Thompson et al., 2011]. Observations of other important non-greenhouse trace gases, like CO or  $\text{O}_3$ , are still sparse

on the continent.

To fill this gap in the global sampling network, the Max Planck Institute for Biogeochemistry has created an atmospheric observatory in southern Africa to continuously measure the long-lived greenhouse gases  $\text{CO}_2$ ,  $\text{CH}_4$ ,  $\text{N}_2\text{O}$ , and the tracers  $\text{CO}$  and  $\delta(\text{O}_2/\text{N}_2)$ . In addition to being radiatively active, the trace gases ( $\text{CO}_2$ ,  $\text{CH}_4$ ,  $\text{N}_2\text{O}$ ,  $\text{CO}$ ) have other key properties: the carbon-containing compounds have significance for the carbon cycle (and  $\text{N}_2\text{O}$  for the nitrogen cycle) and inform on biogeochemical processes.  $\text{CH}_4$ ,  $\text{N}_2\text{O}$ , and  $\text{CO}$  also all have important roles in atmospheric chemistry, particularly in their relationship to ozone. Atmospheric oxygen is interesting to measure because it somewhat mirrors the behavior of  $\text{CO}_2$  except for certain oceanic processes, which makes such data a valuable complement to carbon dioxide time series, particularly in coastal areas. To my knowledge there are no facilities continuously measuring  $\delta(\text{O}_2/\text{N}_2)$  in Africa with the exception of the Cape Verde Atmospheric Observatory, off the coast of Senegal.

Despite rapid atmospheric mixing, molar ratios of many trace gases in the lower troposphere vary in space and time, as sources and sinks can be patchily distributed in both dimensions. Time series of biogeochemically active gases are subject to high-frequency variations, which are often smoothed or filtered to produce a more coherent record. For greenhouse gases, their effect on climate can only be assessed over long (i.e., decadal) time scales, a period over which discreet measurements, if made frequently enough, are adequate for identifying long term trends, interannual differences and growth rates, latitudinal gradients, etc. While much has been learned from a global network of flask samples, this type of sampling is usually conducted during “clean” conditions, meaning that strong sources can be excluded from these signals; hence, continuous measurements, if enough supporting data is available, are superior for identifying and quantifying regional to local scale sources and sinks of important gases [Geels et al., 2004, Huntzinger et al., 2011, Law et al., 2002]. Continuous measurements are also preferable because they provide more statistical power than single measurements, eliminate uncertainty over the accuracy of outliers from flask time series, and reveal diurnal cycles [Uglietti et al., 2008].

A complex time series is usually thought of as being comprised of several different components. For  $\text{CO}_2$ , for instance, this includes the “secular” trend (i.e., the increase of the global background), the seasonal cycle, a diurnal cycle, synoptic variability (anomalies in  $\text{CO}_2$  generated over a strong source or sink, subject to atmospheric transport) and meso- to local scale variance [Mahecha et al., 2010]. Such events typically occur on the order of days, as pressure systems pass over the measurement location. Furthermore, vertical mixing of the atmosphere can have a major impact on trace gas mole fractions; the height and stability of the boundary layer is important as it can push air masses dominated by active processes closer to the earth’s surface, concentrating gases [Pino et al., 2012, Wallace and Hobbs, 2006].

There are many types of investigations into the spatiotemporal distribution of trace gases: aircraft campaigns, eddy flux towers, tall towers, flask samples, and remote sensing. All of these methods provide important information on trace gas distribution, and the best approach is to use a combination of observation types. Measurements made from towers, particularly tall towers, are attractive for regional studies because they can provide continuous data at different heights, and if they extend above the surface layer and into the mixed layer, are more regionally representative than ground-based measurements [Bakwin et al., 1995, Haszpra et al., 2012, Tans, 1993, Vermeulen et al., 2004]. In Europe and North America, for instance, large networks of towers and measurement stations have greatly increased understanding of regional biogeochemical cycles and budgets of important atmospheric constituents on these continents [Bakwin et al., 1995, Vermeulen et al., 2004]. When a tall (i.e., hundreds of meters) tower is not feasible, some type of mast or short tower is still preferred to sample above the immediate surface layer and limit the representation of local influences.

## 1.2 Carbon Dioxide

The major sources of CO<sub>2</sub> to the atmosphere are fossil fuel emissions, cement production, deforestation, biomass burning, and biotic respiration; the major sinks are terrestrial and marine photosynthesis and inorganic ocean uptake [GCP, 2011, Schlesinger, 1997]. Current atmospheric molar ratios of CO<sub>2</sub> are the highest seen in at least the last 800,000 years [Lüthi et al., 2008, Petit et al., 1999]. Growth rates of CO<sub>2</sub> show variability due to volcanic eruptions, changes in the land and ocean sinks, the El Niño / Southern Oscillation (ENSO), fossil fuel emissions, and land use change, but in general are constrained, averaging to ~2 ppm per year [Francey et al., 2010, Raupach et al., 2008]. Studies have confirmed that roughly half of this CO<sub>2</sub> released from fossil fuel combustion between 1960 and 2007 has remained in the atmosphere [Boden et al., 2009]. The rest of the anthropogenic carbon released has been taken up by the surface of the earth. The oceanic sink, which is decreasing slightly, accounts for approximately a third, and the land sink, which is even more uncertain, around 10% [Sarmiento et al., 2010, Takahashi et al., 2009].

## 1.3 Methane

Methane is a powerful greenhouse gas, the most abundant hydrocarbon in the atmosphere, a major sink of OH, and a precursor for other important trace species in the troposphere, such as ozone [Forster et al., 2007, Lelieveld et al., 1998, Wuebbles and Hayhoe, 2000]. Methane is produced biogenically in the absence of oxygen by anaerobic microorganisms and by plants, and geologically through the thermal decomposition of organic matter buried in sediments. Sources include the guts of ruminants, termites, rice paddies, natural wetlands, biomass burning, as well as some geologic sources. A substantial portion of methane emissions each year come from anthropogenic sources; estimates vary greatly, but these sources are probably between 40 and 70% [Bousquet et al., 2006, Kirschke et al., 2013]. Methane has an atmospheric lifetime of 8–9 years [Forster et al., 2007, Prather et al., 2012]. The major sink is the hydroxyl free radical, the variations of which have a large influence on the atmospheric burden [Bousquet et al., 2006, Reeburgh, 2007b]. The mole fraction of CH<sub>4</sub> in the atmosphere is controlled by a somewhat delicate balance of sources and sinks, which has resulted in variable growth rates since data has become available, with several periods of zero growth or decrease having been observed [Dlugokencky et al., 2009, Monteil et al., 2011, Rigby et al., 2008]. Growth rates have been declining since the 1980s, and while the cause of this is still subject to debate, there is good evidence that it is related to reduced fugitive fossil fuel emissions [Aydin et al., 2011, Heimann, 2011, Kai et al., 2011, Simpson et al., 2012].

## 1.4 Nitrous Oxide

N<sub>2</sub>O is a radiatively active gas and an important stratospheric ozone-depleting substance, due to its formation of NO<sub>x</sub> [Forster et al., 2007, Ravishankara et al., 2009]. N<sub>2</sub>O has a long atmospheric lifetime of ~130 years [Prather et al., 2012], and absorbs very strongly in the infrared, giving it a high global warming potential [Myhre et al., 2013]. In the ocean, most N<sub>2</sub>O is formed as a by-product during nitrification (the oxidation of NH<sub>4</sub><sup>+</sup> or NH<sub>3</sub> to NO<sub>2</sub><sup>-</sup> and then NO<sub>3</sub><sup>-</sup>) [Voss et al., 2013, Zamora et al., 2012]. N<sub>2</sub>O is also produced as an intermediate during denitrification (the reduction of NO<sub>3</sub><sup>-</sup> to N<sub>2</sub>), so some release may occur, although denitrification also consumes N<sub>2</sub>O; the net effect depends largely on oxygen concentrations [Bange et al., 2010, McKenney et al., 1997, Voss et al., 2013, Zamora et al., 2012].

The major sources of atmospheric  $\text{N}_2\text{O}$  are microbial activity in soils, with agricultural lands being particularly important, industry, and the world's oceans, especially the coasts [Reay et al., 2012]. The total marine source is somewhere between 1.8 and 9.4  $\text{TgN yr}^{-1}$  [Ciais et al., 2013]. A recent intercomparison of global atmospheric inversions gave a range of 5.3–6.32  $\text{TgN yr}^{-1}$ , or 31–38% of the total annual source [Thompson et al., 2014]. Coastal upwelling regions can be hotspots [Bange et al., 1996a, Kock et al., 2012, Nevison et al., 2004b, Rhee et al., 2009]. The sum of terrestrial sources is about 6.6  $\text{TgN yr}^{-1}$ , albeit also with large uncertainties.

The principal sink is photochemical reactions in the stratosphere, and knowledge of stratospheric mixing is an important factor in interpreting time series of  $\text{N}_2\text{O}$  [Forster et al., 2007, Nevison et al., 2004a, Park et al., 2012]. With precise measurements, seasonal cycles ( $\sim 0.5$  ppb), interannual variability, and interhemispheric differences ( $\sim 0.8$  ppb) have been detected [Ishijima et al., 2009, Nevison et al., 2004a, 2011, Park et al., 2012]. The globally averaged surface background mixing ratio is currently about 325 ppb. The increase is quite linear and is about 0.8 ppb  $\text{yr}^{-1}$  on average [NOAA/ESRL, 2012]. Recent modeling efforts have highlighted the importance of episodic pulses of nitrous oxide from tropical regions in determining the global distribution, and more continuous measurements in these areas are needed to examine this source [Kort et al., 2011].

## 1.5 Carbon Monoxide

CO is a major sink for OH, and its abundance can affect tropospheric ozone, depending on the co-occurrence of  $\text{NO}_x$  [Crutzen, 1973, Seiler, 1974]. CO is toxic to humans and considered a pollutant. While CO is produced during vegetation fires, since it is also produced from combustion of any type of matter, its utility as a unique tracer for biomass burning is limited if there are anthropogenic emissions in the same region, particularly if there is significant dilution, mixing, or ageing of the affected air mass: CO is also a product of the oxidation of methane and non-methane hydrocarbons [Duncan et al., 2007, Seiler, 1974, Wang et al., 2012]. In southern Africa several other non-biomass burning source regions have been identified: charcoal kilns in the central/southern portion of the region, the Copperbelt industrial area in Zambia and the industrial region in South Africa/Lesotho [Kirkman et al., 2000]. There is a small ocean source of CO, but it is quite small compared with other terms in the budget [Bates et al., 1995, Stubbins et al., 2006]. From firm air and modeling analysis, it seems that CO increased throughout the 20<sup>th</sup> century until the 1970s, when concentrations began to decline, likely due to pollution controls [Duncan et al., 2007, Petrenko et al., 2013]. Whether there is a current trend in CO at either the hemispheric or global scale is unclear [Wai et al., 2014, Worden et al., 2013]. For a more detailed discussion of recent trends, see Section 2.3.4.

## 1.6 Atmospheric Oxygen

The variability of atmospheric oxygen is quite small relative to the total mass of oxygen in the atmosphere. As measuring small changes against the large background is technically challenging, it is common practice to measure oxygen relative to atmospheric  $\text{N}_2$ , defining the  $\text{O}_2/\text{N}_2$  ratio as  $\delta(\text{O}_2/\text{N}_2)$ , against a known standard, in per meg, akin to the notation for stable isotopes [Keeling, 1988, Keeling and Shertz, 1992]:

$$\delta(\text{O}_2/\text{N}_2) = \left( \frac{\text{O}_2/\text{N}_2_{\text{sample}} - \text{O}_2/\text{N}_2_{\text{ref}}}{\text{O}_2/\text{N}_2_{\text{ref}}} \right) \times 10^6 \quad (1.1)$$

Atmospheric oxygen can be used as a top-down constraint on the carbon cycle, since the major biogeochemical processes that consume or produce carbon dioxide on the global scale—such as respiration, photosynthesis, decomposition, or combustion—also consume or produce oxygen [Keeling and Manning, 2014, Keeling and Shertz, 1992]. Since both CO<sub>2</sub> and O<sub>2</sub> have long atmospheric lifetimes, the composition of air masses affected by these processes conforms to the stoichiometry of these reactions, such that a characteristic molar exchange ratio or oxidative ratio, OR, can be retained after an air mass has been influenced by a net surface flux. The OR of the consumption or production of organic matter is defined as a unitless stoichiometric ratio,

$$OR = -\frac{\Delta O_2}{\Delta CO_2} \quad (1.2)$$

with both changes expressed in moles.

The oxidative or molar exchange ratio resulting from burning processes will vary with the composition of the organic matter, so that in theory one can distinguish between source types of fossil fuels, for instance, or fossil fuel emissions from biomass burning, based on the relationship between O<sub>2</sub> and CO<sub>2</sub> in the atmosphere [Keeling and Shertz, 1992, Minejima et al., 2012, Steinbach et al., 2011]. The stoichiometry of marine respiration and photosynthesis is not preserved after surface-atmosphere exchange, however, as the ratio of O<sub>2</sub> to CO<sub>2</sub> is altered by the slower equilibration of CO<sub>2</sub> with the atmosphere due to the carbonate equilibrium system. Furthermore, as the world’s oceans are not a long-term sink or source of O<sub>2</sub>, but are a sink for CO<sub>2</sub>, measurements of atmospheric oxygen can be used to constrain the marine uptake of CO<sub>2</sub> [Keeling et al., 1996, 1998b, Stephens et al., 1998]. A data-derived tracer has been standardized to isolate only the portion of atmospheric oxygen that is influenced by marine processes, called atmospheric potential oxygen (APO). APO is defined as:

$$\delta APO = \delta(O_2/N_2) + \frac{1.1}{X_{O_2}}(CO_2 - 350) \quad (1.3)$$

Here 1.1 is the nominal oxidative ratio (OR; see Section 5.1.2) for terrestrial photosynthesis and respiration [Keeling and Manning, 2014, Severinghaus, 1995], and  $X_{O_2}$  is the mole fraction of oxygen in the atmosphere, 0.209392 [Tohjima et al., 2005a]. 350 is a reference CO<sub>2</sub> value, and CO<sub>2</sub> is the in situ mole fraction of carbon dioxide, in ppm.  $\delta APO$  is expressed in per meg [Stephens et al., 1998].

## 1.7 Southern Africa

Southern Africa is dominated by arid regions, with moister climes along the eastern and southern edge of the continent (Figure 1.1). Much of the western and central portions of the region, containing the Namib Desert and the Kalahari, are depopulated [CIESIN, 2005]. The areas with the greatest concentrations of people and industry are in South Africa, and along the coasts. The great majority of the subcontinent is part of a large plateau known as the Great Escarpment (Figure A.1). This topographic feature influences the atmospheric circulation over southern Africa, particularly at the coasts (see Section 2.1.3) [Hills, 1979, Tyson and Preston-Whyte, 2000].

The northern portion of the land surface of southern Africa is dominated by savannas and grasslands. In January, the intertropical convergence zone (ITCZ) is at its southernmost position and its passage to and from this southerly maximum brings summer rains to this region during November–April [Schneider et al., 2014, Tyson and Preston-Whyte, 2000]. During austral winter the ITCZ is in the Northern Hemisphere, and conditions throughout much of the subcontinent are dry, creating a seasonality in precipitation, a cycle to which the activity of the terrestrial biosphere is linked (Figure A.2) [Reason and Mulenga, 1999]. The



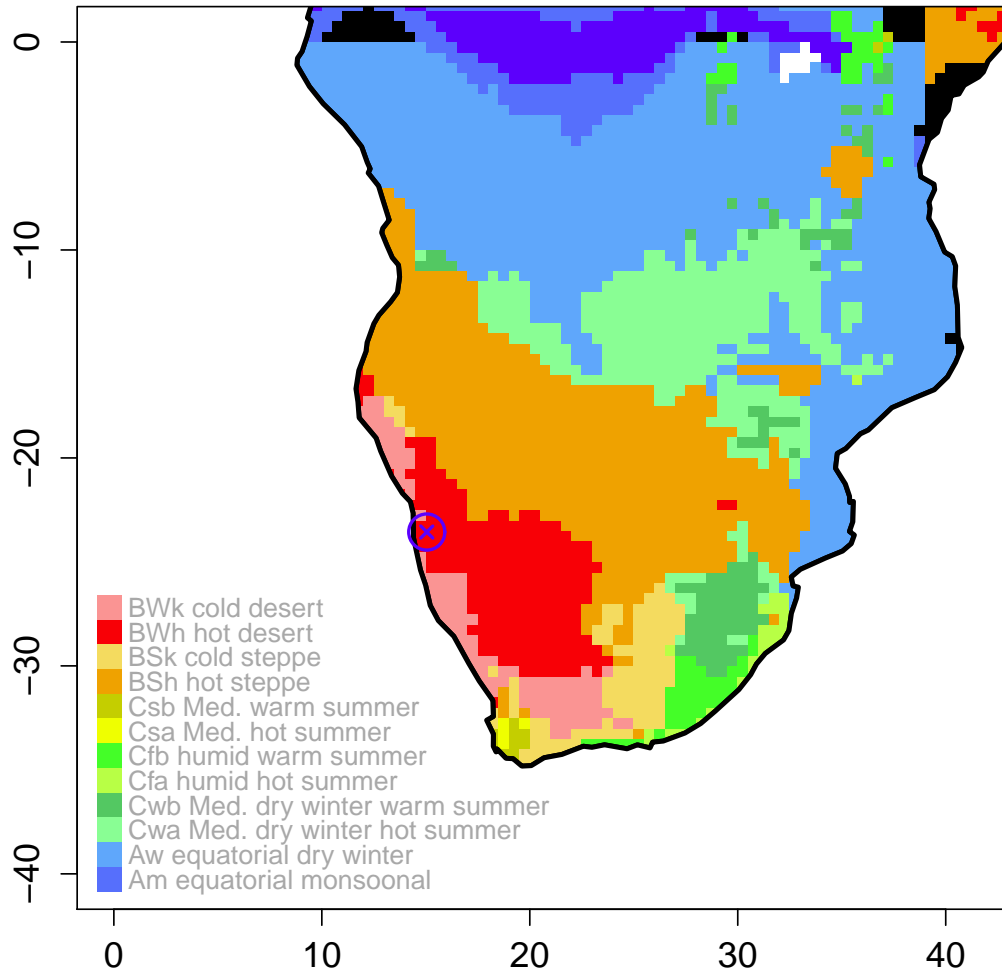


Figure 1.1: The Köppen-Geiger climate zones of southern Africa. Data from [Kottke et al. \[2006\]](#). The “X” marks the location of NDAO. “Med.” stands for Mediterranean.

main synoptic system that produces rainfall over the area are known as tropical-temperate troughs, which are associated with tropical convection, and form when upper atmosphere troughs combine with low-lying tropical disturbances [[Macron et al., 2014](#), [Ratna et al., 2013](#), [Reason and Mulenga, 1999](#)]. Subtropical cut-off lows also bring a substantial amount of rainfall to the region. These structures form when cold air from the stratosphere is isolated from the original source and capped underneath by a pool of warm air; they occur preferentially in March–May [[Singleton and Reason, 2007](#)]. Additionally, the El Niño–Southern Oscillation (ENSO) has a significant effect on precipitation over interannual time scales. During the high/positive phase of the Southern Oscillation (La Niña conditions), the ascending limb of the African Walker cell is over the center of the region, creating dry conditions, whereas during low/negative phase (El Niño conditions), the descending limb of the Walker cell is over central southern Africa, creating unusually wet conditions [[Lyon and Mason, 2007](#), [Muller et al., 2008](#), [Ratnam et al., 2014](#), [Reason and Rouault, 2002](#), [Tyson and Preston-Whyte, 2000](#)]. ENSO is also the major driver of interannual variability in carbon fluxes from southern Africa; ENSO events create positive anomalies in CO<sub>2</sub> flux [[Ciais et al., 2009, 2011](#), [Valentini et al., 2014](#)]. On a global scale, the entire continent accounts for about one quarter

of the interannual variability of the carbon cycle [Valentini et al., 2014, Williams et al., 2007].

On balance, while the entire continent of Africa is probably a small sink for CO<sub>2</sub>, southern Africa considered alone is probably a net source of CO<sub>2</sub> [Bombelli et al., 2009, Ciais et al., 2011, Valentini et al., 2014, Williams et al., 2007]. This is also true for CH<sub>4</sub> and N<sub>2</sub>O. The magnitude of these fluxes is still quite uncertain, and obviously dependent on how much area is integrated [Gurney et al., 2002, Valentini et al., 2014]. Carbon emissions from land-use changes in Africa are larger than the continent’s fossil fuel emissions [Ciais et al., 2011, Valentini et al., 2014, Williams et al., 2007]. South Africa is the largest emitter of CO<sub>2</sub> from the burning of fossil fuels for any African nation, with Zambia, Zimbabwe, the Democratic Republic of the Congo, and Angola also in the top fifteen emitters [Canadell et al., 2009]. Anthropogenic emissions from fossil and biofuels are expected to increase in the coming decades as cities develop and expand; fossil fuel emissions could rival that of biomass burning on the continent by 2030 [Lioussse et al., 2014]. While fossil fuel emissions are low for the depopulated interior (Botswana, Namibia, parts of South Africa), domestic burning of biofuels is an important and unconstrained source of emissions (see Section 1.8). The southernmost coastal region appears, from atmospheric data, to be a net sink. Savanna carbon balances are still quite uncertain; while the biomes is quite productive, biomass burning alters its utility as a long-term sink, and termite activity in these areas could be a substantial source of CH<sub>4</sub> to the atmosphere [Ciais et al., 2011]. The uncertainty in carbon and GHG fluxes for southern Africa is mostly due to data paucity [Ciais et al., 2011]. Atmospheric inversions for Africa are severely hampered by the lack of observations [Gurney et al., 2003, Williams et al., 2007].

## 1.8 Biomass Burning

Biomass burning—referring to the combustion of any type of biomass, whether through prescribed burns, wildfires, or domestic use—is a considerable source of trace gases and aerosols to the atmosphere and has an important role in global ecology, atmospheric chemistry, climate, and human health [Bowman et al., 2009, Crutzen and Andreae, 1990, Langmann et al., 2009]. The savannas and grasslands of southern Africa experience a tremendous number of fires each year during the dry season (typically April to October) [Scholes et al., 1996, Silva et al., 2003, van der Werf et al., 2010]. The humid savanna region between 5–20°S hosts the most fire activity and is a global hotspot for vegetation fires [Hoffa et al., 1999, Justice et al., 1996, Sá et al., 2011, Ward et al., 1996] (Figure 1.2). Inside this latitudinal zone the highest fire activity spans a region shared by Angola, The Democratic Republic of the Congo, and Zambia [Amraoui et al., 2010].

Most savanna fires are anthropogenic [Archibald et al., 2009, Edwards, 1984, Hall, 1984, Lauk and Erb, 2009]. Fires are set by farmers and herders to promote the growth of herbaceous plants for livestock, by hunters and farmers to flush out and manage game, for snake removal, and for landscape management by locals or landscape management authorities [Shaffer, 2010, Sheuyange et al., 2005, van Wilgen et al., 1990]. It is interesting to note that fires are crucial to the maintenance of savanna ecosystems in southern Africa: simulations and empirical studies have shown that most savanna regions would develop into closed-canopy forests without a frequent fire regime [Bond et al., 2005]. Precipitation also exerts a strong control over the distribution and occurrence of fires, by dictating the fuel load [Archibald et al., 2009, Sá et al., 2011]. In the last decade, the incidence of fire has increased in southern Africa by about 10% per year, due mostly to increasing precipitation trends [Andela and van der Werf, 2014]. African savannas and grasslands are likely to be a net carbon sink, as fire emissions are compensated for by the subsequent regrowth after burning [Ciais et al., 2011, Lehsten et al., 2009, Saamak, 2001, Williams et al., 2007].

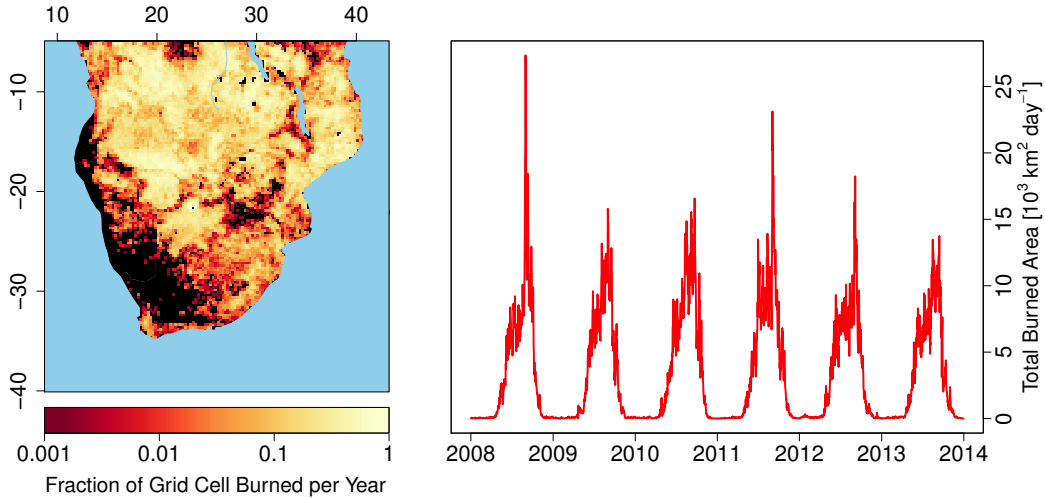


Figure 1.2: The mean fraction of each grid cell that is burned each year (*left panel*), and a time series of the total area burned in the domain per day (*right panel*). Data is from the Global Fire Emissions Database (GFED), Version 4.0 [Giglio et al., 2013].

Excluding South Africa, three quarters of total primary energy consumption in the region comes from biofuels; 81% of households in Sub-Saharan Africa use wood-derived biofuels, with fuelwood usage predominating in rural areas and charcoal in urban centers [AFREA, 2011, Bertschi et al., 2003, FAO, 1999]. In contrast to wildfires, emissions are year-round. Such domestic biomass burning (as distinct from vegetation fires) is also thought to be a globally significant source of trace gases and aerosols to the atmosphere, and particularly prevalent in southern Africa, although there is not as much research on this type of biomass burning as compared to others [Andreae and Merlet, 2001, Bertschi et al., 2003]. Bertschi et al. [2003] estimated that 84% of total  $\text{CH}_4$  emissions from biomass burning in Zambia were from domestic fuel use, and that the contribution of CO was about equal with that from savanna fires. Domestic biomass burning can be composed of fuelwood, nonwoody vegetation, agricultural residues, or dung, in addition to domestic use of charcoal, coal, garbage, and liquid petroleum products; per capita usage rates vary with season, availability, family size, and degree of urbanization [Brocard and Lacaux, 1998, Ludwig et al., 2003, Marufu et al., 1997, 1999, Mulaudzi, 2006].

## 1.9 The African Haze Layer

Due to the extent of these emissions and the vertical stability of the atmosphere over southern Africa (see Section 2.1.2), thick haze persists in the lower troposphere (surface to 3–6 km) and exerts an influence over the region even in areas remote from direct sources, where pollutant levels can rival urban air [Kirkman et al., 2000, Sinha et al., 2003, Swap et al., 2003]. The haze layer is usually well-mixed and is characterized by high levels of aerosols, CO,  $\text{H}_2\text{O}$ ,  $\text{O}_3$ , and other trace species, with the degree of enhancement against the background of these depending on the age of the air [Haywood et al., 2003, Swap et al., 2003]. Most plumes from savanna fires are indistinct from the haze layer within 10–30km of the fire [Yokelson et al., 2003]. Plumes of aged burning products occurring above the boundary layer of trace gases and aerosols resulting from southern African biomass burning are a major source of these products to the southern Atlantic Ocean and the Indian Ocean, primarily the latter [de Laat, 2002, Garstang et al., 1996, Sinha et al., 2004, Thompson et al., 1996, Tyson, 1997,

[Tyson et al., 1996b, Zhang et al., 2010]. Such plumes, of CO<sub>2</sub> for instance, have been shown to extend from southern Africa to as far as Australia [Tyson and D’Abreton, 1998]; one particularly notable event observed during an ENSO year was dubbed the “River of Smoke” [Annegarn et al., 2002]. Model simulations have shown that the climate of southern Africa is sensitive to aerosol loading and GHGs from biomass burning, although the net effect of all direct and indirect effects is uncertain [Paeth and Feichter, 2006, Randles and Ramaswamy, 2010, Roeckner et al., 2006].

Namibia is also subject to these sub-continental trends, although polluted air masses are often separated from the planetary boundary layer by clean layers, or clean air slots (CAS) [Hobbs, 2003]. CAS are thought to be caused by thermally stable, subsiding air from the free troposphere, although mixing of the plume into the haze layer and subsequent recirculation has also been seen [Singh et al., 1996, Sinha et al., 2003, Tyson and D’Abreton, 1998, Yokelson et al., 2003]. During SAFARI 2000, vertical profiles off the Namibian coast showed clean marine air masses close to the surface, underlying the continental outflow characterized by a biomass burning-induced haze region starting at ~2km [Schmid et al., 2003, Sinha et al., 2003, Yokelson et al., 2003].

## 1.10 The Benguela Current Region

The Benguela Current extends poleward from the Angola Current (14–17°S) to the Agulhas Current (35–37°S) along the western coast of southern Africa, and is unique among the other eastern boundary currents in that it is bordered by warmer water at both its northern and southern edges [Hutchings et al., 2009]. The region is considered to represent a biogeochemical province that is distinct from the South Atlantic [Reygondeau et al., 2013]. Generally the Benguela is thought of as being divided into a northern and southern region, separated by the intense upwelling cell at Lüderitz<sup>1</sup> [Fennel, 1999, Veitch et al., 2009]. The system is a major fishery for hake, sardines, and other planktivorous fish, although these are vulnerable to episodes of high sulfide, low oxygen water, the Benguela Niño, and overfishing [Heymans et al., 2004, Hutchings et al., 2009].

Coastal upwelling is a phenomenon in which sustained northerly winds (Northern Hemisphere) or southerly winds (Southern Hemisphere) push the surface waters away from shore due to Ekman transport [Mann and Lazier, 1996, Sverdrup, 1938]. The advected surface water is then replaced through upwelling of bottom water from the continental slope; as water from these depths is usually quite old, much or most of the organic matter has been remineralized during its long storage away from the euphotic zone. As a result, upwelled waters are characterized by high nutrient concentrations and cold temperatures. Phytoplankton blooms are common after upwelling events, as nutrient limitation of growth is removed. Accordingly, many of the eastern boundary currents of the world are highly productive marine systems. There are five major coastal upwelling regions in the world, namely the Peru Current, the Canary Current, the California Current, and the Benguela current; the exception being the Somali Current, which is not an eastern boundary current, but where an upwelling region is created by the monsoon [Mann and Lazier, 1996].

The Benguela upwelling system is the most productive of the eastern boundary-associated upwelling zones, with an annual primary productivity of approximately 0.37 PgC [Carr, 2002] and a maximum areal rate of ~3 gC m<sup>-2</sup> day<sup>-1</sup> [Carr and Kearns, 2003], qualifying it as a hypertrophic system under Nixon’s classification scheme [Nixon, 1995]. Organic carbon

<sup>1</sup>At one point it was reported that the town had been renamed in 2013 to !Nami≠Nûs, as part of a larger effort to restore indigenous names to places named during colonial times. This was a misunderstanding relating to the ambiguous wording of a statement by President Hifikepunye Pohamba, as it was later clarified to pertain to the constituency only [Staff Reporter, August 27, 2013].

settling fluxes on the continental slope were found to be on the order of  $10\text{--}100\text{ gC m}^{-2}\text{ yr}^{-1}$  [Aspetsberger et al., 2007, Inthorn et al., 2006]. The high productivity to be found in this region is mainly a result of the particularly strong and near-continuous nature of the upwelling, the magnitude of which is the largest of the major eastern boundary currents [Bakun and Weeks, 2004].

The magnitude of the advection of the ocean surface layer has considerable consequences for the ecology and biogeochemistry of the region. While phytoplankton populations thrive in this region, herbivorous zooplankton populations, with their longer generation times, are unable to keep pace with the primary producers [Bakun and Weeks, 2004], resulting in the underutilization of the carbon fixed by autotrophs and in significant deposition of autochthonous organic matter to the sediments. It has been suggested that this situation has been greatly exacerbated by the overfishing of sardine populations in the 1970s: sardines are very effective grazers in other coastal upwelling systems and, unlike zooplankton, can move against the offshore transport [Bakun and Weeks, 2004, Boyer, 1996]. The sardine stocks have yet to recover from this overfishing, and their absence may have enabled a large increase in the number of jellyfish [Lynam et al., 2006].

## 1.11 The Namib Desert

The Namib Desert is one of the driest areas on Earth, with annual precipitation usually less than  $25\text{ mm yr}^{-1}$ , although consecutive years without rain are not unusual [Hutchinson, 1995]. A distinctive feature of the area is the common occurrence of fog ( $60\text{--}200\text{ days yr}^{-1}$ ), a result of the nearby cold waters of the Benguela Current; fog is a larger source of moisture than rainfall to the region [Lancaster et al., 1984, Olivier and Stockton, 1989, Shanyengana et al., 2002]. The Köppen-Geiger climate classification is BWh (“hot desert”) or sometimes BWk (“cold desert”) [Kottek et al., 2006]. The Namib Desert extends  $\sim 2000\text{ km}$  along the coast and some  $150\text{ km}$  inland where it terminates at the Great Escarpment. The biomes bordering the Namib are classified as xeric shrublands, drylands or savannas [Olson et al., 2001].

## 1.12 Gobabeb

NDAO ( $23.563118^{\circ}\text{S}$ ;  $15.045660^{\circ}\text{E}$ ) is located at Gobabeb, in the Erongo Region,  $\sim 600\text{ m}$  from Gobabeb Research and Training Centre (GTRC), a desert research station. The station is situated at an elevation of  $408\text{ m}$  above sea level,  $\sim 50\text{ km}$  from the coast, along the Kuiseb River, an ephemeral river that demarcates the northern margin of the Namib Sand Sea from a gravel plain region to the north. There is significant vegetation along the river, though much of it is dead or dormant. In the Sand Sea, years with rain can trigger the growth of psammophilous plants such as the Inara (*Acanthosicyos horridus*) [Sjöskog, 2008].

All of the facilities at Gobabeb are solar powered, although there is a backup generator that runs occasionally when there is fog or if the load on the system is too high. The primary goals of GTRC are to educate and study sustainable living in arid environments and to study dryland ecology. The total number of staff at Gobabeb fluctuates quite a bit but is usually under 30. In recent years atmospheric research has become an increasingly important aspect of the scientific activities at Gobabeb, due to its remote location. Karlsruhe Institute of Technology operates a land surface temperature validation project, as well as a Baseline Surface Radiation Network station. A group from the University of Basel makes micrometeorological measurements including  $\text{CO}_2$ , water vapor, and energy fluxes. From the perspective of NDAO, the most relevant independent atmospheric research activity in the

area is the NOAA ESRL flask sampling site (station ID “NMB”) in the dunes close to the station, the data from which is presented and discussed in Section [2.1.4](#).

## 2

# The Representativeness of Observations at NDAO

### 2.1 Introduction

The atmosphere is generally described as well-mixed. A conservative tracer emitted at any location on the surface will be widely distributed throughout the troposphere in both hemispheres in less than one year. Over shorter time scales, it is also evident that a measurement must be downwind of a local source or sink to detect its influence on the time series. Hence, in order to interpret stationary measurements that are influenced by surface fluxes, it is necessary to consider atmospheric transport to their location. The time interval considered also determines the amount of spatial information that is integrated. For example, the yearly average CO<sub>2</sub> mole fractions measured at the South Pole will be affected by fluxes of CO<sub>2</sub> in the Northern Hemisphere. The first ground stations, such as at Mauna Loa [Pales and Keeling, 1965], were selected as they were determined to be background sites—locations where the measurements were as representative of as large a volume of air as possible, and uninfluenced by near-field fluxes [Tans et al., 1990].

In this chapter the spatial representativeness (as a function of time) of the NDAO time series is discussed in the context of general, regional, and mesoscale circulation. Atmospheric transport to the station was modeled for the operable period and compared to the in situ meteorological record. The NOAA flask time series from the nearby site NMB was also analyzed to extend the current observations back in time, and to assess the seasonal cycle and secular increase in greenhouse gases as seen from the station location.

#### 2.1.1 The Hadley Circulation

A feature of the general circulation with particular relevance to the study region is the southern Hadley Cell. Air ascends in the region of the equator due to high insolation at the intertropical convergence zone (ITCZ), and is replaced by a large-scale meridional pressure gradient—which is deflected by the Coriolis force—resulting in the trade winds [Hadley, 1735, Lorenz, 1967, Webster, 2004]. This pattern creates a global circulation cell that forms a zonal band, causing large-scale subsidence in the subtropics around 30°N or S, transporting heat poleward, exchanging air between the upper troposphere and stratosphere, and causing persistent climatic patterns in precipitation and temperature at the surface [Newell et al., 1972, Quan et al., 2004]. It is this region of large-scale subsidence that causes the zonal band of deserts of which the Namib is a part [Dirmeyer and Shukla, 1996, Webster, 2004].

The width and location of the southern Hadley cell, however, varies seasonally [Cook, 2003, Kang and Lu, 2012]. This is the basis for the distinct seasonality in transport modes seen at NDAO, which will be shown later. During austral summer, atmospheric water vapor is higher, atmospheric pressure is lower, and strong equatorward winds carry marine air

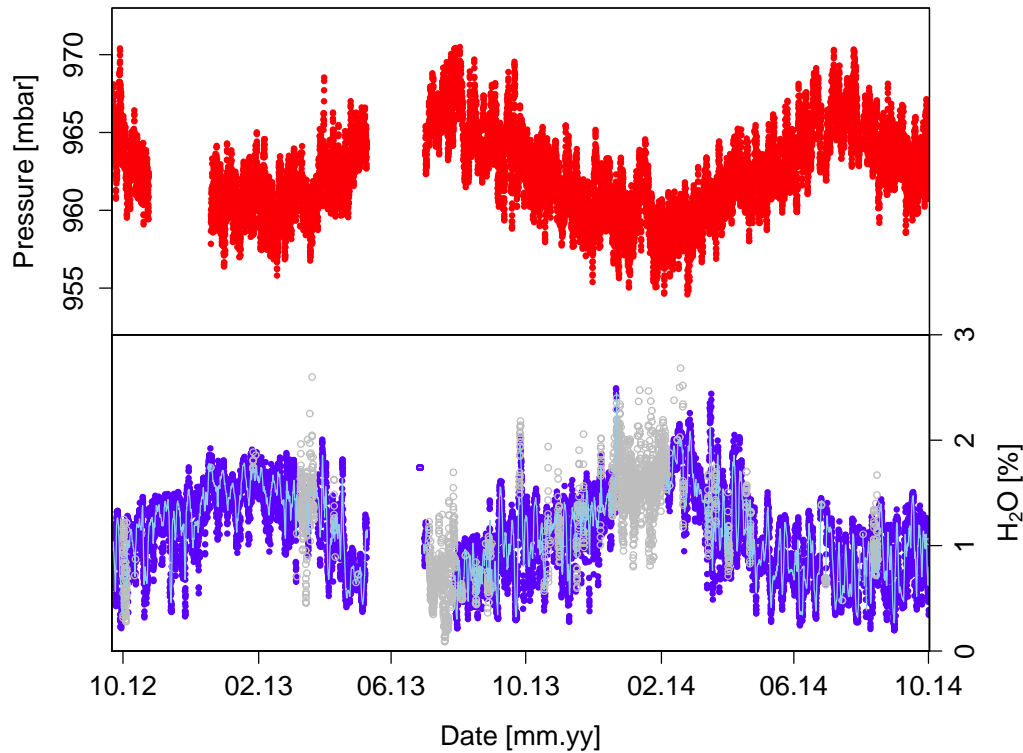


Figure 2.1: Atmospheric pressure and water vapor as seen at NDAO, aggregated to 1-hour means. Pressure is measured with a sensor on the meteorological array. The absolute mole fraction of water vapor is determined with the CRDS after applying a correction. Missing data from the CRDS (blue dots) is supplemented with calculated water vapor mole fractions from the meteorological data (gray dots). Also plotted is a 24-hour running mean (skyblue line). Note that relative humidity shows the same seasonality as water vapor (see Figure 4.2).

masses inland. At this time the descending limb of the southern Hadley cell is well south of NDAO and the ITCZ has moved into the Southern Hemisphere, but is still appreciably to the north of the station. In austral winter, the Hadley cell moves northward and the station is underneath the region of large-scale subsidence, resulting in drier, more stable conditions and higher atmospheric pressure (Figure 2.1).

### 2.1.2 Regional Circulation

The seasonality induced by the general circulation also has an effect on the different modes of synoptic variability. The dominant or most characteristic mode of atmospheric circulation over southern Africa is anticyclonic around a continental high pressure region (Figure 2.2). This mode is most prevalent during austral winter—June through August, roughly—as conditions are more favorable for its formation during the period of the year when the region of large-scale subsidence is overhead [Newell et al., 1972, Tyson et al., 1996b]. In contrast, easterly wave disturbances prevail during the austral summer months.

The other common modes, ridging highs and westerly wave disturbances, have less seasonality and can occur throughout the year [Tyson et al., 1996b]. Ridging anticyclones are a result of westerly disturbances from the South Atlantic Anticyclone, which follow the west-erlies but ridge over the continent [Tyson and Preston-Whyte, 2000, Tyson et al., 1996b].



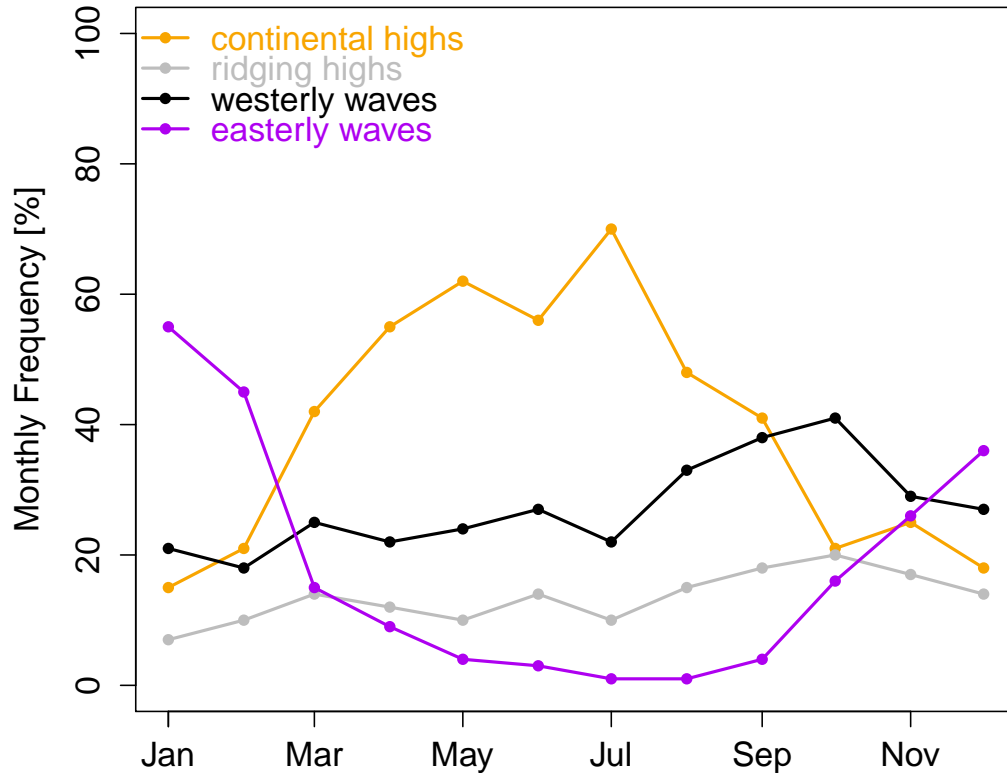


Figure 2.2: Climatology of the major circulation modes of the troposphere over southern Africa. Data is replotted from [Tyson et al. \[1996b\]](#).

Westerly waves also bring moisture and air masses from the South Atlantic, every 6 days on average, and disrupt the stability created by the semi-permanent continental high [[Swap et al., 1996](#), [Tyson et al., 1996b](#)]. Other synoptic modes are possible, of course, and in practice atmospheric circulation does not always conform to these generalizations.

To the west of the continent, the South Atlantic Anticyclone<sup>1</sup> is the most persistent and dominant feature [[Richter et al., 2008](#), [Venegas et al., 2000](#)]. The anticyclone shifts about 13° zonally throughout the course of the year, reaching its westernmost extent in August [[Reason et al., 2006](#), [Vigaud et al., 2009](#)]. The eastern boundary of this pressure system is composed of equatorward winds (Figure 2.3). In this region wind speeds are strong and defined enough to be classified as a coastal jet, according to [Nicholson \[2010\]](#). This jet is analogous to ones found in other eastern boundary current systems. Such coastal jets are a distinct type of low-level jet in that they occur alongshore and are driven, in part, by a land-ocean temperature gradient, and affected by local topography [[Parish, 2000](#)]. The core of the jet is typically located beneath the trade wind inversion, at the top of the marine boundary layer [[Nicholson, 2010](#)]. Wind speeds in the structure are strongest in the area with the highest upwelling, and the seasonality mirrors that of the coastal upwelling, due to the positive feedback between the two: as winds increase in magnitude, upwelling increases and SST drops, in turn strengthening the jet [[Nicholson, 2010](#), [Parish, 2000](#)]. The core is an average of 650 km offshore, at a height of 200–800 m a.s.l., ranging from 17°S to 25°S; it is weakest in May and June, but fairly persistent throughout the year with a maximum in October [[Nicholson, 2010](#)].

<sup>1</sup>Sometimes the South Atlantic High, or St. Helena High

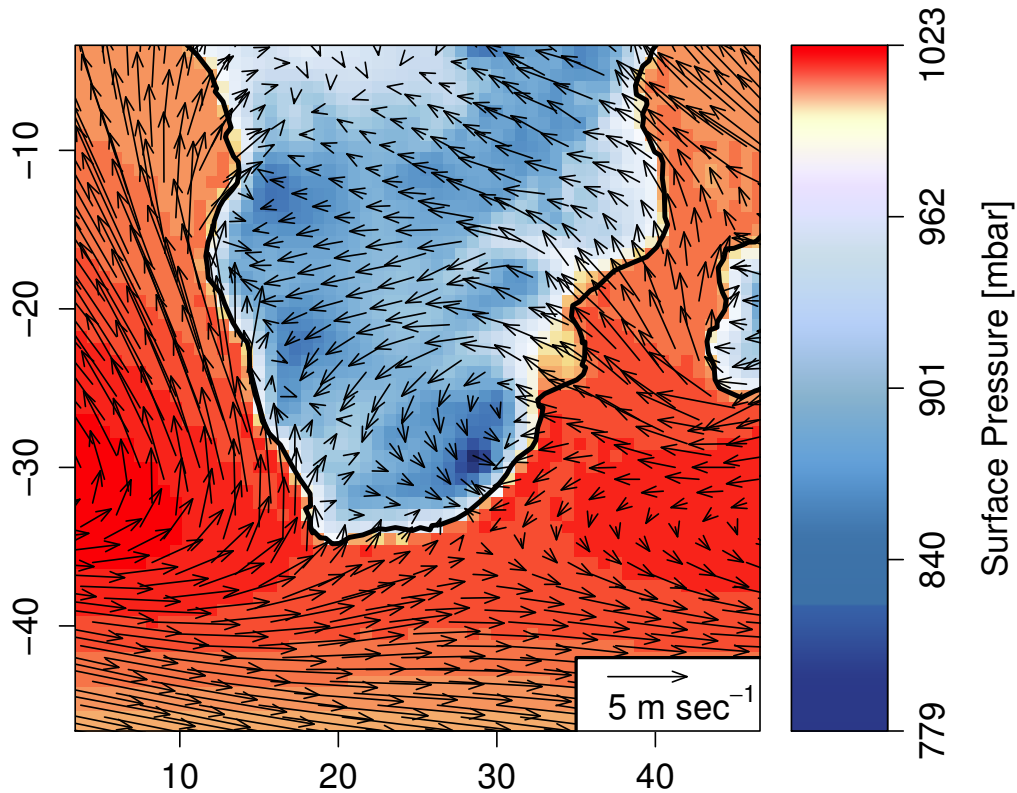


Figure 2.3: Mean sea level pressure and 10 m wind speed over southern Africa for October 2012–October 2014. Data is from the ECMWF ERA-Interim reanalysis [Dee et al., 2011].

The Angola Low is another key feature of southern Africa (see Figure 2.3), due to its role in regional rainfall as a moisture source [Hart et al., 2010, Kuhnel, 1989, Lyon and Mason, 2007, Reason and Mulenga, 1999, Reason et al., 2006]. This heat low has intensified in recent years, thought to be due to the shift towards a more positive Southern Annular Mode, which in turn is linked to the Antarctic ozone hole [Manatsa et al., 2013]. Heat lows are surface disturbances characterized by cyclonic flow, and often form in arid regions with high insolation and a horizontal gradient in temperature, such as at a coastal location [Rácz and Smith, 1999]. The Angola Low and the South Atlantic Anticyclone have a strong connection and act in concert to drive equatorward winds in the region of NDAO. The cyclonic circulation around this low pressure region develops around October and strengthens through February [Piketh and Walton, 2004, Reason et al., 2006].

Also of note are the presence of absolutely stable layers (ASL) above the sub-continent. This well-established feature was noted and investigated during the SAFARI<sup>2</sup> and the NASA Transport and Atmospheric Chemistry near the Equator–Atlantic (TRACE A) campaigns, along with independent aircraft campaigns and modeling studies. The consensus is that there exist one or two temporally persistent ASL in the mid- to upper troposphere [Cosijn and Tyson, 1996, Garstang et al., 1996, Piketh and Walton, 2004, Tyson and Preston-Whyte, 2000]. ASLs, i.e., a layer of the atmosphere where the lapse rate is smaller than the saturated adiabatic lapse rate, can form in regions with large scale subsidence, due to adiabatic

<sup>2</sup>There were two SAFARI campaigns; the first was the South African Fire—Atmospheric Research Initiative (1992). The second was also named SAFARI, but in that case the acronym stood for the “South African Regional Science Initiative” (2000).

warming. These layers were found to preferentially occur at  $\sim 500$  hPa,  $\sim 700$  hPa, and  $\sim 850$  hPa [Freiman and Tyson, 2000, Piketh and Walton, 2004, Swap and Tyson, 1999, Tyson and Preston-Whyte, 2000, Tyson et al., 1996b]. Such discontinuities inhibit vertical mixing between the lower to upper troposphere.

The ASL concept grew partly from the distinct and visible haze layers that commonly occur over southern Africa [Hobbs, 2003], but primarily from radiosonde soundings. Recently, the idea that ASLs preferentially form at two or three geopotential heights has been questioned by Burger and Piketh [2013], using a large dataset of more than 90,000 soundings. The authors point out that data analysis during the SAFARI period of radiosonde data was often restricted to a few heights due to limited computational resources, and that if ASLs are looked for at all observed heights, as many as 100 can be found on a given day. ASLs tend to be found preferentially at certain heights, such as the lower 2 km of the atmosphere, or between 500 and 600 hPa. Thus it seems likely that while the stability of the atmosphere at certain heights, due to regional subsidence and anticyclonic conditions, is well-established and unquestioned, the attribution of this stability to one or two ASLs is likely due to a sampling artifact.

Recirculation of air around the high pressure zone over southern Africa is also an interesting characteristic of the region. Recirculation is defined such that an air mass that passes a meridional plane placed in the center of the anticyclone is recirculated; such recirculation events can last for up to 20 days, averaging to 4–10 days [Tyson et al., 1996a]. One study determined that a little less than half of the mass of aerosols being transported across the continent during the period of a year were recirculated material [Tyson and D’Abreton, 1998]. This phenomenon, in conjunction with the inhibited vertical mixing during anticyclonic conditions, means that aerosols, terrestrially-sourced trace gases, and other continental influences can be concentrated in the southern African boundary layer, and that horizontal transport is maximized [Piketh et al., 2002, Tyson, 1997, Tyson et al., 1996a, 2001].

### 2.1.3 Mesoscale Circulation and the Thermo-Topographic Wind System

The central Namib features pronounced mesoscale circulation patterns that are manifest in the wind field as a distinctive diurnal cycle. This local thermo-topographic wind system has been studied by Tyson and Seely [1980], Lancaster et al. [1984], Lancaster [1985], Lindsay and Tyson [1990], and [Brimelow and van Heerden, 1996]. The system was modeled by Hänsler [2011], with good agreement for the Gobabeb site. For much of the year the near-surface wind field is dominated by mesoscale features, which are said to be decoupled from synoptic activity [Lengoasa et al., 1993]. Goldreich and Tyson [1988] compared the ratio of diurnal variability in wind speed to inter-diurnal variability and found that the Namib was unique in its high degree of mesoscale wind activity when compared to the whole sub-continent. This is due in part to the large temperature contrast between land and ocean in the region, and the high relief between the coastal plain and the Great Escarpment [Tyson and Seely, 1980].

There are five different wind systems in the Namib which are referred to in the literature:

- **Sea breeze (SB).** Strong, southwesterly winds that develop in the morning along the coast and are carried towards the Great Escarpment, penetrating as far inland as Gamsberg (170 km from the coastline) [Lindsay and Tyson, 1990]. The pressure gradient is zonal but due to the Coriolis force the wind direction is SW<sup>3</sup>. The sea breeze reaches Gobabeb in the late afternoon and stops at ground level shortly after

<sup>3</sup>For Gobabeb, 52 km from the coast, and with an average wind speed of 8–10 m sec<sup>-1</sup>, the Rossby number is about 1, hence the Coriolis force is not negligible [Jackson, 1954].

nightfall as the mountain-plain wind (MPW) or plain-mountain wind (PMW) develops, although it persists for a few more hours at the 500–700 m level. The sea breeze occurs year-round.

- **Land breeze (LB)**. The counterpart to the sea-breeze, this wind is weaker, more shallow, and less frequent than the sea breeze.
- **Plain–mountain wind (PMW)**. A northwesterly wind driven by the temperature contrast between the plateau and the large expanse of stone desert to the north of Gobabeb. This is one of the strongest and most consistent modes in the central Namib, although it is less common and weaker during austral winter.
- **Mountain–plain wind (MPW)**. From the SE, occurring at night when the interior has cooled faster than the gravel plains. The MPW is a weaker flow compared to the SB or PMW, and occurs almost exclusively during austral winter. The wind develops during the late evening and blows throughout the night until sunrise.
- **Bergwind (BERG)**. Also known as föhn, the bergwind is synoptically induced by a high pressure system over the interior of southern Africa and a low pressure system at the coast [Tyson, 1964]. The dry air heats adiabatically as it descends the Escarpment. The winds can be quite intense and occasionally cause sandstorms at Gobabeb.

Such wind systems are likely to cause distinct variations in atmospheric composition, since Gobabeb sits in the middle of a gradient in the atmosphere between land and ocean. This is evident in the zonal extent of fog and rain in the central Namib, which follows a declining gradient from the coast to the Escarpment [Eckardt et al., 2013, Hänsler, 2011, Juergens et al., 2013, Lancaster et al., 1984].

#### 2.1.4 NOAA NMB Surface Flask Record

Surface flask samples have been taken near Gobabeb (Figure 2.4) sporadically since 1997 as part of the U.S. National Oceanic and Atmospheric Administration Earth System Research Laboratory Global Monitoring Division (NOAA ESRL GMD) Carbon Cycle Cooperative Global Air Sampling Network. Data coverage is generally low and no samples were taken between March 2001 and July 2006, although after this lacuna the coverage has more than doubled. For a record spanning 5,357 days, approximately 200 days were sampled. Data paucity aside, this historic record augments the in situ measurements at NDAO and affords an opportunity to assess how well large-scale and long-term trends of greenhouse gases are represented through observations at Gobabeb.

The data that are available from the NOAA ESRL flasks are mole fractions of CO<sub>2</sub> [Conway et al., 2011], CH<sub>4</sub> [Dlugokencky et al., 2010], N<sub>2</sub>O, CO [Novelli and Masarie, 2010], SF<sub>6</sub>, and H<sub>2</sub> [Novelli et al., 2010]; also measured are the  $\delta^{13}\text{C}$  [White and Vaughn, 2011] and  $\delta^{18}\text{O}$  [White and Vaughn, 2009] isotopic ratios of CO<sub>2</sub>.

## 2.2 Methods

In this study atmospheric transport was simulated for the station-operable period. Modeled back-trajectories and footprints were compared to in situ meteorological data to assess their accuracy. Back-trajectories were then analyzed to determine the spatial representativity of GHG observations at NDAO as a function of time. Finally, the NMB flask record was used to compare the seasonal cycle and secular increase seen from Gobabeb to other sites in the Southern Hemisphere.

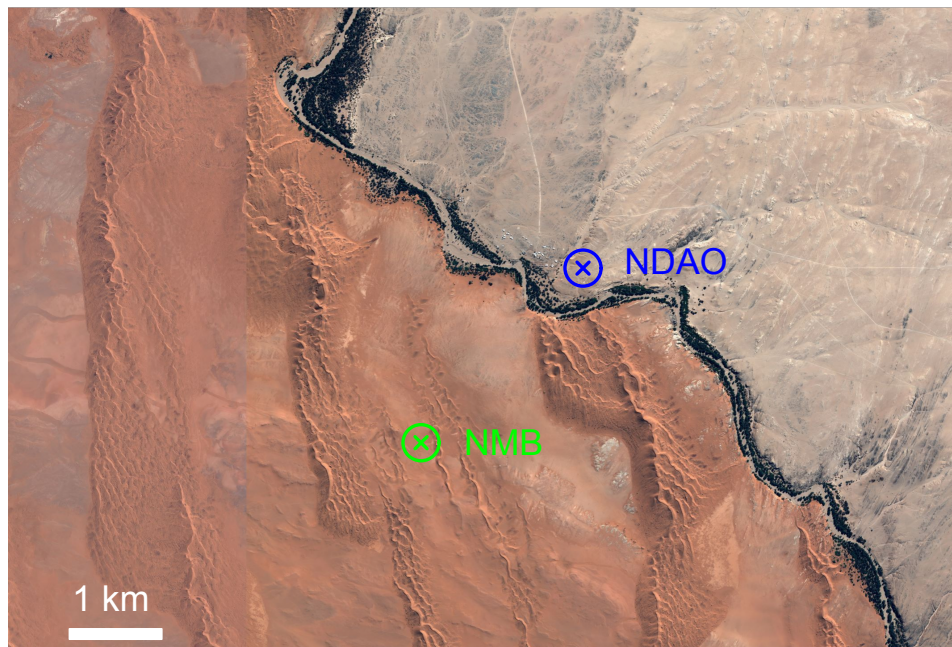


Figure 2.4: Location of the NOAA ESRL flask sampling site (NMB) and NDAO.

### 2.2.1 Atmospheric Transport Modeling

Two transport models were used, one with a regional domain and the other with a global domain. The regional model employed was the Stochastic Time-Inverted Lagrangian Transport (STILT) model [Lin et al., 2003]. The global model employed was the HYbrid Single Particle Lagrangian Integrated Trajectory (HYSPLIT) 4 model [Draxler, 1999, Draxler and Hess, 1997, 1998].

Back-trajectories, which trace the path of a particle from a receptor point backwards in time, can give some impression of the recent origin of air masses that pass over the station. Trajectories were run backwards with the HYSPLIT model from the NDAO tower for 120 hours. The selection of this time length was fairly arbitrary—long enough to see synoptic patterns, but as short as possible, since longer trajectories usually have greater errors. A new trajectory was calculated every six hours, starting at 0:00 UTC, i.e., at 1:00, 7:00, 13:00, and 19:00 local time. The model was run with a spatial resolution of  $1^\circ \times 1^\circ$  and a temporal resolution of 1 hour. A vertical cut-off of 10 km a.g.l. was used. Meteorology was not calculated in the model but taken as model input; the fields selected were from the National Center for Environmental Prediction (NCEP) Global Data Assimilation System (GDAS). It is important to note that back-trajectories can contain considerable errors and should not be interpreted too closely, particularly if they are run for several days or more [Stohl, 1994]. In data-poor regions, such as the South Atlantic, trajectories driven with different meteorology can diverge on the order of several thousand kilometers after a few days [Pickering et al., 1994].

The zone of surface influence around a ground-based station is better realized as a 2-D footprint, either in terms of concentration or flux [Gloor et al., 2001, Horst and Weil, 1994, Schmid, 2002]. This directly quantifies the influence of surface fluxes on the concentration, and giving the potential effect of a unit of flux on the mole fraction or mixing ratio, e.g., in  $\text{ppm}/\mu\text{mol m}^{-2} \text{sec}^{-1}$ . Footprints were calculated using the STILT model. STILT was run with European Centre for Medium-Range Numerical Weather Prediction (ECMWF) meteorological fields on a  $0.25^\circ \times 0.25^\circ$  grid. The domain chosen to run the model was  $5^\circ\text{N}$

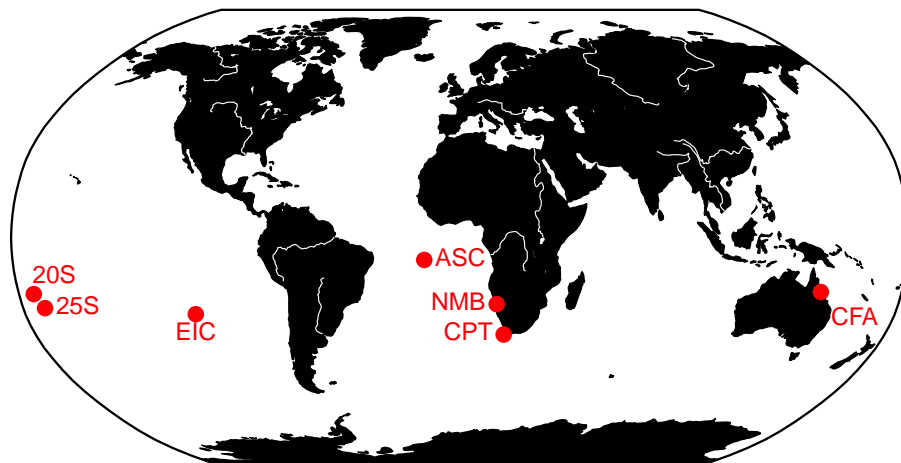


Figure 2.5: Location of marine background flask sampling sites. The sites are, from left to right, **20S**: Pacific Ocean (shipboard measurement) 20°S, 174°W, NOAA; **25S**: Pacific Ocean (shipboard measurement) 25°S, 171°W, NOAA; **EIC**: Easter Island, Chile, NOAA; **NMB**: Gobabeb, Namibia, NOAA; **CPT**: Cape Point, South Africa, SAWS; **CFA**: Cape Ferguson, Australia, CSIRO.

to -45°S; -30°W to 40°E. The model was run backwards for 10 days at one-hour intervals, producing a 10-day integrated footprint for each hour of the day.

### 2.2.2 Flask Data Treatment

In addition to the NMB site, several other flask sampling sites from the NOAA and the Australian Commonwealth Scientific and Industrial Research Organisation (CSIRO) networks were selected for comparison to the NMB record (Figure 2.5 and Table B.1). Each site was a coastal or marine site within 5° latitude of NDAO. The datasets were from a CSIRO site located at Cape Ferguson, Australia (CFA), and three NOAA sites: Easter Island (EIC), and two shipboard measurement sites, at 20°S, 174°W (20S) and 25°S, 171°W (25S). Also included were the NOAA flask sampling site on Ascension Island (ASC), and the continuous measurement site located at Cape Point (CPT), South Africa, run by the South African Weather Service (SAWS).

NOAA ESRL flasks from the NMB site are taken in pairs, which means that if there is a fault with one flask both should be discarded. Data that had been flagged for analytical reasons were excluded entirely, although flask pairs whose absolute difference exceeded WMO/GAW recommendations (see Table 3.2) were used in some instances. In such cases this is clearly specified. Data flagged as preliminary were included in the analysis. All data were acquired from the WMO/GAW World Data Centre for Greenhouse Gases. At the CSIRO site, flasks are taken in triplicate, so if the difference between one flask and the other two was greater than the WMO/GAW compatibility guideline, the single flask was discarded and the remaining two were used. All pairs and triplicates were taken as a mean.

For CPT, continuous observations were available. A filtered, clean marine background time series of CO<sub>2</sub>, CO, and CH<sub>4</sub> was extracted from the full half-hourly Cape Point Observatory (CPT) record. The CPT background data is generated by selecting only observations which have a corresponding wind direction between 170° and 320°, and a <sup>222</sup>Rn concentration less than 350 mBq m<sup>-3</sup> [Brunke et al., 2004]. Data selected in this manner is considered to be

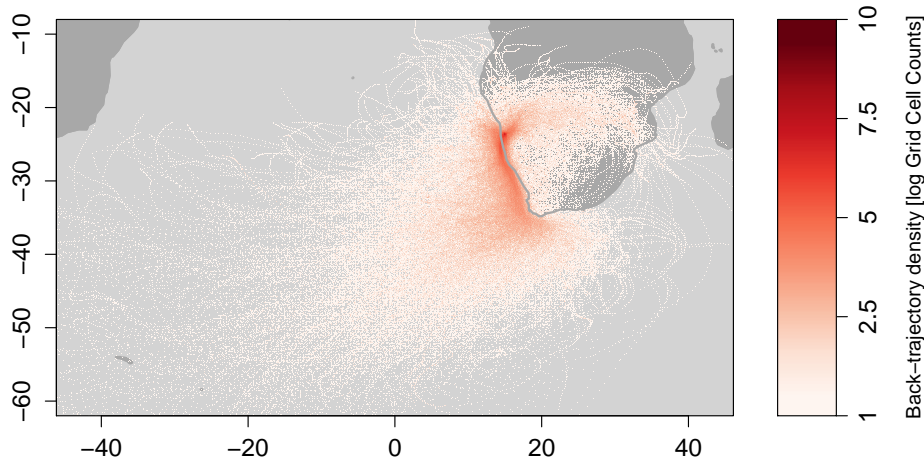


Figure 2.6: Aggregated 5-day back trajectories calculated every 6 hours (1:00, 7:00, 13:00, 19:00 local time) with the HYSPLIT model from October 1, 2012–October 1, 2014. The color gradient shows the log of the number of trajectory points in each  $0.1^\circ$  grid cell.

widely representative of the Southern Hemisphere marine background; the CPT is one of a few global GAW stations.

The isolation of trends and seasonal cycles was done following an approach similar to that of Thoning et al. [1989] and Dlugokencky et al. [1994]. After aggregating to daily means, a smooth curve was fit to the data by fitting a second-order polynomial and up to four harmonics, depending on the significance these terms. Significance was deemed present if the p-value of the F statistic of the null hypotheses test that the coefficient was equal to zero was less than 0.05. Outliers were identified as points that were more than two standard deviations from the resulting curve; these points were then excluded and the curve refit [Tans et al., 1990]. The residuals of this curve were linearly interpolated and subsequently filtered to remove high-frequency variations using a low-pass Butterworth filter with a cut-off frequency of  $\omega = 80$  days. These filtered residuals were then fitted with a smoothing spline ( $\lambda = 0.0015$ ) to obtain the interannual variability. The seasonal cycle was then taken as the sum of all harmonic terms from the final fitted curve, plus the filtered residuals. Average growth rates were calculated as the mean rate of increase after deseasonalizing the final fitted curve and adding the filtered, smoothed residuals.

## 2.3 Results and Discussion

### 2.3.1 Back-Trajectories

Three major structures are readily seen in the HYSPLIT back-trajectories of air from NDAO: the South Atlantic High, the westerlies, and the anticyclone over southern Africa (Figure 2.6). The majority of trajectories pass over the South Atlantic or Southern Ocean (sometimes as far away as the Drake Passage in 5 days) and enter the South Atlantic high pressure system, passing Cape Point and running directly up the coast to NDAO. The other major trajectory pathway captured by HYSPLIT was located in the anticyclonic circulation around the sub-continent. These trajectories travel westwards through Mozambique, Zimbabwe, and Botswana, also touching on the southern portions of Angola, Zambia, and the Democratic Republic of the Congo.

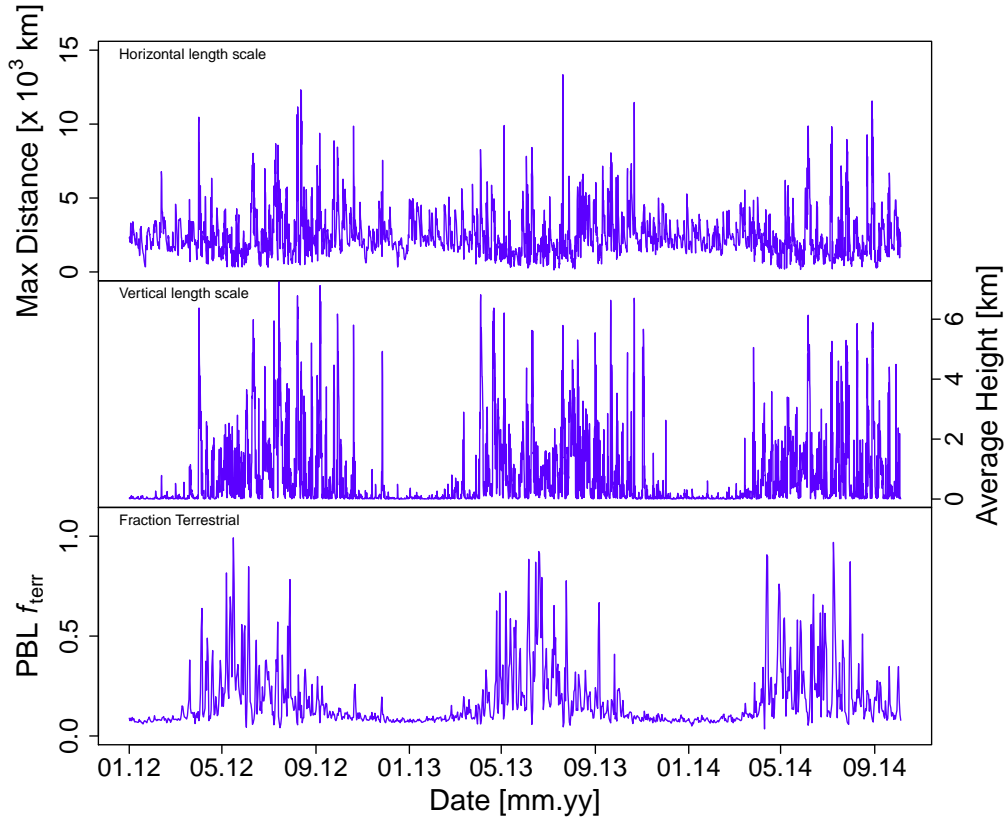


Figure 2.7: *Top panel*: The horizontal length scale of individual back-trajectories, determined as the maximum distance a particle has traveled from NDAO. The scale is in  $10^3$  km. *Middle panel*: the vertical length scale, taken as the average height of each trajectory; note that the model has a vertical cut-off of 10 km. *Bottom panel*: the fraction of each trajectory which resides over land, PBL  $f_{terr}$ , for trajectory points under 1 km, intended to be representative of trajectories in the planetary boundary layer (PBL).

Back-trajectories also exhibited a distinct seasonality. During the height of summer (December–February), trajectories were exclusively marine in origin, while during austral winter (June–August) a mix of marine and terrestrial trajectories were seen (Figure A.3). However, throughout the entire year, the area with the greatest density of back-trajectories, and the most persistent feature represented in HYSPLIT, is the coastline, where the alongshore winds from the South Atlantic High and the Benguela jet occur (see Section 2.1.2).

Selecting only trajectories that were below 1 km made no difference in the distribution. This is because there is a seasonality in the height of air mass recent origin (Figure 2.7, *middle panel*). This annual cycle reflects the formation of the continental anticyclone during periods of large-scale subsidence. Likewise, if air masses are categorized based on the amount of time they reside over land, the degree of terrestrial influence also displays the same seasonality (Figure 2.7, *bottom panel*). There is also a strong seasonal effect on the horizontal range of transport to the site. While trajectories travelled farther over the previous five days during summer, on average, the highest variability and the longest trajectories were found in the winter months (Figure 2.7, *top panel*).



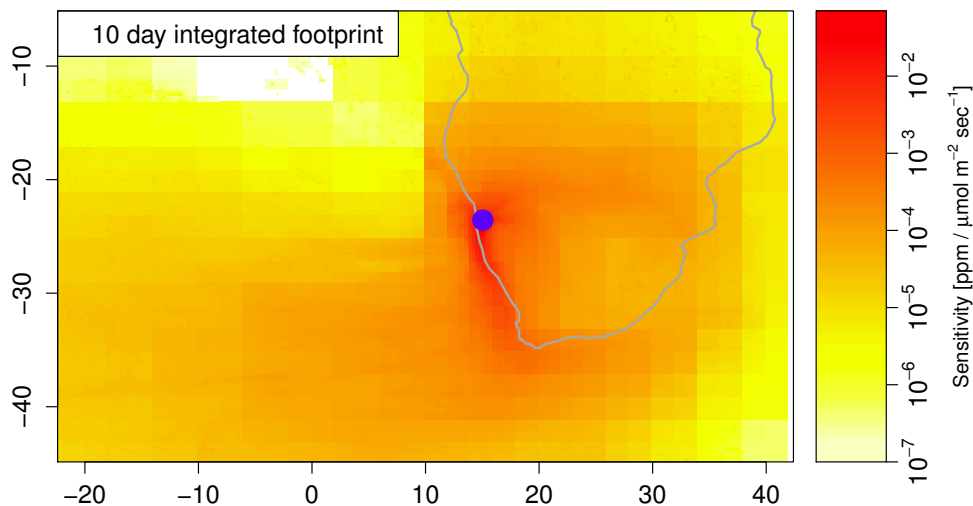


Figure 2.8: The average integrated 10-day footprint, expressed as the sensitivity of the mole fraction of  $\text{CO}_2$  as measured at the receptor point (NDAO), to a unit of flux in each grid cell. Modeled with STILT, for the calendar year 2013. The pixel size increases in distance from NDAO due to the dynamic grid resolution of the model. Location of NDAO is given by a blue dot.

### 2.3.2 Footprints

2-D footprints (Figure 2.8), calculated with the STILT model for  $\text{CO}_2$ , displayed similar patterns in transport, which is not surprising given that the STILT model is a descendant of HYSPLIT [Lin et al., 2003]. Nevertheless, it is encouraging since the models had different resolutions ( $1^\circ$  for HYSPLIT and  $0.25^\circ$  for STILT) and meteorology (NCEP GDAS for HYSPLIT and ECMWF for STILT). Footprints and back-trajectories are also not directly comparable, since footprints explicitly show the sensitivity of the measurements to the entire surface within the domain, (but of course give no information about actual fluxes). The expected seasonal difference in sensitivity due to shifts in transport was also observed (Figure A.4.)

### 2.3.3 Comparison of Back-Trajectories with in situ Meteorology

Given its coarse resolution, it is unrealistic to expect that the HYSPLIT model would perfectly simulate the local wind system in the central Namib. However, the model does capture the shift from the marine sectors to the terrestrial sectors at the end of austral summer (Figure 2.9). This also implies that the local wind system is not largely decoupled from synoptic patterns as suggested by some authors [Hänsler, 2011, Lengoasa et al., 1993]. Or rather, the concept can be qualified: on a diurnal scale, decoupling seems to be a fair description, but not on an annual or seasonal scale.

### 2.3.4 The NMB Flask Record, Compared to Other Marine Background Sites

Determinations relating to the seasonality and average annual growth rates are given in Tables B.2 and B.3, for each flask sampling site by species. Due to the large gap in the NMB flask measurements (see Figure A.5), assessing the degree of interannual variability was not very profitable, so the discussion is confined here to average growth rates and seasonality. It

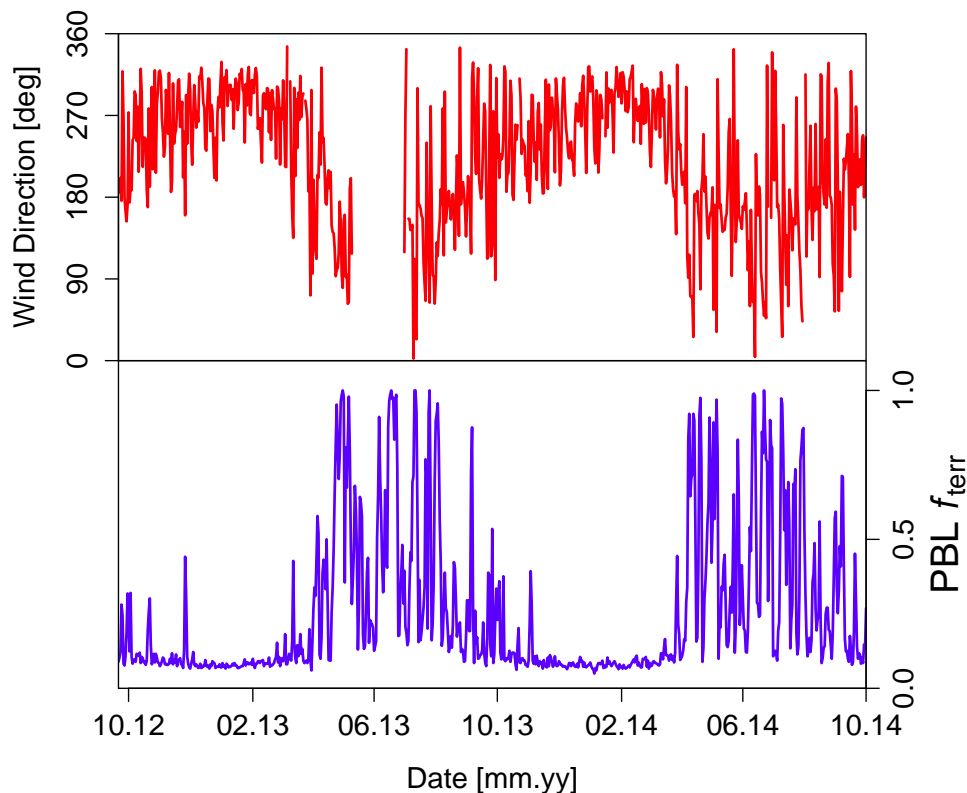


Figure 2.9: Comparison of the seasonality of wind direction, as measured at NDAO (*top panel*), and HYSPLIT back-trajectories, expressed as the fraction of each trajectory that resides over land, PBL  $f_{terr}$ , excluding those points which are greater than 1 km in altitude (*bottom panel*). Wind direction is plotted as a running 24-hour mean, PBL  $f_{terr}$  as a daily mean. Since NDAO is on the western coast, winds coming from the east would result in longer residence time over land.

should be emphasized that the curve fitting procedure described in Section 2.2.2 contains a degree of arbitrariness, and that different approaches to curve fitting and component isolation will yield slightly different results, particularly so if variability components like the seasonal cycle are small [Pickers and Manning, 2015]. However, experimentation with different fitting approaches demonstrated that the results presented here are robust to the method of time series analysis, though admittedly the comparison of different approaches was not done in a formal or exhaustive way.

In general, growth rates of all species were very close between sites. The average annual growth rate for CO at NMB for the period 1997–2014 was  $-0.49 \pm 2.5$  ppb yr<sup>-1</sup>, though since a large portion of the record is missing, this cannot be taken as definitive. In contrast, a positive trend was seen at Ascension Island ( $0.22 \pm 2.5$  ppb yr<sup>-1</sup>), while the other locations experienced declines in CO, on average. Identifying global or hemispheric trends in carbon monoxide is rather complicated as the spatial variability can be quite high, and significant interannual variability (IAV) is seen for this species [Strode and Pawson, 2013]. IAV in biomass burning, fossil fuel emissions, and in atmospheric transport are important determinants of year-to-year differences in CO mole fractions [Langenfelds et al., 2002, Novelli et al., 2003, Szopa et al., 2007]. A trend of 0.33 ppb yr<sup>-1</sup> for the period 2001–2011 was found in the Ascension Island flask record and attributed to increases in biomass burning and in the atmospheric methane content of the Southern Hemisphere [Wai et al., 2014]. A

contrasting result was found for a study of total column observations from satellites [Worden et al., 2013]. For the period 1999–2001 no trend was found for the Southern Hemisphere by Novelli et al. [2003], using the NOAA surface flask network. Zeng et al. [2012] found a significant, negative trend for FTIR measurements in Antarctica and New Zealand for the period 1997–2009; the discrepancy between surface flask measurements and satellite measurements has yet to be fully examined. Trends from satellite measurements must be used with caution, since instruments like MOPITT (Measurement of Pollution in the Troposphere) often have large biases and are not as sensitive to surface emissions [Chevallier et al., 2009, Hooghiemstra et al., 2012]. On the other hand, given the variability in emissions, single stations should not always be taken as indicative of large areas, even if they are meant to be globally representative. Yoon and Pozzer [2014] simulated CO globally with an atmospheric chemistry general circulation model for 2001–2010, and found a decreasing trend in much of the Northern Hemisphere, but an increasing trend for the Ascension Island site, India, and east Asia. For southern Africa, the model returned an increasing trend for southern Africa, but it was not significant, due to the large IAV. Clearly, any long-term trends are region-specific, and not hemisphere-wide.

Growth rates of CO<sub>2</sub>, CH<sub>4</sub>, and N<sub>2</sub>O at NMB were in good agreement with all other sites. There was also a clear decreasing trend in the  $\delta^{13}\text{C}$  content of CO<sub>2</sub>,  $-0.03\text{‰ yr}^{-1}$  at NMB and matched by the other flask sampling sites, a measure of the <sup>13</sup>C Suess Effect [Keeling, 1979]. This is similar to the trend observed at Cape Grim for a longer, but overlapping, period [Allison and Francey, 2007], and is close to the global mean growth rate of  $-0.02\text{‰ yr}^{-1}$  [Langenfelds et al., 2002].

Due to the sometimes sparse data coverage, it is difficult to assess synoptic variability except to say that it can be discerned in the time series, particularly for carbon monoxide (Figure A.5). Seasonality, however, was clearly evident in most species. The phasing and amplitude of the seasonal cycle of CO<sub>2</sub>, CH<sub>4</sub>, and CO varied between sites. For CO<sub>2</sub>, this is not surprising. The Southern Hemisphere has a smaller land mass than the Northern Hemisphere, and consequentially the contribution of terrestrial land plants to the seasonal cycle of CO<sub>2</sub> is reduced in comparison to the Northern Hemisphere. As a result, the seasonal cycle of CO<sub>2</sub> is small in the Southern Hemisphere. Emissions in the Northern Hemisphere from fossil fuel consumption are also greater than in the Southern Hemisphere. Hence, the seasonal cycle of CO<sub>2</sub> in the Southern Hemisphere is influenced by terrestrial plants, biomass burning, fossil fuel consumption, ocean ventilation, and interhemispheric transport, in some cases to a nearly equal degree [Gurney et al., 2004, Heimann et al., 1998, Stephens et al., 2013]. These factors can compete with or enhance one another, depending on their phasing.

The seasonality of CO<sub>2</sub> was essentially identical in phasing and amplitude at the three Pacific Ocean sites (Figure 2.10): Easter Island (EIC), and the two Pacific Ocean sites (20S and 25S). The amplitude of the seasonal cycle was smallest at these sites, reaching a maximum in December/January, and a minimum in April. They also all showed a smaller secondary peak in austral midwinter. Cape Ferguson (CFA) had similar timing to these sites in the occurrence of maximum and minimum values, but showed greater variability throughout the year, which complicated the climatology. At the South Atlantic locations, Ascension Island (ASC) and Cape Point (CPT), the annual peak in CO<sub>2</sub> mole fractions was during austral winter, making them nearly opposite in phase to the Pacific sites. While the NMB site was roughly in phase with the other South Atlantic locations, it had a much larger amplitude.

The small 0.4 ppb seasonal cycle of N<sub>2</sub>O at NMB had a maximum in February and a minimum in late August. This is shifted in phase relative to CFA and also with reported data for Cape Grim [Nevison et al., 2005, Park et al., 2012]. The seasonal cycle of N<sub>2</sub>O in the Southern Hemisphere is due thermal effects on the solubility of N<sub>2</sub>O in seawater, ventilation and biological activity, and stratospheric mixing [Nevison et al., 2005, Park et al., 2012].

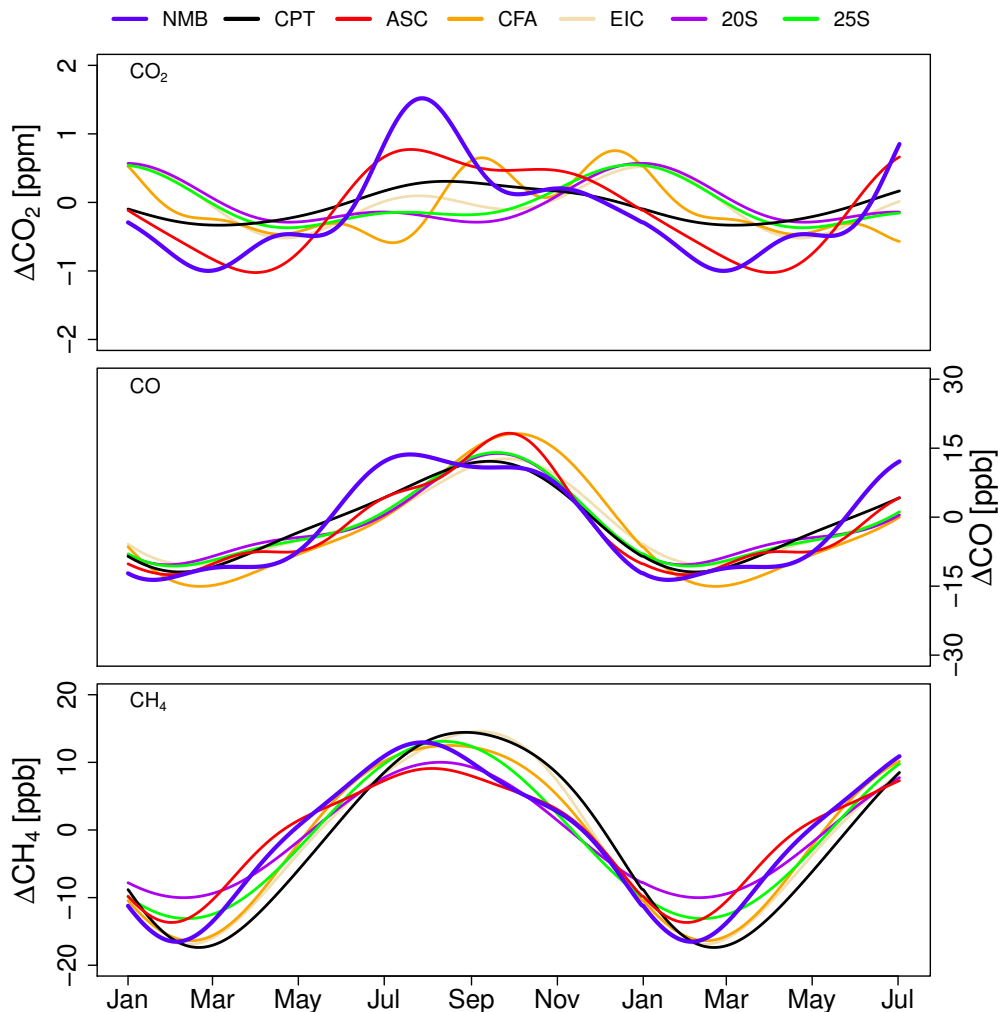


Figure 2.10: Climatology of selected flask sampling sites. The first 6 months of the year are repeated for visual clarity. The location of each site is given in Figure 2.5.

Interestingly, the climatology of  $\text{CH}_4$  and  $\text{CO}$  was synchronized with that of  $\text{CO}_2$  at NMB, while it was not at any other location. The seasonal cycle of  $\text{CO}$  and  $\text{CH}_4$  is due to changes in  $\text{OH}$  abundance and source strength throughout the year [Seiler et al., 1984]. Clearly some regional or local phenomenon influences the NMB measurements which is either absent or only partially exerted at other sites at the same latitude. The causes of this distinctive climatology is discussed at length in Chapter 5.

## 2.4 Summary and Conclusions

Based on the results of transport modeling and in situ observations of wind direction and wind speed, a coherent picture of the representativity of the station has been created. The representativity of the site changes based on seasonal shifts in the general circulation and synoptic modes. In austral summer, the station sees air masses from the South Atlantic that typically travel up the western coast of southern Africa, due to the strong equatorward winds. These air masses experience longer-range transport and generally reside closer to the surface

in the marine boundary layer. As the Hadley cell shifts poleward, the anticyclone develops over the continent underneath subsiding air masses, and a terrestrial influence predominates until the break-up of the anticyclone. Measurements at NDAO remain sensitive to marine fluxes during austral winter, however, and it is during March–October that the greatest variability in synoptic modes is seen. Based on the NMB flask record, a strong regional influence from southern Africa on  $\text{CO}_2$ ,  $\text{CH}_4$ , and CO is detected in austral winter that is seen only weakly at other South Atlantic sites, and not at all at Pacific Ocean sites. As such, it is concluded that NDAO is a regional background site with a high degree of synoptic variability.

# 3

## Station Design and Performance

### 3.1 Introduction

The success of efforts to use atmospheric oxygen to quantify the global carbon cycle is dependent primarily on the availability of data, since coverage is lower for O<sub>2</sub> than for CO<sub>2</sub> [Manning and Keeling, 2006, Rödenbeck et al., 2008]. As oxygen is a major constituent of the atmosphere, measuring small changes against the large background is technically challenging but feasible with several methods, including mass spectrometry, paramagnetic analyzers, gas chromatography, vacuum ultraviolet absorption, and fuel cell techniques [Bender et al., 1994, Keeling et al., 1998a, Manning et al., 1999, Stephens et al., 2003, 2007, Tohjima, 2000].

Absorption spectrometers featuring high-finesse optical cavities are proving to be a highly sensitive and user-friendly approach to measuring trace gases and are being widely adopted by the GHG measurement community [Andrews et al., 2014, Paldus and Kachanov, 2005]. Commercial analyzers using the cavity ring-down spectroscopy and off-axis integrated cavity output spectroscopy techniques can now be purchased to measure all of the major non-synthetic greenhouse gases. While there are a fair number of reports on using such analyzers to measure CO<sub>2</sub>, CH<sub>4</sub>, and the tracer CO [Chen et al., 2010, 2013, Flowers et al., 2012, O’Shea et al., 2013, Rella et al., 2013, Winderlich et al., 2010, Zellweger et al., 2012], there are few assessments of such analyzers for N<sub>2</sub>O, particularly from the field. Given that the natural variability of this gas in the atmosphere is quite small—consider that the seasonal cycle of N<sub>2</sub>O is typically less than 1 ppb in the lower troposphere [Jiang et al., 2007, Park et al., 2012]—the potential for OA-ICOS instruments to greatly increase our understanding of this powerful greenhouse gas is quite high.

### 3.2 Methods

#### 3.2.1 Overview

The top of an aluminum 21 m mast serves as the basis for all atmospheric observations at the observatory. Each of the three main instruments and the flask sampler has its own dedicated sample line. The top of an aluminum 21 m mast serves as the basis for all atmospheric observations at the observatory. Each of the three main instruments and the flask sampler has its own dedicated sample line. The intakes of the sample lines are each protected from suspended material and precipitation with a custom inlet. The inlet is mushroom-shaped and allows for the flow-through of air, such that sample air is drawn from underneath the cap of the inlet, through a 5 μm polyester filter, and then a portion is siphoned into the main sampling line. From the top of the mast to the outer wall of the container the air sampling lines are 12 mm SERTOflex tubing (SERTO GmbH, Kassel, Germany).

Large volume (5 L min<sup>-1</sup>) pumps run continuously to pull sample air down from the tower. Inside the container, sample lines (1/8” O.D. stainless steel tubing) pull a smaller volume of air

Table 3.1: Measurement Scales

Measurand	Scale
CO <sub>2</sub>	WMO X2007
CH <sub>4</sub>	NOAA 2004
N <sub>2</sub> O	NOAA 2006a
CO	WMO X2004
$\delta(\text{O}_2/\text{N}_2)$	SIO

with a lower flow rate from the larger diameter tubing running up the tower via a T-junction. 7 L buffer volumes are located upstream of the large pumps to minimize pressure fluctuations. Three lines of sample air pass through cool (4°C) water traps filled with glass beads, and cryotrap (−80°C), also containing glass beads (Figure A.6 and Figure A.7). All water traps are made from electropolished stainless steel. Sample air then is routed to the instruments: an Oxzilla FC-II dual absolute and differential oxygen analyzer (DFCA), measuring  $\delta(\text{O}_2/\text{N}_2)$  (Sable Systems International, Las Vegas, NV, USA), a Picarro ESP-1000 cavity ring-down spectrometer measuring CH<sub>4</sub> and CO<sub>2</sub>, (Picarro Inc, Santa Clara, CA, USA) and a Los Gatos N<sub>2</sub>O/CO-23d cavity-enhanced absorption spectrometer measuring N<sub>2</sub>O and CO (Los Gatos Research Inc, Mountain View, CA, USA). Downstream of the T-junctions, the flow rates are slightly different between instruments, reflecting their different requirements for gas supply: flows are between 90–95 mL min<sup>−1</sup> for the DFCA, between 150–210 mL min<sup>−1</sup> for the CRDS, and 110–220 mL min<sup>−1</sup> for the OA-ICOS. The larger range for the latter two instruments is given because flow and sample line pressures gradually decline in between filter replacements, due to the very fine dust present at the site.

The DFCA and CRDS are both housed in a rack receiving air directly from the air conditioner, to minimize temperature fluctuations and to provide greater cooling power. Similarly, the OA-ICOS is housed in an actively ventilated insulated box. Temperature control of the laboratory is accomplished with two air-conditioning units which run singly in 12 hour shifts. Total power consumption of the observatory is about 2.5 kW.

A complete diagram of the instrument system can be seen in Figure A.8, and a part list is presented in Table B.4. Four-port, two-way valves, determined to have no cross-port leakage (Bürkert GmbH, Ingelfingen, Germany), are used to switch between reference gas streams and the air sample stream. Small membrane pumps (KNF Neuberger GmbH, Freiburg, Germany) are used to maintain sample flow during measurements of reference gases, so that sample air does not sit stagnate in the lines, and so that no additional purge is necessary upon the completion of a reference cycle. The entire system is under automatic control, using a custom program written in LabVIEW. Data is logged at an interval of 1 second; data generated at a higher frequency than this is averaged by the software. In addition to the control and data acquisition computer running the LabVIEW software, a second computer is used for off-site data transfer and remote access to the laboratory network.

As both the CRDS and OA-ICOS instruments are upstream of their pumps, these sample lines are under-pressurized (100–200 mbar under ambient), and the instruments actively regulate the pressure inside the measurement cavity. The CRDS has been fitted with an external diaphragm pump (Vacuubrand model MD1, Vacuubrand GmbH, Wertheim, Germany) for better ease of maintenance. Since the DFCA does not have its own pump, air is forced through the analyzer via a small membrane pump located upstream of the fridge traps and cryotrap (Figure A.8); consequently in this region the sample lines are over-pressurized.

### 3.2.2 Response Times

Response times vary between instruments, mostly a result of the different residence times of air in the separate inlet systems. Each sample line has slightly different operating conditions (i.e. pressure, flow) due to the differing needs of the instruments. Additionally for CO<sub>2</sub> there are also surface or memory effects to take into consideration, as the molecule can interact with the stainless steel tubing, necessitating longer purging times compared to a species like methane.

The residence time of each species was estimated as:

$$\tau = \frac{V}{F} \quad (3.1)$$

where  $V$  is the volume of the gas handling system and  $F$  is the average flow rate. The response time was also tested for the laboratory portion of the measurement system only, by connecting two working tanks by means of a three-port valve to the point just downstream of the large pumps, this being the highest point upstream of the devices that could be connected a tank. The gas flow to the instrument was switched between the two tanks every 5 min. The response time was then calculated as the length of time between stable values. The design of the test was meant to create an instantaneous change of concentration in the sample air stream under constant conditions.

### 3.2.3 Leak and Fractionation Tests

As the sample lines of the OA-ICOS and CRDS instruments are partially evacuated a pressure gradient exists which threatens to contaminate the sample stream with laboratory air. For carbon monoxide and carbon dioxide this is particularly serious as the air inside the laboratory can be quite enhanced in both species. While the oxygen plumbing is mostly downstream of a pump, meaning that the pressure gradient would force air out of the tubing, portions upstream are also partially evacuated and so leaks are a concern in this region. Downstream of the pump the sample line is overpressurized, so any leak would not force laboratory air into the sample stream. Leaks and T-junctions in this region can fractionate atmospheric oxygen, however, and as a result introduce artifacts [Keeling et al., 1998a, Kozlova and Manning, 2009, Manning, 2001, Stephens et al., 2007].

The original design of the laboratory system was simplified to eliminate as many fittings, junctions, and orifices as possible, and to reduce the total volume where feasible. During installation the system was tested for leaks by both pressurizing and underpressurizing with a hand pump and a coarse resolution pressure sensor (accurate to  $\pm 0.02$  bar). After an artifact in the CO signal developed two weeks after installation, further leak tests were conducted during the following maintenance visit inside the laboratory with high-resolution pressure sensors (accurate to  $\pm 0.02$  mbar); none were found. It was not until the third maintenance visit in July 2013 that an integral leak test from the top of the tower to the device was performed with a high-resolution sensor overnight. This test revealed a leak outside of the laboratory next to the air conditioner unit, which was causing a  $\sim 300$  ppb amplitude diurnal cycle in CO. The design of the alcove housing the air conditioner was modified so that it is no longer necessary to disconnect the 12 mm sample lines to access the A/C.

In the case of the oxygen air sample lines, an integral leak test was not really possible since enough alterations to the system would have to be made to pressurize it without damaging the sensitive pressure transducer (see Section 3.2.6) or venting the added pressure through a release valve which is in effect during normal operation. As a result such a test would not really reflect the system in its normal state, since many adjustments would have to be made. Hence, the system was tested in three separate segments.



### 3.2.4 Carbon Dioxide and Methane Measurements

The Picarro ESP-1000 (Serial No. CFADS-06) instrument is an early-model cavity ring-down spectrometer (CRDS). This optical technique is a type of laser absorption spectroscopy, whereby a continuous wave laser emits a pulse of light into an optical cavity. This high-finesse optical cavity is equipped with highly-reflective mirrors that allow some light to escape. One of the advantages of CRDS is that it creates an large effective path length (tens of kilometers), enabling measurements of high sensitivity. The laser is tuned to several specific wavelengths where the measurand has strong absorption, and to regions without absorption, in order to determine the ring-down time with and without absorption by the measurand. The difference in decay time of the light intensity (as measured by a photo-detector) between the two modes is the signal of the analyzer which is converted to a mole fraction [Crosson, 2008]. Since the CRDS software calculates the mole fractions of CO<sub>2</sub>, CH<sub>4</sub>, and H<sub>2</sub>O, this output can be used directly, after the application of an instrument-specific water correction and a calibration.

The absorption of CO<sub>2</sub> is measured by scanning around 1,603 nm, while the H<sub>2</sub>O and CH<sub>4</sub> peaks are evaluated in a region around 1,650 nm. Since the CRDS is tuned to specific absorption features, it measures only the main isotopologues of each species, namely <sup>12</sup>C<sup>16</sup>O<sub>2</sub>, <sup>12</sup>C<sup>1</sup>H<sub>4</sub> and <sup>1</sup>H<sub>2</sub><sup>16</sup>O [Crosson, 2008]. Therefore, the isotopic composition of calibration standards and other reference gases must be close to that of the sample to avoid artifacts [Chen et al., 2010]. Likewise, standard gases should have the same composition as the sample, meaning that synthetic air standards should not be used [Nara et al., 2012].

As the shapes of these spectral lines are quite sensitive to temperature and pressure, the levels of both must be carefully maintained by the instrument. The cavity is held at a constant pressure of  $186.7 \pm 0.1$  mbar and a constant temperature of  $45 \pm 0.01$ °C.

### 3.2.5 Nitrous Oxide and Carbon Monoxide Measurements

The Los Gatos N<sub>2</sub>O/CO-23d Analyzer employs cavity enhanced absorption off-axis integrated cavity output spectroscopy (OA-ICOS) [Paul et al., 2001, Peltola et al., 2012]. In this technique, light from a laser is emitted into a cavity and the temporally integrated intensity of the transmission of the light out of the cavity is the raw measurement signal [Baer et al., 2002]. Like the CRDS, the OA-ICOS software calculates the mole fractions of N<sub>2</sub>O, CO, and H<sub>2</sub>O; this output is used directly after the application of an instrument-specific water correction, calibrations, and a drift correction.

The optical cavity is equipped with reflecting mirrors that amplify the effective path length. The laser is tuneable and produces a full spectrum over a selected region for each measurement, which can be viewed in real-time by the user. CO and N<sub>2</sub>O are determined from their most prominent absorption feature in a 22 GHz region centered near 1564 nm/191.68 THz. Water vapor is also measured in this spectral range.

As the instrument is fairly new, few published studies on the analyzer are available, particularly those that evaluate both N<sub>2</sub>O and CO. However, the instrument, at least on short-term time scales, performs with excellent precision, particularly for N<sub>2</sub>O. Initial assessments indicate that the instrument has the potential for use in making atmospheric measurements, eddy covariance methods, and aqueous dissolved gas concentrations measured in equilibrated headspace, provided the drift of the analyzer is accounted for and care is taken with respect to gas handling, since the concentration ranges are usually small [Arévalo-Martínez et al., 2013, Blomquist et al., 2012, Zellweger et al., 2012].

### 3.2.6 Atmospheric Oxygen Measurements

The differential fuel cell analyzer (DFCA) does not measure the  $O_2/N_2$  ratio itself but instead measures the  $O_2$  mole fraction directly in dry air through an electrochemical method. There are two sensors in the device, each containing an anode, cathode and weak acid electrolyte. Atmospheric oxygen is reduced on the cathode, generating a current which is the analytical signal. The Oxzilla analyzer was originally developed for respirometry but careful development of the gas handling techniques by the atmospheric oxygen community has enabled it to achieve excellent precision [Stephens et al., 2007, Thompson et al., 2007, 2009]. Differences in pressure on the sensor will necessarily result in a higher signal, therefore pressures and flows must be kept completely uniform. In practice this is quite challenging, so to minimize artifacts measurements of reference gases or sample air are always made differentially against a dedicated reference cylinder that flows continuously while the instrument is operational. Since it is not necessary to know the exact  $\delta(O_2/N_2)$  content of this reference gas, it is not measured; in this work such a cylinder is called a “working tank”. A four-port, two-way valve switches between these two streams every 1.5 min to avoid artifacts from the drift of either fuel cell, and computation of the final  $\delta(O_2/N_2)$  is thus made relative to both the difference between the two fuel cells and between the sample air and reference gas within one fuel cell:

$$\Delta_{raw} = (C_{WT}^1 - C_X^1) - (C_X^2 - C_{WT}^2) \quad (3.2)$$

$$\delta(O_2/N_2) = \frac{\Delta_{cal} + [(CO_2)_M - (CO_2)_{ref}] \cdot XO_2}{(1 - XO_2) \cdot XO_2} \quad (3.3)$$

Here  $C$  is the raw measurement from the DFCA fuel cells, in percent. The subscript refers to a discrete measurement of the working tank ( $C_{WT}$ ), or the gas stream one wishes to quantify ( $C_X$ ), be it a reference gas or sample air. The numbered superscripts refer to fuel cell/channel 1 or 2. Each value of  $C$  represents the average of 1 sec measurements for the duration of the period between switches. The first 30 seconds of this period are discarded, as the fuel cell has to stabilize after a valve switch. Solving Equation 3.2 gives the uncalibrated differential signal,  $\Delta_{raw}$ . After a calibration is applied (see Equation 3.11),  $\Delta_{cal}$  is used to calculate the final concentration in per meg, as per Equation 3.3, after Stephens et al. [2003] and Kozlova et al. [2008].  $(CO_2)_M$  is the final dry mole fraction in ppm as measured by the CRDS and  $(CO_2)_{ref}$  is an arbitrary reference value of the Scripps scale, 363.29 ppm.  $XO_2$  is the mole fraction of  $O_2$  in standard dry air, 0.209392 [Tohjima et al., 2005a].

The working tank gas flow is controlled precisely by a mass-flow controller (MKS Instruments, Andover, MA, USA). A pressure transducer (also MKS) measures the pressure difference between the two gas streams and a proportional valve equalizes the pressures so that they do not vary by more than  $\pm 0.2$  mbar.

### 3.2.7 Meteorological Measurements

A small meteorological sensor array is located at the inlet height on the mast. Wind direction and wind speed are measured with a Thies Clima 2-D sonic anemometer (model 4.3810.30.310), temperature and relative humidity with a combined Galltec-Mela instrument (model C 2.4), barometric pressure with a Young pressure sensor (model 61202V), and solar irradiance with a Kipp and Zonen ISO 9060 first class pyranometer (model CMP11). Data is passed to the LabVIEW system via a controller area network (CAN bus).

### 3.2.8 Flask Sampling

In order to provide an independent corroboration of the in situ data, flask samples were taken on a (nominally) weekly basis, with variations in timing and small gaps due to personnel availability. Since sampling is done manually, the time of day is always between sunrise and sunset, but typically in the afternoon. This preferentially samples the coastal wind sector, since a strong sea breeze is common (but not assured) during the afternoon hours at NDAO. Meteorological conditions are not taken into account during sampling, however, as there are no strong local sources of contamination, provided the generator is not running. All species which are measured continuously at the station are also measured in flasks; additionally the flasks are also analyzed for  $\delta^{13}\text{C}-\text{CO}_2$ ,  $\delta^{13}\text{C}-\text{CH}_4$ ,  $\delta^{18}\text{O}-\text{CO}_2$ ,  $\delta\text{D}-\text{CH}_4$ ,  $\text{H}_2$ ,  $\text{Ar}/\text{N}_2$ , and  $\text{SF}_6$ .

The flasks used by the Max Planck Institute for Biogeochemistry (MPI-BGC) are borosilicate glass and 1 L in volume, with two valves equipped with Kel-F® (polychlorotrifluoroethylene; PCTFE) seals. PCTFE has been shown to have a low permeability to most gases compared to other common sealing materials, as long storage times can change the composition of sample air in flasks [Sturm et al., 2004]. Flasks are shielded from light exposure with a black sheath. Before sampling the flasks are pre-conditioned by evacuation at 60°C for 72 hours and then filled with dry air at a pressure of 1.6 bars.

Samples are taken in triplicate and connected in series upstream of a pump. A dedicated line (identical to the continuous sample lines) is used exclusively for the flasks, although the portion that is downstream of the main pump is not flushed or purged when not in use. The pump body and valve plates are aluminum, and the structured diaphragms are made of PTFE. When in use the flow rate ( $3.2 \text{ L min}^{-1}$ ) is higher than the in situ analyzer flow rates (100–200  $\text{mL min}^{-1}$ ). Air is dried with a cryotrap identical to the one used for the oxygen sampling line. During sampling, the line is flushed for 5 minutes before any air is directed to the flasks, then a bypass is opened and the flasks are flushed for an additional 15 minutes before they are sealed again. After closure, the pressure of the flask is about 1.6 bars.

Due to the lengthy shipping route and remote location of the station storage time of flasks can be lengthy—the mean number of storage days is 100, the maximum thus far is 226—and for reactive species like CO this can result in storage-related artifacts and/or permeation.

Laboratory demands and a large volume of samples from this and other stations in the MPI-BGC network mean that not all flasks are analyzed for all species, and in the case of methane isotopic composition, only two out of three flasks are analyzed.  $\delta(\text{O}_2/\text{N}_2)$  is measured with mass spectrometry;  $\text{CH}_4$ ,  $\text{CO}_2$ , and  $\text{CO}$  with GC-FID; and  $\text{N}_2\text{O}$  with GC-ECD. Isotopic ratios are determined with isotope ratio mass spectrometry (IRMS).

### 3.2.9 Sensor Stability

In order to characterize the stability of the main instruments, a stream of dry air with a constant composition was supplied to each device for a 24-hour period during the final stages of the laboratory installation on site. From this the Allan variance was computed. The Allan variance, a method for computing the frequency stability of clocks, can also be used to analyze the noise of a sensor [Land et al., 2007, Siraya, 2001]. Allan variance is given as:

$$\sigma_y^2(\tau) = \frac{\sum_{i=1}^{N-2n+1} (T_{i+2n} - 2T_{i+n} + T_i)^2}{2\tau^2 \cdot (N - 2n + 1)} \quad (3.4)$$

where  $\tau$  is the sampling interval,  $N$  is the number of measurements of some quantity  $T_i$ ,  $n$  is the number of adjacent values of  $T_i$  in  $\tau$  [Land et al., 2007]. Akin to the standard deviation, the Allan deviation is the square root of the variance,

$$\sigma_y(\tau) = \sqrt{\sigma_y^2(\tau)} \quad (3.5)$$

The advantage of the Allan deviation is that it is determined in the same units as the measurand is reported. In some cases, the minimum value of the deviation is the ideal averaging interval for the sensor, being the integration time for which sensor noise is the lowest. In practice, however, the integration time which yields the lowest deviation may be too large to be practical.

### 3.2.10 Drying and Water Correction

The absolute abundance of water vapor varies widely throughout the atmosphere; even under well-mixed conditions in the troposphere, the mixing ratio of  $\text{H}_2\text{O}_{(\text{g})}$  can span several percent. This dilutes the mixing ratio of trace gases and can obscure their “true” variability if mole fractions are not determined against moles of dry air.

With the meteorological array at NDAO, the mole fraction of water vapor can be determined from the relative humidity, temperature and pressure measured on the mast, as follows:

$$RH = \frac{P_w}{P_{ws}} \cdot 100 \quad (3.6)$$

where  $RH$  is the relative humidity, in percent,  $P_w$  is the partial pressure of water vapor, and  $P_{ws}$  is the saturation water vapor pressure, determined as (hPa):

$$P_{ws} = A \cdot 10^{\left(\frac{m \cdot T}{T + T_n}\right)} \quad (3.7)$$

where  $A$  and  $T_n$  are constants, 6.116441 and 240.7263, respectively, and  $T$  is the air temperature in °C. Note that this is only valid over ambient temperatures of  $-20$  to  $50^\circ\text{C}$ . Then, if the atmospheric pressure,  $P_{tot}$ , is known, the mole fraction of water vapor ( $\text{H}_2\text{O}_{act}$ ) is simply

$$\text{H}_2\text{O}_{act} = \frac{P_w}{P_{tot} - P_w} \cdot 10^6 \quad (3.8)$$

in ppm.

As both the CRDS and OA-ICOS instruments measure water vapor, they afford the opportunity to dispense with sample drying and apply a water correction instead. There are drawbacks to any water correction or drying method. Sample drying introduces a physical alteration of the sample matrix, and increases the total number of seals and connections of the gas handling system which must be rendered gas-tight. Drying also generally requires additional consumables. Finally, depending on the method used there is also contingent maintenance required to remove the collected water, which can be problematic at remote sites.

Water corrections, on the other hand, require continuous, extremely precise and stable measurements of water vapor, which is analytically challenging. It is also a newer approach, and as such represents a major break in methodological continuity, a concern for long-term time series. Switching between humid (sample) and dry (reference) air streams is also not ideal. Nevertheless, the method has been shown to be robust for measurements of  $\text{CO}$ ,  $\text{CO}_2$  and  $\text{CH}_4$  with the type of instrumentation at NDAO [Chen et al., 2010, Nara et al., 2012, Rella et al., 2013, Winderlich et al., 2010, Zellweger et al., 2012].

It was decided to forgo sample drying for the CRDS and OA-ICOS instruments at NDAO for several reasons: first, the station is in a desert environment, where water vapor concentrations are typically low and water corrections perform best; second, since the site is remote and there are no formally trained technicians available, simple maintenance procedures are

greatly preferred; third, the precise, continuous measurements of H<sub>2</sub>O made by the CRDS can be corrected to yield accurate observations of water vapor, data which otherwise would be unavailable [Winderlich et al., 2010]; and fourth, obviating the need for drying greatly simplifies the plumbing system for these two instruments, both of which operate under ambient pressure, reducing the potential for leaks inside the laboratory.

A version of the ‘water droplet’ method was used to humidify the air stream of a target gas cylinder, using a slight variant of one of the methods in Rella et al. [2013] (Method 2, “Empa variation”). The apparatus allows the operator to easily switch between dry and humidified gas streams with the aid of the manual valves. The gas stream passes over the surface of a water droplet (< 200 μL) placed in a small well. After the water droplet is completely evaporated and the residual humidity in the tubing is fully removed, the entire shape of the correction function is delimited. The ‘tuning’ parameters used to achieve a sufficient initial water vapor concentration are the height of the tubing over the droplet, the absolute pressure in the trap, and the temperature of the lab (J. Winderlich, personal communication).

Due to broadening effects on the spectral lines, both the CRDS and the OA-ICOS must be corrected for each species,  $X$ , with a second-order function, in the form of

$$\frac{X_{wet}}{X_{dry}} = 1 + a \cdot \text{H}_2\text{O}_{rep} + b \cdot \text{H}_2\text{O}_{rep}^2 \quad (3.9)$$

$\text{H}_2\text{O}_{rep}$  is the mole fraction of water vapor measured by the instrument in question without correction, usually in percent, and  $a$  and  $b$  are empirically determined factors determined by the experiment described above. In the case of the CRDS,  $\text{H}_2\text{O}_{act}$  can be determined as [Winderlich et al., 2010]:

$$\text{H}_2\text{O}_{act} = 0.0292 + 0.7718 \cdot \text{H}_2\text{O}_{rep} + 0.0197 \cdot \text{H}_2\text{O}_{rep}^2 \quad (3.10)$$

This relationship is thought to hold between Picarro CRDS instruments, since they are all calibrated on the same scale during manufacture. A major assumption here is that the absolute drift of the water vapor signal is negligible. It should also be noted that the OA-ICOS instrument was not used for determining  $\text{H}_2\text{O}_{act}$ , since tests showed that it was both less accurate and less sensitive than the CRDS; the water vapor data is used only for correction.

### 3.2.11 Calibrations and System Performance Evaluation

All reference gases are stored horizontally in an insulated box to minimize stratification and temperature fluctuations. Reference gases are calibrated against primary standards at the Max Planck Institute for Biogeochemistry (MPI-BGC) GASLAB for CO<sub>2</sub>, N<sub>2</sub>O, CO and CH<sub>4</sub>. The O<sub>2</sub>/N<sub>2</sub> ratio of reference cylinders is measured at MPI-BGC by mass spectrometry. All reference gases were tied to primary standards on the measurement scales given in Table 3.1. All reference gases are comprised of dry, ambient air and stored in 50 L aluminum cylinders. The initial pressure of each cylinder is 200 bar. Calibration of the instruments is done through four working secondary standards and instrument performance is periodically checked with “target” cylinders (i.e., tanks of known mole fraction which are regularly re-measured). In addition 3 long-term reference gases (“archives”) are available to ensure accuracy over the course of the station lifetime. Atmospheric concentrations of CO<sub>2</sub>, CH<sub>4</sub>, N<sub>2</sub>O, and CO all are reported as dry air mole fractions, e.g., 1 μmol mol<sup>-1</sup> = 1 ppm.

Instrument calibrations are performed automatically by the LabVIEW program using four working secondary standards. The mole fractions of these tanks were selected to bracket the natural variability which was expected for this site. Mole fraction ranges were 370–410 ppm for CO<sub>2</sub>, 1,600–1,920 ppb for CH<sub>4</sub>, 300–340 ppb for N<sub>2</sub>O, 40–250 ppb for CO, and between –300 and –700 per meg for  $\delta(\text{O}_2/\text{N}_2)$ . The interval between calibrations was 123 hours for

the CRDS and OA-ICOS, and 71 hours for the DFCA. Target measurements were made every 49 hours for the CRDS, and every 35 hours for the OA-ICOS and DFCA. Various schemes were implemented, but the ones used represent the best compromise between the need to save reference gases and the drift of the sensors. As preparation, shipment, customs clearance and local delivery of a pallet of cylinders to NDAO from MPI-BGC in Germany usually takes about one year, we implemented the most conservative (in terms of gas usage) calibration frequency possible without unduly compromising measurement accuracy.

Reference gases (working secondary standards or targets) were measured for a total of 12 minutes after a two minute, high flow rate (250 mL/min) purge of the sample line. During purges the reference gas flow is not directed to the instrument, but vented at the junction closest to the instrument. A stable signal is generally reached after 6 minutes of measurements for all measurands. During purges the reference gas flow is not directed to the instrument but vented at the junction closest to the instrument. As non-linearity was not observed for any instrument in the concentration ranges of tanks used at NDAO, the instrument response functions for all species were taken as a linear fit of the average of the last 5 min of working secondary standards (WSS) measurements and the mole fraction determined by the MPI-BGC facilities (all WSSs are traceable to NOAA or Scripps primary standards):

$$y = mx + b \quad (3.11)$$

where  $x$  is the “true” value of the measurand, supplied by the analytical facilities at MPI-BGC, and  $y$  is the dry air mole fraction or  $O_2$  to  $N_2$  ratio measured by the instrument during a specific calibration. The slope ( $m$ ) and intercept ( $b$ ) are linearly interpolated between calibrations.

A dedicated reference cylinder was used as a target tank to assess long-term repeatability and instrument precision. Target measurements are an imperfect descriptor of system performance, or at least not a complete guarantor of data quality, since such measurements would not reveal a leak in air sampling lines upstream of the common tee. In the case of our measurement system, the pressure of sample line of the CRDS and OA-ICOS while measuring target gas is slightly over ambient and dry, meaning it is measured under different conditions from sample air. For some species, like  $CO_2$ , there can be small adsorption-related artifacts during gas storage or gas handling which might appear to be due to poor instrument performance, but would not be shared by the in situ time series. Nevertheless, regular target measurements can reveal long-term problems or biases, and can give an estimate of measurement uncertainty and repeatability.

Following in part the recommendations of [Andrews et al. \[2014\]](#), we report the measurement uncertainty as the target-derived measurement uncertainty (see equations 9a–9d in [Andrews et al. \[2014\]](#)). This quantity,  $u_{TAR}$ , was calculated as the 67th percentile of the absolute value of the difference between the laboratory assigned value or “setpoint”, and the individual mean target determination in a moving window of 1 week.

### 3.2.12 Drift Correction of the OA-ICOS Analyzer

During laboratory tests before the deployment of the OA-ICOS instrument, it became apparent that it is susceptible to temperature and pressure-related drift. Our Los Gatos analyzer does not have the improved temperature control that later models do (the “enhanced performance” feature). We opted to attempt to correct this drift empirically by measuring a working tank at 2-hour intervals, a determination arrived at through consideration of the rate and magnitude of the sensor drift, the loss of in situ data, and the usage rate of the working tank.

Table 3.2: WMO/GAW Recommendations for Measurement Compatibility [WMO/GAW, 2013]

Measurand	Compatability Goal	Unit
CO <sub>2</sub>	± 0.05	ppm
CH <sub>4</sub>	± 2	ppb
N <sub>2</sub> O	± 0.1	ppb
CO	± 2	ppb
δ(O <sub>2</sub> /N <sub>2</sub> )	± 2	per meg
H <sub>2</sub>	± 2	ppb
SF <sub>6</sub>	± 0.02	ppt
δ <sup>13</sup> C-CO <sub>2</sub>	± 0.01	‰
δ <sup>18</sup> O-CO <sub>2</sub>	± 0.05	‰

Data is corrected for drift after the water correction but before applying the calibration. Each working tank measurement lasts 8 min, without a line purge, and only the last 2 min are used. A spline is fit through the average of all working tank measurements made on the same tank, and the difference of these interpolated measurements from the mean of the tank is then applied to each time step as a correction factor.

### 3.2.13 Performance Goals

The Global Atmosphere Watch Programme of the World Meteorological Organization (WMO/GAW) is the international authority on atmospheric measurements of greenhouse gases (GHGs) and related tracers. The WMO/GAW Experts' biennial meeting produces a set of recommendations for stations within the GAW network. Even for stations which are not GAW certified, it is advantageous to follow these recommendations, and they have served as a guideline for the design and implementation of NDAO. WMO/GAW recommendations for compatibility of measurements are given in Table 3.2. There are no recommendations from this body for δ<sup>13</sup>C-CH<sub>4</sub>, δD-CH<sub>4</sub>, or Ar/N<sub>2</sub>. These compatibility goals were used as guidelines for evaluating target measurements and instrument error.

## 3.3 Results and Discussion

### 3.3.1 General Performance of the Measurement System

High temperatures are a major challenge of working at this site, and maintaining a constant temperature in the laboratory and for the devices is crucial. The CRDS and DFCA are both housed in an insulated rack, which reduces the range of temperatures the devices are exposed to compared to the variation in the laboratory itself. The standard deviation of the air temperature laboratory was 1.5°C over the operational lifetime of the station and 0.77°C for the instrument rack; for comparison the value for the in situ air temperature was 6.8°C. The CRDS cavity temperature was stable within 0.02°C. The OA-ICOS fared less well since it was too large to fit inside the rack ( $1\sigma = 0.90^\circ\text{C}$ ). An insulated box was built for it instead, with active ventilation control. The insulated box performed better than no protection at all, but is still not as efficient as the rack, which is reflected in the OA-ICOS instrument temperature; it should be noted, however, that the CRDS has superior temperature control for its measurement cell. For the DFCA, which also has active temperature control, the standard deviation was 0.05°C.

Table 3.3: Total System Leak Rates

Measurand	Leak Rate (mbar L sec <sup>-1</sup> )	Max. Artifact
CO <sub>2</sub>	$6.3 \times 10^{-4}$	0.014 ppm
CH <sub>4</sub>	$6.3 \times 10^{-4}$	0.0017 ppb
N <sub>2</sub> O	$3.0 \times 10^{-4}$	$7.6 \times 10^{-5}$ ppb
CO	$3.0 \times 10^{-4}$	0.0052 ppb

There is one large gap in the record during July 2013 when the hard drive of the measurement computer failed. This was a solid-state drive (SSD), and there is some evidence to suggest that these drives are more prone to failure than traditional hard drives [Ku, 2011]. Given that the SSD of the communication computer also failed in January 2014, we have forsworn the use of SSDs at NDAO in favor of traditional hard drives.

The second large gap in the records of  $\delta(\text{O}_2/\text{N}_2)$ , CO<sub>2</sub>, CH<sub>4</sub>, and H<sub>2</sub>O are due to a dust storm during a bergwind event which clogged the CRDS sample line shortly after the communication computer failed and remote connection with the site was no longer possible. The DFCA sample line was not as affected but  $\delta(\text{O}_2/\text{N}_2)$  requires in situ CO<sub>2</sub> data. Due to the large amount of fine dust at the site, filters have to be exchanged frequently and flow rates generally slowly decline as they are clogged; sudden events, however, can cause a rapid decline in flow and pressure in the sample lines and necessitate shutdown until the filters can be replaced.

The data stream also has smaller gaps, due to calibrations, target measurements, LabVIEW software issues, or maintenance. Software and computer issues, rather than instrument failure, is probably the more common cause of data gaps related to technical problems; the exception to this was from March to July 2013, when the station was plagued by frequent (sometimes daily) power outages. Nevertheless, absolute data coverage since October 2012 is approximately 75% or higher for most measurands.

The time series for N<sub>2</sub>O and CO start 8 months after the beginning of the station operation due to a leak in the tower line developed a few weeks after installation and contaminated the line with air conditioner exhaust.

### 3.3.2 Response Times

Calculated residence times ( $\tau_{calc}$ ) of the major measurands can be found in Table B.5. For the CRDS and OA-ICOS measurands, the total system residence time is around 10 seconds; for the DFCA the residence time is much longer, due to the slightly lower flow rate and the much greater volume, due to the more complicated gas handling and the drying system.  $\tau_{calc}$  for the 12 mm sampling lines on the tower was 3.9 seconds, lower than the residence time in the 1/8" tubing sections due to the higher flow rate created by the large volume pumps.

In practice the residence time can be longer due to surface interactions with tubing, as can be seen in the case of CO<sub>2</sub> and CO. The response time, or apparent residence time ( $\tau_{app}$ ), as we define it, also includes some stabilization time for the sensor, which is negligible for the OA-ICOS and CRDS, but substantial for the dual-differential fuel cell analyzer; full stabilization of the signal can take some minutes. This test also to some extent includes some mixing in the gas stream of the two tanks, and a slight delay due to the speed of the valve used to switch between the two streams.



### 3.3.3 Leak and Fractionation Tests

The results of the integral leak test for can be seen in Figure 3.1 and Table 3.3. Most of the observed variability in pressure was caused by temperature variations. The sudden increase in observed pressure towards the end of the integral leak tests is likely due to an underestimate of temperature-based pressure changes in the SERTOflex tubing on the mast. This is the larger volume and it seems reasonable to assume that there is some significant enhanced heating of this tubing relative to the surrounding air temperature due to the protective black coating. This also indicates that the calculated leak rate is likely a large overestimate, since it was assumed that any increase above what would be expected due to temperature change in the calculated final pressure was due to leakage.

For the atmospheric oxygen gas handling system, downstream of the membrane pump (C104) a linear leak rate of  $< 0.17$  mbar L sec<sup>-1</sup>; upstream of C104 no detectable leak was seen over a period of 12 hours. The main portion of this loss came from the two fridge traps which are connected by Tygon tubing to the bottom of the fridge trap to remove pooling water via a peristaltic pump. Fractionation was tested by introducing a constant flow from a working tank directly into the instrument, and the point of introduction upstream. If the gas handling system were to cause some fractionation of atmospheric oxygen, the difference should be readily seen by the averages of the concentrations of the measurements made at different points in the system. The results of the fractionation test of the atmospheric oxygen sample line can be seen in Figure 3.2; no significant fractionation was detected, as the means of the concentrations measured of gas introduced directly into the instrument and introduced upstream of the entire gas handling system were indistinguishable.

It should be noted that estimating the leak rate and its impact on the observed mole fraction of a given measurand involves several assumptions and oversimplifications, such as the concentration of each species in the laboratory. Accordingly the leak rates and change in signal reported here represent “worst-case” scenarios, using concentration values for contaminated air that were the highest ever measured for each species inside the lab. Furthermore, separate testing of different portions of the plumbing system indicated that the observed leak rate was more likely to be outside the laboratory than in, where air is more likely to be closer to ambient—with the exception of CO.

### 3.3.4 Stability of the CRDS

The Allan deviation of both CO<sub>2</sub> and CH<sub>4</sub> exhibit minima around the 1 to 1 $\frac{1}{2}$  hour window (Figures 3.3 and 3.4), after which the drift of the sensor begins to dominate. In the case of CO<sub>2</sub>, this drift was clearly (inversely) dependent on the air temperature surrounding the working tank, as measured by a temperature sensor inside the insulated box housing all cylinders. Correlations were not seen with rack temperature, regulator temperature (housed outside of the insulated box for cylinders), or room temperature. While it is not atypical for Picarro CRDS analyzers to drift with temperature to this degree [Crosson, 2008], the evidence points to an artifact related to the tank. The effect is about  $-0.06$  ppm °C<sup>-1</sup> over a 24 hour period (Figure A.9). A weaker relationship with opposite sign was seen for methane.

Using the raw (i.e., uncalibrated) target measurements as an assessment of the long-term drift of the instrument, we note that long-term drift was not linear over the entire measurement period, but wandering due to a slight seasonality in the temperature of the laboratory. The absolute range of raw target measurements on one tank was 0.4 ppm for CO<sub>2</sub> and 2.3 ppb for CH<sub>4</sub>.

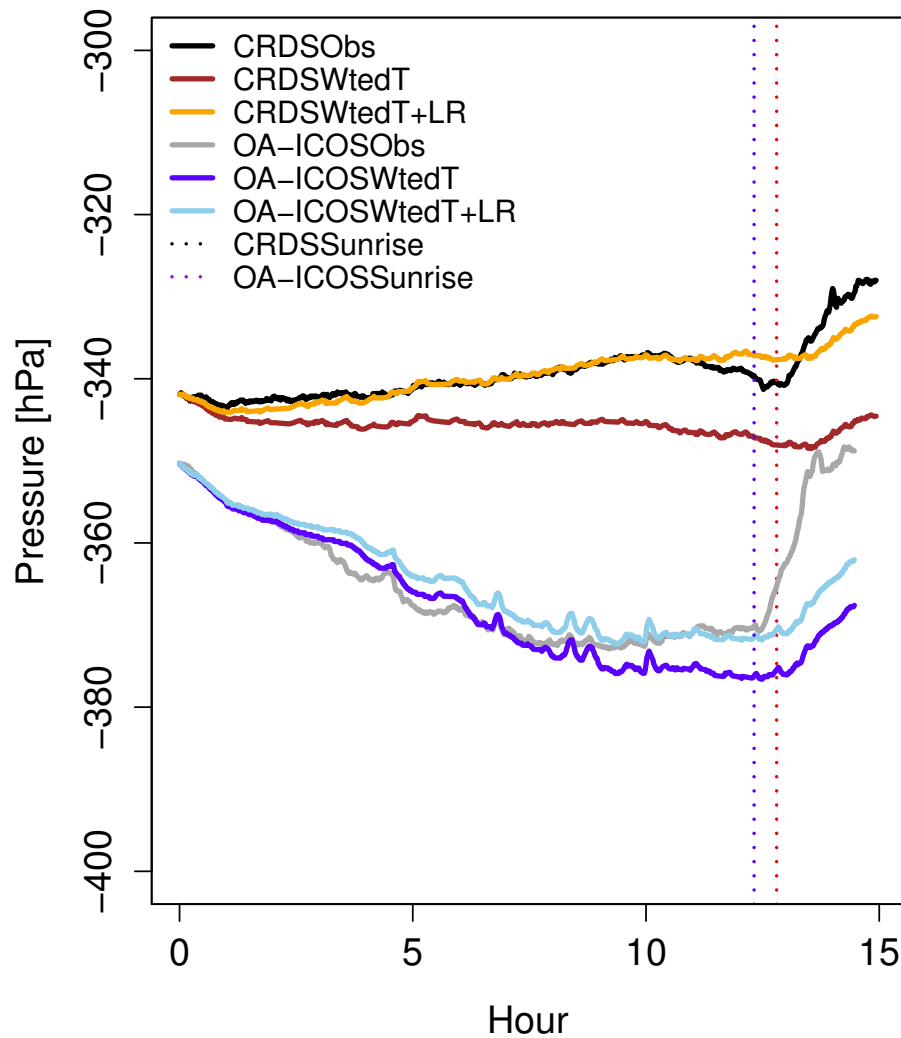


Figure 3.1: Pressure measured in the OA-ICOS (OA-ICOSObs) and CRDS (CRDSObs) sample lines with a high-resolution pressure sensor (P303 and P205). Also included are a modeled pressure weighted by the volumes of the 12 mm tubing outside of the laboratory and the  $1/8$ " tubing inside the laboratory (CRDSWtedT and OA-ICOSWtedT), and these modeled pressures plus the linear leak rate (+LR). The two vertical lines mark sunrise for both tests, which were conducted on different days. The leak rate was calculated after fitting the modeled pressure to the observations, excluding the portion of the test after sunrise, when the 12 mm tubing on the mast began to heat relative to the surrounding air temperature.

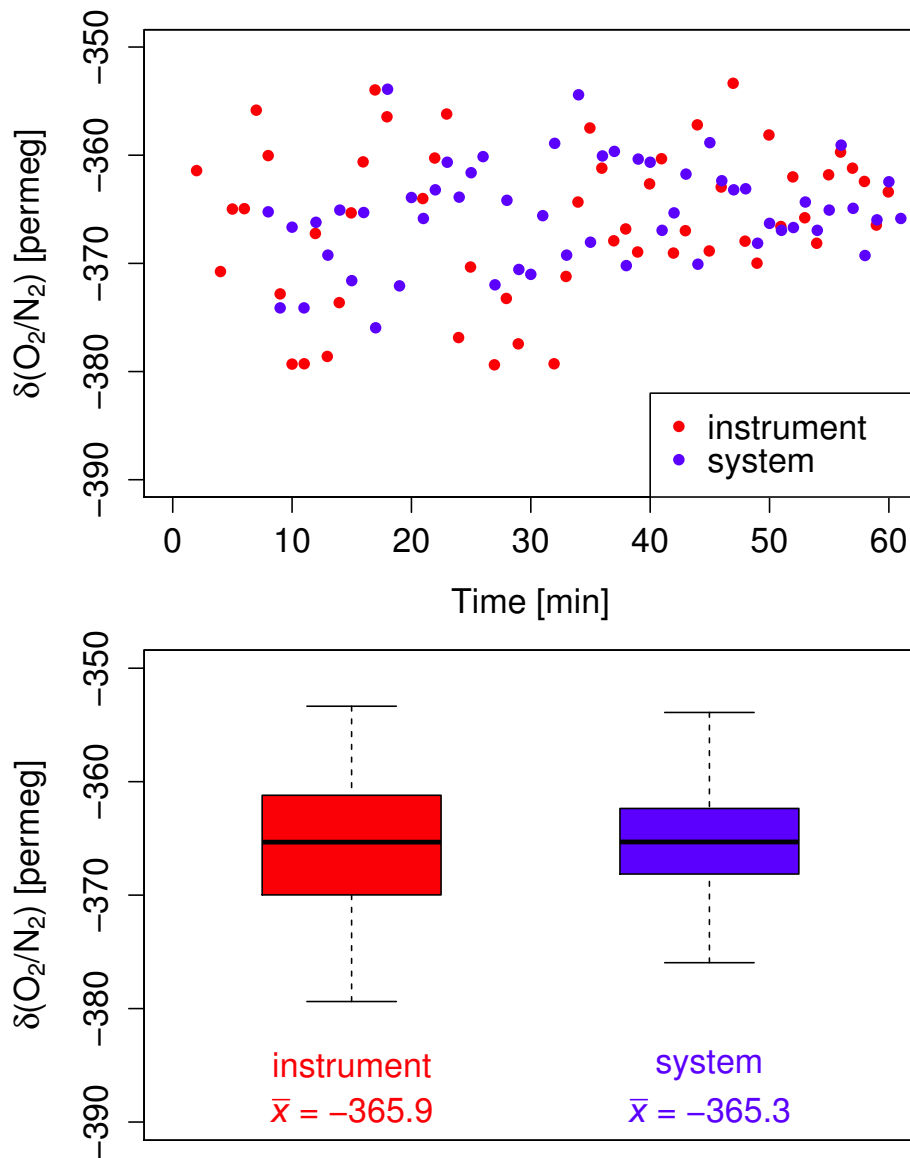


Figure 3.2: Comparison of two 1 hr measurements of the same working tank with the DFCA, once with the flow going directly into the instrument (“instrument”) and once with the flow passing through the whole plumbing system (“system”). Data is shown both as a concentration evolution from the beginning of each test (*top panel*) and as boxplots of both populations (*bottom panel*).

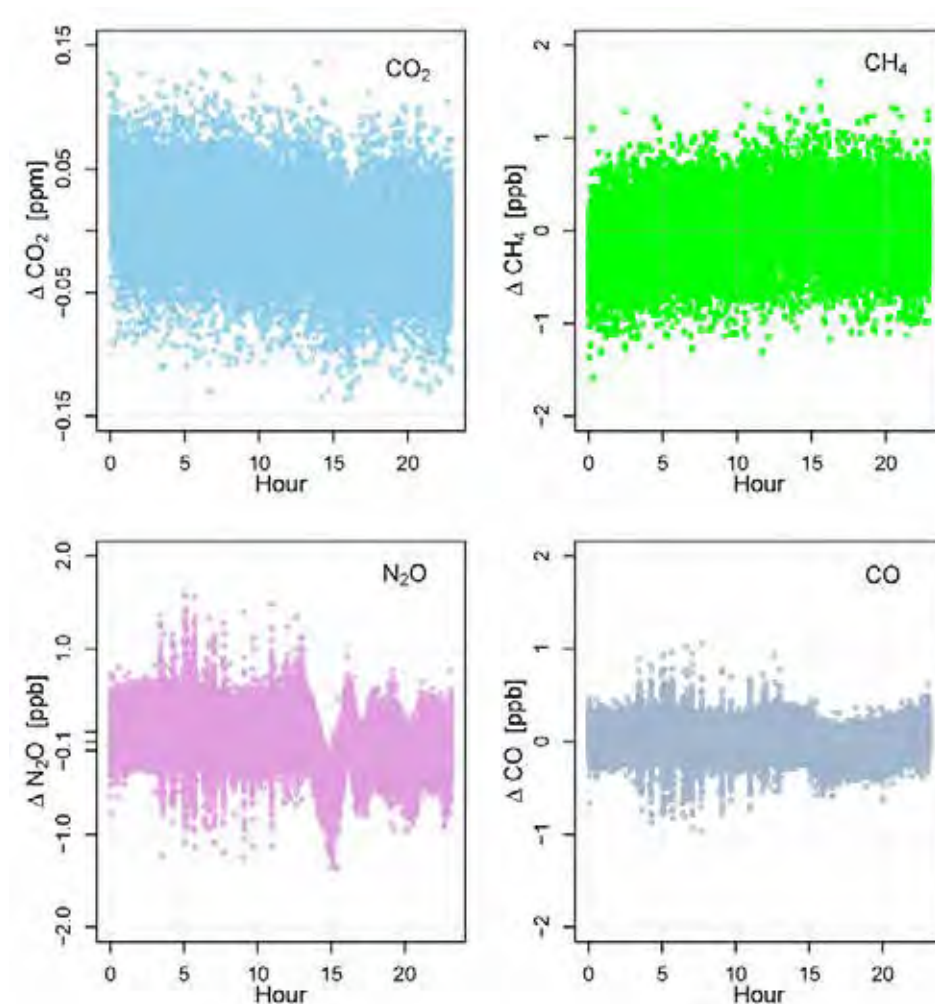


Figure 3.3: Anomaly of measurands of the CRDS and OA-ICOS, calculated as the instantaneous data minus the mean of the whole test.

### 3.3.5 Stability of the OA-ICOS

While the OA-ICOS is very precise over short intervals, it is much more prone to drift than the CRDS. The optimal averaging interval for this instrument is around 100 seconds for both species, after which drift begins to dominate the sensor error. The OA-ICOS is prone both to sudden spikes and rapid linear drift when the instrument heats or cools the cavity to maintain a constant temperature. Raw target measurements over 2 years showed a maximal spread of 2.9 ppb for  $\text{N}_2\text{O}$  and 0.8 ppb for CO, although the long-term drift was not linear but governed by laboratory temperature.

### 3.3.6 Stability of the DFCA

Due to the differential nature of the DFCA, characterizing the noise of the individual sensors would serve little purpose, since the operator expects that the absolute signal of both fuel cells will drift. The simplest and most meaningful test of sensor stability in the case of this instrument was to provide both fuel cells with flow from a working tank, and calculate

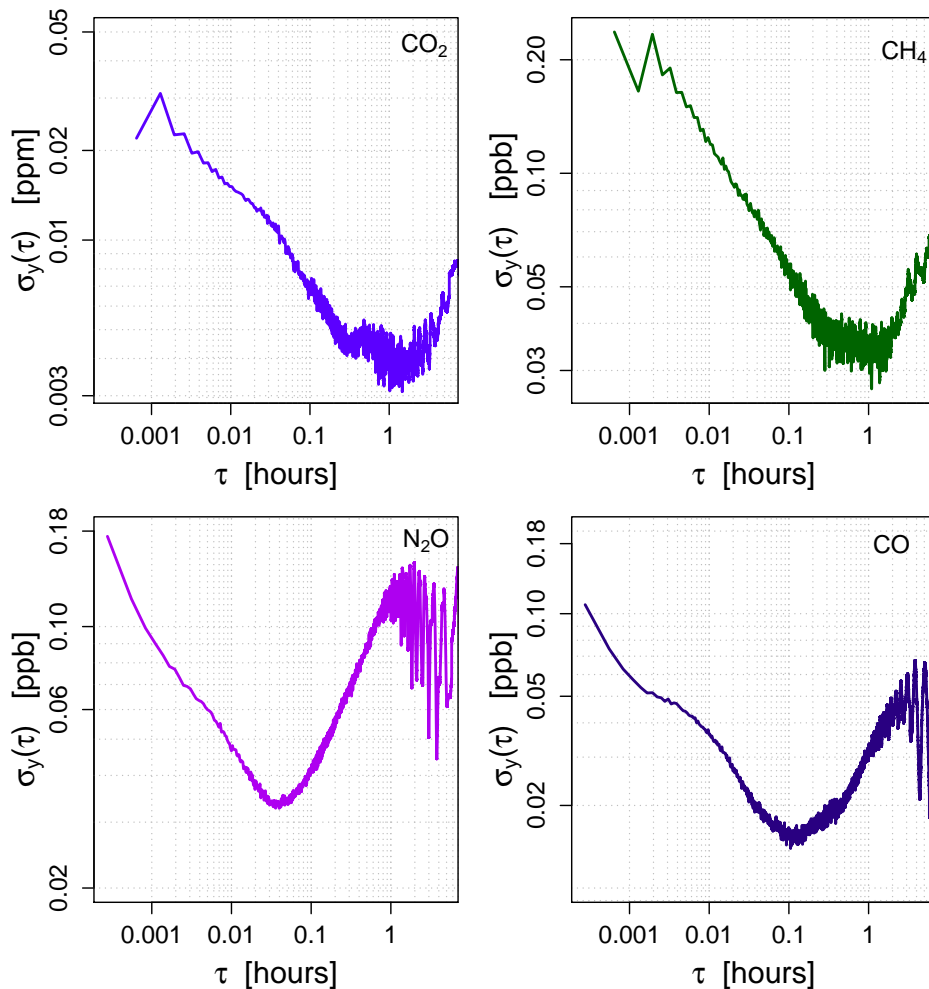


Figure 3.4: Log-log plots of the Allan deviations of the output of the CRDS and OA-ICOS instruments as they received gas flow from a working tank for 24 hours.

the Allan deviation of the differential signal (Figure 3.5, *top panel*), regardless of the low frequency of measurements.

From the time series of the DFCA output (3.5, *bottom panel*), it seems that the analyzer took roughly 5 hours to stabilize during the stability test. This apparent start-up drift is fairly small and could represent a gradual flushing of the regulator. Despite some small, sudden spikes, the DFCA shows the least dependence of the main instruments on the temperature and pressure of its environment, not surprising since the nature of the dual differential measurement should cancel out temperature effects. WMO/GAW compatibility goals for  $\delta(\text{O}_2/\text{N}_2)$  can be reached with an averaging interval greater than 7 minutes.

While the fuel cells have been monitored for degradation, no detectable loss in sensitivity has been noticed over the 2 years of operation.

### 3.3.7 Water Correction of the CRDS

The aggregated results of several water correction tests can be seen in Figure 3.6. The fit parameters determined from the aggregate tests show some small but significant differences from other values reported in the literature for similar instruments (Table B.6), highlighting

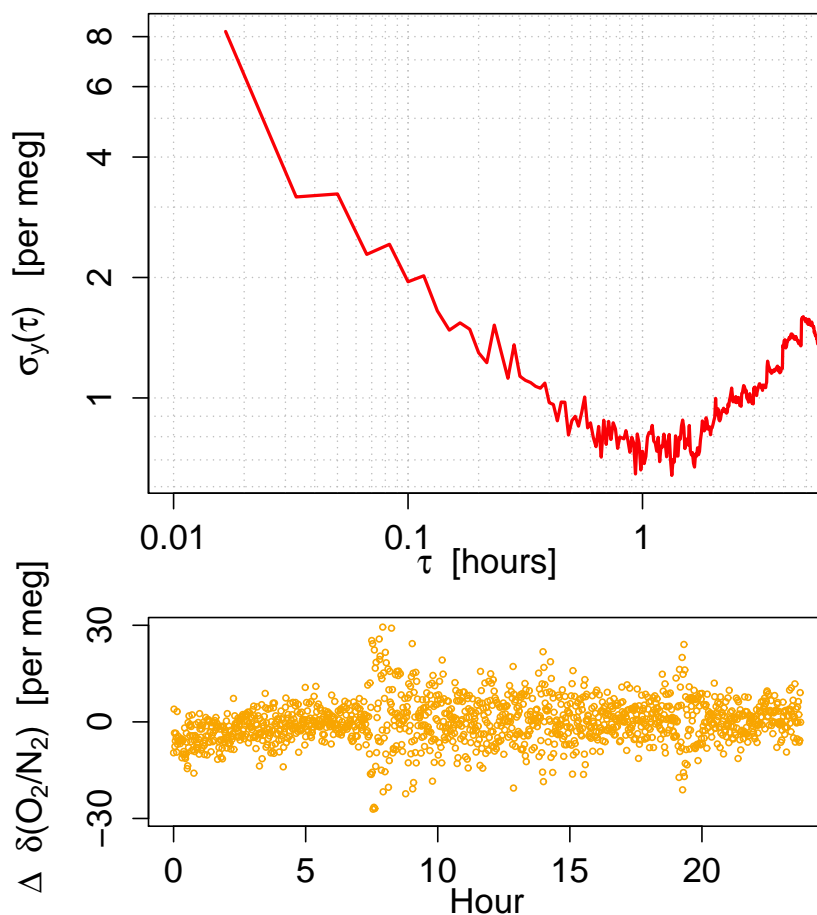


Figure 3.5: Log-log plot of the Allan deviation of the DFCA for the 24 hours of working tank flow (*top panel*) and anomaly of  $\delta(\text{O}_2/\text{N}_2)$ , calculated as the instantaneous data minus the mean of the whole test (*bottom panel*).

the importance of performing instrument-specific water correction tests with this class of CRDS. For instance, using the values from [Rella et al. \[2013\]](#) to correct a NDAO  $\text{CO}_2$  wet value of 390 ppm at 1.5% water vapor content would result in a difference of 0.23 ppm. It should be noted that the reference values cited from the literature were obtained using different models of the same CRDS instrument.

An earlier test, in which the absolute pressure of the target gas was increased to reduce the humidity level, is also included. A stainless steel trap of the same make as the small cryotrap (Figure [A.7](#)) used for the DFCA line was placed in a water bath (4°C) with a water droplet at the bottom of the trap. The pressure of the target gas was then increased stepwise from 0.2 bar (gauge, not absolute) to 1.5 bars. This method was discarded for the simpler water droplet test, as it proved to be cumbersome and did not yield high enough initial water vapor concentration, likely due to the low temperature of the water bath. The results agreed well with the other method, however.

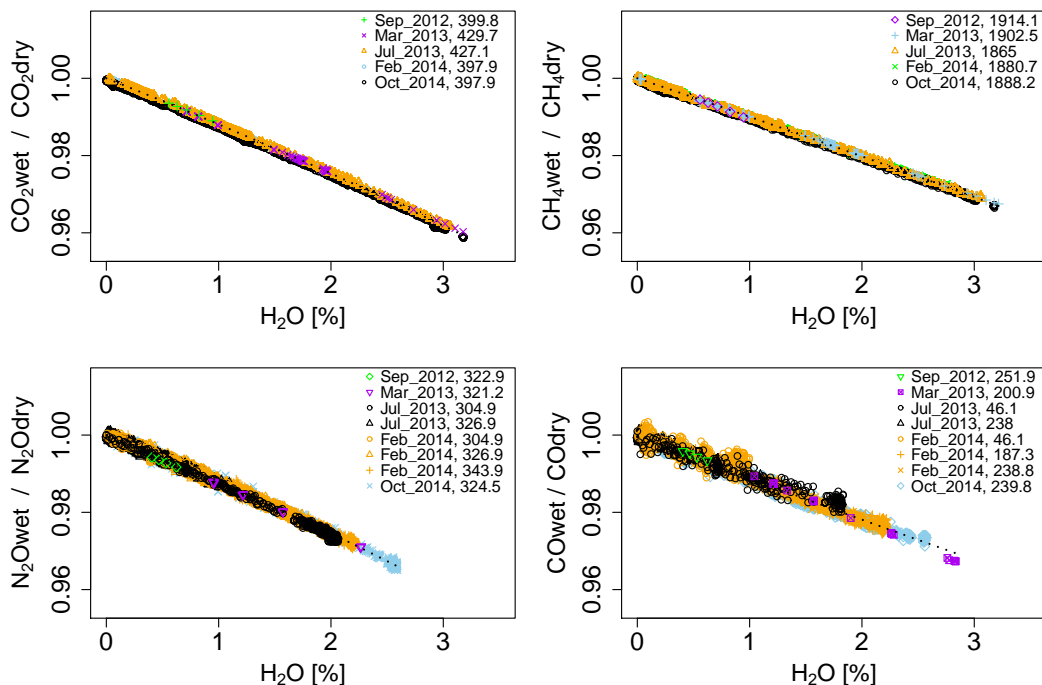


Figure 3.6: Water correction functions (dotted lines, see Equation 3.9) from different tests for all measurands, and test data. Colors represent different dates, and shapes represent specific mole fractions of the cylinder used for the test, all in ppb, except for CO<sub>2</sub>, which is in ppm.

### 3.3.8 Water Correction of the OA-ICOS

Table B.6 gives the values of the coefficients for a second-order water correction for both N<sub>2</sub>O and CO. Given the only recent availability of the instrument, and the greater prevalence of drying, there are no coefficients to compare to. Zellweger et al. [2012] performed a thorough comparison of the response of several different analyzers to water vapor, including the OA-ICOS N<sub>2</sub>O/CO-23d, but only considered carbon monoxide.

We also note that the absolute concentration of water vapor reported by the OA-ICOS disagrees considerably with that of the CRDS (which in part accounts for the lower water vapor concentrations displayed in Figure 3.6 for the OA-ICOS), the OA-ICOS values being 2,329 ppm ( $1\sigma = 342$  ppm) lower on average. We verified the accuracy of the CRDS water vapor measurements by comparing it to values calculated from the meteorology. Effectively, this means that the OA-ICOS instrument cannot detect values below  $\sim 2,000$  ppm, which results in artifacts during reference gas cycles (targets and calibration runs), as the air stream continues to dry after the instrument returns a 0 value for water vapor and the water correction cannot be applied. In fact, much of the scatter in the N<sub>2</sub>O time series is related to periods of higher relative humidity and water vapor concentration in the in situ measurements.

Finally it should be mentioned that OA-ICOS's internal water correction is not sufficient to remove the full influence of water vapor, and does not account for the quadratic nature of the response curve to water vapor for both N<sub>2</sub>O and CO. If one compares the dry air mole fraction using the OA-ICOS linear internal water correction to the second-order water correction function used in this work, the two diverge with increasing water vapor concentration. For instance, an error of approximately 1.8 ppb at an ambient water vapor concentration of

$\text{H}_2\text{O}_{rep} = 20,000$  ppm or  $\sim 3.5$  ppb at a concentration of 30,000 ppm would be produced for  $\text{N}_2\text{O}$  using the linear function relative to the quadratic. For CO the effect was less pronounced but would result in errors of 0.7 and 1.5 ppb, respectively.

### 3.3.9 Calibrations

Calibrations were subjected to quality control (QC) assessments and discarded if they failed to meet specific QC targets for individual species.

For the CRDS, 4% of calibrations were excluded, based on the following QC criteria: a coefficient of determination greater than 0.9999, a deviation from the mean slope greater than 0.002 (unitless; ppm/ppm), or a deviation from the mean intercept larger than 1 ppm. For  $\text{CH}_4$ , the QC flags were 0.999, 0.02, and 10 ppb, respectively. This approach ensures that anomalous calibration coefficients were not used in producing the final time series. In most cases the poor calibrations were related to recent power outages or large variations in temperature in the laboratory, and the species causing the flag was  $\text{CO}_2$ . The mean  $R^2$  was 0.9999987 for  $\text{CO}_2$  and 0.999995 for  $\text{CH}_4$ .

20% of the OA-ICOS calibrations were rejected, in almost all instances due to  $\text{N}_2\text{O}$  not meeting QC standards. The QC standards were: greater 0.9999 coefficient of determination, slope deviation from the mean not greater than 0.015, and an intercept within  $\pm 5$  ppb of the mean of all intercepts. For CO the corresponding values were: 0.99996, 0.02, and 1 ppb. The mean  $R^2$  was 0.99997 for  $\text{N}_2\text{O}$  and 0.999989 for CO.

In the case of atmospheric oxygen, 33% of calibrations were discarded, most of these during a period of frequent power outages and hence poor temperature control in the instrument rack. The QC criteria were an  $R^2 > 0.99$ , a slope not deviating more than 0.01 from the mean, and an intercept within 25 per meg of the average. The mean  $R^2$  was 0.996.

### 3.3.10 Target Measurements

Target measurements (tanks of known concentrations which are treated as unknowns) for the time series are presented in Figure 3.7. Periods of poorer performance are associated with inadequate electricity supply, dust events, and/or degraded temperature control of the laboratory or a specific instrument. The target tank had to be changed several times during the first 6 months of operation due twice to the loss of target gas during power outages before a more robust power-down procedure was implemented. In the new procedure, after power loss the control computer, while running on an uninterrupted power supply (UPS) system, returns all valves to a configuration that prevents the loss of gas. Other target tank changes were due to the necessity of switching which tanks served as target and which as working secondary standards as the calibration scheme was adjusted to conserve gas before more cylinders could be delivered. Bias (mean offset) between the assigned values obtained from MPI-BGC laboratories of reference tanks and the average of all target measurements at NDAO are given in Table B.7.

For oxygen this bias is large enough to warrant some speculation. As the target gas shares the same plumbing lines as the calibration gases, a leak or fractionation effect is unlikely, since it would effect the calibration gases as well. It is always possible that the target was contaminated during installation due to blowback when installing the regulator, which might account for the slightly enhanced  $\text{CO}_2$  and CO, and the depleted  $\delta(\text{O}_2/\text{N}_2)$ , while  $\text{N}_2\text{O}$  and  $\text{CH}_4$  are unaffected, as this is the sort of profile one would expect in the laboratory environment. The slope of the linear fit to the calibration data is also quite sensitive to the absolute value of the cylinder with the lowest concentrations, so these small biases could also be due to inter-laboratory differences at the low end of the scale for those three species.



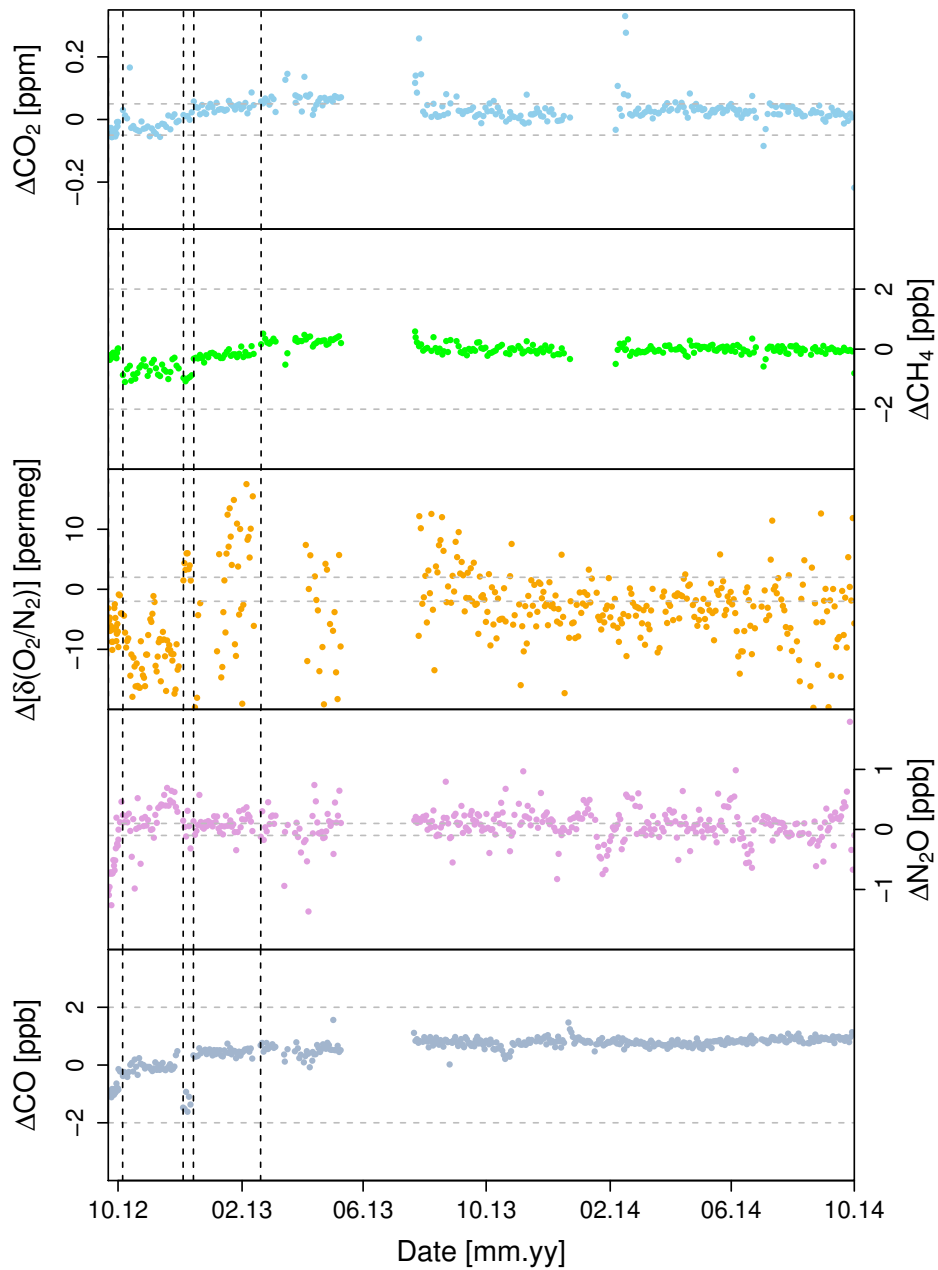


Figure 3.7: Target measurements for all measurands over the station lifetime, plotted as measured value minus setpoint.

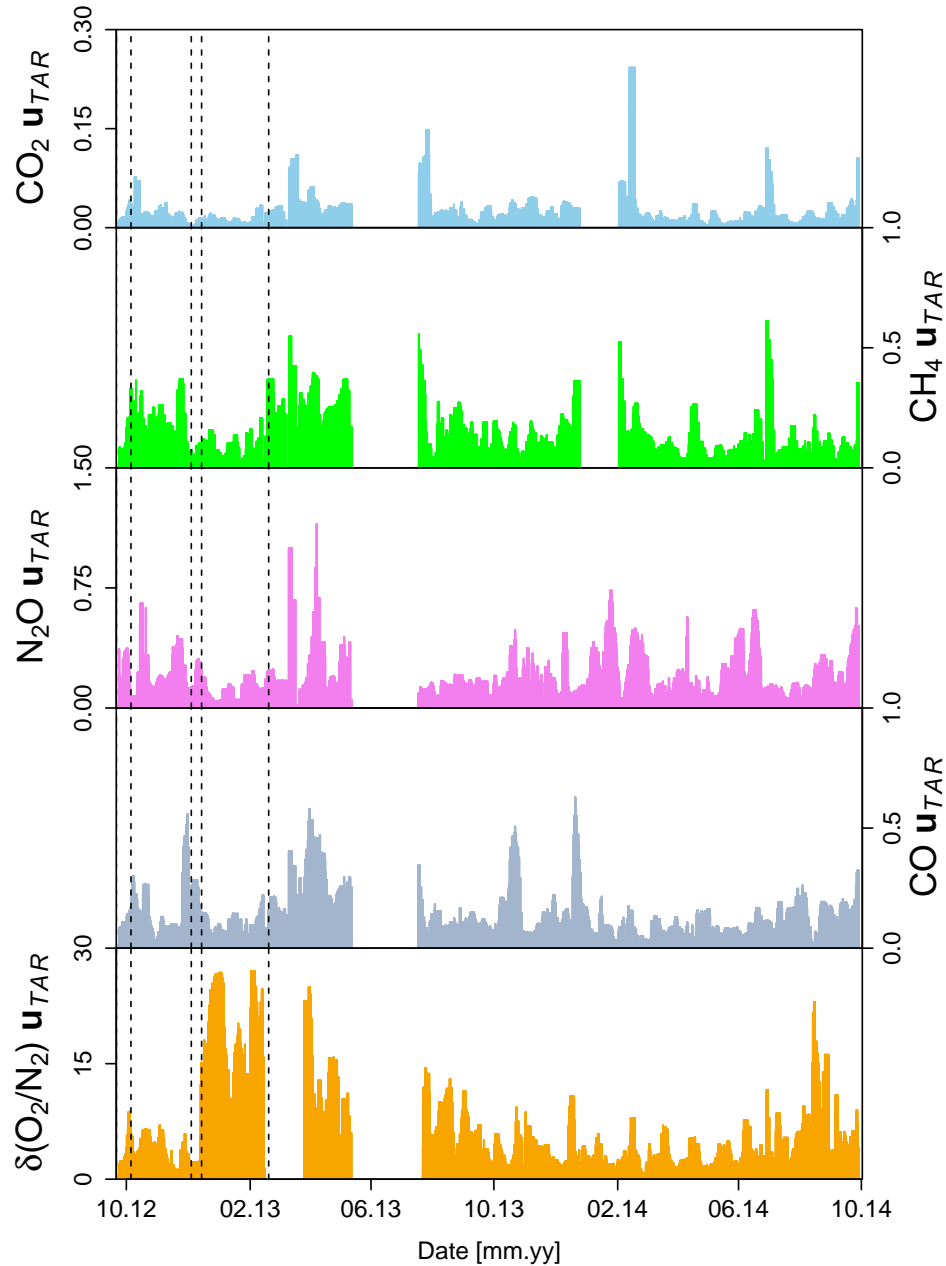


Figure 3.8: Measurement uncertainty derived from target measurements ( $\mathbf{u}_{tar}$ ). Mean bias (i.e., differences from MPI-BGC determinations of target tank setpoints from NDAO’s determination) for each tank has been removed to better approximate the sample uncertainty. Vertical lines indicate a target tank change.

Measurement uncertainty was estimated from the target tank time series ( $\mathbf{u}_{TAR}$ ) to give a time-varying quantity (Figure 3.8). The average bias of each target tank was removed to calculate the measurement uncertainty since this varied from tank to tank and would not necessarily impinge on sample uncertainty of the in situ data. Note that this bias was not removed from the target tank time series in Figure 3.7.

The mean uncertainty for each species was: 0.21 ppb for  $\text{N}_2\text{O}$ , 0.15 ppb for  $\text{CO}$ , 0.028 ppm

Table 3.4: Measurement Compatibility with Cape Point Observatory and MPI-BGC (flask vs. in situ)

Measurand	MPI-BGC	Cape Point	Unit
CO <sub>2</sub>	0.14	0.1	ppm
CH <sub>4</sub>	1.6	1.2	ppb
N <sub>2</sub> O	0.33	1.3	ppb
CO	4.5	0.2	ppb
$\delta(\text{O}_2/\text{N}_2)$	9.4	—	per meg

for CO<sub>2</sub>, 0.17 ppb for CH<sub>4</sub>, and 6.5 per meg for  $\delta(\text{O}_2/\text{N}_2)$ .

### 3.3.11 Drift Correction of the OA-ICOS

The average drift correction over each two hour period for the N<sub>2</sub>O data was  $\pm 0.47$  ppb (or 0.2 ppb per hour), with a maximum of  $\pm 1.9$  ppb. The corrections for CO were a little lower, with an average of  $\pm 0.31$  ppb (or 0.16 ppb per hour) and a maximum of  $\pm 1.1$  ppb. The application of this empirical drift correction significantly improved the data quality for both species as measured through the target cylinders (Figure 3.9). In the case of N<sub>2</sub>O, this allowed for the performance goal for this species to be reached, on average.

### 3.3.12 External Validation

A small inter-laboratory comparison was performed with the global GAW station run by the South African Weather Service at Cape Point, South Africa. A cylinder of dry background air from Cape Point was measured at both sites for CO<sub>2</sub>, CH<sub>4</sub>, N<sub>2</sub>O, and CO. The absolute value of the difference between the final determinations, i.e., the compatibility, was 0.1 ppm, 1.2 ppb, 1.3 ppb and 0.2 ppb, respectively. More comparisons are planned.

Flask samples also offer a kind of external validation of the in situ measurements, through assessing the compatibility of the flask and continuous data. The flask time series begins in mid-2013 and is ongoing. The average standard deviation of the flask triplicates were 0.04 ppm for CO<sub>2</sub>, 1.6 ppb for CH<sub>4</sub>, 0.06 ppb for N<sub>2</sub>O, 1.1 ppb for CO, 4.0 per meg for  $\delta(\text{O}_2/\text{N}_2)$ ; and 3.9 per meg for APO.

Measurement compatibility between flask and in situ measurements are given in Table 3.4. The difference between the flask measurement and the in situ is displayed as a time series in Figure A.10. Most of the bias seen between flask and in situ measurements can be explained for carbon monoxide. CO mole fractions are known to increase in flasks during storage [Brenninkmeijer et al., 2001, Novelli et al., 1998]. At MPI-BGC, tests showed rates between 0.02 and 0.03 ppb day<sup>-1</sup>, in some cases as high as 0.05 ppb day<sup>-1</sup> (Armin Jordan, personal communication). Additionally, the offset showed some dependency on storage time (Figure 3.10); the specific mechanism is unknown.

Additionally, the NDAO in situ time series was compared to the available dataset from the nearby NOAA ESRL GMD sampling site NMB (Figure 3.11). It should be noted that this is not a direct assessment of the compatibility between the two measurement programs, since the two stations do not really measure the same air masses; the sites are about 2 km apart and have a height differential of 32 m. This can be of consequence since the boundary layer oscillations in the local wind field often create considerable heterogeneity in flow, creating spatial and temporal gradients [Lindesay and Tyson, 1990]. While small differences between concurrent measurements at the two sites would be expected, the synoptic variability, seasonality, and long-term trend should be the same, and this is what is observed (Figure 3.11,

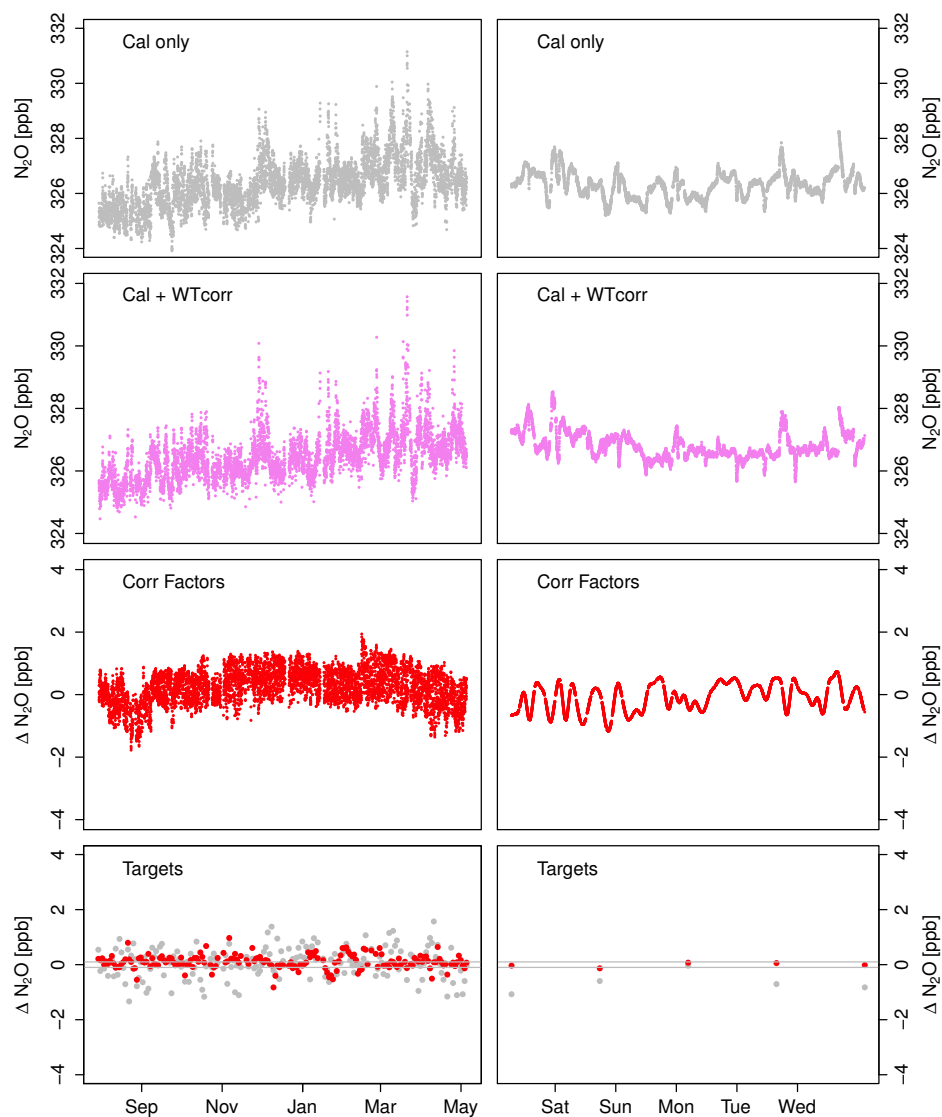


Figure 3.9: Detail of the working tank correction for the OA-ICOS instrument, showing the correction process for the entire time series (*left*) and an arbitrarily selected week (*right*) for  $\text{N}_2\text{O}$  only. In the first row,  $\text{N}_2\text{O}$  is shown with only calibrations applied (“Cal only”). In the second row, a drift correction based on the working tank measurements has been applied to the calibrated data (“Cal + WTcorr”). In the third row, the correction factors that were used to produce the data in the second panel are shown (“Corr Factors”). These are determined by calculating the difference between each working tank measurement and the average of all working tank measurements and fitting a curve to groups of consecutive working tank measurements with no gaps (i.e., every two hours). In the fourth panel, target measurements (“Targets”) are shown using the calibrated only data (gray points) and the drift corrected and calibrated data (red points).

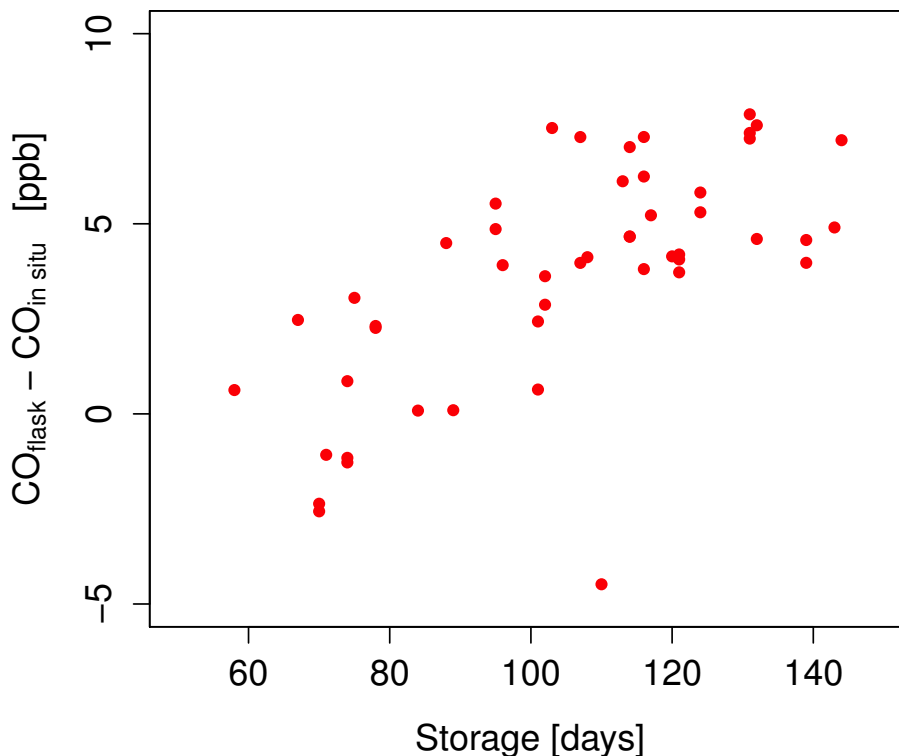


Figure 3.10: Evidence for a carbon monoxide storage-related artifact.

Sections 4.3.4 and 4.3.5). After excluding outliers greater than  $3\sigma$ , the average absolute difference of all concurrent measurements (using one-hour means for the in situ data) was 0.43 ppm for  $\text{CO}_2$ , 2.2 ppb for  $\text{CH}_4$ , 0.25 ppb for  $\text{N}_2\text{O}$ , and 3.5 ppb for CO.

### 3.4 Summary and Conclusions

Generally it is found that the gas handling, instrumentation, and conservative reference gas scheme perform acceptably. Using water corrections in lieu of drying is feasible but complicates calibrations and target measurements as the gas lines switch between dry and humidified air. The reduction in maintenance, gas handling complexity, and drying related artifacts, however, make this approach preferable.

The differential fuel cell analyzer is a successful approach to the challenge of measuring atmospheric oxygen in a remote location. The CRDS was found to be quite robust and stable. The OA-ICOS instrument gives good performance if instrument drift can be corrected for with a working tank.

NDAO is not totally impervious to the harsh environment, notably dust and heat, and the whole system is sensitive to the large diurnal temperature variation. Most challenging was the inadequate electricity supply, which reduced temperature control in the laboratory, and destroyed two hard drives. Overall, when basic requirements for laboratory operation are met, the measurement system presented can yield much-needed data from a remote and sometimes harsh location.

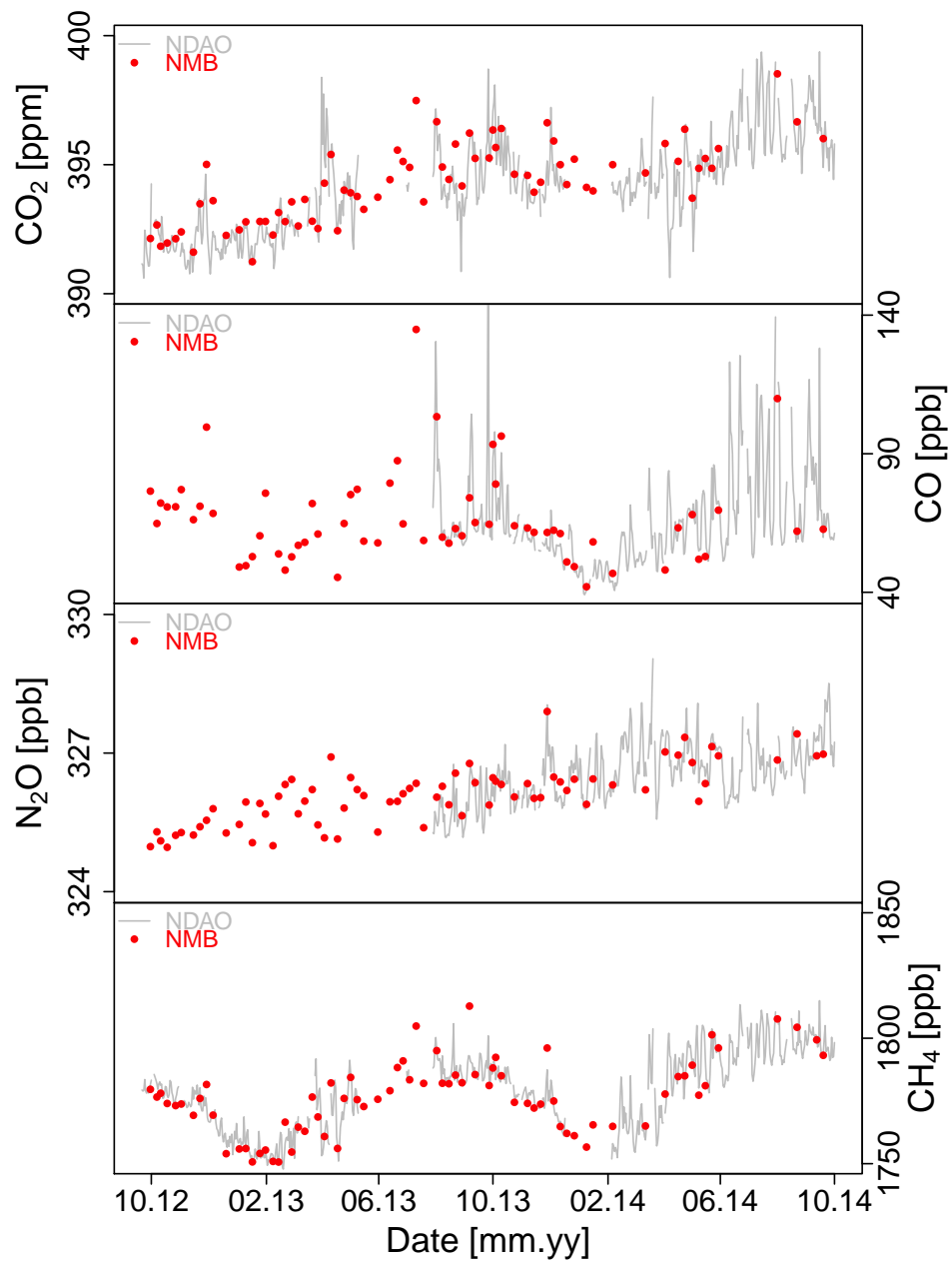


Figure 3.11: NDAO in situ measurements compared to NMB (NOAA) flask measurements. NDAO values are daily averages, NMB values are averages of the flask pair.

# 4

## The NDAO Time Series

### 4.1 Introduction

Stationary time series of atmospheric constituents can demonstrate variability over multiple time scales. The decomposition of a time series through spectral analysis can yield insight into the causes of this variability if a spatial scale can be inferred from the temporal scale. For example, diurnal variability in CO<sub>2</sub> or O<sub>2</sub> is often a result of local fluxes, while seasonal cycles are influenced by hemispheric-scale fluxes. Intraseasonal or sub-seasonal variability is generally related to the passage of synoptic-scale weather systems. Such temporal variability can be related quantitatively to a spatial scale by modeling atmospheric transport. For the NDAO site, for instance, examining the distance traveled by particles released in the HYSPLIT model throughout the evolution of each back-trajectory shows that, on average, synoptic scale levels of transport are reached after a period of 5 days (Figure A.11).

In this chapter, the main time series from the NDAO is presented and decomposed, to better understand the causes of the variability of each measurand.

### 4.2 Methods

Planetary boundary layer (PBL) heights were taken from the European Centre for Medium-Range Weather Forecasting's (ECMWF) ERA-Interim dataset [Dee et al., 2011]. The product has a time step of 3 hours.

Diurnal cycles were calculated for each measurand and some additional meteorological variables, using hourly means. In all cases, the mean value for the entire day was subtracted from each hourly value; the resulting anomaly for each hour was then averaged for all days in a month, or all days in a year.

#### 4.2.1 Data Treatment

The NDAO time series was processed using the methods discussed in Section 2.2.2. NDAO data was also compared to other marine background flask sampling sites, which are detailed in the same section, for the only overlapping time period available, October 2012–December 2013. Since this is a relatively short period of time, average growth rates were determined by calculating a regression line using the Theil-Sen estimator, a non-parametric technique that determines the slope as the median of slopes of all pairs of sample points [Sen, 1968, Theil, 1950]. This technique was used since it is less sensitive to outliers than ordinary least squares, a concern when dealing with smaller datasets. For slopes of measurand–measurand regressions, the reduced major axis method was employed.

### 4.2.2 Singular Spectrum Analysis

Singular spectrum analysis is a nonparametric technique that can be used to decompose a noisy time series into a trend and periodic components. SSA was performed using the “Rssa” package for R. The details are beyond the scope of this work, but the technique is briefly described as follows [Ghil et al., 2002, Schoellhamer, 2001]: first, a covariance matrix is constructed of the time series  $X(t)$  and  $K$  lagged vectors of  $X(t)$ , with length  $L$ , where  $K = N - L + 1$ .  $L$  is the window length, and should be less than  $N/2$ . This yields a matrix,  $\mathbf{X}$ , upon which a singular value decomposition is performed. The eigentriples from this SVD are then grouped by shared characteristics (determined by the operator) and the components are reconstructed to form a component of the original time series, such as diurnal variations, seasonal variations, etc. These isolated oscillatory components of the time series should be robust with regards to the selection of window length.

For each measurand, SSA was performed on the complete, unfiltered time series consisting of hourly averages, using window lengths that varied from 100 to 500 and 7000 to 9000. The range in window lengths was necessary to identify both high- and low-variability components. Diurnal variations, if they existed, were identified by period length. All oscillations greater than one day and less than six months were summed together to form a single intraseasonal component. For consistency, and since the NDAO time series is short, trends and seasonal amplitudes and phasing were determined identical to the method described in Section 2.2.2. In practice, the selection of eigentriples and window length is done through experimentation and requires judgments from the operator that would result in small differences if the SSA is repeated with small variations (i.e., it is unlikely that two different operators working on the same time series would come up with the same exact trend and oscillatory components). Since the goal of employing SSA in this work was simply to identify and extract modes of variability in the time series in order to better understand the behavior of each species, some small uncertainty in the final results was deemed acceptable.

## 4.3 Results and Discussion

The full station time series consists of the five main measurands— $\text{CO}_2$ ,  $\text{CH}_4$ ,  $\delta(\text{O}_2/\text{N}_2)$ ,  $\text{N}_2\text{O}$ , and  $\text{CO}$ —plus atmospheric potential oxygen (APO), and is presented in its entirety in Figure 4.1. The six meteorological parameters measured at the station are presented in Figure 4.2.

### 4.3.1 Variability of Basic Meteorological Parameters

Air temperature at NDAO displayed seasonal variability, but due to synoptic dependence, had a distorted cycle. Temperatures peaked in mid-April and reached a low at the end of July, five months out of phase with the peak of insolation, in late November. Instead, the seasonal peak of temperature is roughly in phase with the proportion of air masses that are terrestrial in origin, PBL  $f_{terr}$ . (see Section 2.3.1 and Figure 2.7). Barometric pressure reached a maximum in late July and a minimum in mid-February. This appears to reflect the passage of the Hadley cell (see Section 2.1.1). Relative humidity also showed some seasonality, similar to that of atmospheric water vapor, although there was considerable variability. Wind speed showed almost no appreciable annual cycle, although the highest wind speeds slightly favored the winter months.

All meteorological measurands also showed consistent diurnal variability. The daily cycle of air temperature ranged between 10 and 18°C, comparable to the amplitude of the harmonic fit to the seasonal cycle, 8.1°C. Air temperature peaked on average in the early afternoon,



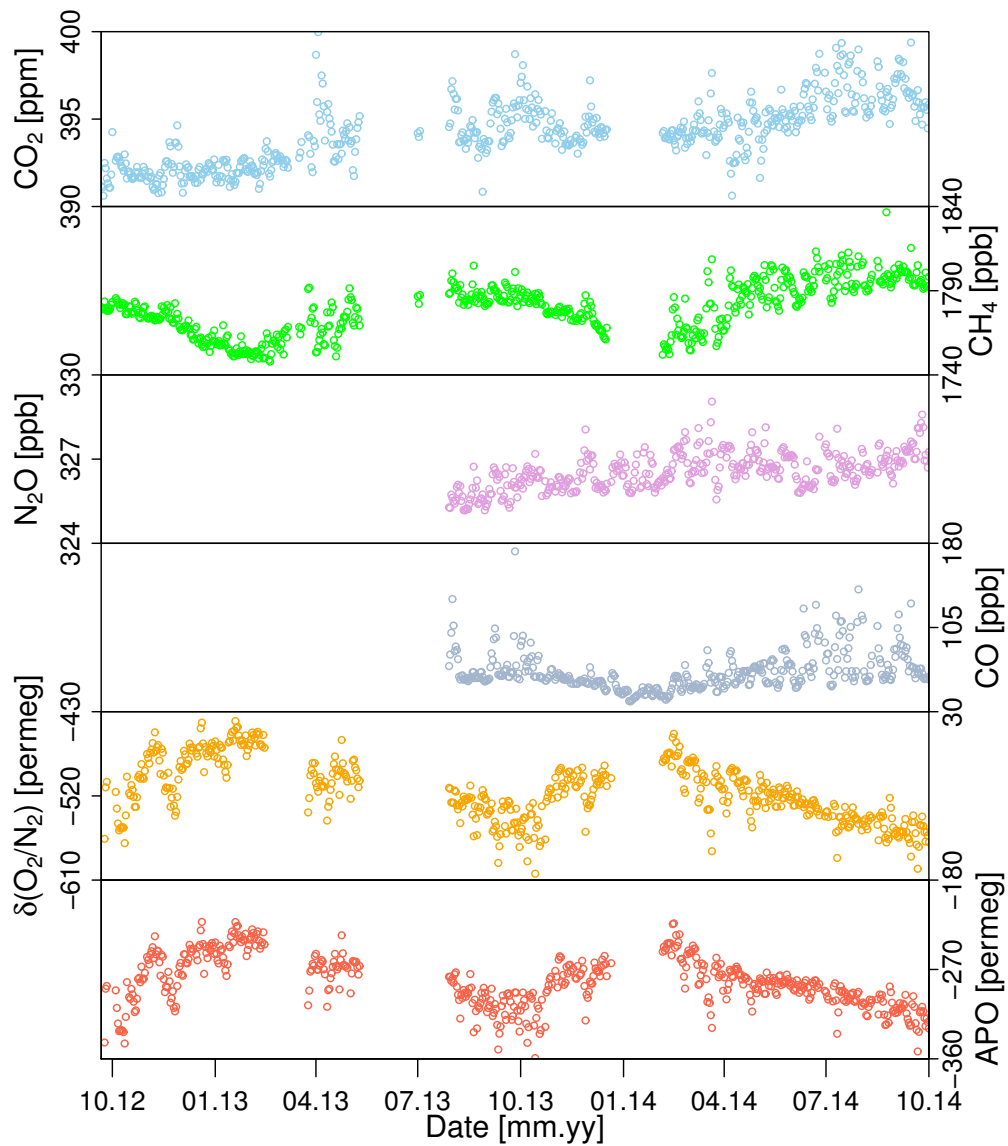


Figure 4.1: Main time series from NDAO, plotted as daily averages.

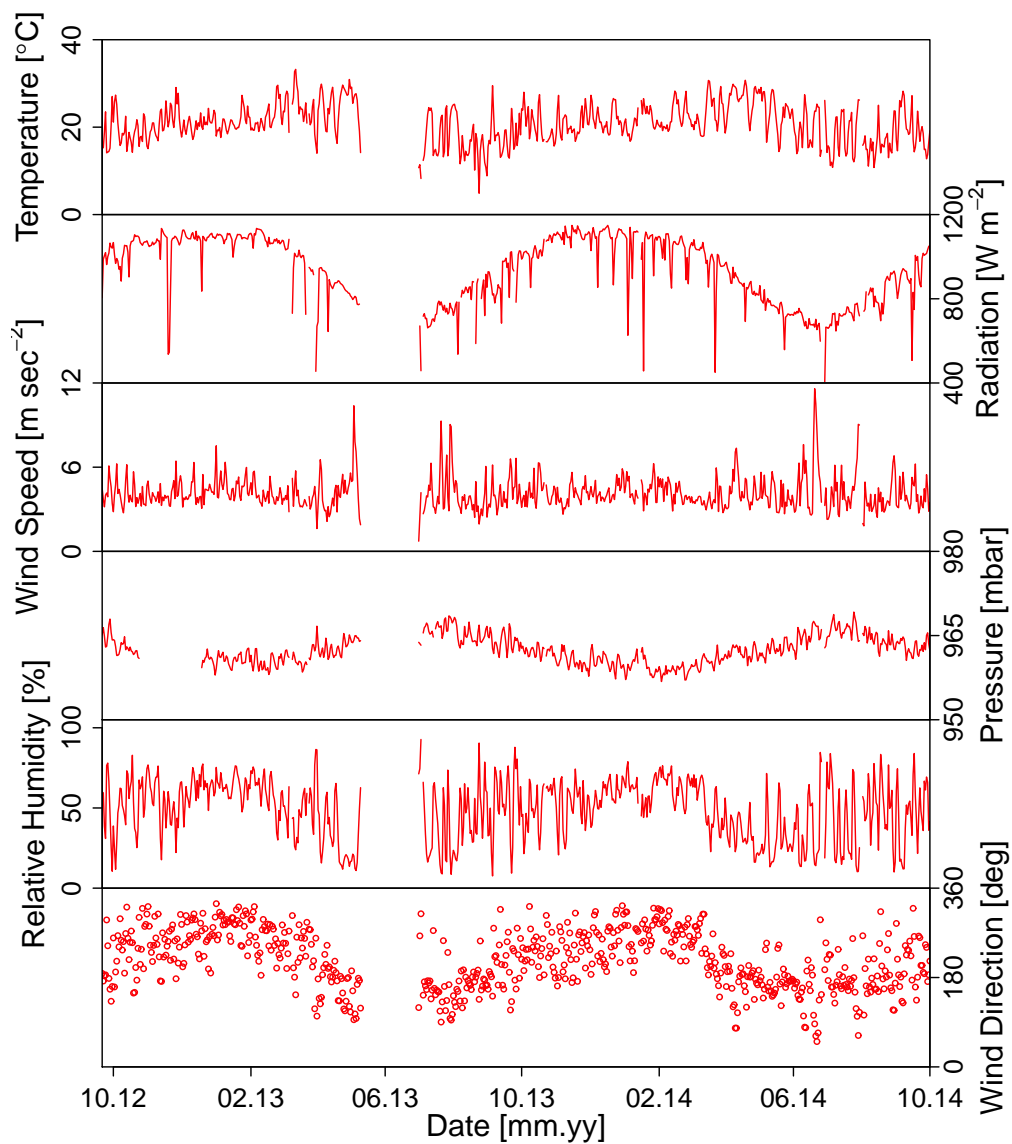


Figure 4.2: Meteorological time series from NDAO, plotted as daily averages, except for solar radiation, which is plotted as a daily maximum value.

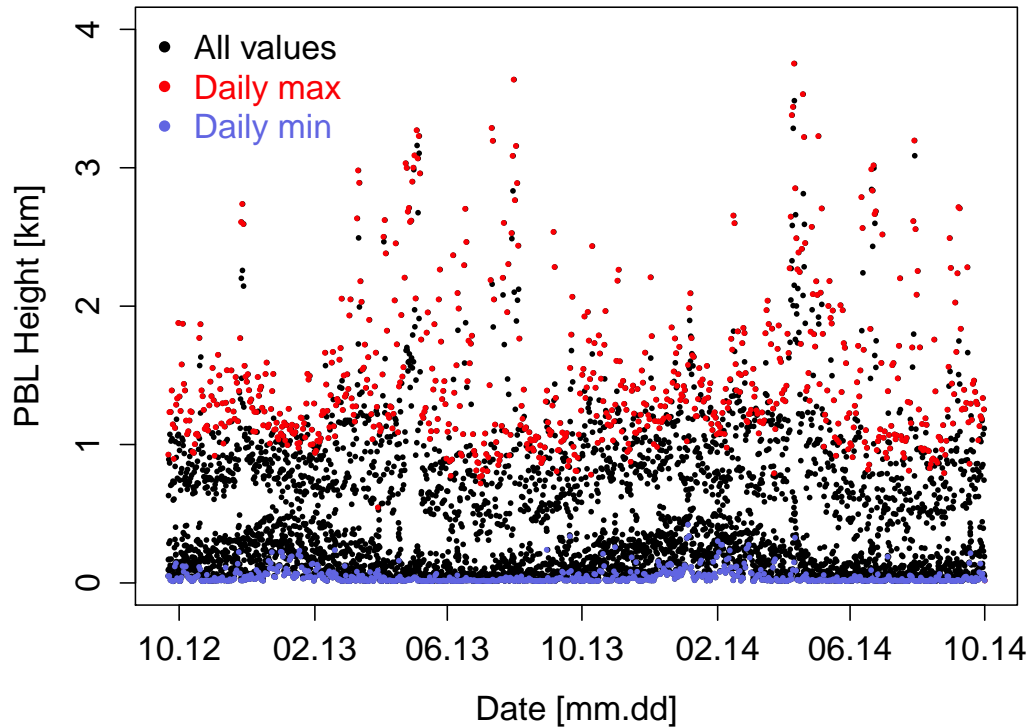


Figure 4.3: Planetary boundary layer (PBL) height data from the ECMWF ERA Interim meteorological fields. The daily maximum and minimum values are plotted as red and blue points, respectively.

between 15:00 and 16:00, with the coldest daily temperature occurring between 3:00 and 5:00 in the morning. Barometric pressure reached a maximum around 10:00 local time, with a minimum at 16:00 local time, but also showed semidiurnal variations, due to the atmospheric lunar tide [Paulino et al., 2013]. The diurnal variability of wind speed was much less well-defined than other meteorological variables, but generally winds were higher by 3–4 m sec<sup>-1</sup> at 16:00–17:00, when the sea breeze was at its peak. Winds were generally weakest in the morning, between 6:00 and 7:00.

The average maximum height of the planetary boundary layer (PBL) was 1439.1 m, and the average minimum was 38.8 m. PBL heights consistently peaked around 13:00 ± 2 hours, local time (Figure 4.4). The nocturnal boundary layer reached its smallest height between 22:00 and 4:00. PBL height showed a slight seasonality in its maximum and minimum daily value; higher maximums minimums were seen in austral summer (December and January). Similar to the characteristics of back-trajectories (see Section 2.3.1), the greatest values and largest variability in daily maximum PBL height were seen during austral summer (Figure 4.3).

#### 4.3.2 The Local Wind System

Four prominent sectors were visible in the wind direction time series (Figure 4.5 and Figure A.12). These corresponded well to the thermo-topographic wind system described by other authors in the literature [Brimelow and van Heerden, 1996, Hänslér, 2011, Lancaster et al., 1984, Lancaster, 1985, Lindesay and Tyson, 1990, Schulze, 1969, Tyson and Seely, 1980]

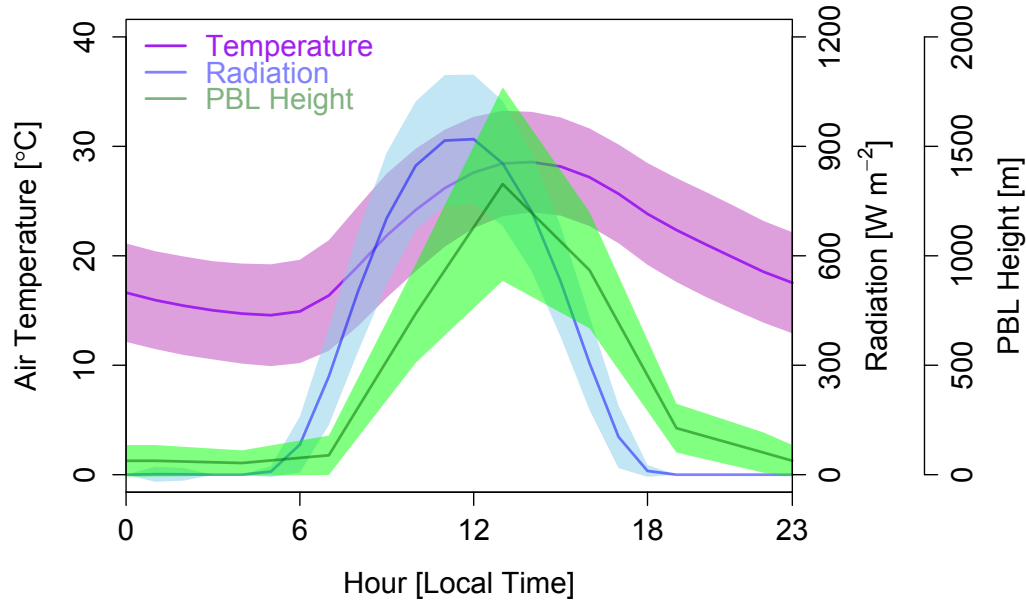


Figure 4.4: The average diurnal cycle of temperature, radiation, and PBL height. The light-colored ribbon shows one standard deviation, and the dark line the mean.

(see also Section 2.1.3). The sectors with the strongest winds were the sea breeze (SB), the plain-mountain wind (PMW), and the bergwinds (BERG). Bergwinds are only identifiable from the land breeze if temperature and humidity are taken into account. When wind speeds less than  $1 \text{ m sec}^{-1}$  are ignored, the five components of the thermo-topographic wind system account for 68% of all observations.

The sea breeze sector exhibited a double-peaked distribution, likely due to blocking by Station Dune<sup>1</sup>. The sector spanning  $187\text{--}197^\circ$  (SB1) covers the plain to the west of Station Dune, and sees winds stronger by  $1.0 \text{ m sec}^{-1}$  than SB2. Land breezes (LB) were the weakest winds, with an average of  $4.4 \text{ m sec}^{-1}$ , and bergwinds were the strongest, with an average of  $7.7 \text{ m sec}^{-1}$ .

The sea breeze occurs throughout the year with only occasional interruptions of its regularity due to strong synoptic events (Figure 4.6). Plain-mountain winds are more frequent during austral summer but are seen year round. Bergwinds, land breezes, and mountain-plain winds are almost entirely restricted to the austral winter months. Hence, westerly winds (from the ocean) predominate during austral summer and easterly winds (from the interior) predominate during austral winter (see also Figure 2.9). Wind sector prevalence also showed a pronounced diurnal variability (Figure 4.6). Sea breezes develop at Gobabeb in the late afternoon, between 12:00 and 18:00, stopping shortly after sunset. The rest of the diurnal period is typically dominated by PMWs, MPWs, or LBs, depending on the season. Bergwinds are more preferentially a daytime phenomenon, but can blow throughout the night on occasion.

<sup>1</sup>“Station Dune” is the name given to this specific sand dune by the GRTC community. The closest portion of the crest is 674 m from NDAO, lying in the  $185\text{--}215^\circ$  sector (SW); the front of the dune is oriented NNW–SSE. See Figure 2.4.

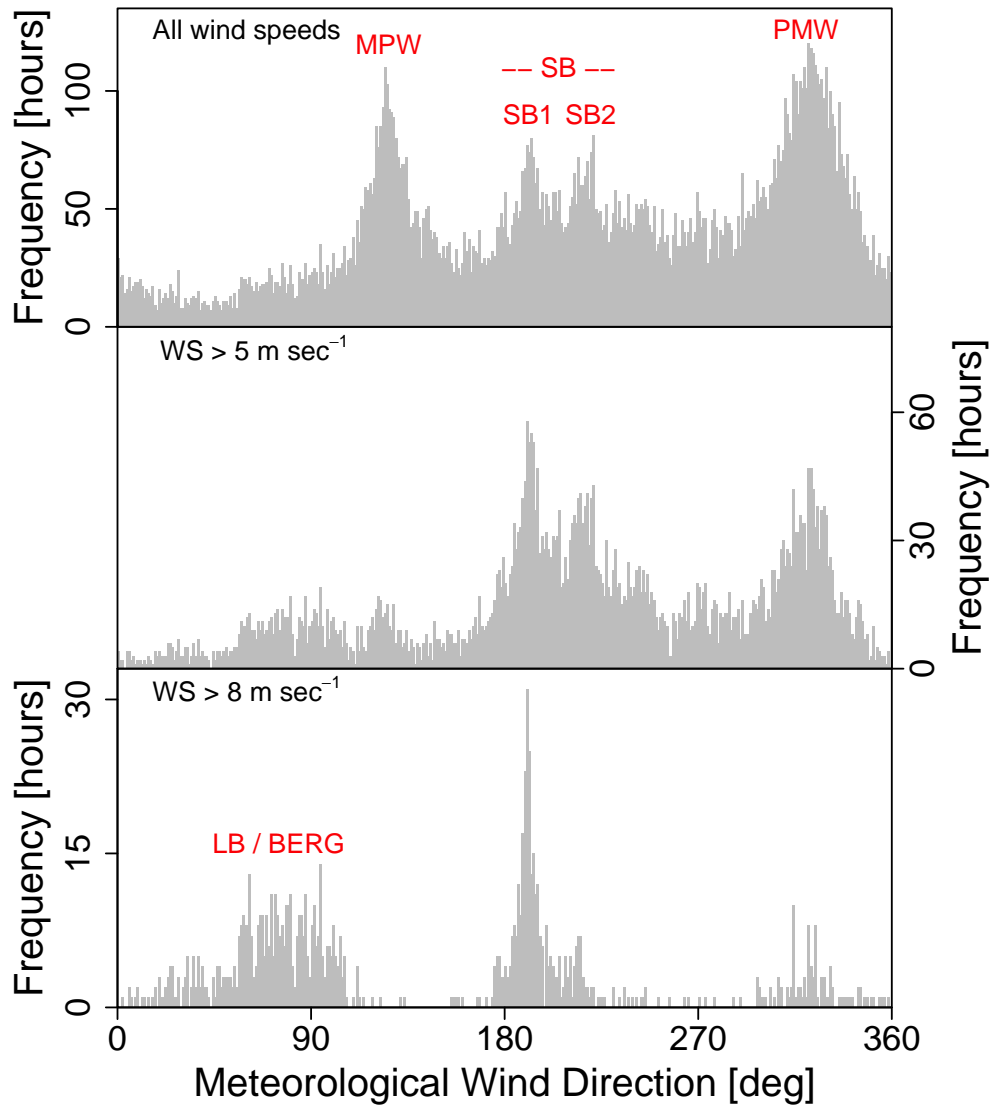


Figure 4.5: Histograms of meteorological wind direction measured at NDAO from the mast, using 1-hour means for the period October 2012–October 2014. Prominent sectors are labeled over their peaks, in red: “MPW” stands for mountain-plain wind, “SB” for sea breeze, “PMW” for plain-mountain wind, “LB” for land breeze, and “BERG” for bergwinds. The SB sector is further split into two sub-sectors, acknowledging the split distribution of this sector. See Section 2.1.3 for a discussion of the different sectors, and Table B.8 for a list of the bounds of each sector. In the *top panel*, no filtering is done of the wind direction dataset; in the *middle* and *bottom panels*, the dataset has been filtered by wind speed (WS).

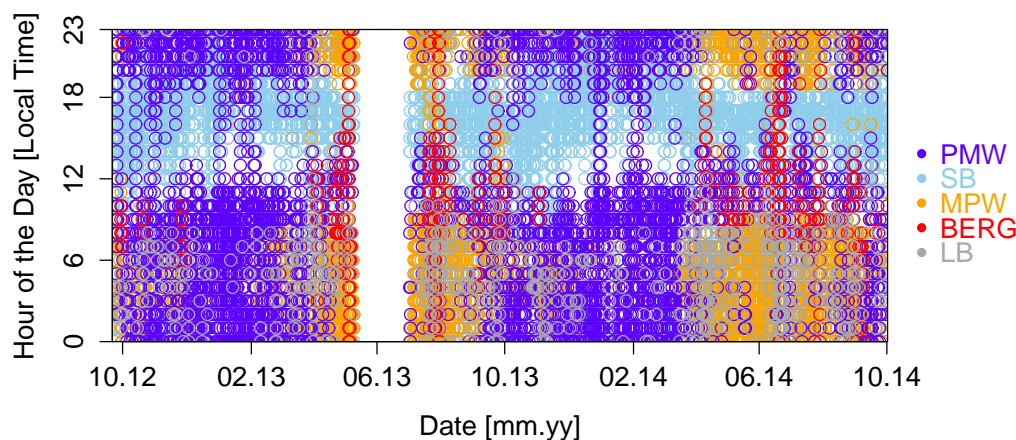


Figure 4.6: The diurnal variability of wind direction, separated by sector. Non-sector data points and data points corresponding to wind speeds of  $< 1 \text{ m sec}^{-1}$  are not plotted. Sector definitions are given in Table B.8.

### 4.3.3 Diurnal Variability of the Main Measurands

Some diurnal variability was observed for all measurands, though for  $\text{CO}$ ,  $\text{N}_2\text{O}$ ,  $\text{CH}_4$ , and  $\text{CO}_2$ , this was often negligible or lost within intradiurnal variability. A diurnal cycle was very prominent and consistent for  $\delta(\text{O}_2/\text{N}_2)$ . Diurnal variability is shown both in the results of the SSA for each species (Figures A.13 through A.17), and in the average monthly diurnal cycles (Figures A.18 through A.22).

These diurnal cycles appeared to be a result of boundary layer oscillations, which are large at Gobabeb, combined with horizontal advection of air via the local wind system. The two processes can create competing or complementing influences on the daily concentrations of NDAO measurands. This is because of a distinct vertical gradient in airflow, a fact noted in both the early empirical descriptions of the local wind system of the central Namib and in high-resolution (18 km) model simulations for the region [Hänsler, 2011, Lengoasa et al., 1993, Lindesay and Tyson, 1990, Tyson and Seely, 1980]. In summer, when PMWs dominant the surface flow, a LB or MPW can be found at height (ca. 1000 m). In winter, when MPW and LBs are found at the surface, a PMW can form above as a return flow [Hänsler, 2011, Lengoasa et al., 1993]. As the PBL height increases throughout the day, convection would mix the upper air masses with the dominate surface flow.

The degree to which species followed the local wind system or the PBL height gives some insight into the regional sources and sinks of these gases. For  $\text{CO}_2$ , for instance, the amplitude of the diurnal cycle extracted with SSA ranged from essentially 0 to as much as 4 ppm. Diurnal variability in  $\text{CO}_2$  and  $\text{O}_2$  at background sites is usually a result of surface fluxes due to vegetation and boundary layer oscillations [Stephens et al., 2007]: during daytime, when the boundary layer height is large, the flux signal from the surface is diluted with air at greater height. At night, as the ground cools, a stable, lower-lying nocturnal boundary layer typically forms that traps emissions from the surface [Aubinet et al., 2012]. Since the vegetation is very sparse or non-existent at Gobabeb except for a thin strand of brush and trees along the Kuiseb River, one would expect there to be little in the way of near-field fluxes due to photosynthesis and respiration of plants. Though there have been some reports of high  $\text{CO}_2$  uptake by desert soils with high carbonate content [Ma et al., 2014, Serrano-Ortiz et al., 2010, Wohlfahrt et al., 2008, Xie et al., 2009], this has been challenged [Schlesinger et al.,

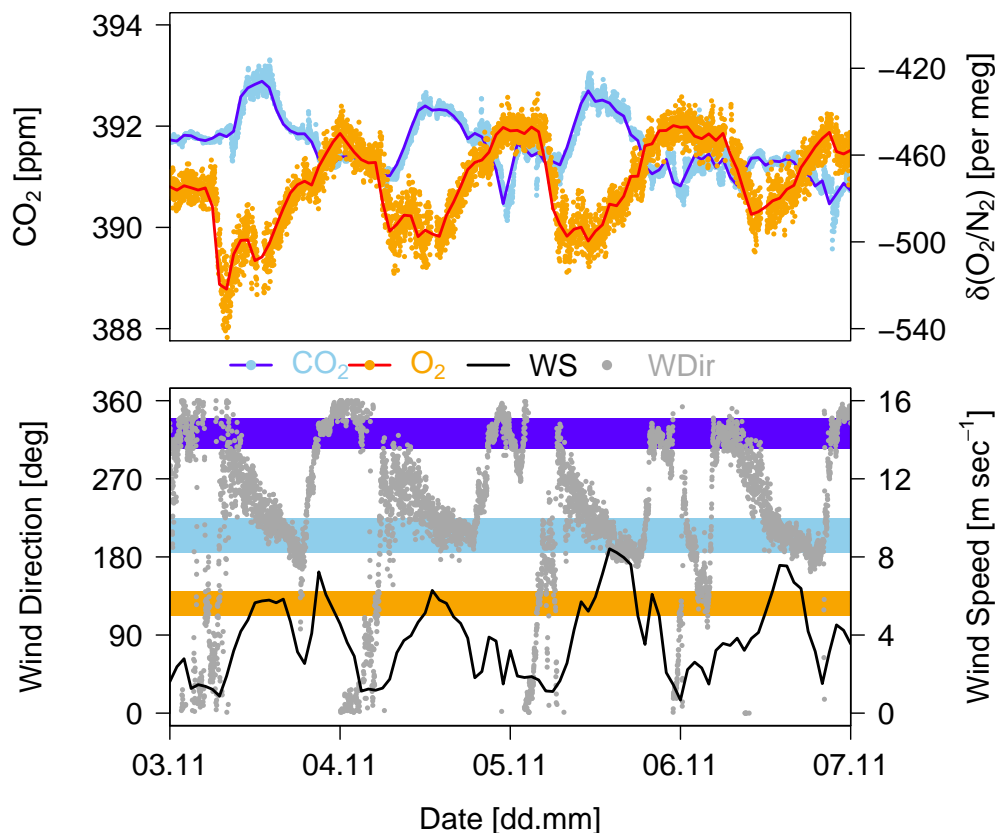


Figure 4.7:  $\text{CO}_2$ ,  $\delta(\text{O}_2/\text{N}_2)$ , wind direction, and wind speed over four days in November 2012. The wind direction shows a typical PMW/SB alternation, which induces a diurnal cycle in both  $\text{CO}_2$  and  $\text{O}_2$ . In the bottom panel, the dark blue bar shows the PMW sector, the light blue bar shows the SB, and the orange bar shows the MPW.

2009, Stone, 2008], and, regardless, the central Namib does not fit the special characteristics of the sites where such abiotic fluxes have been reported.

A photosynthetic/respiratory signal can be discounted as the cause of the diurnal variability of  $\text{O}_2$  and  $\text{CO}_2$  for most of the time series, since the cycle was typically the inverse of this pattern: the peak of  $\text{CO}_2$  occurs during the afternoon, around 14:00 (Figure A.18 and Figure 4.7). The diurnal cycles of  $\text{CO}_2$  and  $\text{O}_2$  were also slightly out of phase. For example, on November 3<sup>rd</sup>, 2012, the decline in  $\delta(\text{O}_2/\text{N}_2)$  began shortly after 7:00 and reached a minimum at 8:00, a decrease of about 75 per meg (Figure A.23). During this period of time, wind speeds were low and the wind direction changed from a typical PMW to the NE, and the nocturnal boundary layer was beginning to break up. As the sea breeze developed throughout the afternoon, the boundary layer deepened,  $\text{CO}_2$  mole fractions rose and  $\delta(\text{O}_2/\text{N}_2)$  declined. It is not fully clear from these data what caused the additional variability in  $\text{O}_2$ . It could be related to the break-up of the nocturnal boundary layer, although this would not explain the very steep slope found between  $\text{CO}_2$  and  $\text{O}_2$ . A full explanation would need to include a much more detailed study of the micrometeorology of the Gobabeb site.

The exchange ratio (see Section 1.6) of these typical PMW/SB cycles was indicative of a marine signal; the exchange ratio of the entire two-year dataset for all combined PMW and SB data was  $-7.6 \pm 0.2$ , while the exchange ratios for the easterly sectors—MPW, LB, and

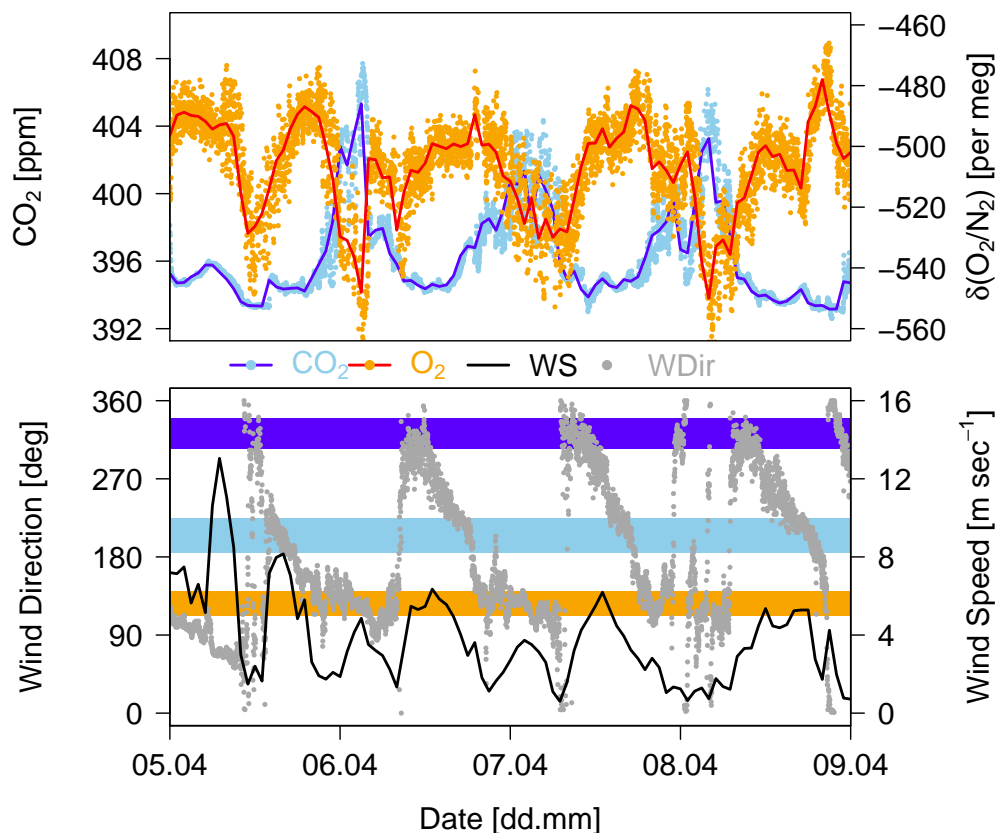


Figure 4.8:  $\text{CO}_2$ ,  $\delta(\text{O}_2/\text{N}_2)$ , wind direction, and wind speed over four days in November 2012. The wind direction shows a typical PMW/SB alternation, which induces a diurnal cycle in both  $\text{CO}_2$  and  $\text{O}_2$ . In the bottom panel, the dark blue bar shows the PMW sector, the light blue bar shows the SB, and the orange bar shows the MPW.

BERG—were close to  $-1$  (Figure 4.9). Likewise, the exchange ratio of the monthly average diurnal cycles was very negative for July through March, but close to  $-1$  for April through June. During those months with a strong MPW occurring at night, the terrestrial exchange ratio dominated most of the day, appearing to overwhelm the marine influence on the diurnal cycle (Figure A.24 and Figure A.25).

In contrast,  $\text{CO}$  and  $\text{CH}_4$  had a much less pronounced or consistent diurnal variation (Figure A.20–A.22 and Figures A.15–A.17). For carbon monoxide, the diurnal variability became greatest when the synoptic variability was greatest, which created a seasonality in daily variations for this species. During winter months, the diurnal cycle became more pronounced and its peak was associated with the maximum PBL height, while smaller peaks coincided with changes in wind sector and/or wind speed (Figure A.26). Since the local wind system and the PBL are not in phase, this created semi-diurnal oscillations that could be fairly prominent for  $\text{CH}_4$  and  $\text{CO}$  at times (Figure A.20 and Figure A.21). A daily peak in  $\text{CO}$  coincident with the greatest extent of vertical mixing is consistent with more polluted layers at height, a phenomenon discussed at length in Chapter 5.

The diurnal variability evident from the results of the SSA on  $\text{N}_2\text{O}$  was dwarfed by noise and intradiurnal variations, and should be viewed with caution. These sporadic, small diurnal cycles were largest during times of increased synoptic variability. While this species was also



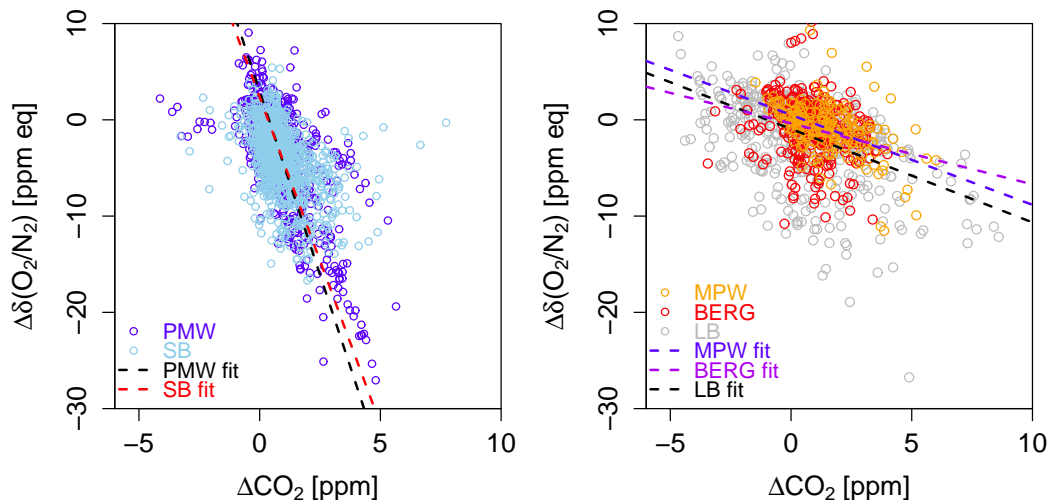


Figure 4.9:  $\delta(\text{O}_2/\text{N}_2)$  and  $\text{CO}_2$  by wind sector.  $\delta(\text{O}_2/\text{N}_2)$  is given in ppm equivalents. Both  $\delta(\text{O}_2/\text{N}_2)$  and  $\text{CO}_2$  have been deseasonalized. Slopes were: PMW =  $-6.8 \pm 0.2$ , SB =  $-7.6 \pm 0.1$ , LB =  $-0.97 \pm 0.1$ , MPW =  $-0.93 \pm 0.2$ , BERG =  $-0.63 \pm 0.3$ .

of course responsive to changes in boundary layer height, wind sector, or wind speed (i.e., meso- and microscale transport), the magnitude of these changes was—unlike CO—very small compared to the drift of the OA-ICOS. It was shown in Chapter 3 that while the drift correction removes most of the influence of daily temperature changes on the time series, it does not account for all artifacts.

To summarize, the diurnal cycles of  $\text{O}_2$  and  $\text{CO}_2$  were found to be mostly due to the daily contrast between coastal background air, from the NW (the PMW), and air that was more directly influenced by air–sea exchange of  $\text{CO}_2$  and  $\text{O}_2$ , advected to NDAO by the sea breeze. During April through June of each year, when the SE winds (MPW) are seen at night, terrestrial exchange by land plants dominated the diurnal cycle of  $\text{CO}_2$  and  $\text{O}_2$ . The most likely source of this signal would be the trees and brush along the Kuiseb River, since the MPW is channeled through this area [Tyson and Seely, 1980]. The influence of the Benguela Current region on the NDAO time series is discussed at length in Chapter 6. CO and  $\text{CH}_4$  were both dependent on oscillations in the height of the PBL, which appeared to create a rise in both species during specific synoptic conditions. This was restricted mostly to austral winter, and is discussed at length in Chapter 5.

#### 4.3.4 Seasonal Cycles

While the time period considered was relatively short, seasonality was apparent for all measurands (Table 4.1 and Figure 4.1). Seasonal cycles were also evident in the meteorological time series (Figure 4.2), although in the case of air temperature, the diurnal and synoptic variability masked much of the small seasonal cycle; this is to be expected for a near-tropical site. For  $\text{CO}_2$ ,  $\text{CH}_4$ , and CO, the phasing of the seasonal cycle agreed well with the NMB flask record (Chapter 2), peaking in early July and reaching a minimum in late January or early February. Atmospheric oxygen and APO were in opposite phase with  $\text{CO}_2$ . As the observational period for CO and  $\text{N}_2\text{O}$  was too short to see more than one seasonal cycle, the seasonal characteristics should be treated with caution, though it is noted that the NDAO amplitude and phasing also agreed well with the NMB record for these measurands. While

Table 4.1: NDAO Seasonal Cycles and Growth Rates: Oct. 2012–Oct. 2014<sup>a</sup>

Measurand	Amplitude <sup>b</sup>	Peak <sup>c</sup>	Trough <sup>d</sup>	Growth Rate <sup>e</sup>
CO <sub>2</sub>	2.36 ppm	Jul. 11	Feb. 6	1.82 ± 0.07 ppm yr <sup>-1</sup>
CH <sub>4</sub>	30.5 ppb	Jul. 7	Feb. 2	8.0 ± 0.4 ppb yr <sup>-1</sup>
CO	37.0 ppb	Jul. 2	Jan. 23	—
N <sub>2</sub> O	0.8 ppb	Mar. 22	Jul. 10	1.2 ± 0.06 ppb yr <sup>-1</sup>
δ(O <sub>2</sub> /N <sub>2</sub> )	61.0 per meg	Jan. 31	Jun. 28	-16.1 ± 1.1 per meg yr <sup>-1</sup>
APO	49.7 per meg	Jan. 30	Jun. 28	-7.7 ± 0.9 per meg yr <sup>-1</sup>

<sup>a</sup> For CO<sub>2</sub>, CH<sub>4</sub>, δ(O<sub>2</sub>/N<sub>2</sub>), and APO. For N<sub>2</sub>O and CO, the observational period is July 2013–October 2014.

<sup>b</sup> Average peak-to-trough amplitude.

<sup>c</sup> Day at which the peak of the seasonal cycle is reached.

<sup>d</sup> Day at which the trough of the seasonal cycle is reached.

<sup>e</sup> Determined through ordinary least squares regression.

the phasing of APO and δ(O<sub>2</sub>/N<sub>2</sub>) is in good agreement with measurements from the Pacific at the same latitude, the amplitude of both is a little higher than is observed in that region [Tohjima et al., 2005b, 2012].

#### 4.3.5 Annual Growth Rates

Growth rates were determined for the study period (Oct. 2012–Oct. 2014) and were found to be close in agreement to the background sites discussed in Chapter 2. Additionally, NOAA flask data from the Cape Grim Observatory (CGO) was included. For this comparison, growth rates were compared for the period Oct. 2012–Dec. 2013 (Table B.9). During this period, the growth rate of CO<sub>2</sub> at NDAO, NMB, and ASC was 2.8 ppm yr<sup>-1</sup>; these sites are all impacted by biomass burning emissions from southern Africa. At the marine background sites CPT<sup>2</sup>, EIC, CFA, and CGO, the growth rate was a little lower: 2.6–2.7 ppm yr<sup>-1</sup>. Some of this discrepancy may be due to the short time span and low frequency of sampling, which makes the calculation sensitive to outliers. The average global growth rate of CO<sub>2</sub> for the calendar year 2013 was 2.9 ppm yr<sup>-1</sup> [WMO/GAW, 2014].

The only δ(O<sub>2</sub>/N<sub>2</sub>) data available to the author for comparison was from the Cape Grim Observatory (CGO); the growth rate was a little more negative at NDAO, by about 6 per meg yr<sup>-1</sup> for δ(O<sub>2</sub>/N<sub>2</sub>), and 2 per meg yr<sup>-1</sup> for APO, though given the uncertainties involved in determining a growth rate for such a short period of time, it would be unwise to read too much into this difference.

The average global increase of methane during 2013 was 6 ppb yr<sup>-1</sup> [WMO/GAW, 2014], which is close to the range of values seen here: 3.4–6.8 ppb yr<sup>-1</sup>. As growth rates of methane vary with location and latitude [Dlugokencky et al., 1994, Langenfelds et al., 2002], small differences between sites are to be expected. At NMB, NDAO, and CGO, the growth rate of N<sub>2</sub>O was 1.3 ppb yr<sup>-1</sup>. This is higher than the globally averaged value of 0.8 [WMO/GAW, 2014].

<sup>2</sup>Recall that the CPT is a GAW global background station, as the data are filtered to remove any continental influence.

#### 4.4 Summary and Conclusions

In this chapter the main time series from the Namib Desert Atmospheric Observatory was presented. Small diurnal cycles were noted for  $\text{CO}_2$  and  $\delta(\text{O}_2/\text{N}_2)$ , as well as occasionally for  $\text{CH}_4$ ,  $\text{CO}$ , and  $\text{N}_2\text{O}$ . This was attributed to boundary layer oscillations, and the local wind system, which advects air masses that possess a strong gradient between marine and terrestrial influences. Low seasonality was noted for  $\text{CO}_2$ ,  $\text{CH}_4$ , and  $\text{CO}$ , similar to other marine background sites from this latitude. Growth rates were fairly high for the last 10–15 years, although this appeared to be consistent with other observations for 2013. Most importantly, the NDAO time series agreed very well with the NMB flask record presented in Chapter 2, in terms of annual growth rates and seasonal characteristics. Considerable synoptic variability for all species was observed, notable for a background site; the causes of such synoptic variability are discussed in the final chapters.

# 5

## Seasonally Occurring Anomalies of CO<sub>2</sub>, CH<sub>4</sub>, and CO, Induced by Biomass Burning and Variability in Atmospheric Transport

### 5.1 Introduction

Variability in biomass burning has been shown to have a significant effect on the interannual variability of CO<sub>2</sub>, CH<sub>4</sub>, and CO [Langenfelds et al., 2002]. Due to its semi-arid climate and agricultural practices that are common in the region, southern Africa is a global hotspot for biomass burning emissions. The yearly fire season (May–November) sees the development of an area of elevated CO over the savanna region between 5 and 20°S [Hooghiemstra et al., 2012, Inness et al., 2013, Kopacz et al., 2010, Reeves et al., 2010, Scholes et al., 1996, Sinha et al., 2003, van Leeuwen et al., 2013, Yoon and Pozzer, 2014]. The amount and relative proportions of the trace gases that are emitted from savanna fires vary widely depending on the type of vegetation, soil, land use, combustion, climate, and fire frequency [Andreae and Merlet, 2001, van Leeuwen and van der Werf, 2011, van Leeuwen et al., 2013, Ward et al., 1996]. Since emissions occur at the surface, concentrations are highest in the planetary boundary layer. As the sensitivity of satellite measurements decreases towards the surface [Chevallier et al., 2009], the lack of in situ measurements from this region hampers attempts to quantify these emissions using inverse techniques.

Despite its location in a sparsely populated, sparsely vegetated coastal environment, atmospheric observations at Gobabeb, both with flasks (the NOAA record, referred to here by its ID, NMB) and continuous measurements (NDAO), have demonstrated that the site sees greater variation in carbon monoxide and methane than one might at first expect. In fact, the original motivation for selecting this specific location for the NMB flask measurement site was because it was hoped that the site was impacted by southern African biomass burning, which was not well-constrained by atmospheric observations [Novelli, 2014].

There is little direct wildfire activity at Gobabeb or in the Namib Desert, since there is so little vegetation (Figure 1.2). Yet, inspection of the CO NDAO record reveals large intraseasonal variability, which is not constant in magnitude, but which varies with the seasonal cycle. This chapter is focused on exploring the distinctive seasonal cycles for CO<sub>2</sub>, CH<sub>4</sub>, and CO presented in Chapter 2 and Chapter 4, in the context of synoptic variability and biomass burning.

### 5.1.1 Enhancement Ratios

The relative proportions of trace gases released from the combustion of organic matter can be quantified as either as an emission factor, i.e., the mass of a compound emitted per unit of dry biomass consumed, or as an emission ratio, i.e., as the molar ratio of two trace gases as measured directly in the fresh smoke of a fire, compared to a background. Emission ratios (ER) are defined as:

$$ER_{\Delta X/\Delta Y} = \frac{\Delta X}{\Delta Y} = \frac{X_{plume} - X_{background}}{Y_{plume} - Y_{background}} \quad (5.1)$$

where  $X$  and  $Y$  are the dry air mole fractions of two species of interest. Emission ratios typically vary with both combustion phase, i.e., whether it is a predominately flaming or smoldering process, and fuel source [Akagi et al., 2011, Andreae and Merlet, 2001, van Leeuwen and van der Werf, 2011]. This means that there is often not a single characteristic emission factor or ratio that characterizes a given ecosystem. Within savannas, for instance, emission ratios can vary by more than a factor of 6 [Ward et al., 1996]. In many cases, it is not the vegetation type that determines the ERs, but the environmental conditions during the fire [Yokelson et al., 2011]. ERs can also vary throughout the lifetime of a single fire [Wooster et al., 2011].

The species chosen as  $Y$  from Equation 5.1 is most often either CO or CO<sub>2</sub> [Akagi et al., 2011, Andreae and Merlet, 2001]. The relative amounts of CO and CO<sub>2</sub> released from a fire are largely dependent on the combustion phase. CO is usually the choice for smoldering combustion, although CO<sub>2</sub> is preferable for large-scale estimates because it is the dominant species for biomass burning emissions as a whole, and has a longer atmospheric lifetime [Andreae and Merlet, 2001]. However, both of these compounds have high emission factors from all types of fires, and are followed by CH<sub>4</sub> as the next-most abundant species released from typical wildfires [Akagi et al., 2011].

The term enhancement ratio (EN) is sometimes employed when measurements are made far from the emission source, or if the species involved are affected by secondary reactions; this quantity is calculated identically to the emission ratio [Hobbs et al., 2003, Jost et al., 2003a, Wada et al., 2011, Wooster et al., 2011, Yokelson et al., 1999]. Enhancement ratios are also sometimes called “normalized excess mixing ratios” [Akagi et al., 2011]. Enhancement ratios can be calculated with two or more measurement points or can be taken as the slope of the regression line between two species; either the excess mole fractions or the absolute mole fractions can be used as a means of comparing the in situ covariance of two compounds directly with their emission ratio [Guyon et al., 2005, Keene et al., 2006, Wada et al., 2011, Wofsy et al., 1992, Wooster et al., 2011]. In this text, if the absolute mole fractions are referred to, the nomenclature EN <sub>$X/Y$</sub>  will be used; normalized excess mole fractions will be denoted as EN <sub>$\Delta X/\Delta Y$</sub> . In some works enhancement ratios are also simply called correlation slopes. It is important to note that while such ratios can yield some insight into the biogeochemical process causing a departure from the background during a synoptic event, photochemistry and atmospheric mixing alter the composition of an air mass over the lifetime of a plume, causing the EN <sub>$\Delta X/\Delta Y$</sub>  to diverge from the original emission ratio [Mauzerall et al., 1998, McKeen and Liu, 1993].

### 5.1.2 O<sub>2</sub> and CO<sub>2</sub> Molar Exchange Ratios

The oxidative ratio (OR) is a unitless molar ratio that quantifies the stoichiometric relationship between the amount of O<sub>2</sub> consumed and CO<sub>2</sub> produced during the oxidation of organic matter [Keeling, 1988]. This can be either determined through chemical analysis or calculated theoretically, based on the elemental composition of the organic matter in question [Keeling,

1988, Masiello et al., 2008, Severinghaus, 1995, Steinbach et al., 2011]. It is perhaps useful to distinguish between the oxidative ratio as a theoretical or analytically derived value, and the OR of ecosystem gas exchange, which would be the ratio of the net fluxes of  $O_2$  and  $CO_2$ . In this work we will refer to such values as the molar exchange ratio,  $\Delta O_2:\Delta CO_2$ , on a  $\text{mol mol}^{-1}$  basis.

Over time,  $\Delta O_2:\Delta CO_2$  resulting from surface fluxes due to net ecosystem exchange (NEE) should converge to the OR of the dominant type of organic matter within the ecosystem [Keeling and Manning, 2014]. The value of the OR varies somewhat depending on the composition of the organic matter being created or destroyed through reactions like photosynthesis, respiration, decomposition, and combustion [Hockaday et al., 2009, Keeling, 1988, Masiello et al., 2008, Severinghaus, 1995]. In field and modeling studies, a considerable range of  $\Delta O_2:\Delta CO_2$  is observed, especially over shorter spatial and temporal scales [Angert et al., 2015, Ishidoya et al., 2013, Randerson et al., 2006, Seibt et al., 2004, Steinbach et al., 2011, Stephens et al., 2007]. Molar exchange ratios determined from a regression of atmospheric  $\delta(O_2/N_2)$  and  $CO_2$  will integrate and alias signals from a wide variety of ecosystem fluxes [Sturm et al., 2005, van der Laan et al., 2014]. If the ecosystem is not in steady state, the exchange ratio of the biosphere–atmosphere flux can differ from the exchange ratio of atmosphere–biosphere flux [Hockaday et al., 2009, Randerson et al., 2006].

If the observed exchange ratio differs substantially from the OR range of organic matter, it can be inferred that significant additional biological reactions or processes that do not involve organic matter are present [Seibt et al., 2004]. The most important example of this is the more negative exchange ratios observed during air–sea gas exchange.  $CO_2$ , upon dissolving in seawater, is subject to further reactions with the carbonate system, while  $O_2$  remains relatively inert. This results in exchange ratios typically less than  $-2$  [Keeling and Manning, 2014, Keeling et al., 1993, Manning et al., 1999].

## 5.2 Methods

### 5.2.1 Determination of Slopes

$EN_{\Delta X/\Delta Y}$  were determined by subtracting a background fit from the original time series (see Chapter 4) and finding the slope of the regression line between the resulting  $\Delta X$  and  $\Delta Y$ . The slopes of simple linear regressions of any two selected species were determined using the reduced major axis method.

### 5.2.2 Back-Trajectory Classification

Back-trajectories from HYSPLIT (see Section 2.2.1) were matched to hourly means of the main measurands. Back-trajectories were then pooled into classes. Trajectories with a mean height less than 200 m, a maximum height less than 500m, and a  $f_{terr}$  less than 0.2 ( $f_{terr}$  is the fraction of each trajectory that resides over land, see Section 2.3.1) were classified as “marine boundary layer” (MBL) air. Trajectories with a mean and maximum height less than 1,000 m, a  $f_{terr}$  greater than or equal to 0.3, and lying east of  $14^\circ E$  were classified as “anticyclone boundary layer” (ABL). Trajectories with a mean and maximum height greater than 2,000 m, a maximum distance at any point on the trajectory less than 2,000 km, and a significant and negative slope were classified as “descending air masses” (DAM). The classification criteria are somewhat arbitrary but were chosen to select the largest clusters of like trajectories.

### 5.2.3 Remote Sensing Data

A normalized difference vegetation index (NDVI) dataset was acquired from the Oak Ridge National Laboratory Distributed Active Archive Center (ORNL DAAC), i.e., the International Satellite Land-Surface Climatology Project (ISLSCP) Initiative II Global Inventory Modeling and Mapping Studies (GIMMS) Monthly NDVI, 1981–2002 [Tucker et al., 2010]. This 22-year NDVI dataset was used to create a climatology of NDVI for southern Africa, using the domain between 10–42°E and 0–35°S.

In order to obtain an indicator or metric of fire activity, data giving the extent of burned area were obtained from the Global Fire Emissions Database (GFED), Version 4.0 [Giglio et al., 2013]. The data have a daily time step and a 0.25° resolution. This product combines a MODIS burned area product with active fire data from the algorithm 2 Along-Track Scanning Radiometer (ATSR) World Fire Atlas (ATSR), and from the Visible and Infrared Scanner (VIRS). Data from 2008–2013 were combined to create a climatology for fire activity in southern Africa for the 10–42°E and 0–35°S domain.

## 5.3 Results and Discussion

### 5.3.1 Seasonal Divergences from the Marine Background

NDVI showed a predictable seasonal pattern following the general climatology of the ITCZ; greening occurred during the wet season and browning during the dry (Figure 2.1 and Figure A.2). Fire activity, expressed as the extent of total burned area in southern Africa, had a close, inverse relationship with NDVI (Figure 5.1). In the absence of extensive wetlands, a greening landscape would not have as much influence on CO and CH<sub>4</sub> as biomass burning would. For CO<sub>2</sub> and O<sub>2</sub>, this would imply that biomass burning and land plants act in concert to produce the seasonal cycles described in Chapter 2 and Chapter 4. Biomass burning is a known source of CO and CH<sub>4</sub>, and has been shown to produce a substantial contribution to the seasonal cycle of CO<sub>2</sub> at background sites, particularly in areas where the contribution of land plants is lower [Wittenberg et al., 1998].

A striking feature of the NDAO CO time series is the high degree of intraseasonal variability between March and October (Figure 5.2). These positive anomalies cause a seasonal divergence from the marine background signal as seen from the Cape Point Observatory (CPT; see Section 2.2.2), and occur on the ascending portion of the seasonal cycle. This pattern is also observed in methane, and to a lesser extent, CO<sub>2</sub>.

From this continuous record, it is clear that the distinctive seasonal cycle seen at NMB and NDAO in CO<sub>2</sub>, CH<sub>4</sub>, and CO is not really due to a change in the background. Rather it is due to a peak in synoptic activity during July, when the likelihood of a flask sample being elevated is highest, since mole fractions of these species are only rarely close to the CPT background. This is also when anticyclonic circulation is at its peak, and trapping/recirculation of polluted air over the continent is more likely [Tyson et al., 1996b].

The month of July is also when the tiny seasonal cycle of SF<sub>6</sub> peaks. As this greenhouse gas is emitted solely from industrial sources, its emission rates are thought to be constant throughout the year [Patra et al., 2009, Ravishankara et al., 1993]. Back-trajectories imply that during July there is a lot of direct transport from the South African Highveld, where the Guateng conurbation is located. This region contains a high density of SF<sub>6</sub> emissions (Figure A.27.)

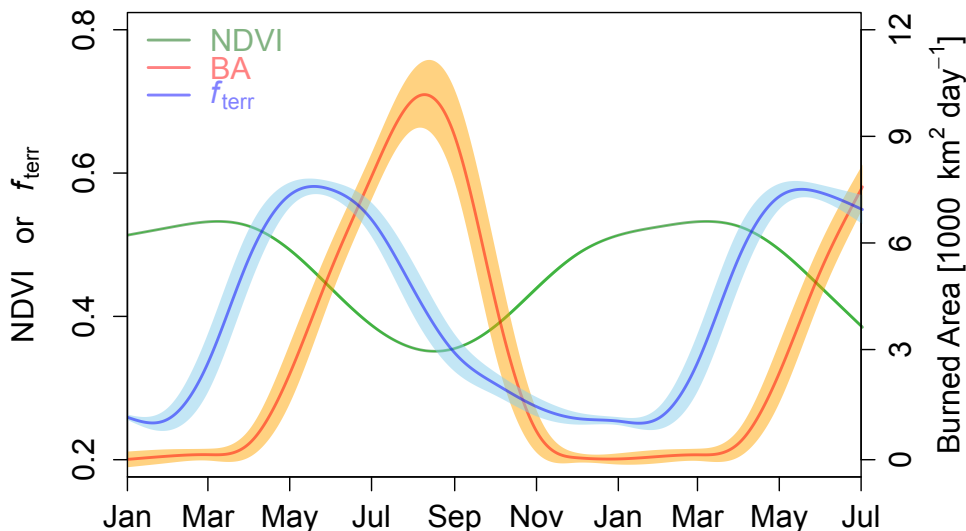


Figure 5.1: Annual cycles of the normalized difference vegetation index (NDVI), averaged for southern Africa; biomass burning (BA) averaged for the same region; and the average annual cycle of the fraction of each back-trajectory that resides over land arriving at NDAO,  $f_{terr}$ . Envelopes show one  $\sigma$ , and lines the average seasonal cycle. NDVI and  $f_{terr}$  share the same axis. The first 6 months of the year are repeated for visual clarity.

### 5.3.2 Pathways of Polluted Air Masses

Synoptic events with elevated mole fractions of  $\text{CH}_4$  and CO were often associated with the ABL and DAM classes of back-trajectories, while baseline values were more often seen when back-trajectories were of the MBL class (Figure A.28). This implied two common pathways or routes for polluted air masses to NDAO: the first, characterized by the ABL class, was for surface trajectories via the southern African anticyclone. The second pathway was via a descending air mass, which had mostly been residing over the coast or interior of the continent. The interpretation here is that mixing or descent of polluted layers at height was often a source of high CO air. This interpretation is well-supported by previous aircraft campaigns in the Namibian region, which have often found elevated concentrations of CO and  $\text{CH}_4$  above the continental or marine boundary layer, in the 2–6 km region [Bartlett et al., 1996, Hobbs, 2003, Jost et al., 2003a,b, Mauzerall et al., 1998, Mühle et al., 2002, Sinha et al., 2003, 2004, Tyson and D’Abreton, 1998].

### 5.3.3 Stiochiometry: Enhancement and Molar Exchange Ratios

The covariation of carbon monoxide and methane observations was dominated by two linear subpopulations, after diurnal variations were removed (Figure A.29). The second population was mostly composed of the anticyclonic and subsiding trajectory classes, while the first population was dominated by MBL trajectories. The distinction is not perfect, as it is both an oversimplification and reliant on the accuracy of back-trajectories. But, we can say that high CO events tend to have certain trajectory types associated with them. MBL-associated data had an  $\text{EN}_{\text{CH}_4/\text{CO}}$  of  $1.32 \pm 0.07$  ppb ppb $^{-1}$ . This population represented background values of  $\text{CH}_4$  and CO: the correlation slope matched that of the Cape Point background ( $\text{EN}_{\text{CH}_4/\text{CO}} = 1.64 \pm 0.4$  ppb ppb $^{-1}$ ), and the strength of the correlation ( $R^2 = 0.54$ ;  $n = 549$ ;  $p < 2 \times 10^{-16}$ ) decreased when the data were deseasonalized ( $R^2 = 0.27$ ;



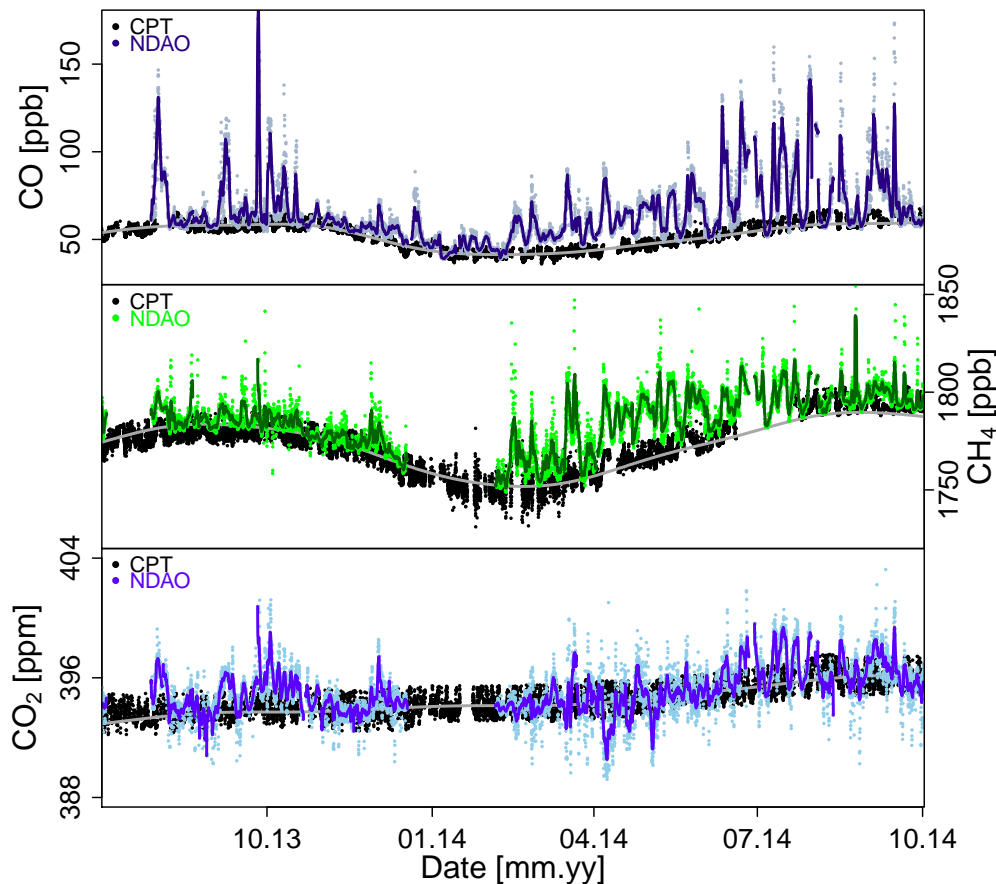


Figure 5.2: Hourly averages of  $\text{CO}_2$ ,  $\text{CH}_4$ , and  $\text{CO}$  (colored points) and running 24-hour means (colored lines) from NDAO, compared with filtered half-hourly, marine background values from Cape Point (CPT; black points and grey lines).

$n = 549$ ;  $p < 2 \times 10^{-16}$ ). That the NDAO and CPT  $\text{EN}_{\text{CH}_4/\text{CO}}$  agree so well is due to the synchronization of the seasonal cycles of  $\text{CH}_4$  and  $\text{CO}$ . Both the ABL and DAM data were characterized by higher  $\text{CO}$  anomalies, with a combined  $\text{EN}_{\Delta\text{CH}_4/\Delta\text{CO}}$  of  $0.28 \pm 0.05$   $\text{ppb ppb}^{-1}$  (with outliers greater than  $2\sigma$  removed). The  $\text{CH}_4$  and  $\text{CO}$  of these two populations were also significantly correlated ( $R^2 = 0.45$ ;  $n = 91$ ;  $p = 2.1 \times 10^{-13}$ ).

As  $\text{CH}_4$  and  $\text{CO}$  are produced primarily during smoldering combustion, the range of  $\text{ER}_{\Delta\text{CH}_4/\Delta\text{CO}}$  reflects more the fuel composition than combustion dynamics. Grassland and savanna fires, for instance, produce smaller ratios than woodland fires [Akagi et al., 2011, Andreae and Merlet, 2001, Bartlett et al., 1996]. Most savanna fires have a high combustion efficiency and are predominately flaming [Hao et al., 1996]. The emission ratio—and the enhancement ratio if measured close to the source—of  $\text{CH}_4$  to  $\text{CO}$  is between 0.01 and 0.1 [Akagi et al., 2011, Andreae and Merlet, 2001, Bartlett et al., 1996, Hobbs et al., 2003].  $\text{CO}$  is progressively lost in plumes, however, due to photochemical reactions, so ageing of the plume alters the  $\text{EN}$  from the original  $\text{ER}$  [Mauzerall et al., 1998]. In a campaign using a commercial airliner, Mühle et al. [2002] encountered a plume over Namibia with an  $\text{EN}_{\Delta\text{CH}_4/\Delta\text{CO}}$  of  $0.227 \pm 0.035$ . Working with data from TRACE A aircraft campaigns over the South Atlantic and southern Africa, Mauzerall et al. [1998] found an  $\text{EN}_{\text{CH}_4/\text{CO}}$  of  $0.16 \pm 0.05$  ( $\text{ppb ppb}^{-1}$ ) for fresh plumes,  $0.37 \pm 0.003$  for recent plumes,  $0.6 \pm 0.076$  for aged plumes, and  $0.44 \pm 0.12$  for old plumes. In their classification scheme, old refers to plumes less than 1 week in age,

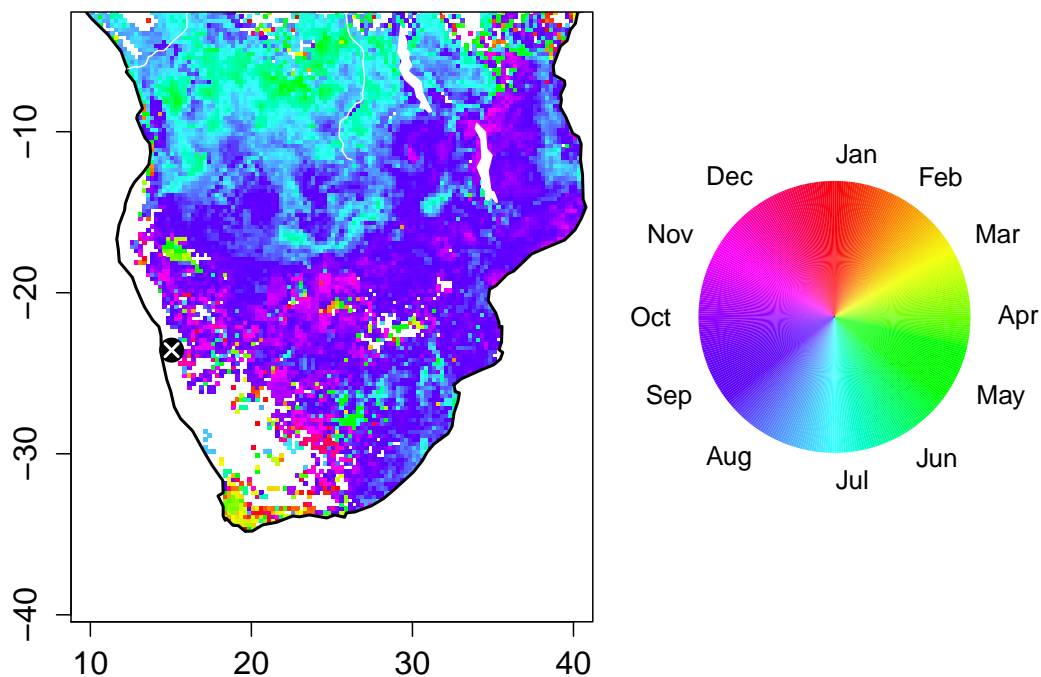


Figure 5.3: The day of the year with the most common (i.e., median) fire occurrence for all pixels, using the period 2008–2013. Location of NDAO is given by a black circle with a white “x”.

aged less than 5 days, recent less than 1 day, and fresh less than half a day. Since the average enhancement ratio for terrestrial air masses in the present study was  $0.28 \pm 0.05$  ppb ppb<sup>-1</sup>, this supports the conjecture that most of the polluted air masses arriving at NDAO were influenced by biomass burning rather recently.

The enhancement ratio of CH<sub>4</sub> and CO at NDAO had a seasonal component as well. During austral summer,  $EN_{\Delta CH_4/\Delta CO}$  hovered around the background value of around 1 or greater. In May, as the synoptic variability of CH<sub>4</sub> and CO increased, the average  $EN_{\Delta CH_4/\Delta CO}$  dropped to around 0.3 (Figure 5.4). The largest synoptic events were in July, which was also when the lower  $EN_{\Delta CH_4/\Delta CO}$  pointed to more recent combustion. This observation agreed well with the timing of biomass burning events from the GFED database, which showed a southward progression of biomass burning throughout the year (Figure 5.3). The fires that occur before June were located primarily north of -10°S; anticyclonic surface trajectories were rarely seen north of -16°S. Taken together with the transport modeling discussed in Section 5.3.2, this implied that starting in March, CO and CH<sub>4</sub> synoptic events began to occur due to the seasonal shift towards more terrestrial air masses. In April and May, the  $EN_{\Delta CH_4/\Delta CO}$  remained elevated since NDAO was farther away from the combustion source, and most of the enhanced CO and CH<sub>4</sub> was transported to NDAO via the DAM-type circulation. By July,  $EN_{\Delta CH_4/\Delta CO}$  dropped, indicating a more recent combustion source, which was consistent with the observation that more active fires were closer to the station. As shown previously, emissions from biomass burning events can arrive at NDAO through either ABL- or DAM-type circulation. Without relying too heavily on atmospheric transport modeling—the errors associated with back-trajectories can be high, particularly in regions of the world where meteorological data is lacking—it is encouraging that the model results support the evidence from the stoichiometry of the synoptic events.

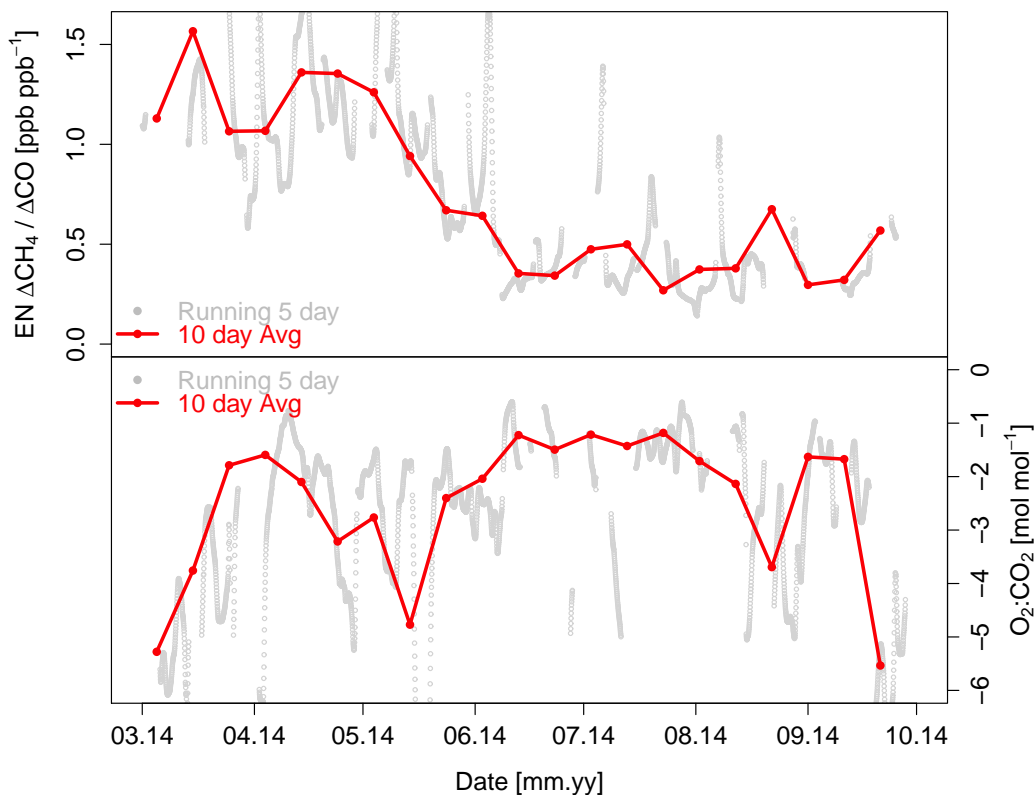


Figure 5.4: The enhancement ratio of  $\text{CH}_4$  and  $\text{CO}$  ( $\text{EN}_{\Delta\text{CH}_4/\Delta\text{CO}}$ ) for a portion of 2014 (*top panel*).  $\text{EN}_{\Delta\text{CH}_4/\Delta\text{CO}}$  are determined by calculating a running slope in a 5-day window (gray points) on the  $\Delta\text{CH}_4$  and  $\Delta\text{CO}$  time series which have been smoothed with a running 24-hour mean. If the  $R^2$  is less than 0.6, the slope is excluded. The resulting  $\text{EN}_{\Delta\text{CH}_4/\Delta\text{CO}}$  were then aggregated to 10-day means to produce the red line. Also plotted is the  $\text{O}_2:\text{CO}_2$  molar exchange ratio, calculated in the same manner as the  $\text{EN}_{\Delta\text{CH}_4/\Delta\text{CO}}$ .

Throughout most of the year, the molar exchange ratio of  $\text{CO}_2$  and  $\delta(\text{O}_2/\text{N}_2)$  were substantially more negative (i.e., less than  $-2$ ) than the range of molar exchange ratios associated with terrestrial plants and soils, combustion, decomposition, etc. Such lower values pointed to air–sea exchange as the type of surface flux that caused these events; this phenomenon is explored further in Chapter 6. In July, however, when the intraseasonal variability of  $\text{CH}_4$  and  $\text{CO}$  reached its maximum, the 10-day average apparent molar exchange ratio of  $\text{O}_2:\text{CO}_2$  was between  $-1.2$  and  $-1.5$ . This is very close to the range of  $-1.1$  to  $-1.4$  found by Lueker et al. [2001] over the course of a forest fire in northern California. A more negative value is indicative of incomplete combustion, such as would occur in a smoldering fire. However, given the uncertainty in the slope determination, the unknown degree of atmospheric mixing, and what are likely large distances between NDAO and any active fires, nothing definitive can be concluded about the type of combustion. The point here is more that the stoichiometry of  $\text{O}_2$  and  $\text{CO}_2$  switched from marine-dominated exchange process during most of the year, to likely combustion-dominated exchange during July, when the influence of fire activity was most likely to be strongest at the station.

## 5.4 Summary and Conclusions

Striking seasonality in the synoptic variability of CO and CH<sub>4</sub> is observed at NDAO. Beginning in March, the magnitude of these positive anomalies increases until July. At this time, CO<sub>2</sub> and O<sub>2</sub> also show covariation with CH<sub>4</sub> and CO, and background observations of all species are uncommon. By November, these large synoptic events have become rare and CO and CH<sub>4</sub> are mostly background values for the remainder of austral summer. The cause of this annual pattern is attributed to greater variability in atmospheric transport, which alternates between air masses that have been altered by the marine or terrestrial environment. The magnitude of synoptic variability increases as biomass burning events move southward through the dry season. This is reflected in the enhancement ratio of CH<sub>4</sub> and CO, which shows a more aged value in April through June, and ratios indicative of more recent events in July and September, when more fires are located closer to the station. At this time, the exchange ratios of O<sub>2</sub> and CO<sub>2</sub>, which usually point to marine surface fluxes, are also in accordance with biomass burning.

# 6

## Top-Down Estimates of Greenhouse Gas Emissions from the Lüderitz and Walvis Bay Upwelling Cells

### 6.1 Introduction

Coastal margins, particularly those associated with the upwelling of nutrient-rich bottom waters, are very biogeochemically active regions [Levin et al., 2015]. The air–sea fluxes of greenhouse gases (GHGs; referring here to the long-lived, natural greenhouse gases  $\text{CO}_2$ ,  $\text{CH}_4$ , and  $\text{N}_2\text{O}$ ) from or to such systems can vary markedly, both spatially and temporally [Evans et al., 2011, Naqvi et al., 2010, Reimer et al., 2013, Torres et al., 1999]. This is because coastal upwelling events are episodic in nature, as they are forced by surface winds that occur under specific synoptic conditions; even large events happen only on a time scale of days [Blanke et al., 2005, Desbiolles et al., 2005, 2014, Goubanova et al., 2013]. Coastal upwelling regions also tend to be very productive, due to high nutrient availability, but such productivity is dependent on the resupply of remineralized bottom waters, which is largely wind-driven [Mann and Lazier, 1996]. As a result of this high primary productivity, coastal upwelling systems can also be associated with large oxygen minimum zones (OMZs), due to the respiration at depth of exported organic matter from the photic zone [Capone and Hutchins, 2013, Paulmier et al., 2008]. Of the major eastern boundary upwelling systems, the Benguela is probably the least sampled for air–sea fluxes of GHGs [Laruelle et al., 2014, Naqvi et al., 2010, Nevison et al., 2004b].

In the Benguela, upwelled waters are brought to the surface from a depth between 100 and 300 m [Boyer et al., 2000, Mohrholz et al., 2014, Shannon and Nelson, 1996]. The upwelling zone is some 200 km wide, although filaments can extend much farther, up to 1000 km long [Fennel, 1999, Lutjeharms et al., 1991, Veitch et al., 2009]. In the northern Benguela upwelling activity is highest during the winter, while the opposite is seen in the southern Benguela [Campillo-Campbell and Gordo, 2004, Veitch et al., 2009]. Upwelled waters can be sourced from different water masses; at Cape Frio, for instance, this is usually the aged ( $\sim 50$  years) and hypoxic Eastern Tropical South Atlantic Central Water (Eastern Tropical SACW, sometimes called Angola Basin SACW), whereas the better-ventilated Cape Basin SACW upwells through the Lüderitz cell [Duncombe Rae, 2005, Mohrholz et al., 2008, Monteiro et al., 2006, Poole and Tomczak, 1999, Shannon and Nelson, 1996]. The region between Lüderitz and Walvis Bay sees the transition between the dominance of the two types of water masses.

Adding additional complexity, upwelling is not homogeneous along the coast. Specific upwelling events cluster geographically, forming upwelling cells [Lutjeharms and Meeuwis, 1987]. Seven semi-distinct cells have been recognized [Demarcq et al., 2003, Lutjeharms and

Meeuwis, 1987, Lutjeharms and Stockton, 1987, Veitch et al., 2009]. However, there is some limit to the utility of this classification, since large events are often observed that span more than one cell. The region of coastal shelf near Lüderitz is subject to the strongest upwelling fluxes in the Benguela region [Hagen et al., 2001, Hutchings et al., 2009, Lutjeharms and Meeuwis, 1987, Veitch et al., 2009]. The Lüderitz cell frequently overlaps with the Walvis Bay upwelling cell [Lutjeharms and Meeuwis, 1987], and in this study the two cells are considered together. At Lüderitz, the surface winds are the strongest, and surface chlorophyll is at a minimum (as compared to the rest of the Benguela) [Demarcq et al., 2007, Hutchings et al., 2009]. While upwelling in this area is perennial, seasonality is seen in the intensity of upwelling due to the annual migration of the South Atlantic Anticyclone, with a minimum in austral winter [Hagen et al., 2001, Hardman-Mountford et al., 2003, Peard, 2007, Veitch et al., 2009]. The Lüderitz upwelling cell separates the Benguela region into a northern and southern portion, distinct from one another both biogeochemically and physically [Agenbag and Shannon, 1988, Duncombe Rae, 2005, Hutchings et al., 2009].

A large oxygen minimum zone is endemic to the shelf area between 20°S and 25°S [Brüchert et al., 2006, Monteiro and van der Plas, 2006, Monteiro et al., 2008]. Water on the inner shelf, where surface waters are more productive and biological oxygen demand is highest, is more hypoxic than water on the outer shelf [Monteiro and van der Plas, 2006]. The presence of the OMZ is attributable both to the substantial remineralization of particulate organic carbon from the photic zone and to the advection of low-oxygen Eastern SACW onto the shelf [Brüchert et al., 2000, 2003, Mohrholz et al., 2008, 2014, Monteiro and van der Plas, 2006, Monteiro et al., 2006, Weeks et al., 2004], though the importance of water column biogeochemistry in sustaining the OMZ has been challenged by Monteiro et al. [2008]. Oxygen concentrations on the shelf are highest during periods of the greatest ventilation, both on seasonal and interannual time scales; concentrations are usually lowest—and can reach an anoxic state—in austral summer [Mohrholz et al., 2008, Monteiro et al., 2008].

Ventilation of older water masses that have been removed from the atmosphere for decades or more can deviate substantially from atmospheric equilibrium in their trace gas content [Hamme and Keeling, 2008, Nevison et al., 2005]. As water masses age away from the euphotic zone, microbial respiration remineralizes organic matter, reducing concentrations of oxygen and increasing  $p\text{CO}_2$ . Upwelled water is usually cold, which means that the solubility of dissolved gases will decrease with increasing temperature as water masses warm at the surface. A competing influence for  $\text{CO}_2$  exists in that the supply of inorganic nutrients from an upwelling events can lead to blooms of phytoplankton and a net drawdown of atmospheric  $\text{CO}_2$  (Figure 6.1). Hence, coastal upwelling regions can oscillate between being sources and sinks of  $\text{CO}_2$  [Cao et al., 2014, Evans et al., 2015, González-Dávila et al., 2009, Gregor and Monteiro, 2013a, Santana-Casiano et al., 2009, Torres et al., 1999].

Additionally, most coastal upwelling systems are also known to be regional hotspots of  $\text{N}_2\text{O}$  emission [Bange et al., 2001, Bianchi et al., 2012, Cornejo et al., 2006, Lueker et al., 2003]. Since  $\text{N}_2\text{O}$  production is enhanced at low oxygen concentrations, OMZs can consequently be significant source regions to the atmosphere [Bianchi et al., 2012, Farías et al., 2007, Nevison et al., 2003, Paulmier et al., 2008, Suntharalingam and Sarmiento, 2000, Zamora et al., 2012]. Methane release from coastal upwelling regions is also possible [Kelley and Jeffrey, 2002, Kock et al., 2008, Rehder et al., 2002, Upstill-Goddard et al., 1999]. Supersaturation of  $\text{CH}_4$  in surface waters can occur as a result of methanogenesis within the anaerobic microenvironments of particles and in the guts of zooplankton [Bates et al., 1996, de Angelis and Lee, 1994, Karl and Tilbrook, 1994]. There is evidence that aerobic methane production is also possible as a by-product of methylphosphonate decomposition [Karl et al., 2008]. If there exists a mechanism by which bottom waters can be quickly ventilated (such as coastal upwelling), methane from in situ biological production in low-oxygen water or even from

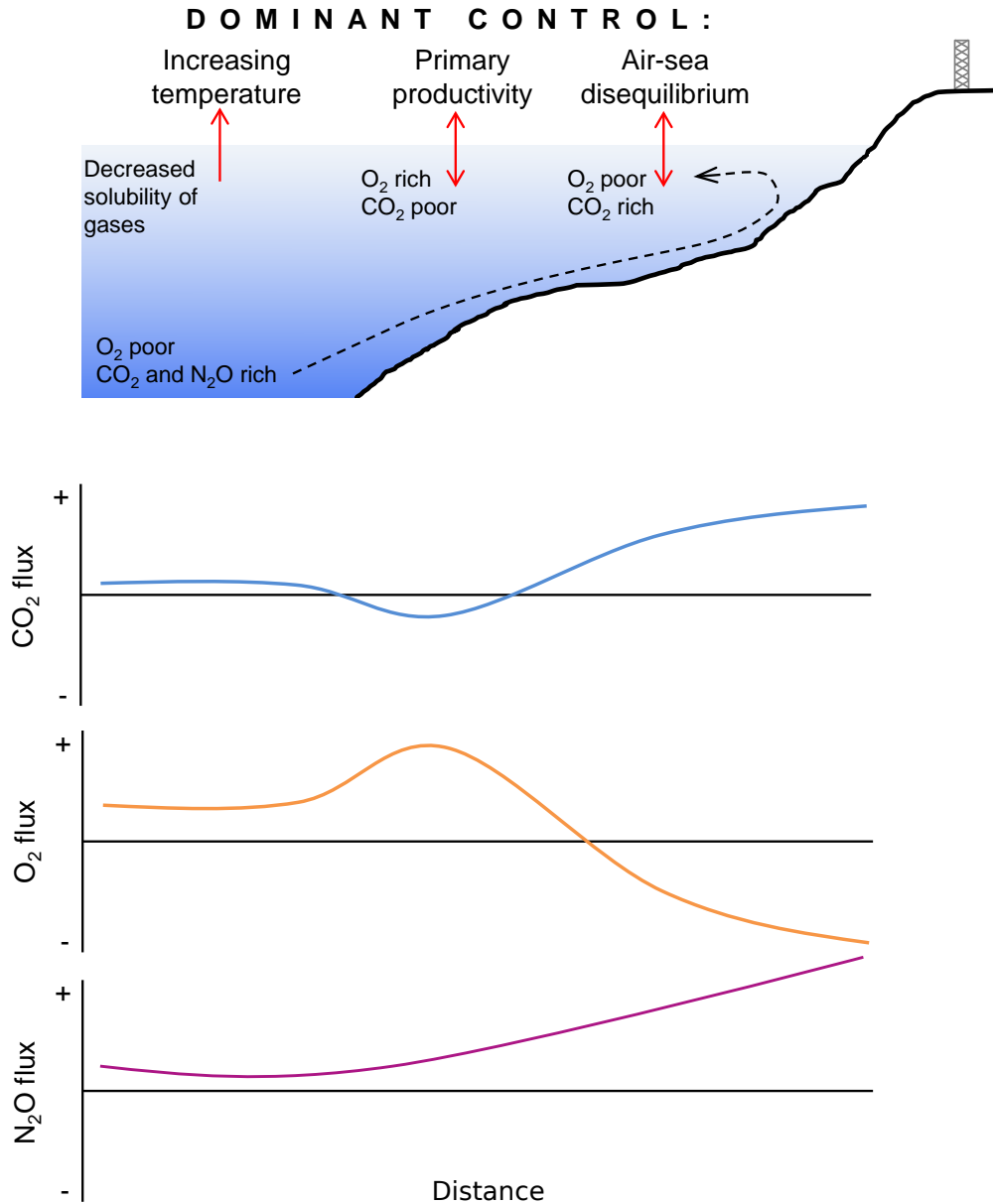


Figure 6.1: Simplified conceptual diagram of the competing influences on air-sea gas exchange in a coastal upwelling system. In the top panel, the dominant controls are shown in their expected locations relative to the coast, with the dotted line showing the movement of bottom water to the surface during an upwelling event. A mast is depicted on land, representing NDAO. Initially water is brought to the surface that has been extensively remineralized, and is out of equilibrium with the atmosphere. The presence of inorganic nutrients in the photic zone spurs primary productivity. As upwelled waters warm at the surface, the solubility of gases decreases, though this effect is smaller for  $\text{CO}_2$ , which is buffered by the inorganic carbonate system. Expected sign and relative magnitude of fluxes for different species are also shown.

sedimentary/geological sources can be released to the atmosphere [Bange et al., 1998, Hu et al., 2012, Kelley and Jeffrey, 2002, Owens et al., 1991, Rehder et al., 2002, Solomon et al., 2009].

Concentrations of methane in bottom waters on the Namibian shelf are likely the highest ever measured in an open coastal system. Values as high as 475  $\mu\text{M}$  in the bottom waters and greater than 5,000  $\mu\text{M}$  in sediment porewaters have been observed [Brüchert et al., 2009, Monteiro et al., 2006, Naqvi et al., 2010, Scranton and Farrington, 1977]. In the water column, the concentration maxima is usually at the seabed or in bottom water, but it is variable and can even occur at the surface (1 m) [Brüchert et al., 2009]. Dissolved methane concentrations are tightly coupled with  $\text{O}_2$  and show considerable variability, with elevated concentrations being triggered by episodes of hypoxia [Brüchert et al., 2009, Monteiro et al., 2006]. The pulse-like nature of  $\text{CH}_4$  in the Benguela means that the full range of dynamics cannot be captured with a campaign-based sampling approach [Brüchert et al., 2009]. What is clear is that there is a tremendous amount of methane production at depth, but that the source is variable in strength [Brüchert et al., 2009, Emeis et al., 2004]. In light of the fact that large pockets of free methane gas are contained in the sediment in the Walvis Bay region, as well as the existence of craters and pockmarks on the seafloor, combined with observation of bubble streams from the seabed, suggest a mechanism by which methane produced in sediments can be abruptly transported to the surface and hence, avoid oxidation [Brüchert et al., 2006, 2009, Emeis et al., 2004]. Consequently, the Benguela Current is a suspected source of  $\text{CH}_4$  to the atmosphere, but the amount is unconstrained [Naqvi et al., 2010].

The most common method of estimating yearly budgets of air–sea fluxes for GHGs is to take wind fields and interpolated or representative surface measurements, use them to calculate a flux density, and scale it up over a selected area. The high variability of air–sea exchange means that determining yearly budgets of air–sea fluxes of GHGs is challenging without a high degree of spatial and temporal sampling. Flux density calculations from bulk measurements are typically made in the upper 10 m of the ocean, but not at the surface. The method assumes a homogeneous distribution between the measurement depth and the surface, which is often a poor assumption [Calleja et al., 2013]. The flux density ( $F$ , in units of  $\text{mol m}^{-2} \text{sec}^{-1}$ ) is typically determined according to [Garbe et al., 2014, Wanninkhof et al., 2009]:

$$F = k_w(C_w - \alpha C_a) \quad (6.1)$$

where  $k_w$  is the gas transfer (or piston) velocity, in  $\text{m sec}^{-1}$ ,  $C_w$  is the dissolved concentration in the water phase ( $\text{mol m}^{-3}$ ), and  $C_a$  is the concentration of the species in the air in the same units. The formulation can also be altered to accommodate units of partial pressure in both phases. The expression  $\alpha C_a$  gives the dissolved concentration in the water phase directly at the surface;  $\alpha$  is the Ostwald solubility coefficient: the reciprocal of the dimensionless air–water partition coefficient ( $K_{AW}$ ) for some temperature,  $T$ , and salinity,  $S$  [Mackay and Shiu, 1981].

This approach is valid for lightly soluble gases and assumes an aqueous mass boundary layer with a uniform temperature, negligible chemical or biological enhancement, bulk concentrations in air and water that are well-mixed, and that the surface boundary layers are in equilibrium, so that the concentration directly at the top of the aqueous mass boundary layer can be calculated from  $C_a$ , using Henry’s Law [Garbe et al., 2014, Wanninkhof, 1992, Wanninkhof et al., 2009].

Even if the analytical uncertainty in  $C_w$  and  $C_a$  is low, one must know the correct value of  $k_w$ , which is dependent on environmental conditions. There are many approaches suggested for gas transfer velocity parameterization in the literature, most of them based on wind speed measured at 10 m above the sea surface. Such  $k_w$ – $U_{10}$  relationships vary from linear to cubic



and  $k_w$  is a large source of uncertainty in determining air–sea gas fluxes [Johnson et al., 2011, Otero et al., 2013, Takahashi et al., 2009]. While some of the range of  $k_w-U_{10}$  results is related to experimental uncertainty, much of the factor-of-two spread [Ho et al., 2011, Johnson et al., 2011] reflects what is probably the real, natural variability in piston velocities under different conditions involving varying importances of additional forcers (bubbles, sea spray, surfactants, rain, etc.) [Garbe et al., 2014]. Parameterizing  $k_w$  based on wind speed means that not only is the uncertainty in the correct parameterization significant, but that uncertainty in the wind speed data itself is also important to account for [Otero et al., 2013].

Another approach, and one that sidesteps some of these difficulties, is to use a top-down method, i.e. using atmospheric measurements to infer fluxes from the surface, using simple models [Lueker, 2004, Lueker et al., 2003, Nevison et al., 2004b, Thompson et al., 2007, Yamagishi et al., 2008] or more complex inverse methods (e.g., Rödenbeck et al. [2008]). The top-down approach has been successfully employed to detect air–sea fluxes of  $O_2$ ,  $CO_2$ , and  $N_2O$  from the California Current upwelling zone from a coastal atmospheric monitoring station at Trinidad Head, California [Lueker, 2004, Lueker et al., 2003, Nevison et al., 2004b]. In the present, a simple Lagrangian model is employed to create a top-down constraint for the air–sea exchange of GHGs, oxygen, and carbon monoxide from two prominent upwelling cells in the Benguela Current region, using the NDAO time series. These estimates are then validated with shipboard measurements from a cruise in the two upwelling centers, and scaled up to create annual flux estimates due to upwelling events for these gases of interest.

## 6.2 Methods

### 6.2.1 Remote Sensing Data

Following the reasoning of Goubanova et al. [2013], sea surface temperature (SST) data were obtained from the Remote Sensing Systems (<http://www.remss.com/>) data archive. The Tropical Rainfall Measuring Mission (TRMM) Microwave Imager (TMI) daily optimally interpolated SST product was selected. The major advantage this instrument has is its ability to measure SST through clouds, which are considerable over the coast, as the TMI measures frequencies in the microwave region (4–11 GHz). The drawback of this dataset is that there is no data within 100 km of the coast. Large upwelling features, however, extend much farther out than this and are readily seen by TMI [Goubanova et al., 2013]. Even with this loss of near-shore data, the data coverage is still superior to that of optical sensors like the Moderate-Resolution Imaging Spectroradiometer (MODIS). The TRMM SST data presented in this work is deseasonalized by subtracting a second harmonic fit to the data, as it showed a strong seasonal cycle which masked some of the intraseasonal variability when plotted as a time series.

Wind speed data for the South Atlantic was also derived from the TMI instrument on the TRMM satellite. This dataset is a level 3 product which gives the 10 m wind speed over marine areas within the sensor’s field of view. The 18.7 GHz channel data product was selected. Like the SST data, a major drawback of this dataset is the absence of data within 100 km of land.

Unfortunately, for measurements of surface chlorophyll *a* (chl-*a*), optical sensors are the only option. Chl-*a* is a proxy for phytoplankton biomass. Two surface chlorophyll products were used, both level 3 binned products that combined data from multiple satellites, accessed through ESA GlobColour website (<http://www.globcolour.info/>). The first is denoted CHL1-GSM; this dataset is a merged product of two different sensors (during the time period considered), MODIS and the Visible Infrared Imaging Radiometer Suite (VIIRS). The data is merged using the Garver, Siegel, Maritorena (GSM) model, which blends the normalized

water-leaving radiances instead of the end product (chl-*a* concentrations) [Maritorena and Siegel, 2005]. The second product is denoted CHL1-AVW; these data are merged using a weighted average method (AVW). Like CHL1-GSM, it combines data from MODIS and VIIRS for the time frame considered.

### 6.2.2 Identification of Upwelling Events and Selection of Atmospheric Anomalies

A subset of the coastal region was extracted to represent the Lüderitz and Walvis Bay upwelling cells, hereafter referred to as the “Lüderitz/Walvis Bay domain.” The boundaries of this domain were at 13°E, 15°E, 23°S, and 27°S (Figure 6.2, *right panel*), representing an ocean area of 56,196 km<sup>2</sup>.

Upwelling events were identified based on SST and 10 m wind speed anomalies. Specifically, an event was determined to occur if the average deseasonalized SST of the domain was 0.5°C or lower than a smoothed, second-degree polynomial fit to the entire time series, and the average 10 m wind speed of the study area was 2.5 m sec<sup>-1</sup> above a smoothed, second-degree polynomial fit to the wind data. These thresholds were arrived at through visual inspection of maps and time series of SST and wind speed data, and are specific to the domain chosen, since the data considered were averages of the entire area. That is, the actual SST of a pool of recently upwelled water is more on the order of 4–5°C cooler than its surroundings. Since the resolution of the SST and wind speed time series is daily, all higher resolution data falling within a day during which an upwelling event occurred was similarly flagged.

Through inspection of the time series, it was noted that large atmospheric anomalies of a few hours’ duration were associated with upwelling events. The manner in which such features appear in the atmosphere is controlled both by the timing and location of surface fluxes and atmospheric dynamics. Specific events were identified and quantified in the following manner: a second-harmonic fit was generated iteratively to all data, excluding all points that lay above the curve for the subsequent iteration for CH<sub>4</sub>, N<sub>2</sub>O, and CO. For  $\delta(\text{O}_2/\text{N}_2)$  the process was the same, only points which lay below the curve were excluded, since the majority of anomalies are negative for this species. For CO<sub>2</sub>, points that lay above or below one standard deviation of the initial fit were excluded from the final fit, since anomalies for this species are both positive and negative. Once a background curve was obtained, the NDAO time series was filtered by wind (wind speeds greater than 2 m sec<sup>-1</sup> and wind direction within the NNW–SSW sector) and back-trajectory to exclude anomalies which were not associated with marine air masses. For the latter, trajectories could not reside for more than 36 hours of the total 120 hours over land, and could not travel more than 50 km inland past NDAO.

### 6.2.3 Top-Down Air–Sea Flux Estimates

In order to estimate the surface flux associated with atmospheric anomalies due to upwelling events, the approach of Lueker et al. [2003] was adopted. A simple model was employed to describe the change in the concentration of a species within a well-mixed column of air as it moves over a source region [Jacob, 1999]:

$$\Delta C = \begin{cases} \frac{F}{hk} \left( 1 - e^{-\frac{kx}{U}} \right), & \text{for } 0 \leq x \leq L \\ \Delta C_L \left( e^{-\frac{k(x-L)}{U}} \right), & \text{for } x \geq L \end{cases} \quad (6.2)$$

Here  $\Delta C$  is the concentration of the species of interest, in mol m<sup>-3</sup>, expressed as an anomaly against the background.  $\Delta C$  is a function of  $x$ , which is the distance along a back-trajectory

from NDAO to the area affected by upwelling.  $L$  is the point at which the column (with height  $h$ , in m) leaves this region, characterized by a constant flux,  $F$ , in  $\text{mol m}^{-2} \text{hr}^{-2}$ , and a constant wind speed,  $U$ , in  $\text{m hr}^{-1}$ . After the column leaves the flux region ( $x \geq L$ ), the loss of  $\Delta C$  from its peak at  $L$  ( $\Delta C_L$ ) is governed by dilution due to mixing of background air. This requires the dilution rate constant,  $k_{dil}$ , in  $\text{hr}^{-1}$ , to be known.

Since NDAO is well-outside the flux region, one solves for  $\Delta C_L$  and then for  $F$ . Wind speeds were obtained from satellite data (Section 6.2.1) and the in situ data from NDAO.  $h$  was taken as the average height of the planetary boundary layer (PBL) for the Lüderitz/Walvis Bay domain<sup>1</sup> over the course of any given event. PBL data was acquired from the European Centre for Medium-Range Weather Forecasting’s (ECMWF) ERA-Interim dataset [Dee et al., 2011]. The dilution rate constant was estimated by comparing measurements of  $\text{CO}_2$  and  $\text{CH}_4$  made on the Meteor during M99. Back-trajectories from NDAO were matched to the closest ship location at the appropriate time. Any back-trajectory points that were within 100 km of the ship—both horizontally and vertically—within the space of 1 hour were identified, and a dilution rate constant was calculated for both  $\text{CO}_2$  and  $\text{CH}_4$ , as [Price et al., 2004]:

$$k_{dil} = \frac{1}{t} \ln \left( \frac{C_{M99} - C_b}{C_{NDAO} - C_b} \right) \quad (6.3)$$

The  $k_{dil}$ s that were obtained from this exercise were then filtered for poor agreement between  $k_{dil}$ s for  $\text{CO}_2$  and  $\text{CH}_4$ , and the average was taken to arrive at a single value,  $0.011 \pm 0.006 \text{ hr}^{-1}$ .

#### 6.2.4 Determination of Spatially Integrated Annual Flux Rates

To obtain an estimate of the total, annual mass flux of the NDAO measurands from the Lüderitz and Walvis Bay upwelling cells, the flux density estimates obtained from the approach described in Section 6.2.2 were integrated over a surface area determined as follows. Grid cells with wind speeds above  $3.5 \text{ m sec}^{-1}$  and a deseasonalized SST below  $-0.1^\circ\text{C}$ , were identified, and then all assumed to have the same flux rate (Figure A.30). The aim here was to simply exclude portions of the domain that were not affected by upwelling, rather than to develop a predictive empirical relationship between fluxes of different species and upwelling activity, since for species like  $\text{CO}_2$ , no such simple relationship exists [Santana-Casiano et al., 2009]. Since the TRMM SST data contains no values within 100 km of the coast, for any grid cell passing the thresholds that bordered this area, it was assumed that the upwelling extended to the coast. The daily summed net flux was then integrated over the whole time series to obtain a total annual flux rate for the two upwelling cells. This approach necessarily resulted in an underestimate, since transport conditions were not always conducive to observing an upwelling event.

#### 6.2.5 FS Meteor Cruise M99

Cruise M99 of the FS *Meteor* left Walvis Bay on July 31<sup>st</sup>, 2013, and returned to port on August 23<sup>rd</sup>. The ship called at Lüderitz on the 11<sup>th</sup> and 12<sup>th</sup>. Throughout the cruise, continuous or semi-continuous measurements were made of atmospheric  $\text{CO}_2$ ,  $\text{CH}_4$ , and  $\text{N}_2\text{O}$ , and dissolved  $\text{CO}_2$ ,  $\text{CH}_4$ ,  $\text{N}_2\text{O}$ , and  $\text{O}_2$ .

Atmospheric measurements of  $\text{CO}_2$  and  $\text{CH}_4$  were made with a CRDS analyzer (model G1301, Picarro Inc, Santa Clara, CA, USA) located in the atmospheric chemistry laboratory. The instrument’s internal pump was used to draw air through a 7 m length of  $1/4$ ” SERTOflex

<sup>1</sup>NDAO is within the N-S boundaries of the domain and only 4 km outside the eastern boundary.

tubing, at a flow rate  $150 \text{ mL min}^{-1}$ . Inlets identical to those used at NDAO (Section 3.2.1) were placed on the starboard railing of the 6<sup>th</sup> superstructure deck, just above the atmospheric chemistry lab, at a total height of  $\sim 21 \text{ m}$  above sea level. A second-order, instrument-specific water correction was performed in lieu of physical or chemical drying (see Section 3.2.10). As the instrument’s pressure control seemed to be affected by strong vessel motion, measurements were excluded if the cavity pressure deviated by more than 0.04 torr. Calibrations were conducted on average every three days and target measurements were made once per day. Reference gases were calibrated at MPI-BGC GASLAB. The uncertainty, derived from the target measurements as at NDAO, was determined to be  $\pm 0.03 \text{ ppm}$  for  $\text{CO}_2$  and  $\pm 0.43 \text{ ppb}$  for  $\text{CH}_4$ . The dataset was filtered for contamination by the ship’s exhaust using the relative wind direction data from the ship’s meteorological instrumentation.

A complete description of the instrumentation setup used for dissolved gases is given in Arévalo-Martínez et al. [2013], with a few modifications that are mentioned here. Briefly, surface water was drawn at a flow rate of  $2 \text{ L min}^{-1}$  from the ship’s moonpool at a depth of ca. 6 m with a subpump. A 25 m line brought sample water from the moonpool into the laboratory, where seawater was routed to a Weiss-type equilibrator. Water vapor was removed from the sample air stream with a condenser in an ice bath and a Nafion<sup>®</sup> dryer (model MD-070-72F-4). After drying, the equilibrated sample air was routed ( $235 \text{ mL min}^{-1}$ ) to an OA-ICOS analyzer (model RMT-200, Los Gatos Research Inc, Mountain View, CA, USA), using the instrument’s internal pump, and then to a non-dispersive infrared (NDIR) gas analyzer (model LI-6262, LI-COR Biosciences, Lincoln, Nebraska, USA) for  $\text{CO}_2$ . After measurement, sample air was returned to the equilibration chamber. Every six hours the system measured atmospheric mixing ratios and reference gases for calibration and/or drift correction. The headspace of the equilibration chamber was open to the atmosphere to maintain the pressure at ambient levels. Dissolved oxygen was measured with an Aanderaa oxygen optode (Model 4330, Aanderaa Data Instruments AS, Bergen, Norway).

The estimated uncertainty of the dissolved  $\text{CO}_2$  measurements was  $\pm 2 \text{ } \mu\text{atm}$ ; of dissolved  $\text{O}_2$  measurements,  $\pm 4 \text{ } \mu\text{mol L}^{-1}$ ; of dissolved  $\text{N}_2\text{O}$ ,  $\pm 0.1 \text{ nmol L}^{-1}$ . The uncertainty of the atmospheric measurements of  $\text{N}_2\text{O}$  was  $\pm 0.9 \text{ ppb}$ .

In situ oceanographic and meteorological data were taken from the *Meteor*’s instrumentation. In order to determine the total dissolved inorganic carbon (DIC) content of surface waters, total alkalinity was estimated from temperature and salinity data, using the algorithm of Lee et al. [2006]. The dissociation constants of carbonic acid were also determined from temperature and salinity using the formulations of Millero et al. [2006]. The total DIC content was then estimated from the total alkalinity and  $f\text{CO}_2$ . Meteorological data (air temperature, barometric pressure, wind speed, etc.) was observed at a height of 37 m above sea level. The absolute wind speed measured on the *Meteor* was converted to  $U_{10}$  through the relationship [Justus and Mikhail, 1976]:

$$U_{10} = U_{meas} \left( \frac{z_{10}}{z_{meas}} \right)^n \quad (6.4)$$

$$n = \frac{0.37 - 0.0081 \cdot \ln(U_{meas})}{1 - 0.0881 \cdot \ln\left(\frac{z_{meas}}{10}\right)} \quad (6.5)$$

where  $U_{meas}$  is the wind speed in  $\text{m sec}^{-1}$ , measured at some height  $z_{meas}$ , in m.

### 6.2.6 Shipboard Air–Sea Flux Density Estimates

Marine surface flux densities of  $\text{CO}_2$ ,  $\text{N}_2\text{O}$ , and  $\text{O}_2$  were estimated for the vessel location throughout M99 from shipboard measurements of atmospheric dry air mole fractions and dis-

solved aqueous concentrations, according to Equation 6.1. In the case of  $O_2$ , the atmospheric concentration was not measured, so it was taken as the mole fraction of  $O_2$  in standard dry air, 0.209392 [Tohjima et al., 2005a]. The in situ aqueous solubility of  $O_2$  was calculated using the equations of García and Gordon [1992], of  $N_2O$  using those in Weiss and Price [1980], and of  $CO_2$  using Weiss [1974]. Sea-to-air fluxes (net evasion) are positive.

As there is no definitive  $k_w-U_{10}$  parameterization, fluxes were computed with four different parameterizations of  $k_w$ : that of Liss and Merlivat [1986] ( $k_{L\&M}$ ), Wanninkhof [1992] ( $k_{W92}$ ), Nightingale et al. [2000] ( $k_{N00}$ ), and McGillis et al. [2001] ( $k_{McG01}$ ).

$$k_{L\&M} = \begin{cases} (0.17U_{10})\left(\frac{Sc}{600}\right)^{-2/3} & \text{for } U_{10} \leq 3.6 \\ (2.85U_{10} - 9.65)\left(\frac{Sc}{600}\right)^{-0.5} & \text{for } 3.6 < U_{10} \leq 13 \\ (5.9U_{10} - 49.3)\left(\frac{Sc}{600}\right)^{-0.5} & \text{for } U_{10} > 13 \end{cases} \quad (6.6)$$

$$k_{W92} = 0.31U_{10}^2 \left(\frac{Sc}{660}\right)^{-0.5} \quad (6.7)$$

$$k_{N00} = (0.222U_{10}^2 + 0.333U_{10}) \left(\frac{Sc}{600}\right)^{-0.5} \quad (6.8)$$

$$k_{McG01} = (3.3 + 0.026U_{10}^3) \left(\frac{Sc}{660}\right)^{-0.5} \quad (6.9)$$

In these equations,  $U_{10}$  is the wind speed at 10 m's height, and  $Sc$  is the Schmidt number of a particular gas at in situ conditions [Jähne et al., 1987, Wanninkhof, 1992]. The Schmidt number is scaled to the reference conditions of the parameterization, i.e. 600 or 660, which is the  $Sc$  of  $CO_2$  at 20°C in fresh water or seawater, respectively. The Schmidt number is dimensionless and  $k_w$  and  $U_{10}$  must be in the same units, e.g.,  $m \text{ sec}^{-1}$ .

## 6.3 Results and Discussion

### 6.3.1 Chlorophyll $a$ and SST

As the chl- $a$  products suffered from low data coverage, the median was chosen as being more representative than the mean value, since the inclusion of a few pixels with low or high values could greatly effect the mean. Chl- $a$  within the Lüderitz domain was fairly constant over the two-year study period; the variability was almost entirely driven by intraseasonal events (Figure A.31) and was more pronounced spatially than temporally. In contrast, SST showed a pronounced seasonality, peaking in February and reaching a minimum in October (Figure A.31 and Figure A.32). During the summer months, when upwelling fluxes tend to be stronger, the contrast between the coast and South Atlantic is quite readily seen.

Despite the poor data coverage for chl- $a$ , results were in agreement with previous assessments of the nature of productivity and upwelling for the Lüderitz cell. While the upwelling in this area is extremely intense—some of the strongest volume fluxes in the world are seen here—phytoplankton biomass is at a minimum compared to the rest of the Benguela system; presumably this is because phytoplankton are light-limited due to the high winds that deepen the mixed layer and carry phytoplankton to depth [Carr, 2002, Chavez and Messié, 2009, Demarcq et al., 2003, 2007]; the high-nutrient, recently upwelled water at Lüderitz is

carried northward by surface currents, and as a result the area of highest productivity and most intense hypoxia is located around 24°S [Brüchert et al., 2006].

### 6.3.2 Dissolved Gas Concentrations and Air–Sea Fluxes During M99

N<sub>2</sub>O surface concentrations were rather low for an upwelling region, but agreed well with previously reported values, with the maximum observed concentration of 20.5 nM being comparable to the highest values seen by Frame et al. [2014] for surface measurements in the same region as the M99 cruise. The only other in situ measurements of N<sub>2</sub>O in the Benguela region known to the author are in the Marine Methane and Nitrous Oxide (MEMENTO) database<sup>2</sup> [Bange et al., 2009], from a single cruise in 2009 aboard the FRS *Africana*, as part of the Geochemistry and Ecology of the Namibian Upwelling System (GENUS) project. In this dataset, dissolved N<sub>2</sub>O concentrations for surface waters (the top 15 m) were in the range of 1–19 nM, which brackets the range measured during M99. Even when one considers the Frame et al. [2014] and GENUS measurements made at depth reported by the (a maximum not exceeding 50 nM for either), this would put the Benguela an order of magnitude or so lower below the maximum values measured in the Chilean and Peruvian upwelling systems, but on par with the Mauritanian system [Bakker et al., 2014, Naqvi et al., 2010].

All three species measured underway in the water phase showed the largest deviation from atmospheric equilibrium closest to shore (Figure A.33). The dissolved oxygen was mostly at saturation or slightly above, although close to shore the concentration dropped to a minimum of 180.8  $\mu$ M (67% saturation). CO<sub>2</sub> concentrations, expressed as the fugacity ( $f$ CO<sub>2</sub>) ranged from 355.5 to 852.3  $\mu$ atm (87.8% to 207.3% saturation), with most of the observed oversaturation occurring under upwelling conditions.

The main upwelling event of the cruise, in the Lüderitz/Walvis Bay cells, began on August 4<sup>th</sup>, 2013, and lasted until August 11<sup>th</sup>. Wind speeds declined rapidly after the 8<sup>th</sup>. The upwelling event was encountered by the *Meteor* starting on the 8<sup>th</sup> as the vessel reached an upwelling filament, the outer edge of which was subject to net evasion of all three gases (CO<sub>2</sub>, O<sub>2</sub>, N<sub>2</sub>O), likely a result of warming temperatures that would reduce the solubility. The highest flux rates (positive for N<sub>2</sub>O and CO<sub>2</sub>, and negative for O<sub>2</sub>) were seen within the recently upwelled waters experiencing high wind speeds (Figure A.34). Fluxes displayed coupling between all three species, though the area of high flux density for O<sub>2</sub> and N<sub>2</sub>O was more sharply defined than for CO<sub>2</sub>.

Only CO<sub>2</sub> and CH<sub>4</sub> were measured continuously in the atmosphere on M99. During the first days of the cruise, a synoptic event brought elevated mixing ratios of CO<sub>2</sub> and CH<sub>4</sub> offshore (Figure A.35 and Figure A.36). The shipboard measurements of CH<sub>4</sub> show a clear enhancement relative to the background seen at NDAO. This coincides with the regions of higher flux closer to the coast encountered under upwelling conditions. In contrast, methane was consistently at background levels, usually below the value seen at NDAO.

### 6.3.3 Atmospheric Anomalies Due to Upwelling Events

In all, 173 days with upwelling events were identified, representing 24% of the two-year study period. Of these 173 days, 157 of them had atmospheric transport conditions favorable for detecting an event. Despite the greater prevalence of equatorward winds during austral summer, the distribution of events displayed little seasonality (Figure A.31), reflecting the fact that upwelling is a short-term, intraseasonal phenomenon, forced by specific atmospheric conditions [Goubanova et al., 2013, Risien et al., 2004]. Note that while the occurrence of

---

<sup>2</sup><https://memento.geomar.de/>

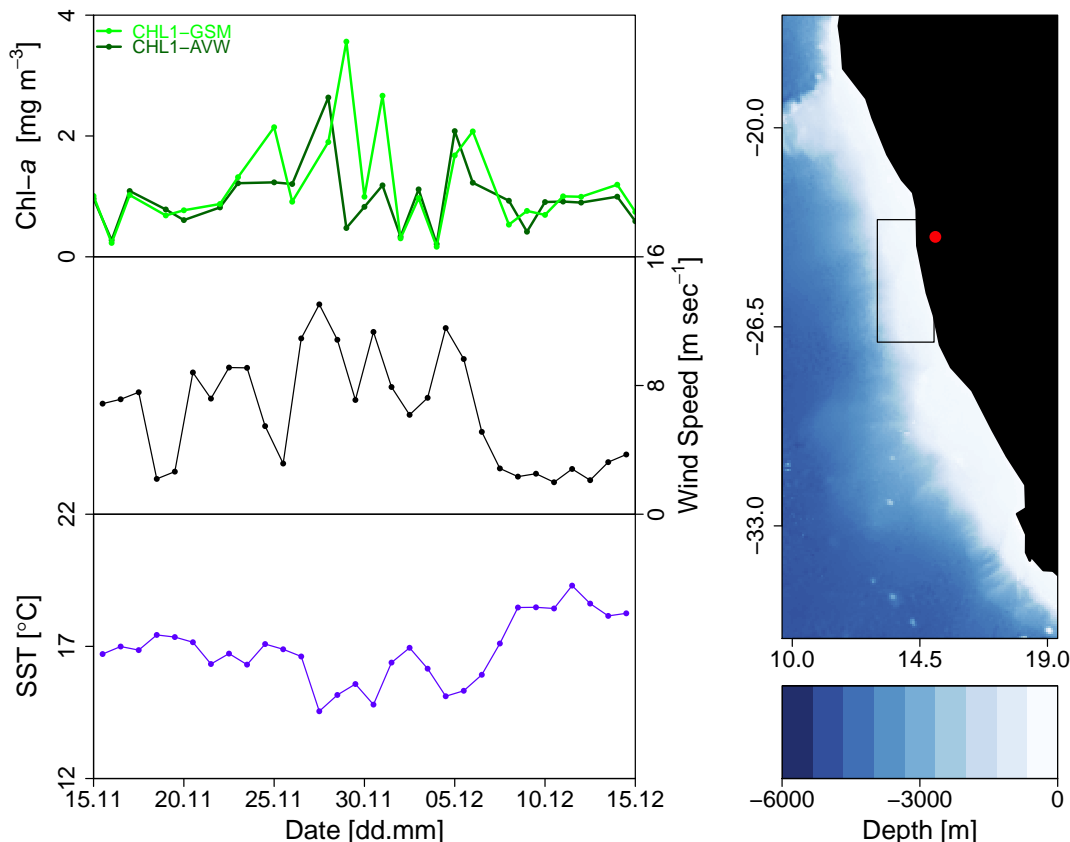


Figure 6.2: An example of an upwelling event at the end of 2013. The median chlorophyll  $a$  of the domain is shown over a period of one month, along with the domain-averaged 10-m wind speed and sea surface temperature (*left panel*). The Lüderitz/Walvis Bay domain is shown, overlain on a bathymetric map (*right panel*). Data is from [Amante and Eakins \[2009\]](#). Location of NDAO is given by a red dot.

upwelling has little seasonal signal at Lüderitz, the magnitude of the volume flux does display seasonality [[Veitch et al., 2009](#)].

Atmospheric data corresponding to these days with upwelling events were then selected, using the filtered, marine-only observations. Visualization of the back-trajectories corresponding to these events confirmed that the selection of atmospheric data was successful (Figure [A.37](#)). An example of such an event is given in Figure [6.2](#), Figure [6.3](#), and Figure [A.38](#). On November 27<sup>th</sup>, 2013, high winds resulted in the creation of a very large pool of colder water on the surface that persisted for four days, until winds relaxed and the upwelling temporarily ceased until the 4<sup>th</sup> of December. During both upwelling events, chl- $a$  values were higher. A change in the background values of APO, N<sub>2</sub>O, and CH<sub>4</sub> was seen, with a smaller anomaly for CO<sub>2</sub>. The peak for each species came during the sea breeze on August 28<sup>th</sup> (Figure [A.39](#)).

If the area of high flux is close to the coast, anomalies could arrive within a few hours at NDAO, with the sea breeze. If the region of flux is closer to Lüderitz, the arrival time could be delayed by as much as 50 hours, depending on the wind speed and the degree of meandering of the air mass. Back-trajectories implied that despite the high wind speeds usually seen in this coastal zone, significant travel time (1 to 2 days) could be expected for most air masses of interest. Hence the marine surface flux associated with an atmospheric

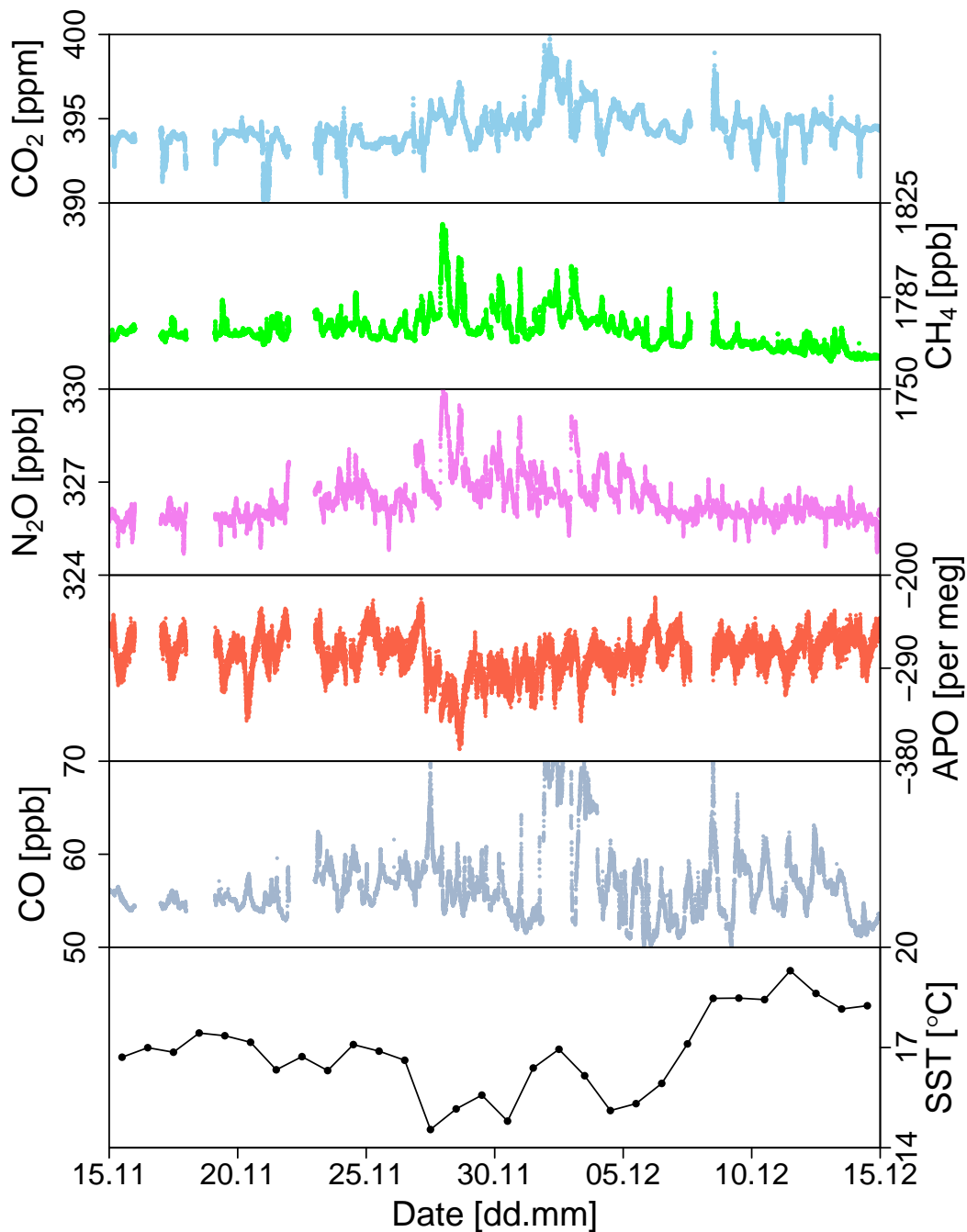


Figure 6.3: Atmospheric time series at NDAO throughout the upwelling event displayed in Figure 6.2. For a close-up of the peak of each anomaly, see Figure A.39.



Table 6.1: Means of All Atmospheric Anomalies and Top-Down Flux Density Estimates for Identified Upwelling Events

Species	Mean Anomaly $\pm 1\sigma$	Mean Flux Density $\pm 1\sigma$
O <sub>2</sub>	$-49.7 \pm 24.9$ per meg	$-3.9 \pm 2.6$ $\mu\text{mol m}^{-2} \text{sec}^{-1}$
CO <sub>2</sub>	$1.69 \pm 1.37$ ppm	$0.45 \pm 0.4$ $\mu\text{mol m}^{-2} \text{sec}^{-1}$
CH <sub>4</sub>	$19.36 \pm 16.40$ ppb	$6.0 \pm 5.0$ $\text{nmol m}^{-2} \text{sec}^{-1}$
N <sub>2</sub> O	$1.5 \pm 0.9$ ppb	$0.5 \pm 0.4$ $\text{nmol m}^{-2} \text{sec}^{-1}$
CO	$9.7 \pm 4.3$ ppb	$2.7 \pm 1.7$ $\text{nmol m}^{-2} \text{sec}^{-1}$

anomaly could only be said to have taken place with 50 hours of its detection. The magnitude of the average atmospheric anomaly and its corresponding flux density estimate are given in Table 6.1.

### 6.3.4 Estimated Flux Densities

The moderate, positive methane spikes ( $\sim 20$  ppb) seen during upwelling events corresponded to an average flux density of about  $6 \text{ nmol m}^{-2} \text{ sec}^{-1}$  and a maximum of  $24.7 \text{ nmol m}^{-2} \text{ sec}^{-1}$ , a high value even for coastal waters, though it must be emphasized that these flux densities correspond only to specific events and are not constant throughout the year. There are few reported measurements of flux densities or dissolved CH<sub>4</sub> for the Benguela region to place these estimates in context. In what are likely the first measurements of dissolved methane in the Benguela, [Scranton and Farrington \[1977\]](#) observed concentrations near Walvis Bay at multiple depths in the 200–900 nM range. The only other available data known to the author are from the 2009 GENUS cruise. These concentrations were also taken at a variety of depths (up to 400 m) and ranged from 3.7 to 140.0 nM. Using the three samples taken from the top 15 m from this cruise, at in situ conditions, a flux of  $\sim 0.3 \text{ nmol m}^{-2} \text{ sec}^{-1}$  would be expected. [Naqvi et al. \[2010\]](#) used the data from [Scranton and Farrington \[1977\]](#) and from [Monteiro et al. \[2006\]](#) to estimate flux densities of 0.03–8.7  $\text{nmol m}^{-2} \text{ sec}^{-1}$ , the upper end-member of which compares favorably with the rates found in this study for the same ocean region. Though the latter study observed concentrations at a mooring near Walvis Bay as high as 10  $\mu\text{M}$ , these data were from an uncalibrated probe and are not usable for a direct comparison to other campaigns. In other eastern boundary upwelling systems, reported flux densities are much lower. For the Chilean/Peruvian upwelling systems, shipboard measurements have determined fluxes to be on the order of  $5 \times 10^{-4}$  to  $1.3 \text{ nmol m}^{-2} \text{ sec}^{-1}$  [[Farías et al., 2009](#), [Kelley and Jeffrey, 2002](#), [Naqvi et al., 2010](#)], a little higher than that found for the Mauritanian upwelling region, 0.005–0.02  $\text{nmol m}^{-2} \text{ sec}^{-1}$  [[Kock et al., 2008](#)]. In the shelf waters of the Black Sea, where rates are high due to inputs from rivers, in situ methanogenesis, and seepage from the sediments, representative values were found to be 0.37–0.61  $\text{nmol m}^{-2} \text{ sec}^{-1}$  [[Amouroux et al., 2002](#)].

The average flux density attributable to specific upwelling events for N<sub>2</sub>O was  $0.5 \pm 0.4 \text{ nmol m}^{-2} \text{ sec}^{-1}$ , moderate for a coastal upwelling system. Surface data from the 2009 GENUS cruise would have yielded a maximum flux density of about 0.2–0.3  $\text{nmol m}^{-2} \text{ sec}^{-1}$ . [Frame et al. \[2014\]](#) observed flux rates as high as 0.52  $\text{nmol m}^{-2} \text{ sec}^{-1}$  in the Cape Frio upwelling cell. The 3-D coupled physical/biogeochemical model of [Gutknecht et al. \[2013a,b\]](#) predicts an 8-year mean flux density of 0.02–0.16  $\text{nmol m}^{-2} \text{ sec}^{-1}$  for the Walvis Bay region, including both shelf and deeper waters as far west as 10°E. The mean flux density of the entire M99 cruise was  $\sim 0.03 \text{ nmol m}^{-2} \text{ sec}^{-1}$ . The model predicts a maximum flux density at the coast (22–24°S) of 0.6  $\text{nmol m}^{-2} \text{ sec}^{-1}$ . Sea–air flux densities from the anal-

ogous Chilean OMZ during upwelling events fall between 0.04 and 3.8 nmol m<sup>-2</sup> [Cornejo et al., 2006, Paulmier et al., 2008]. Large fluxes reported for the Indian continental shelf in an OMZ were a result of flux densities of 0.46–3.1 nmol m<sup>-2</sup> sec<sup>-1</sup> [Naqvi et al., 2000], and later up to 38 nmol m<sup>-2</sup> sec<sup>-1</sup> [Naqvi et al., 2010]. Values as high as 3–5.7 nmol m<sup>-2</sup> sec<sup>-1</sup> have been reported from the Somali upwelling region [de Wilde and Helder, 1997]. In the Mauritanian upwelling region, the highest flux densities are around 2 nmol m<sup>-2</sup> sec<sup>-1</sup> [Wittke et al., 2010], with values more typically in the 0.5–1.5 nmol m<sup>-2</sup> sec<sup>-1</sup> range, similar to that seen here for the Lüderitz region. In the Arabian Sea, coastal upwelling events yield flux densities of 0.7–1.4 nmol m<sup>-2</sup> sec<sup>-1</sup> [Bange et al., 1996b]. During a strong upwelling event in the California system, Lueker [2004] observed a value of 2 nmol m<sup>-2</sup> sec<sup>-1</sup> using the same top-down approach adopted in the present study.

CO<sub>2</sub> fluxes were positive for all upwelling events, with an average flux density of 0.45 ± 0.3 μmol m<sup>-2</sup> sec<sup>-1</sup> and a maximum value of 2.4 μmol m<sup>-2</sup> sec<sup>-1</sup>. During upwelling conditions, it is not uncommon to see such strong outgassing of CO<sub>2</sub> in a coastal upwelling region; the biological response to new nutrients takes some days to draw down DIC levels [Cao et al., 2014, Loucaides et al., 2012, Torres et al., 1999]. In the waters off of central Chile, upwelling events can cause a net evasion of CO<sub>2</sub> on the order of 0.03–0.2 μmol m<sup>-2</sup> sec<sup>-1</sup> [Torres et al., 1999, 2002]. In an area containing a large OMZ off of the coast of Mexico, outgassing was as high as 0.04 μmol m<sup>-2</sup> sec<sup>-1</sup> [Franco et al., 2014]. Supersaturated waters during upwelling events in the Arabian Sea reached values as high as 1.4 μmol m<sup>-2</sup> sec<sup>-1</sup> [Körtzinger et al., 1997]. The southern Benguela, for instance, has been found to have an average net sink of 0.04 to 0.09 μmol m<sup>-2</sup> sec<sup>-1</sup> [González-Dávila et al., 2009, Gregor and Monteiro, 2013a, Santana-Casiano et al., 2009], although during upwelling events, outgassing can result in the region, on the order of 0.6 μmol m<sup>-2</sup> sec<sup>-1</sup> [Gregor and Monteiro, 2013b]. Santana-Casiano et al. [2009] used underway systems on cargo ships and weekly wind speeds to arrive at a mean flux between ca. –0.06 and 0.03 μmol m<sup>-2</sup> sec<sup>-1</sup> for the Lüderitz region, with peak rates as high as 0.06 μmol m<sup>-2</sup> sec<sup>-1</sup> in August. González-Dávila et al. [2009] found that the Lüderitz region is under-saturated with respect to CO<sub>2</sub>, with only upwelled waters seeing oversaturation, with average fluxes on the order of –0.03 ± 0.3 μmol m<sup>-2</sup> sec<sup>-1</sup>. The flux densities for CO<sub>2</sub> reported in the present study are not necessarily in conflict with these studies, since a yearly-averaged flux density is a different quantity from the event-based flux densities. The implication instead is that flux densities attributed to upwelling events are high enough to contribute significantly to the carbon balance of the Lüderitz and Walvis Bay regions.

Typical O<sub>2</sub> flux densities were about –4 μmol m<sup>-2</sup> sec<sup>-1</sup>, and the direction of exchange was always into the ocean. The estimated average flux density for the entire mid-South Atlantic (encompassing the latitudinal range of the whole Benguela, but extending to the coast of South America) was ~0.03 μmol m<sup>-2</sup> sec<sup>-1</sup> in the inverse modeling study of Gruber et al. [2001], and ca. 0.06 μmol m<sup>-2</sup> sec<sup>-1</sup> in the forward run of a coupled climate and ocean biogeochemistry model of Bopp et al. [2002]. For a strong upwelling event, Lueker [2004] reported –18.5 μmol m<sup>-2</sup> sec<sup>-1</sup> as a representative value for the California Current region. For a region in the Southern Ocean experiencing a phytoplankton bloom, Thompson et al. [2007] estimated fluxes to be approximately 4.7 μmol m<sup>-2</sup> sec<sup>-1</sup>.

The determined flux densities for carbon monoxide were much higher than values reported previously for upwelling regions and the open ocean. Kitidis et al. [2011] observed flux densities in the range of 0.05–0.1 nmol m<sup>-2</sup> sec<sup>-1</sup> within a filament in the Mauritanian upwelling region. A study in the California upwelling system resulted in estimated air–sea fluxes with an average of 0.06 nmol m<sup>-2</sup> sec<sup>-1</sup> and a maximum value of 0.3 [Day and Faloon, 2009]. In the equatorial Pacific upwelling region, Ohta [1997] measured flux densities of 0.05 nmol m<sup>-2</sup> sec<sup>-1</sup>. The average evasion of the South Atlantic Ocean has been estimated to be 0.03

Table 6.2: Estimated Annual Fluxes of the Lüderitz and Walvis Bay Upwelling Cells

Species	Flux	Unit
O <sub>2</sub>	$-1.4 \pm 0.2$	Tmol yr <sup>-1</sup>
CO <sub>2</sub>	$208 \pm 34$	Gmol yr <sup>-1</sup>
CH <sub>4</sub>	$2.2 \pm 0.3$	Gmol yr <sup>-1</sup>
N <sub>2</sub> O	$124 \pm 13$	Mmol yr <sup>-1</sup>
CO	$577 \pm 60$	Mmol yr <sup>-1</sup>

nmol m<sup>-2</sup> sec<sup>-1</sup> [Stubbins et al., 2006]. CDOM, the photolysis of which is the major source of CO in surface waters, is often elevated in coastal upwelling systems even in the absence of major riverine input, due to higher concentrations in remineralized water and to degradation of organic matter [Coble et al., 1998]. Remote sensing of ocean color has shown that the northern Benguela has high concentrations of CDOM [Siegel et al., 2014].

### 6.3.5 Comparison of Top-Down Flux Density Estimates with M99 Shipboard Determinations

Due to local wind variability, suitable conditions for detecting the upwelling event encountered by the *Meteor* were only seen at NDAO on the 6<sup>th</sup>, 8<sup>th</sup>, and 10<sup>th</sup> of August, 2013. As the vessel was not always in the upwelling cell, only a single atmospheric anomaly at NDAO could be matched to in situ shipboard measurements, namely an anomaly occurring on August 10<sup>th</sup>. The top-down estimates,  $0.43 \pm 0.04$   $\mu\text{mol m}^{-2} \text{sec}^{-1}$  for CO<sub>2</sub>,  $-2.5 \pm 0.2$   $\mu\text{mol m}^{-2} \text{sec}^{-1}$  for O<sub>2</sub>, and  $0.40 \pm 0.03$   $\text{nmol m}^{-2} \text{sec}^{-1}$  for N<sub>2</sub>O, agreed well with the corresponding mean shipboard estimates of  $0.48 \pm 0.31$   $\mu\text{mol m}^{-2} \text{sec}^{-1}$  for CO<sub>2</sub>,  $-3.2 \pm 2.2$   $\mu\text{mol m}^{-2} \text{sec}^{-1}$  for O<sub>2</sub>, and  $0.29 \pm 0.25$   $\text{nmol m}^{-2} \text{sec}^{-1}$  for N<sub>2</sub>O (Figure 6.4). While this provides a measure of confidence in the top-down flux density estimates, it should be noted that the neither of the estimated uncertainties for the top-down or bottom-up approaches account for errors incurred by the simplifying assumptions within their formulations.

### 6.3.6 Spatially Integrated Annual Fluxes

Scaling measurements or estimates of flux densities to a spatially and temporally integrated domain can be fraught with uncertainty. The estimates here (Table 6.2) are limited in that the approach assumes a constant flux over the area of upwelled water that reaches the surface, an assumption that is certainly unrealistic. They are also likely underestimates, since about 10% of upwelling events during the two-year time series occurred when atmospheric transport was unsuitable for observing the flux.

Much like the flux density, the estimated annual net release from Lüderitz and Walvis Bay of methane,  $2.2 \pm 0.3$  Gmol yr<sup>-1</sup> ( $35 \pm 6$  Gg yr<sup>-1</sup>), was very large for the marine environment. This estimate is two to three times higher than the net evasion from the Arabian Sea [Bange et al., 1998], and 10 to 20 times greater than the annual release of CH<sub>4</sub> from the entire Mauritanian upwelling system [Brown et al., 2014, Kock et al., 2008]. For further context, the estimate for the annual flux from the Black Sea is 6.7–11.7 Gmol yr<sup>-1</sup> (107.5–187.7 Gg yr<sup>-1</sup>) [Amouroux et al., 2002]. Nevertheless, the ocean source is a small term in the global budget, being 25–1,247 Gmol yr<sup>-1</sup> (0.4–20 Tg yr<sup>-1</sup>) of the total estimated global source term of ca. 31–38 Tmol yr<sup>-1</sup> (500–600 Tg yr<sup>-1</sup>), with coastal regions dominating [Bange et al., 1994, Bates et al., 1996, Dlugokencky et al., 2011, Ehhalt, 1974, Houweling et al., 2014, Kirschke et al., 2013, Lambert and Schmidt, 1993, Reeburgh, 2007a,b, Rhee et al.,

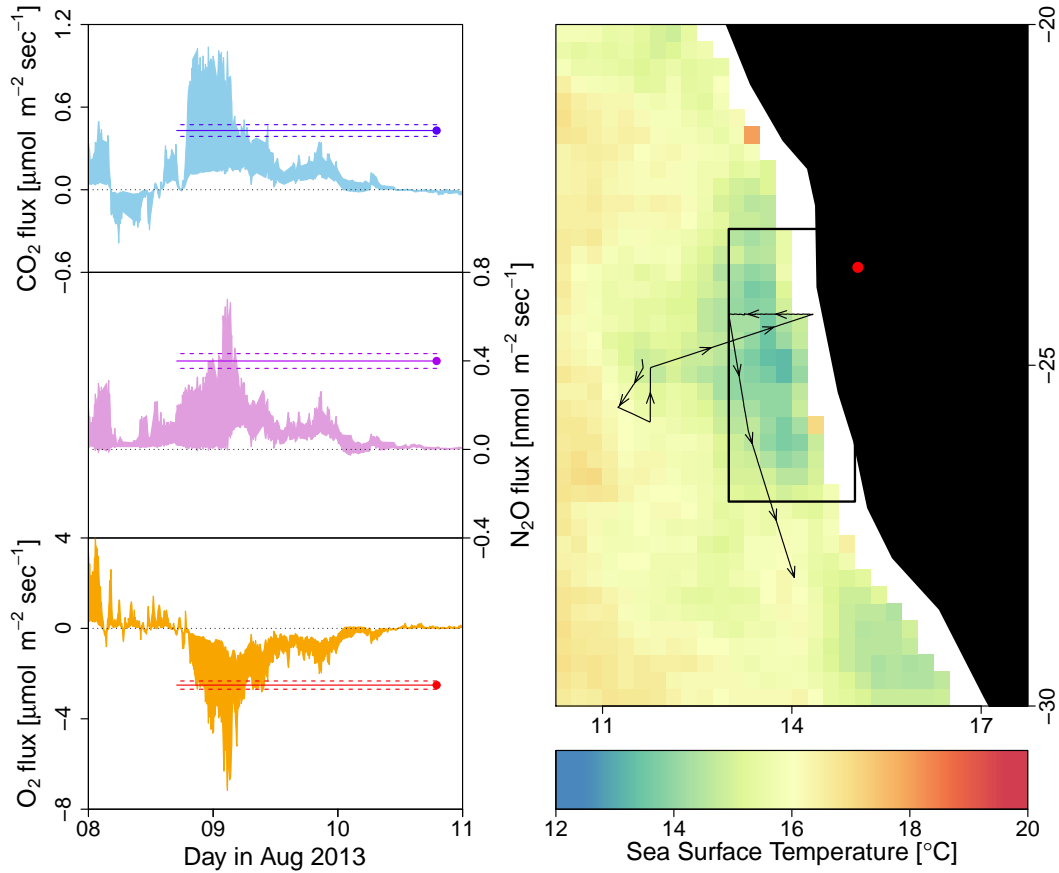


Figure 6.4: Air–sea flux densities for CO<sub>2</sub>, N<sub>2</sub>O, and O<sub>2</sub> using bottom-up methods (*left panel*), with a shaded envelope depicting the estimated surface flux and its uncertainty. A positive value indicates net evasion. The top-down flux density estimate is plotted as a dot at the time of detection of the associated atmospheric anomaly. The horizontal line extending from each dot represents the time period during which the flux density associated with the anomaly must have occurred. Dotted lines indicate the uncertainty of the top-down estimate. Grid-cell average TRMM SST data for the three-day period is overlain with a cruise track and the Lüderitz/Walvis Bay domain (*right panel*). Location of NDAO is given by a red dot.

2009]. The large range of estimates is partially due to whether the coastal environment is considered or not [Kelley and Jeffrey, 2002]. While small compared to global-scale or even regional-scale terrestrial budgets [Bergamaschi et al., 2013, Ghosh et al., 2015, Reeburgh, 2007a], these fluxes are nevertheless large for the marine environment, especially when one considers that these two upwelling cells are two out of the total seven or eight (depending on how they are defined).

Unlike methane, the emissions of N<sub>2</sub>O,  $124 \pm 13 \text{ Mmol yr}^{-1}$  ( $3.5 \pm 0.4 \text{ Gg-N yr}^{-1}$ ), are more modest when compared to the budgetary calculations of other coastal regions. As the global coastal upwelling source of N<sub>2</sub>O is estimated to be  $7,140 \text{ Mmol yr}^{-1}$  ( $200 \pm >70\% \text{ Gg-N yr}^{-1}$ ) [Nevison et al., 2004b], the emissions for the Lüderitz/Walvis Bay region would represent 3.2% of this area but only 1.8% of these emissions. In the Nevison et al. [2004b] study, the whole Benguela Current region (5–30°S) is assigned a yearly flux of only  $571 \text{ Mmol yr}^{-1}$  ( $16 \text{ Gg-N yr}^{-1}$ ), which means a contribution of approximately 20% from these two upwelling cells to the emissions of the whole system. While these two upwelling cells do emit substantial amounts of N<sub>2</sub>O, it is regionally significant but not a source of global

importance. For reference, the entire Mauritanian upwelling region emits 21–350 Mmol yr<sup>-1</sup> (0.6–9.8 Gg-N yr<sup>-1</sup>) [Rees et al., 2011, Wittke et al., 2010], with the large range depending on the area considered. The Arabian Sea has an annual sea-air flux of 7,500 to 15,900 Mmol yr<sup>-1</sup> (210–446 Gg-N yr<sup>-1</sup>) [Bange et al., 2001], and a global ocean source of 45–386 Gmol yr<sup>-1</sup> (1.2–10.8 Tg-N yr<sup>-1</sup>) [Bange et al., 1996a, Nevison et al., 1995, Rhee et al., 2009, Suntharalingam and Sarmiento, 2000].

The CO<sub>2</sub> source, 208 ± 34 Gmol yr<sup>-1</sup> (2.5 ± 0.4 Tg-C yr<sup>-1</sup>), is quite substantial when compared to the net flux that Laruelle et al. [2014] estimated of -424.9 Gmol yr<sup>-1</sup> (-5.103 Tg-C yr<sup>-1</sup>) for the entire Benguela region, or the -141.5 Gmol yr<sup>-1</sup> (-1.7 Tg-C yr<sup>-1</sup>) found by Gregor and Monteiro [2013a] for the southern Benguela. While the Benguela is not an outsize source or sink for carbon relative to its area, the Benguelan air-sea fluxes of CO<sub>2</sub> are large enough to warrant consideration in regional budgets. For an area of 1,900 km<sup>2</sup> off the coast of central Chile, Torres et al. [1999] estimated a daily release of 0.010 Gmol day<sup>-1</sup> (0.121 Gg-C day<sup>-1</sup>) under upwelling conditions. The average daily flux for upwelling for the Lüderitz and Walvis Bay upwelling cells was 2.5 Gmol day<sup>-1</sup> (30.0 Gg-C day<sup>-1</sup>). That the flux from the Lüderitz and Walvis Bay area is so much greater (on a per area basis) is a reflection both of the higher wind speeds and the more remineralized character of the South Atlantic Central Water that upwells at Lüderitz.

Using inverse methods, Gruber et al. [2001] constrained the net flux of oxygen for the temperate South Atlantic (an area of 1.5 × 10<sup>7</sup> km<sup>2</sup>) to be 15.5 Tmol yr<sup>-1</sup> (10.8 if the global budget is closed), which, if correct, would indicate that upwelling events in the Lüderitz region (-1.4 ± 0.2 Tmol yr<sup>-1</sup>) are regionally significant.

Finally, the yearly sea-air flux of CO associated with upwelling events has been estimated to be 0.6 Gmol yr<sup>-1</sup> (7.2 Gg-C yr<sup>-1</sup>). The total annual source of CO from this region is surely larger, since, while CDOM concentrations are supplemented by upwelling, the photodegradation of dissolved organic matter would not be restricted to upwelling conditions. On the other hand, productivity in the area of Lüderitz is lower than the rest of the Benguela [Demarcq et al., 2007, Hutchings et al., 2009], anomalies in the atmospheric CO record were only observed during upwelling events, and the diurnal variability of this species was quite low; if production of CO was high during non-upwelling conditions, this would be manifest in a peak associated with the sea breeze. For context, the Mauritanian upwelling region emits ca. 1.4 Gmol yr<sup>-1</sup> (17 Gg-C yr<sup>-1</sup>) to the atmosphere [Kitidis et al., 2011]. While the ocean source of carbon monoxide is not terribly important to the global budget, it is quite uncertain, likely between 308–4,163 Gmol yr<sup>-1</sup> (3.7–50 Tg-C yr<sup>-1</sup>) [Bates et al., 1995, Stubbins et al., 2006].

### 6.3.7 Stoichiometry

Correlation slopes of atmospheric species can provide further confidence and insight into source processes, if there is an underlying biogeochemical relationship. The well-known inverse relationship between N<sub>2</sub>O and O<sub>2</sub> in the ocean, for instance, is a result of organic matter decomposition and nitrification [Cohen and Gordon, 1979, Frame et al., 2014, Naqvi et al., 2010, Nevison et al., 2003]. The tight coupling between N<sub>2</sub>O and O<sub>2</sub> seen in surface concentrations during M99 is preserved during air-sea gas exchange, as these gases behave similarly (Figure 6.4 and Figure 6.5). That the stoichiometric ratio is the same for atmospheric anomalies attributed to upwelling events, for their estimated flux densities, the shipboard measurements of air-sea flux densities during M99, and for surface water concentrations, is consistent evidence that observations at NDAO are directly influenced by ventilation signals from the Benguela, and highlights the importance of the OMZ as a hotspot of N<sub>2</sub>O release. The approximate molar ratio of the ventilation flux, -1 × 10<sup>-4</sup> (N<sub>2</sub>O:O<sub>2</sub>; mol mol<sup>-1</sup>), is the

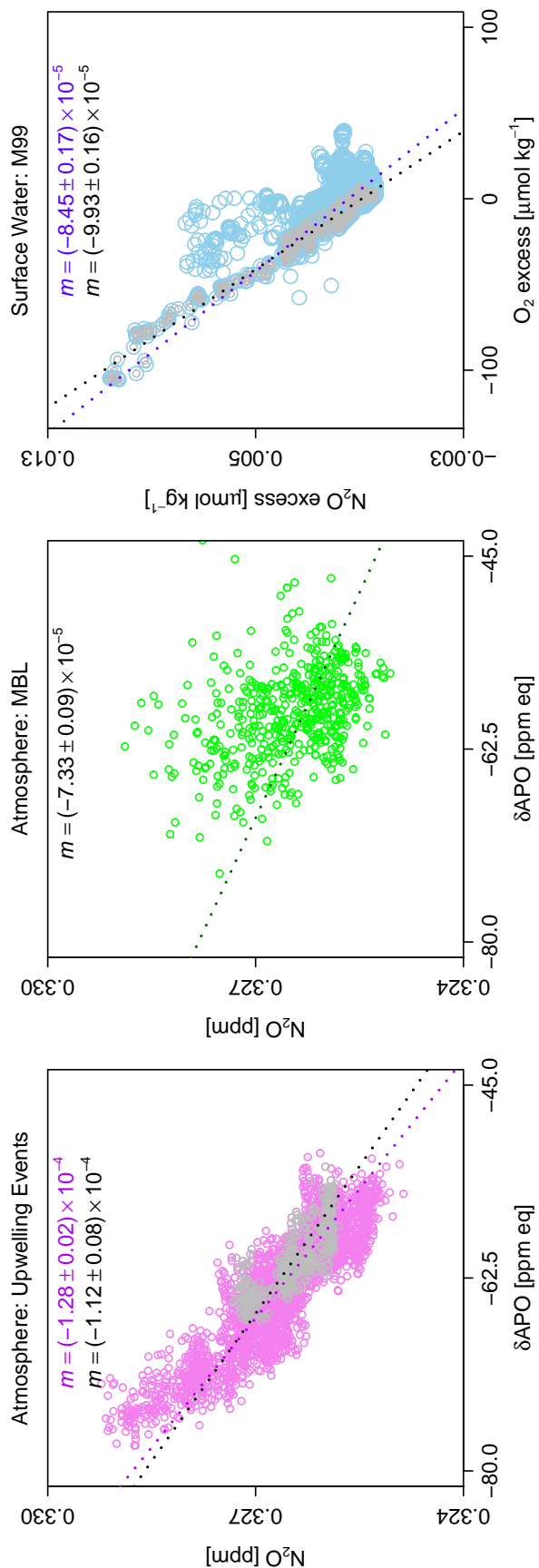


Figure 6.5: Comparison of the variability of  $\text{O}_2$  with respect to  $\text{N}_2\text{O}$  at NDAO and in surface water. Displayed are the data corresponding to atmospheric anomalies associated with upwelling events (*left*), of all marine boundary layer air masses as selected by back-trajectories (*center*), and dissolved concentrations of  $\text{N}_2\text{O}$  and  $\text{O}_2$  during M99 (*right*). Atmospheric  $\text{O}_2$  is expressed as APO in ppm equivalents, and dissolved concentrations are expressed as the difference between the measured concentration and the concentration at saturation, i.e., an excess. Slopes ( $m$ ) are given at the top of each plot.

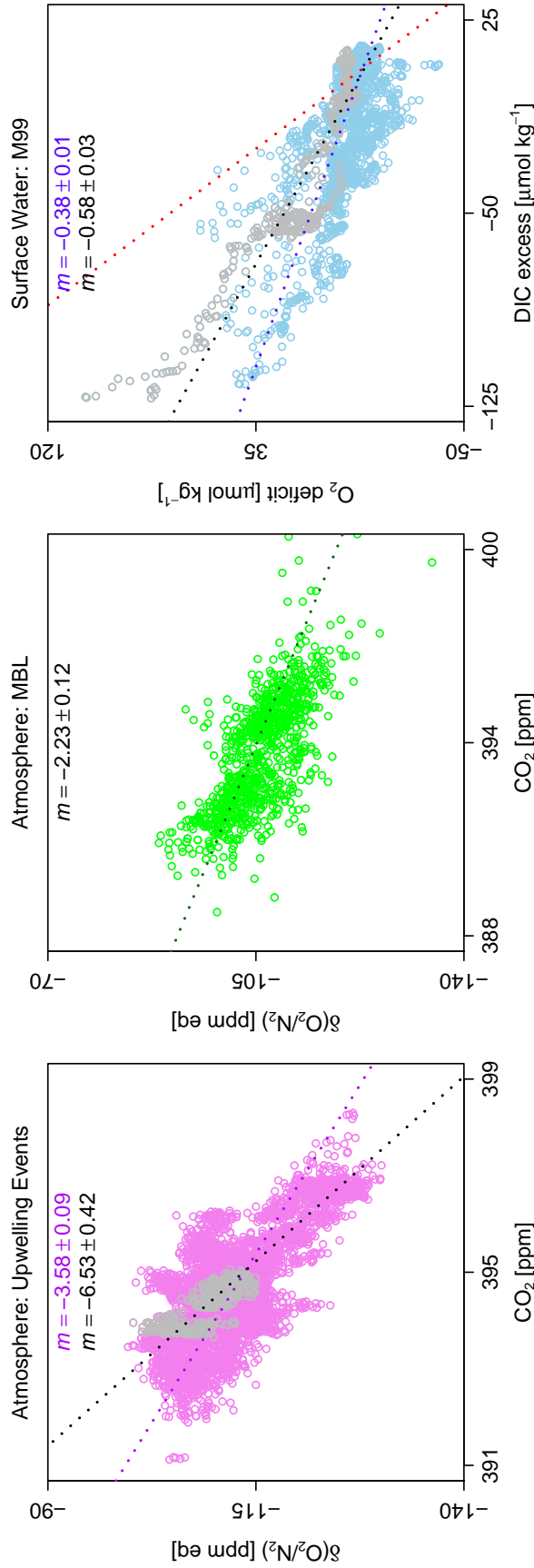


Figure 6.6: Comparison of the variability of CO<sub>2</sub> with respect to O<sub>2</sub> at NDAO and in surface water. Displayed are the data corresponding to atmospheric anomalies associated with upwelling events (*left*), of all marine boundary layer air masses as selected by back-trajectories (*center*), and dissolved concentrations of CO<sub>2</sub> and O<sub>2</sub> during M99 (*right*). Atmospheric O<sub>2</sub> is expressed in ppm equivalents, and dissolved concentrations are expressed as the difference between the measured concentration and the concentration at saturation, i.e., an excess, in the case of CO<sub>2</sub>, and as a deficit in the case of O<sub>2</sub>. Dissolved concentrations of CO<sub>2</sub> are expressed in terms of the total dissolved inorganic carbon (DIC) concentration. In this plot, the Redfield ratio of 1.45 is plotted as a dotted red line for reference. Slopes ( $m$ ) are given at the top of each plot.

same observed by Lueker et al. [2003] for the Trinidad Head region, and appears to be a globally consistent value [Manizza et al., 2012, Nevison et al., 2005].

This linear regression slope is often expressed in terms of the excess  $\text{N}_2\text{O}$  (measured  $\text{N}_2\text{O}$  minus  $\text{N}_2\text{O}$  at saturation) and apparent oxygen utilization (saturation minus observed),  $\Delta\text{N}_2\text{O}$ -AOU in  $\text{nmol } \mu\text{mol}^{-1}$ . Quantified in this way, it has been used as an estimate of the yield of  $\text{N}_2\text{O}$  as a function of the amount of oxygen consumed [Nevison et al., 2003]. However, the relationship is not strictly linear, since  $\text{N}_2\text{O}$  production is enhanced at low oxygen levels [Naqvi et al., 2010, Nevison et al., 2003].  $\Delta\text{N}_2\text{O}$ -AOU is also sensitive to mixing, as  $\text{N}_2\text{O}$  production rates vary widely in the ocean, meaning that the mixing of water masses with different compositions can overwhelm the in situ production signal [Nevison et al., 2003, Suntharalingam and Sarmiento, 2000]. The  $\Delta\text{N}_2\text{O}$ -AOU for M99 was  $0.088 \pm 0.003 \text{ nmol } \mu\text{mol}^{-1}$ , with an intercept of  $1.6 \pm 0.04 \text{ nmol}$ , and an  $R^2$  of 0.69. This is a low value, nearly identical to results from the eastern basin of the sub-tropical North Atlantic, where South Atlantic Central Water is found [Cohen and Gordon, 1979, Suntharalingam and Sarmiento, 2000, Walter et al., 2006], and low compared to the Tropical Atlantic ( $> 0.2$ ) [Oudot et al., 2002]. Most of the  $\text{N}_2\text{O}$  in the Benguela is produced in the water column and in the sediment by nitrifier denitrification [Frame et al., 2014]; annamox is the dominant nitrogen removal process in the low-oxygen areas, which produces less  $\text{N}_2\text{O}$  than denitrification [Kartal et al., 2007, Kuypers et al., 2005]. Modeling studies and observations suggest that a substantial portion of the  $\text{N}_2\text{O}$  that is produced in the sediment, or in the water column below the mixed layer, remains at depth (concentration maximum at 200–400 m) and is advected away from the region, without the chance for atmospheric release [Frame et al., 2014, Gutknecht et al., 2013a,b]. Hence, the low  $\Delta\text{N}_2\text{O}$ -AOU value found for the *Meteor* cruise probably reflects both physical and biogeochemical dynamics.

In the case of variations of  $\text{O}_2$  and  $\text{CO}_2$ , the stoichiometry of surface waters is not preserved after air-sea exchange, as the majority of carbon is speciated in the carbonate system, and only the portion that remains as dissolved  $\text{CO}_2$  is available for air-sea gas exchange. This leads to a change in the molar exchange ratio ( $\Delta\text{O}_2/\Delta\text{CO}_2$  on a mol/mol basis), for instance, from  $0.58 \pm 0.03$  in surface waters to  $-6.53 \pm 0.42$  in the atmosphere, for the upwelling event encountered by the *Meteor* (Figure 6.6). For reference, marine boundary layer air that has not been affected by upwelling shows an average exchange ratio of  $-2.23 \pm 0.12$ . These two species can become decoupled through the influences of changing solubility, which would drive evasion of both gases, and net biological production, which would drive evasion of  $\text{O}_2$  and invasion of  $\text{CO}_2$ . These complicating influences are the likely reason for the poorer correlation seen between these two species when compared with  $\text{N}_2\text{O}$  and  $\text{O}_2$ .

Interestingly, methane was not well-correlated with either APO or  $\text{CO}_2$  in the atmosphere during all upwelling events, suggesting a spatial decoupling (since a cross-correlation analysis indicated this was not a result of lag/temporal decoupling) between methane and these two species (Figure 6.7). While background observations of  $\text{CH}_4$  were generally well-correlated with  $\text{CO}_2$  and  $\text{O}_2$  at NDAO, only some upwelling events showed such coupling; it seems there is a general relationship between methane and oxygen, but it is not consistent and is occasionally non-existent. Unfortunately, since there are still very few measurements of water-column  $\text{CH}_4$  in the Benguela, a full explanation of the methane source remains elusive. From these atmospheric trends it can only be deduced that there is some separate biogeochemical influence on methane that is not exerted over  $\text{CO}_2$ ,  $\text{O}_2$ , or  $\text{N}_2\text{O}$ . This observation is arguably consistent with the concept of a dominant sedimentary source of methane that is more localized within the inshore mud belt, where high POC fluxes have created a thick layer of diatomaceous ooze containing free methane gas pockets [Brüchert et al., 2006, 2009, Emeis et al., 2004, van der Plas et al., 2007].

Finally, it is noted that the  $\Delta\text{CH}_4/\Delta\text{CO}$  (ppb ppb $^{-1}$ ) of  $1.7 \pm 0.05$  is much greater than



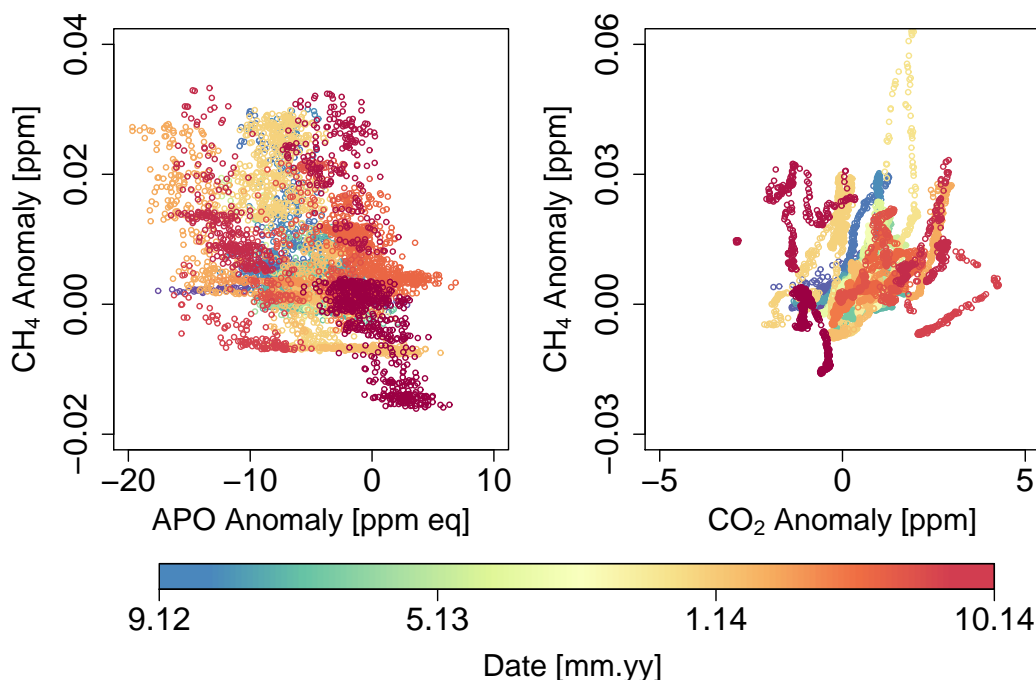


Figure 6.7: Comparison of the variability of  $O_2$  and  $CO_2$  with respect to  $CH_4$  at NDAO during upwelling events, colored by date to separate specific events. Anomalies are calculated against a harmonic fit to the background.

emission ratios seen for combustion processes (see Section 5.3.3), which gives further evidence that the CO atmospheric anomalies detected following upwelling events are marine in origin and attributable to in situ production.

#### 6.4 Summary and Conclusions

It has been shown that atmospheric anomalies of  $CO_2$ ,  $CH_4$ ,  $N_2O$ , CO, and  $O_2$  can be related to upwelling events in the Lüderitz and Walvis Bay cells. A simple model has allowed these fluxes to be constrained within the limitations of its assumptions. These top-down estimates of surface fluxes have been validated with in situ surface fluxes determined from shipboard measurements. Observations at NDAO provide the opportunity to capture these episodic and short-lived events that cannot be seen without continuous monitoring.

The Lüderitz and Walvis Bay upwelling cells have been shown to be an unusually large source of methane to the atmosphere for the marine environment. In contrast, the region is a weaker source of  $N_2O$ , compared to other upwelling regions, a fact which has been predicted from modeling studies and noted in observations of dissolved concentrations and air-sea fluxes. This upwelling area also functions as a minor source of CO to the atmosphere, and is a significant source term in the  $CO_2$  budget of the Benguela Current.

Trends in the intensity or duration of coastal upwelling can be difficult to assess, as the results can be sensitive to region selection or use of proxies which may be affected by other factors (SST, wind speeds, wind stress, etc.). Decadal or interdecadal variability can also be substantial. There is some evidence to show that upwelling at Lüderitz or in the northern Benguela has declined [Hutchings et al., 2009, Monteiro et al., 2008, Peard, 2007]. Yet, other research has shown that the duration and intensity of coastal upwelling in the Benguela in general is likely increasing and will continue to increase with climatic change in the coming

decades, driven by an increasing land–sea temperature gradient [Bakun, 1990, Demarcq, 2009, Narayan et al., 2010, Santos et al., 2012, Sydeman et al., 2014, Wang et al., 2015]. Meanwhile, warming trends in the broader Benguela region can already be detected [Monteiro et al., 2008, Santos et al., 2012]. Whatever the result, it is clear from the present study that coastal upwelling events near Lüderitz and Walvis Bay result in a large net invasion of  $O_2$  and regionally significant emissions of the major greenhouse gases.

# 7

## Summary and Outlook

### 7.1 Summary

Two years of continuous atmospheric measurements of  $\text{CO}_2$ ,  $\text{CH}_4$ ,  $\text{N}_2\text{O}$ ,  $\text{CO}$ , and  $\delta(\text{O}_2/\text{N}_2)$  at a new background site in the central Namib Desert have been presented and analyzed. The station, located at Gobabeb, in the Erongo Region of Namibia, is a remote site with minimal local infrastructure. As such, the measurement system used to make these observations was designed to require as little maintenance and operator intervention as possible.

Carbon dioxide and methane were measured with cavity ring-down spectroscopy (CRDS), nitrous oxide and carbon monoxide with off-axis integrated cavity output spectroscopy (OA-ICOS), and atmospheric oxygen with a differential fuel cell analyzer (DFCA). The DFCA instrument met quality criteria goals when adequate electricity demands and temperature control were present; performance suffered during a period of frequent power outages. The CRDS performed quite well and yielded stable, accurate measurements, as assessed with target tank measurements and other tests, even with a relatively long interval between calibrations. The OA-ICOS was determined to be quite a precise instrument, but subject to temperature-related drift. This was corrected with frequent measurements of a working tank. Neither of the sample air streams were dried prior to measurement with the OA-ICOS or CRDS instruments; instead, a second-order water correction function was applied.

The representivity of NDAO as a measurement point was assessed using a ca. 20-year, multi-species flask sampling record from the NOAA network (site code NMB). While growth rates were similar between the NMB data and other marine background reference sites at a similar latitude, the seasonal climatologies constructed from this record showed consistent differences in phasing and amplitude when compared to these other background locations. This was demonstrated to be a result of continental influence, which was expressed at NDAO primarily during austral winter, when the formation of anticyclonic conditions over southern Africa made the transport of air masses influenced by terrestrial surface fluxes to NDAO more likely. Conversely, during austral summer, strong equatorward winds brought marine boundary layer air to NDAO. This regular progression in atmospheric transport was due to the meridional movement of the southern Hadley cell.

As a result of these atmospheric dynamics, NDAO was affected by biomass burning during austral winter. The influence of biomass burning was most notably manifest as large, positive anomalies of  $\text{CO}$  and  $\text{CH}_4$ , as well as smaller positive anomalies of  $\text{CO}_2$  and negative anomalies of  $\delta(\text{O}_2/\text{N}_2)$ . Two distinct pathways were identified that could bring polluted air to NDAO: anticyclonic surface trajectories, originating in eastern southern Africa and traveling westward to the Namib, and subsiding air masses, which brought biomass burning-influenced air masses from the African haze layer down to the surface. The stoichiometry of the major measurands, particularly that of  $\text{CO}$  to  $\text{CH}_4$  and  $\text{CO}_2$  to  $\text{O}_2$ , indicated that the source fires creating the emissions detected at NDAO occurred closer to Gobabeb throughout

the fire season. This was corroborated with data from the Global Fire Emissions Database (GFED).

During austral summer, however, little burning occurs in southern Africa, and the prevailing winds at Gobabeb are from the ocean. These winds, which blow equatorwards along the coast, are responsible for the upwelling of water along the Benguela current region. Upwelling events dominate the intraseasonal variability for  $\delta(\text{O}_2/\text{N}_2)$ , APO, and  $\text{N}_2\text{O}$  during austral summer. Since upwelling events occur only under certain atmospheric conditions, the duration of anomalies caused by upwelling is not more than a day or two, and sharp peaks in the atmospheric record only last several hours. Upwelling events at NDAO were carefully identified based on multiple criteria relating to sea surface temperature, surface winds over the ocean, local wind variability at NDAO, and back-trajectories from NDAO.

A simple Lagrangian model was employed to estimate the flux density necessary to create the atmospheric anomalies seen during upwelling events. Despite its simplifying assumptions, the model calculations agreed quite well with flux densities calculated from shipboard flux density determinations, which were based on underway measurements of bulk concentrations in surface water and in the atmosphere. This provided a measure of confidence in the modeling approach, and was the rationale for estimating the total mass flux from the Lüderitz and Walvis Bay upwelling cells on an annual basis, due to upwelling events. Upwelling from these two cells proved to be a significant source of  $\text{CO}_2$  to the atmosphere when compared to estimated budgets for the northern and southern Benguela upwelling systems. The Lüderitz and Walvis Bay upwelling cells were moderate sources of  $\text{N}_2\text{O}$  compared to other coastal upwelling regions, but a surprisingly large source of methane to the atmosphere. Based on previous research presented in the literature, it seems likely that this methane source is ultimately due to an unusually large sedimentary source in the shallow shelf waters surrounding Walvis Bay.

## 7.2 Outlook

Now that the basic phenomonolgy and representivity of the site has been described, it is clear that NDAO can provide background observations that contain valuable information about two major biogeochemical processes: biomass burning and coastal upwelling. This makes the station fairly unique, especially when one considers that it is almost entirely free of local influence, and is not directly impacted by anthropogenic emissions. Inverse modeling of the NDAO dataset could provide a better constraint on upwelling emissions than the simple approach adopted here. Use of the  $\text{CO}_2$  atmospheric record from NDAO could also inform on carbon cycling in southern Africa in such a modeling study. A successful inverse modeling effort would require a high-resolution regional transport model that could accurately simulate the unusual mesoscale phenomena that control much of the diurnal variability at Gobabeb<sup>1</sup>, or at least the NDAO data would need to be carefully selected. The station provides a valuable top-down perspective on the northern Benguela upwelling system, and it would be a shame not take advantage of it. Methane biogeochemistry in the Benguela, for instance, remains a rather intriguing subject, and there is plenty of scope for future work on this issue, particularly on sedimentary methane release and the infamous hydrogen sulfide “eruptions” seen in the region.

Likewise, inverse or forward modeling of biomass burning emissions could produce some valuable new constraints on the magnitude of emissions from southern Africa. The original selection of Gobabeb as a flask sampling site in the NOAA network was motivated by the

---

<sup>1</sup>Note that H<sub>ä</sub>nsler [2011] was able to represent the thermo-topographic local wind system at Gobabeb fairly well, using the REMO model.

hope that it would be influenced by southern African vegetation fires, and this has proven to be the case. NDAO is currently the only site in southern Africa that can make background measurements of greenhouse gases and atmospheric oxygen during the burning season. It should also be mentioned that aerosol measurements would be fairly easy to implement at the station, given that there already exists a sample line and filter apparatus for such work.

Africa is a very large and understudied continent; it is developing rapidly, and is expected to be hard-hit in future decades by climatic change. The inclusion of more stations in the fledgling African network would only improve our understanding of carbon cycling and surface-atmosphere fluxes of greenhouse gases in this region. Atmospheric time series like those produced at NDAO are a cornerstone of biogeochemistry, and their value only increases with the length of the record. To this end, I can only hope that the measurements at NDAO continue for many years to come.

# Appendices

# A

## Supplementary Figures

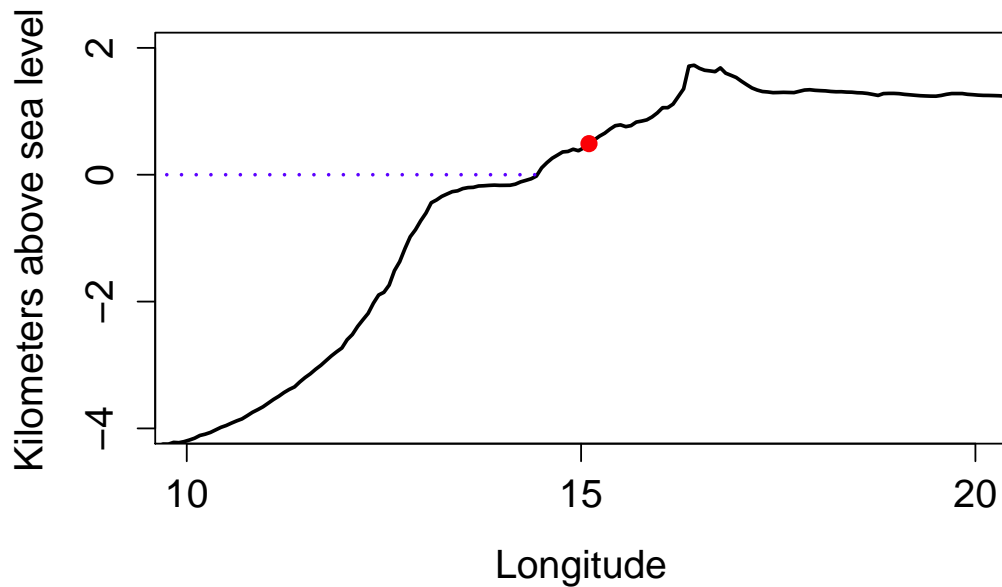


Figure A.1: Elevation along a longitudinal transect of southwestern Africa at the latitude of NDAO, showing the continental shelf and the western edge of the Great Escarpment. The location of NDAO is given by a red dot and sea level is indicated by a dotted blue line. Elevation data is from [Amante and Eakins \[2009\]](#).

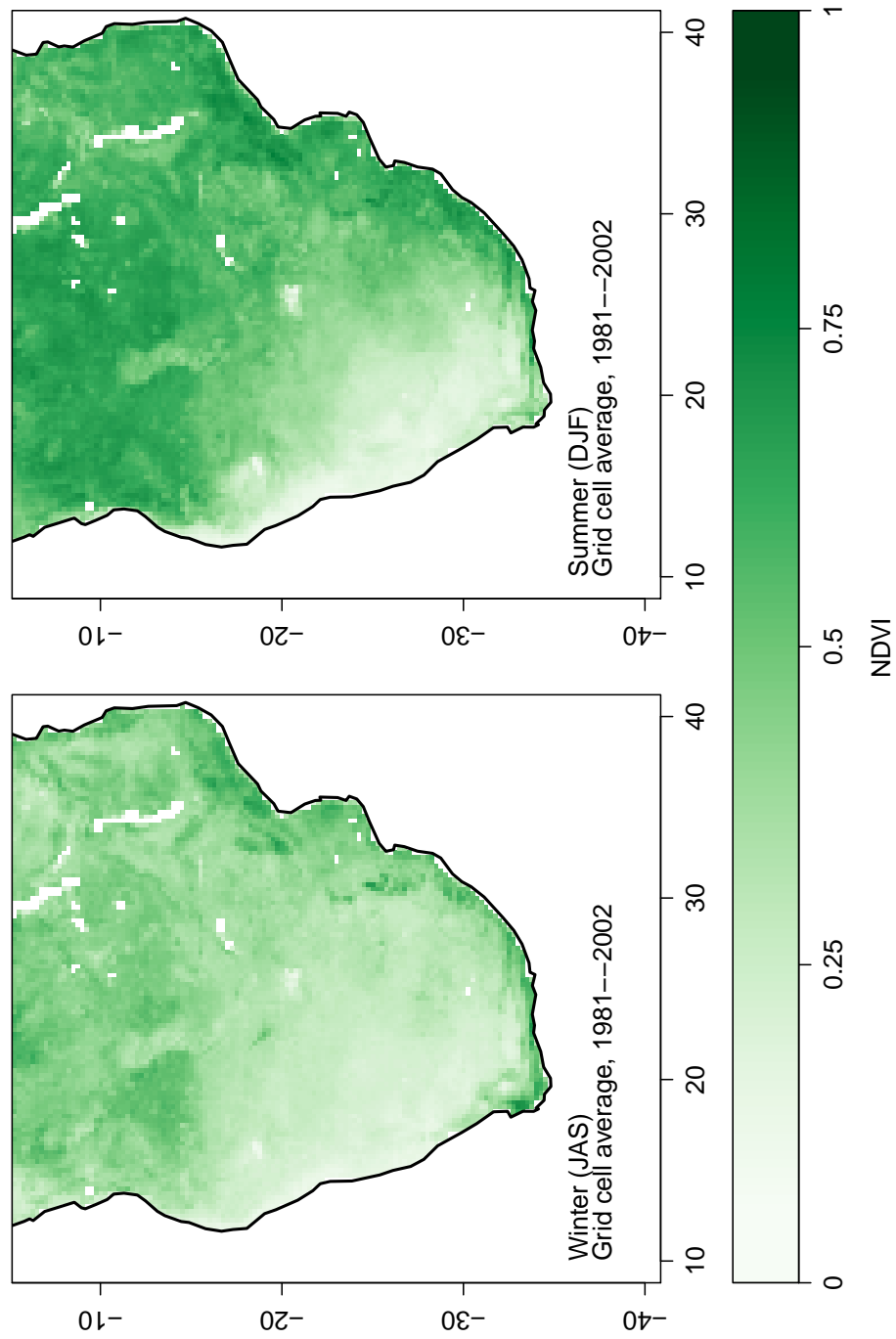


Figure A.2: The average Normalized Difference Vegetation Index (NDVI) for southern Africa, separated by season. Data from [Tucker et al. \[2010\]](#).



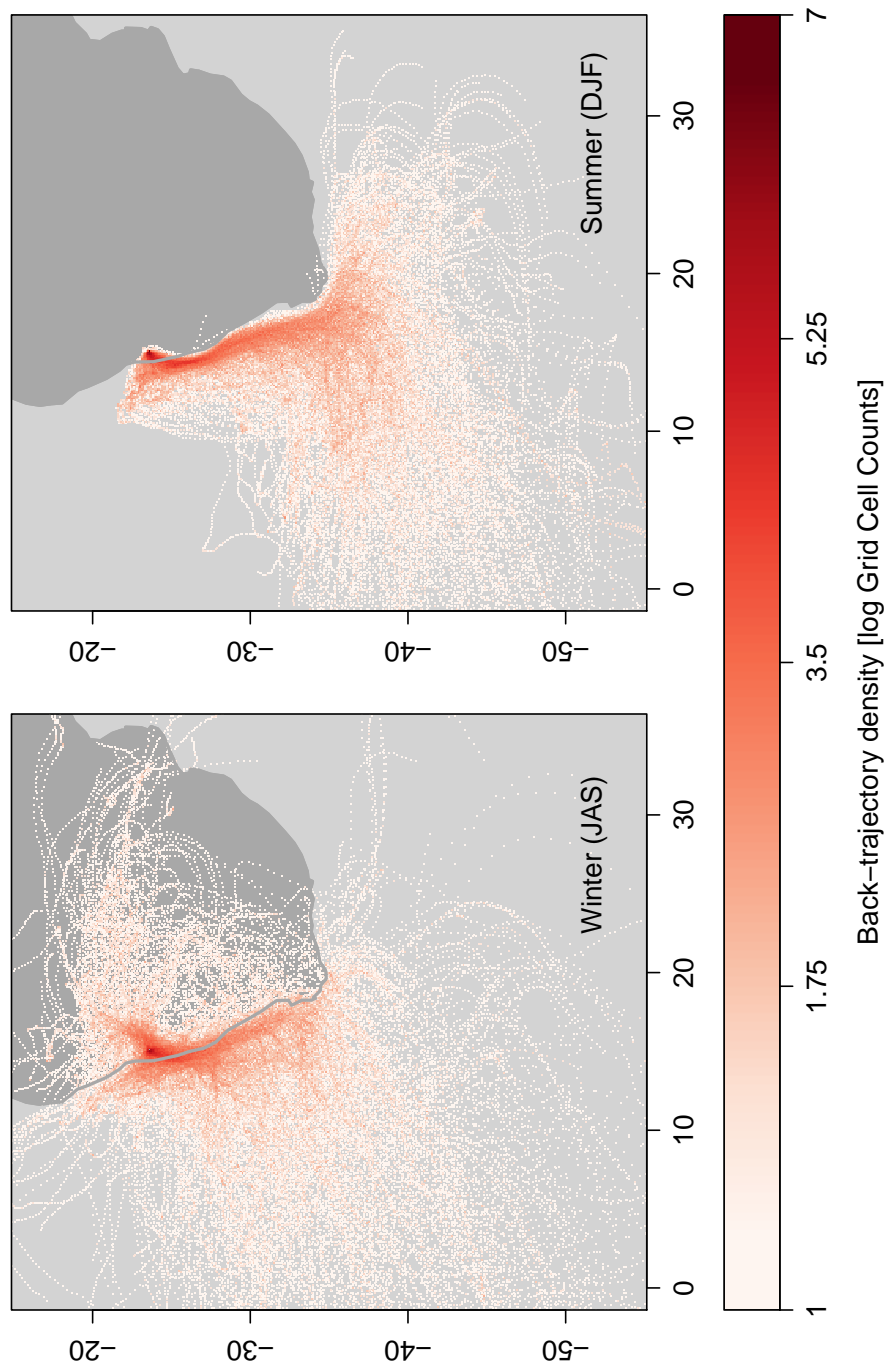


Figure A.3: Comparison of austral winter and summer HYSPLIT back-trajectories, for the period spanning October 2012 to October 2014. The color gradient shows the log of the number of trajectory points in each  $0.1^\circ$  grid cell.

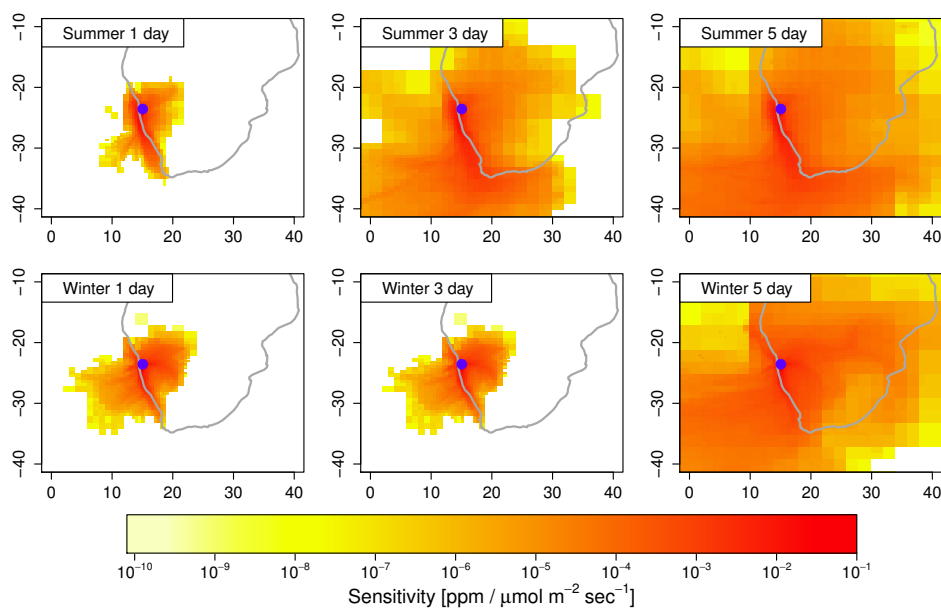


Figure A.4: Average integrated footprints for NDAO during 2012–2013, using the STILT model. Average austral summer (November–February) footprints are shown in the top row and average austral winter (June–September) footprints are shown in the bottom row, integrated over 1, 3, and 5 days. The pixel size increases in distance from NDAO due to the dynamic grid resolution of the model.

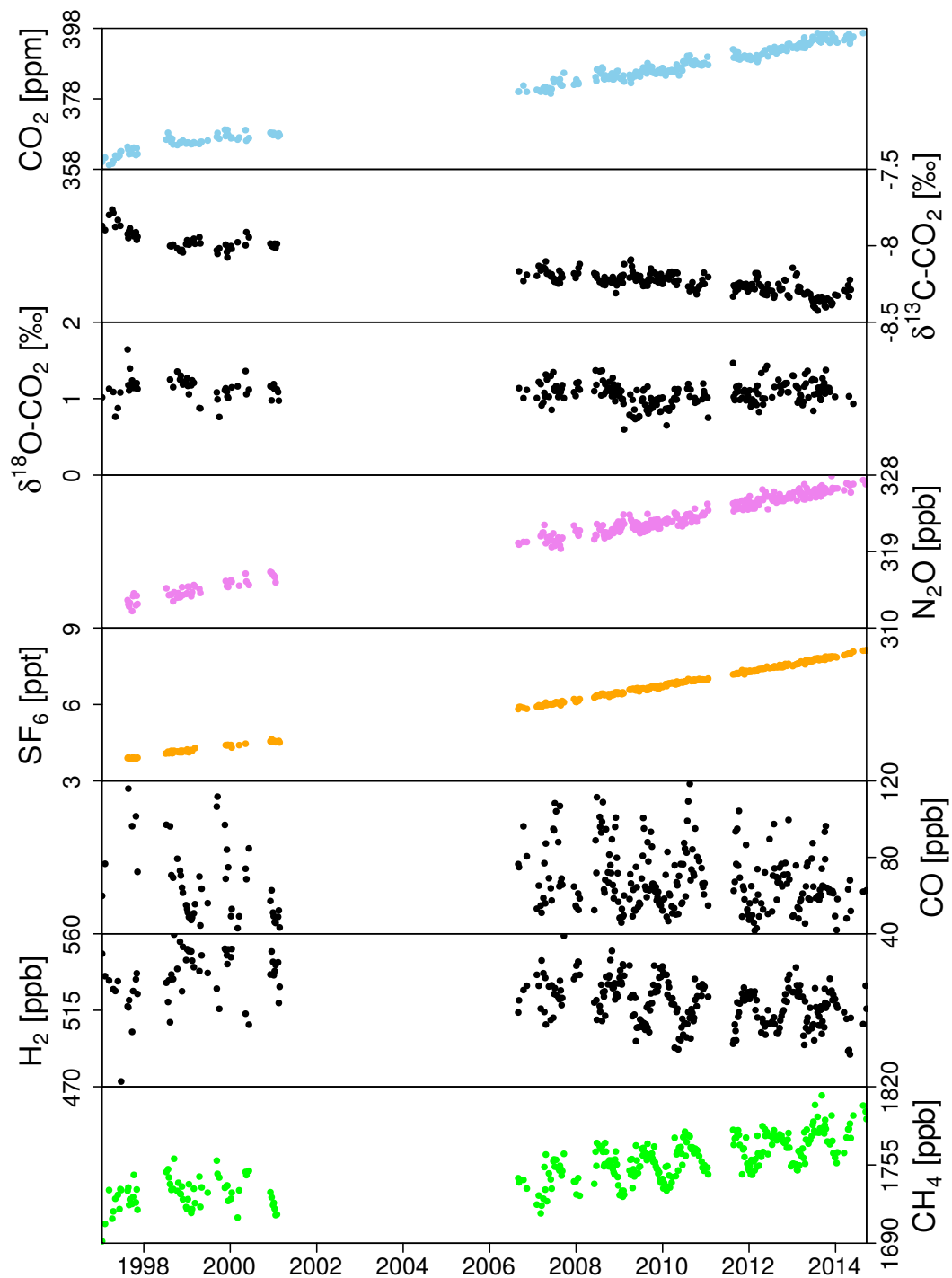


Figure A.5: Main time series of the NOAA ESRL GMD surface flask sampling site NMB, 1997–2014.

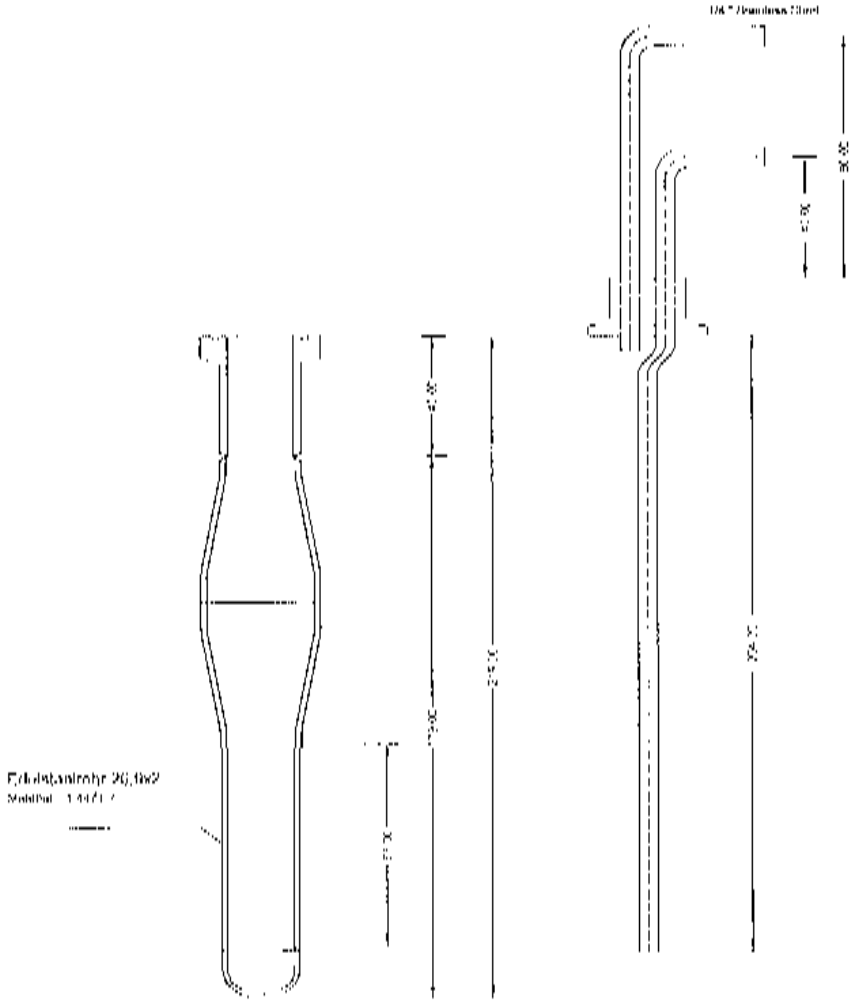


Figure A.6: Specifications of the large cryotrap used for drying the oxygen sample lines (Technical drawing by Uwe Schultz).

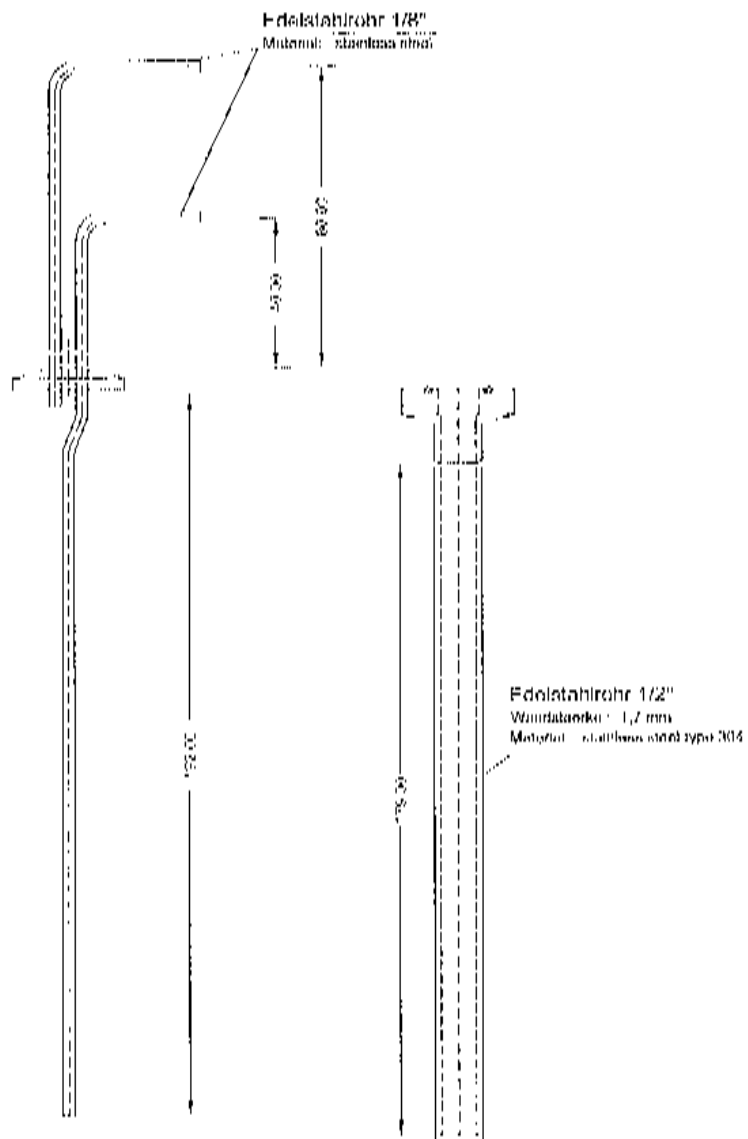


Figure A.7: Specifications of the small cryotrap used for drying the oxygen sample lines (Technical drawing by Uwe Schultz).

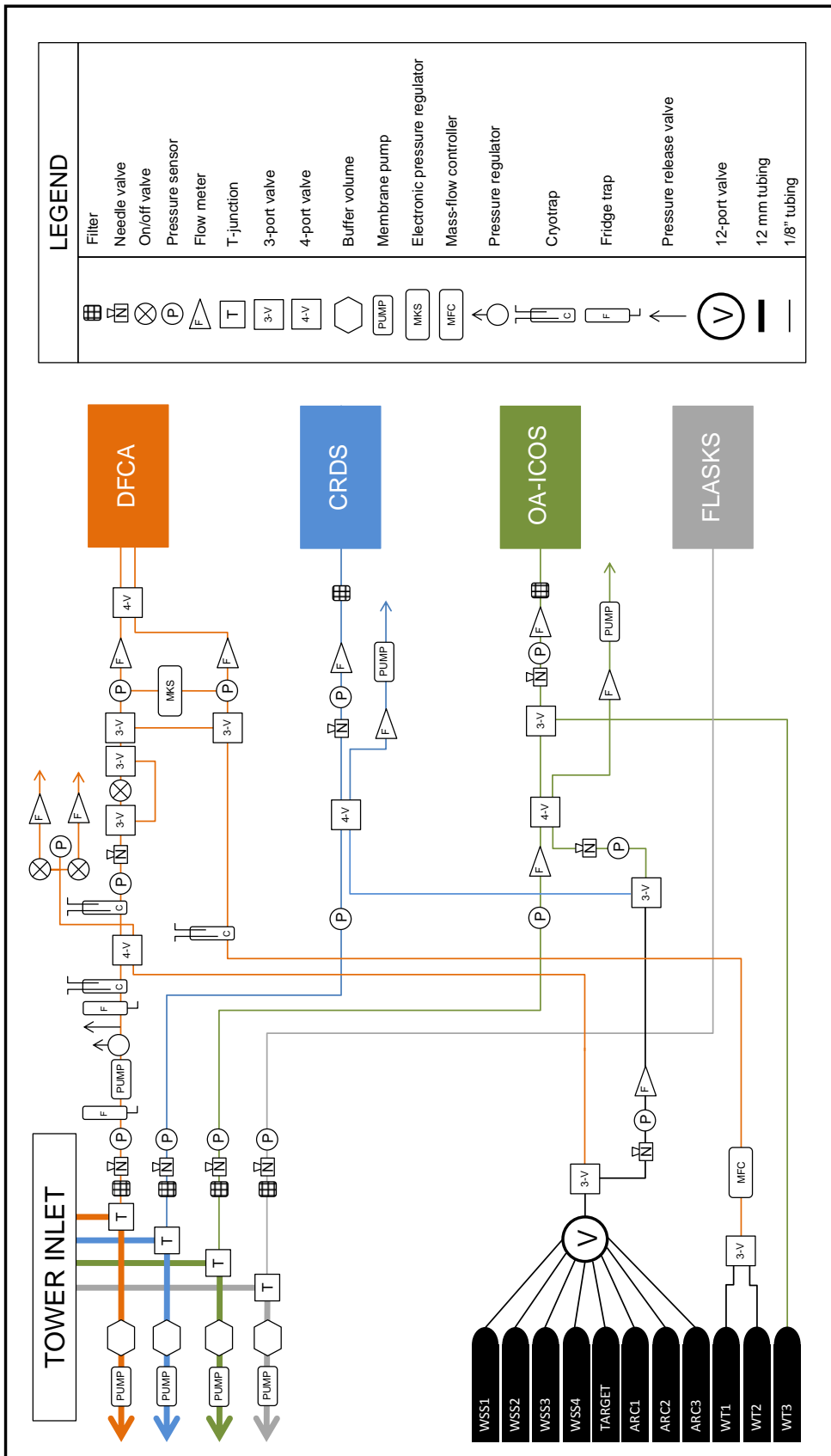


Figure A.8: Diagram of the measurement system.

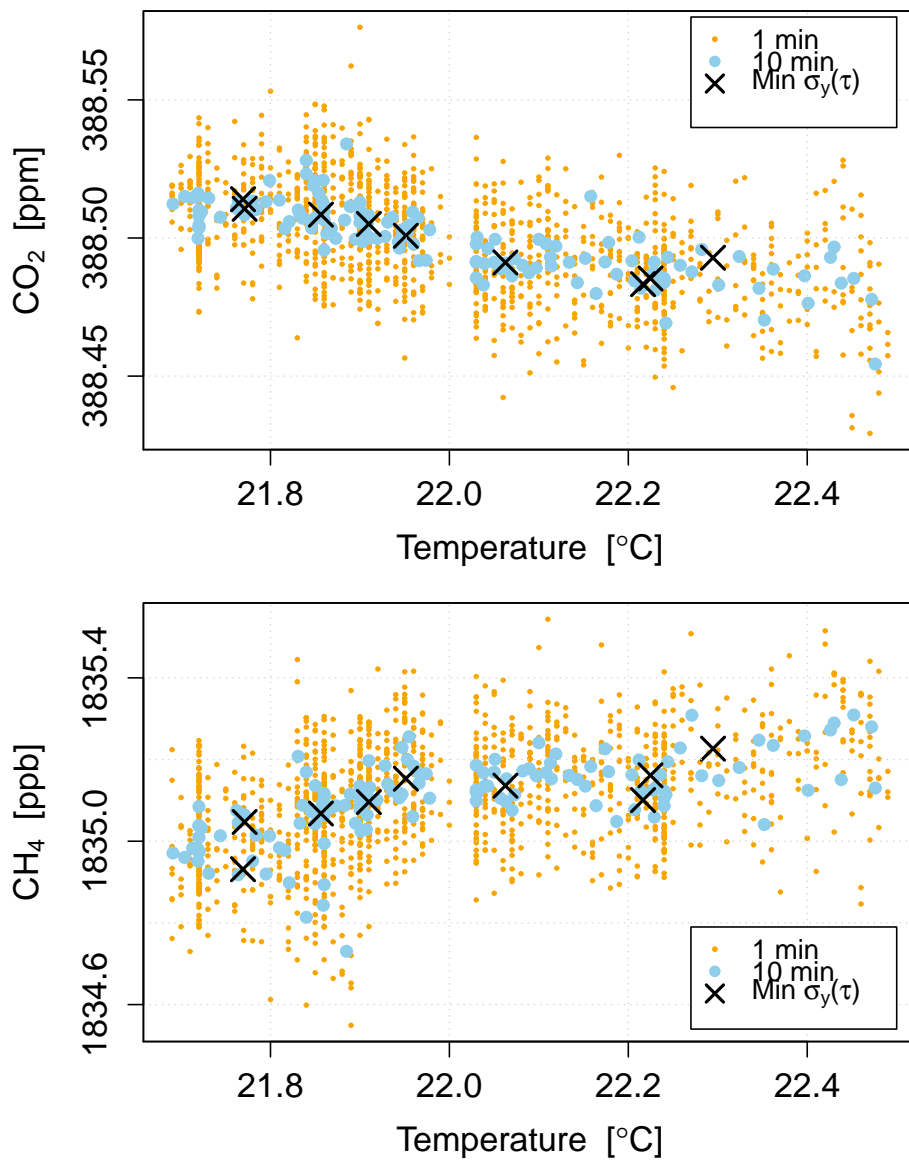


Figure A.9: Relationship between working tank temperature and CO<sub>2</sub> (*top panel*), and CH<sub>4</sub> (*bottom panel*)

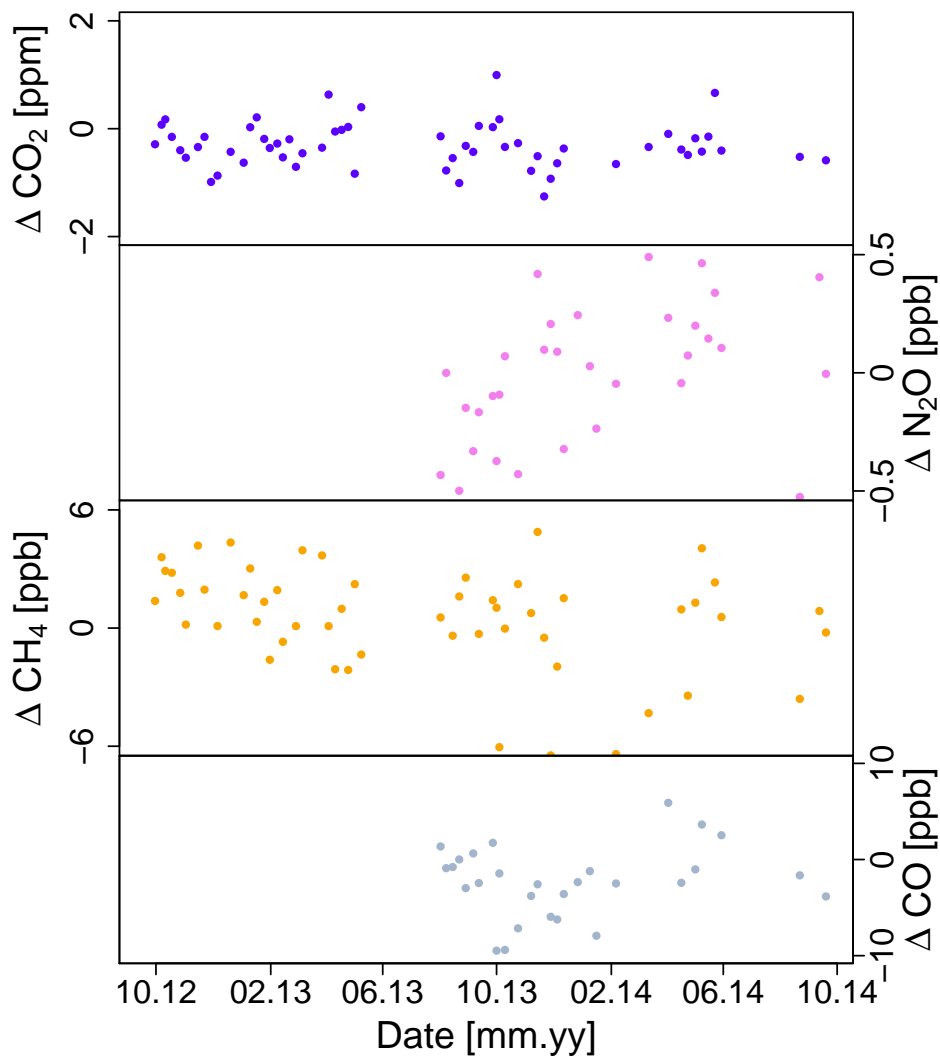


Figure A.10: Measurement compatibility of flask and in situ time series, plotted as difference between individual flasks and the in situ observations (flask - in situ).



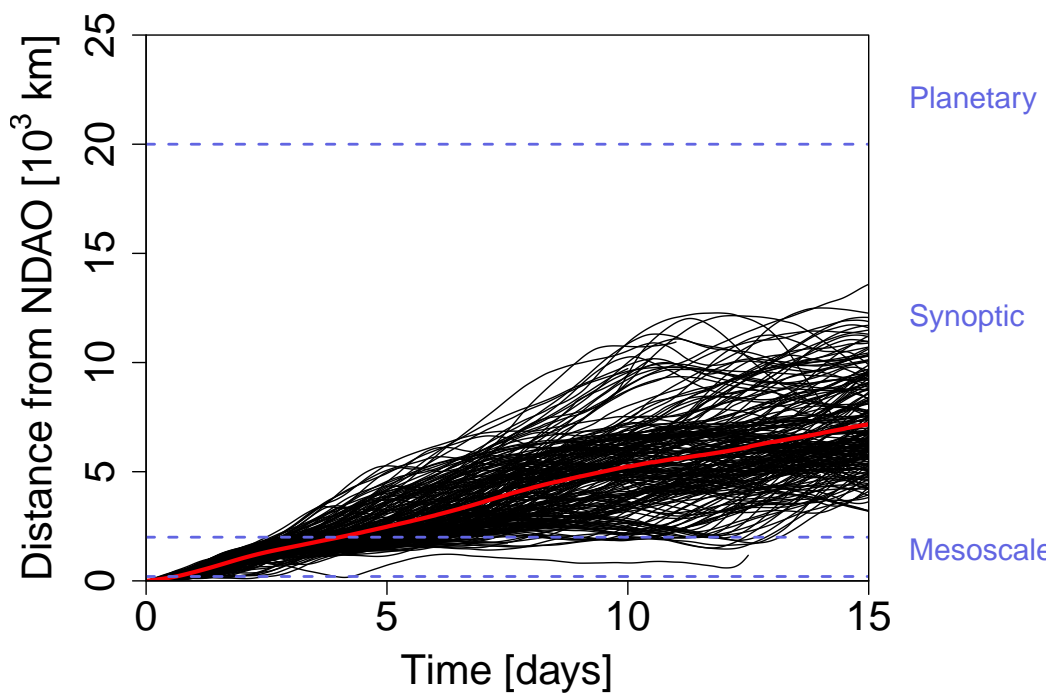


Figure A.11: Relationship between the temporal and spatial scale of atmospheric transport for the NDAO site. The dotted horizontal lines denote the approximate transitions between different horizontal spatial scales in the atmosphere. The red line is the average of all HYSPLIT back-trajectories, which are plotted as thin black lines. The x-axis is the time backwards from the receptor point, in days.

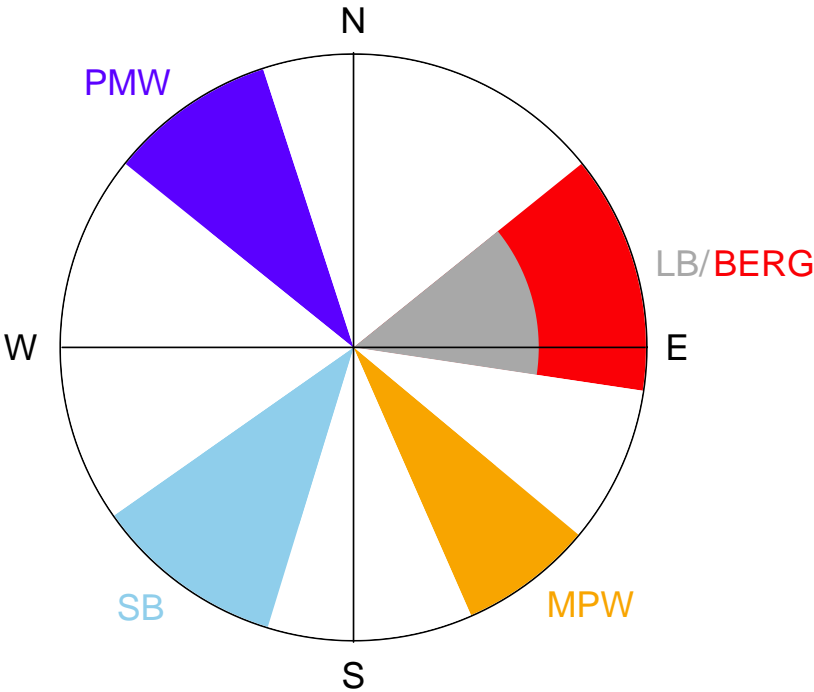


Figure A.12: Wind sectors visualized on a compass rose. LB stands for land breeze, BERG for bergwind, MPW for mountain-plain wind, SB for sea breeze, PMW for plain-mountain wind.

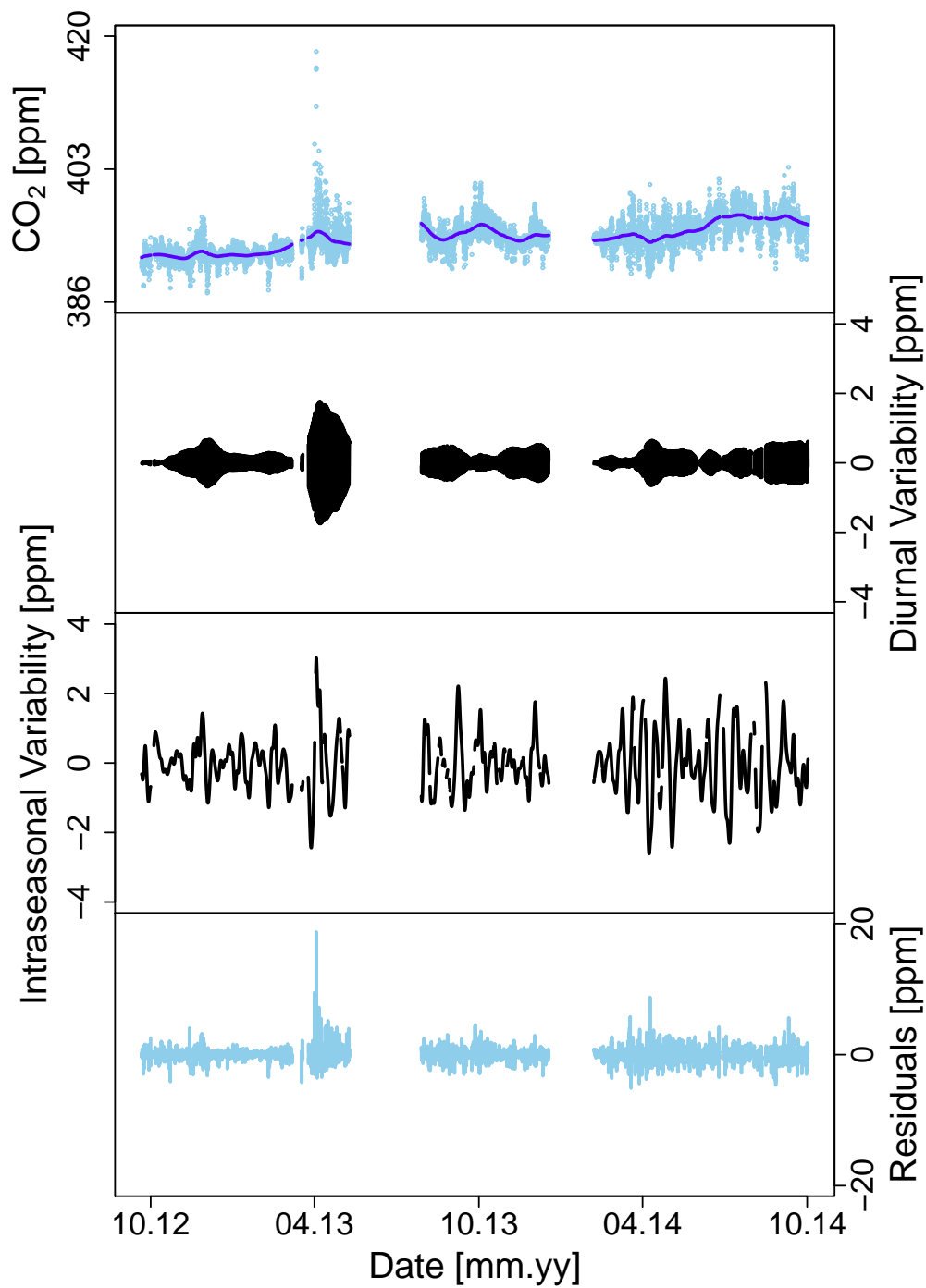


Figure A.13: Decomposed time series of CO<sub>2</sub>, showing the original time series, the diurnal cycle, synoptic variability, and residuals.

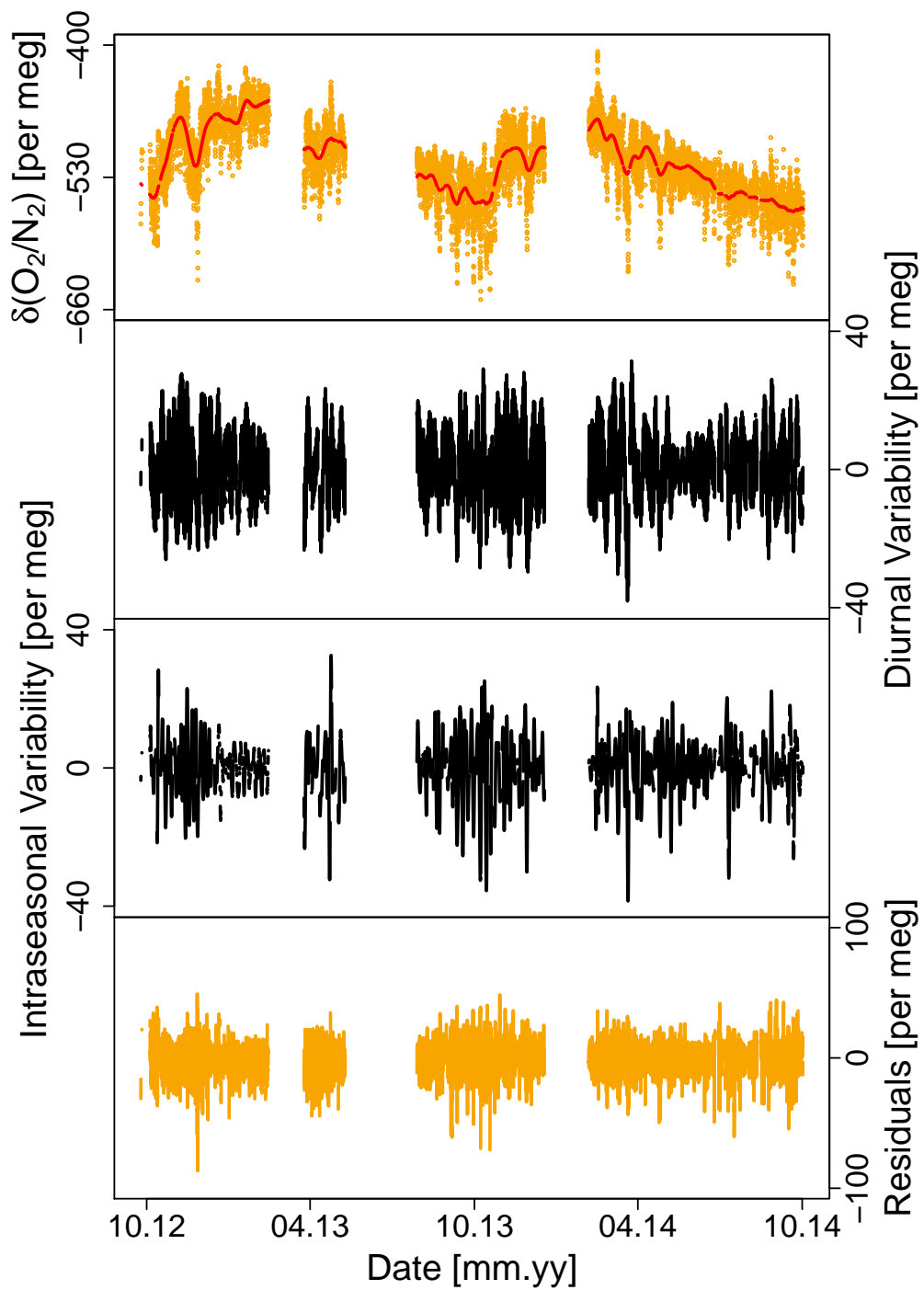


Figure A.14: Decomposed time series of  $\delta(\text{O}_2/\text{N}_2)$ , showing the original time series, the diurnal cycle, synoptic variability, and residuals.

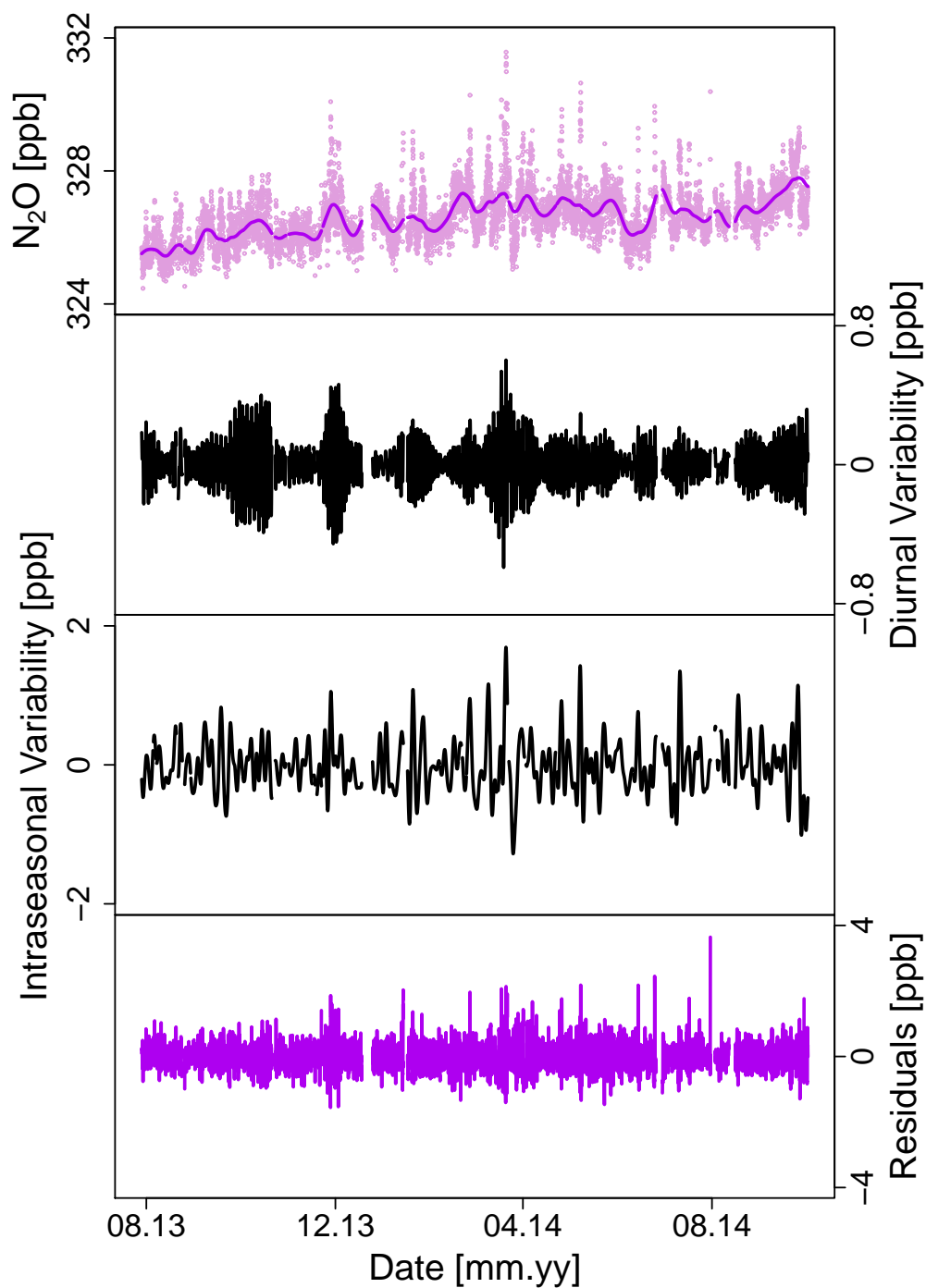


Figure A.15: Decomposed time series of N<sub>2</sub>O, showing the original time series, the diurnal cycle, synoptic variability, and residuals.

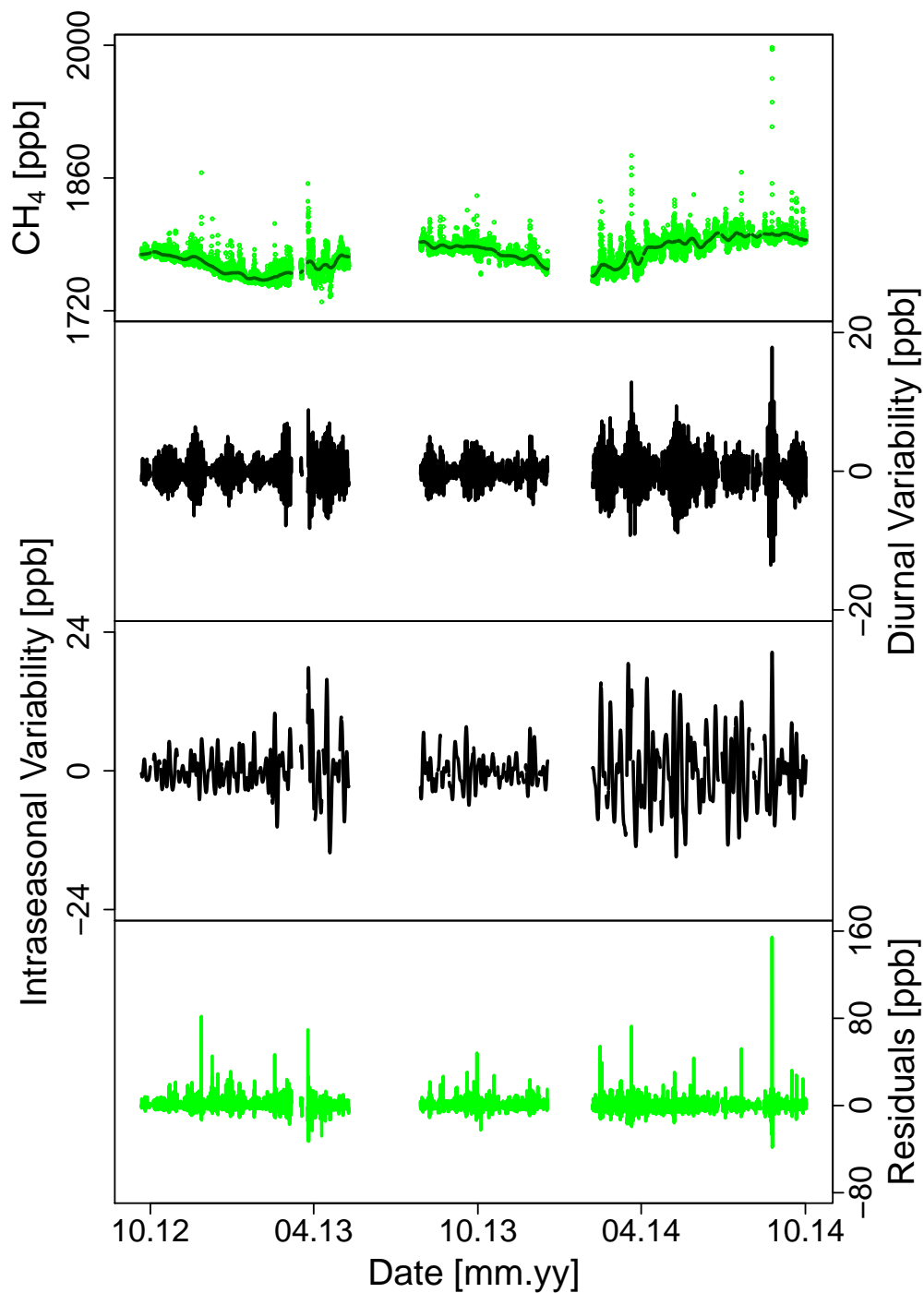


Figure A.16: Decomposed time series of CH<sub>4</sub>, showing the original time series, the diurnal cycle, synoptic variability, and residuals.

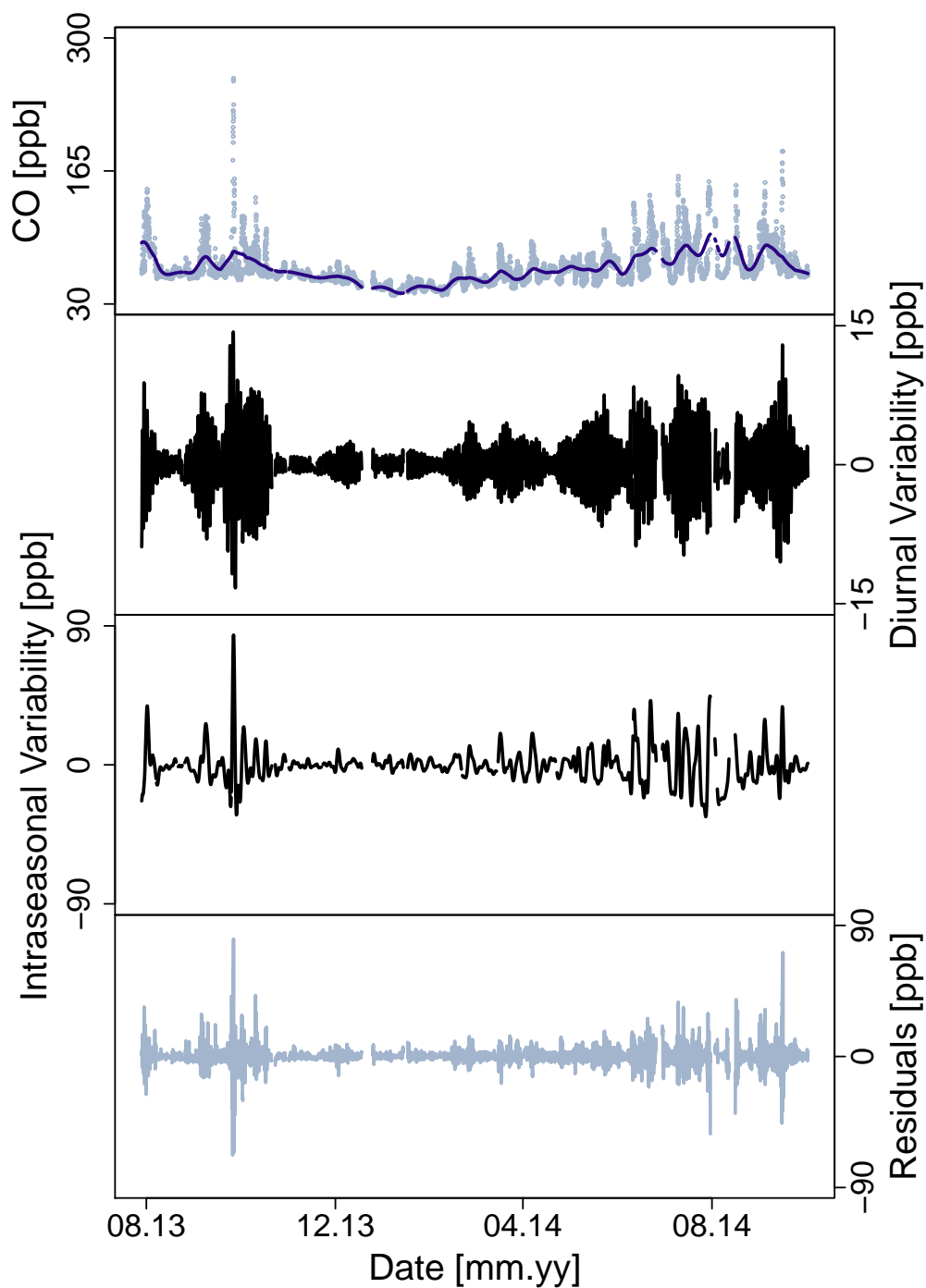


Figure A.17: Decomposed time series of CO, showing the original time series, the diurnal cycle, synoptic variability, and residuals.

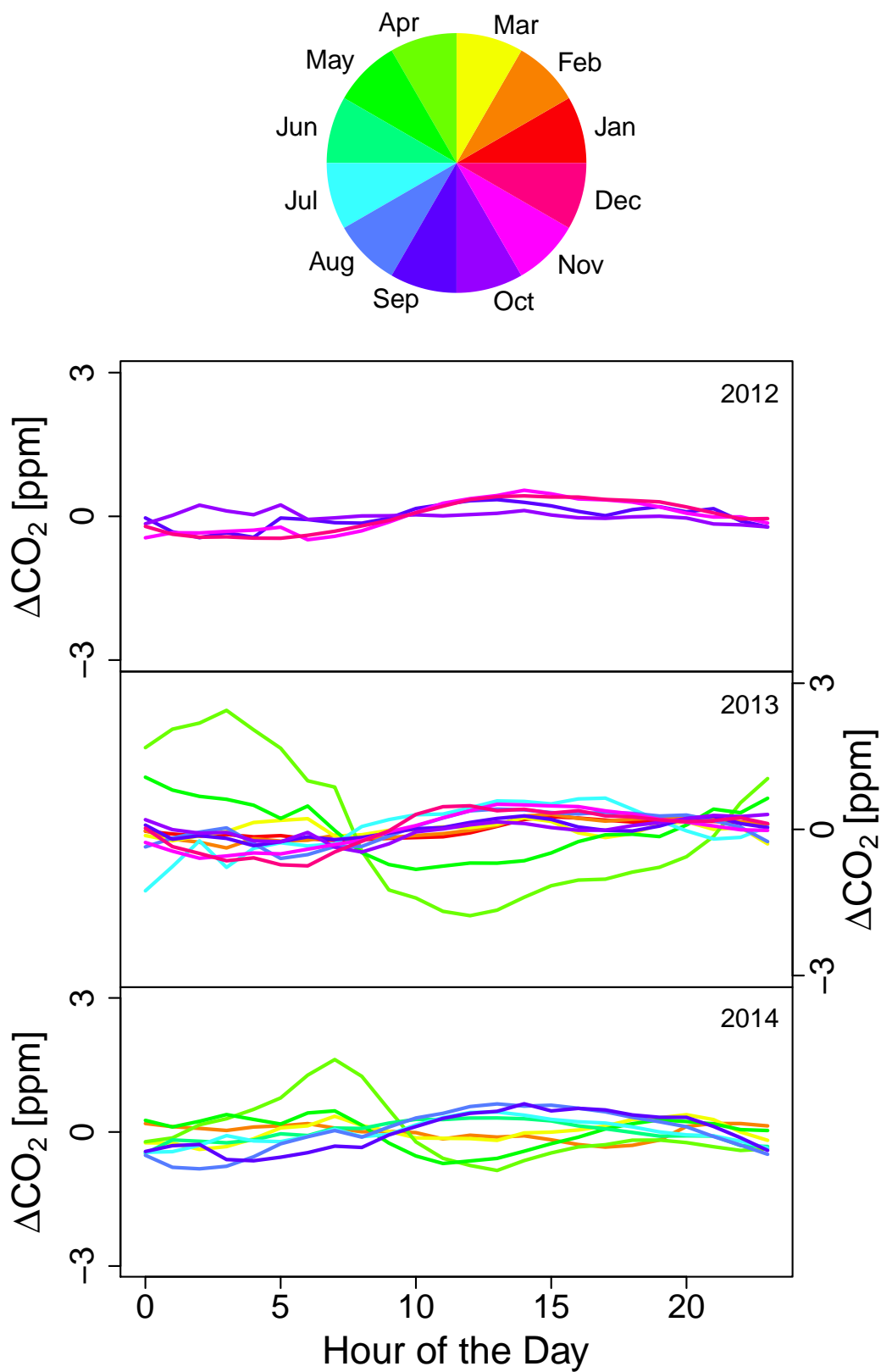


Figure A.18: The diurnal cycle of  $\text{CO}_2$ , averaged for each month.



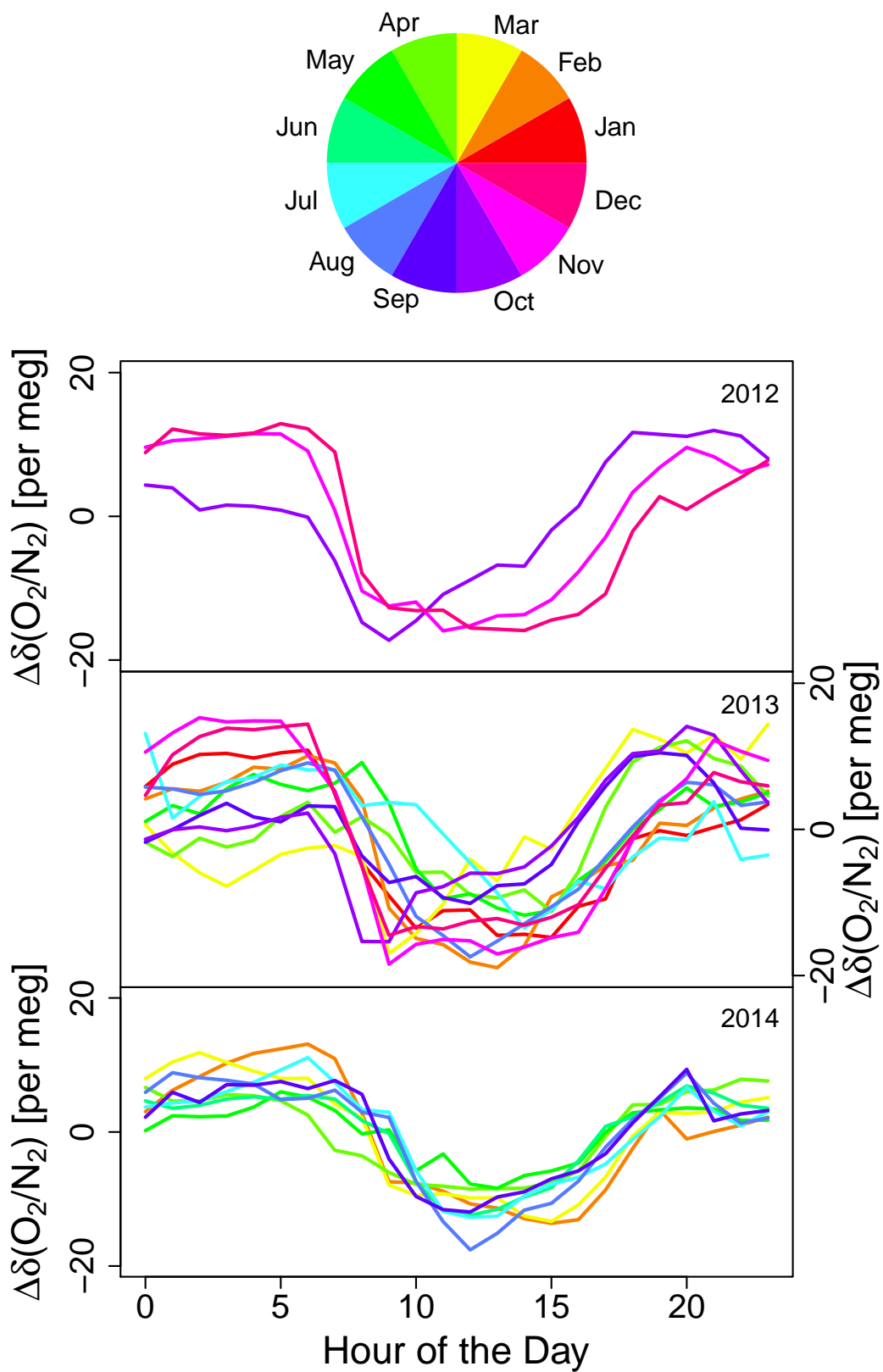


Figure A.19: The diurnal cycle of  $\delta(\text{O}_2/\text{N}_2)$ , averaged for each month.

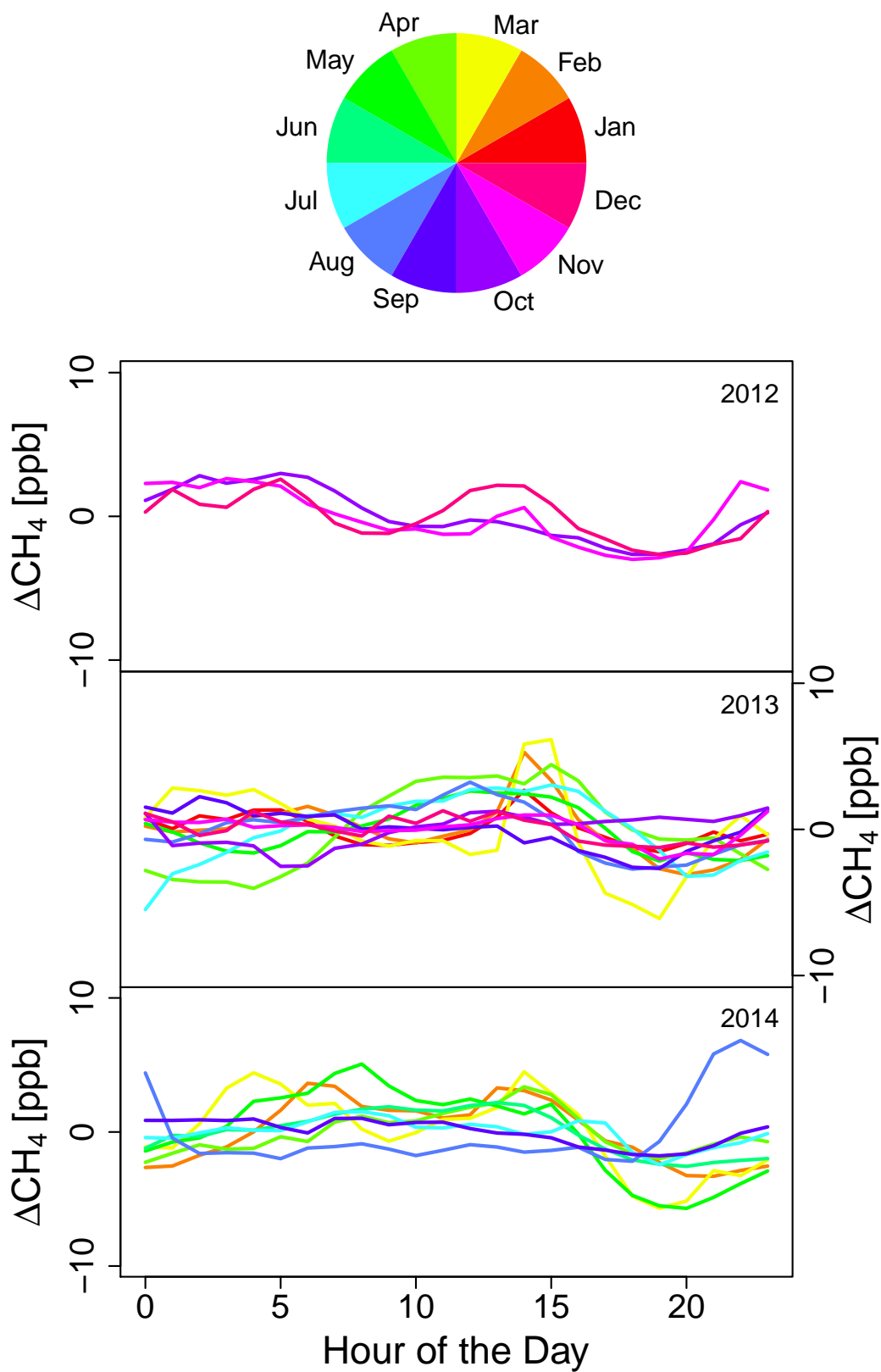


Figure A.20: The diurnal cycle of  $\text{CH}_4$ , averaged for each month.

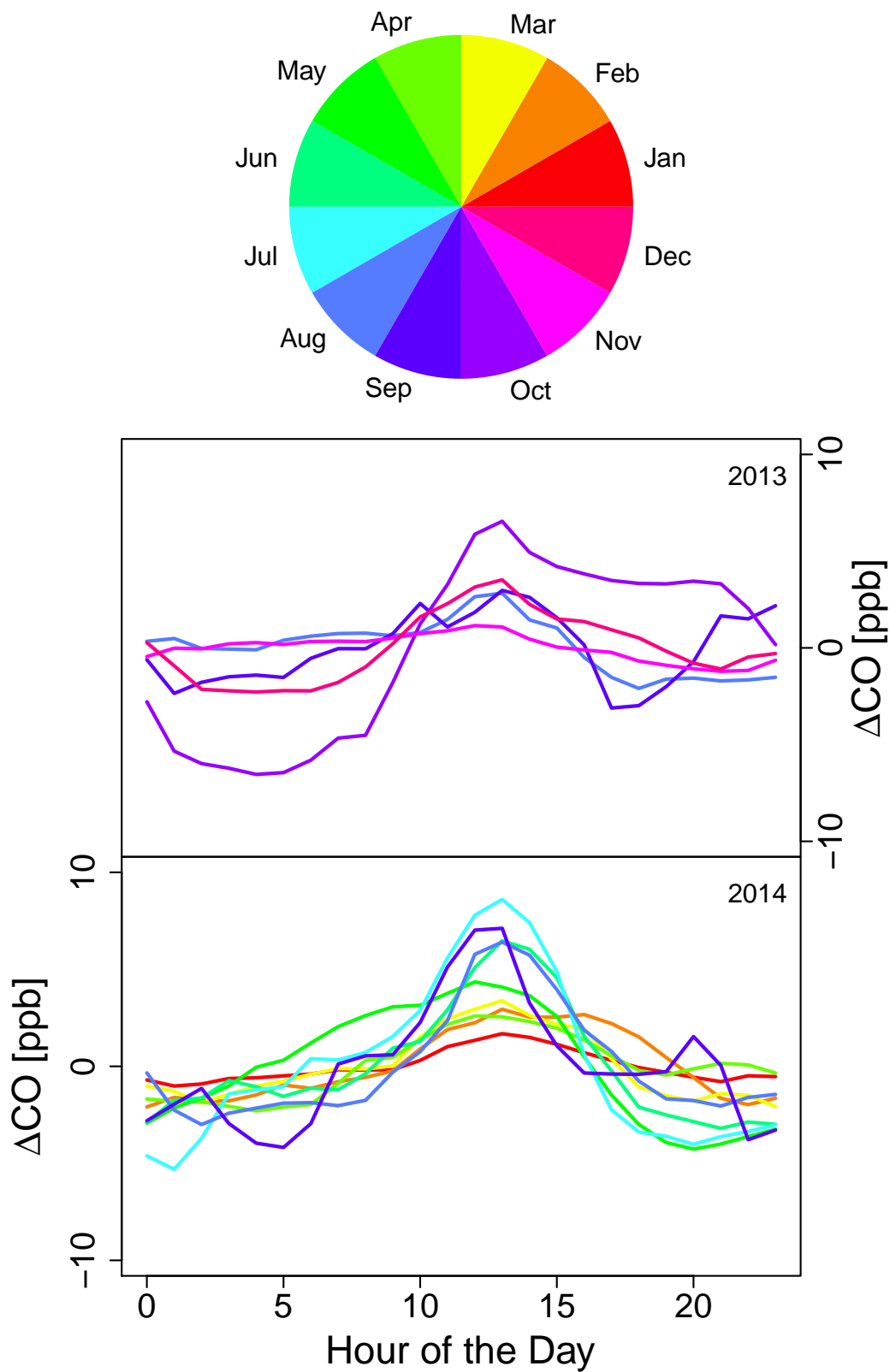


Figure A.21: The diurnal cycle of CO, averaged for each month.

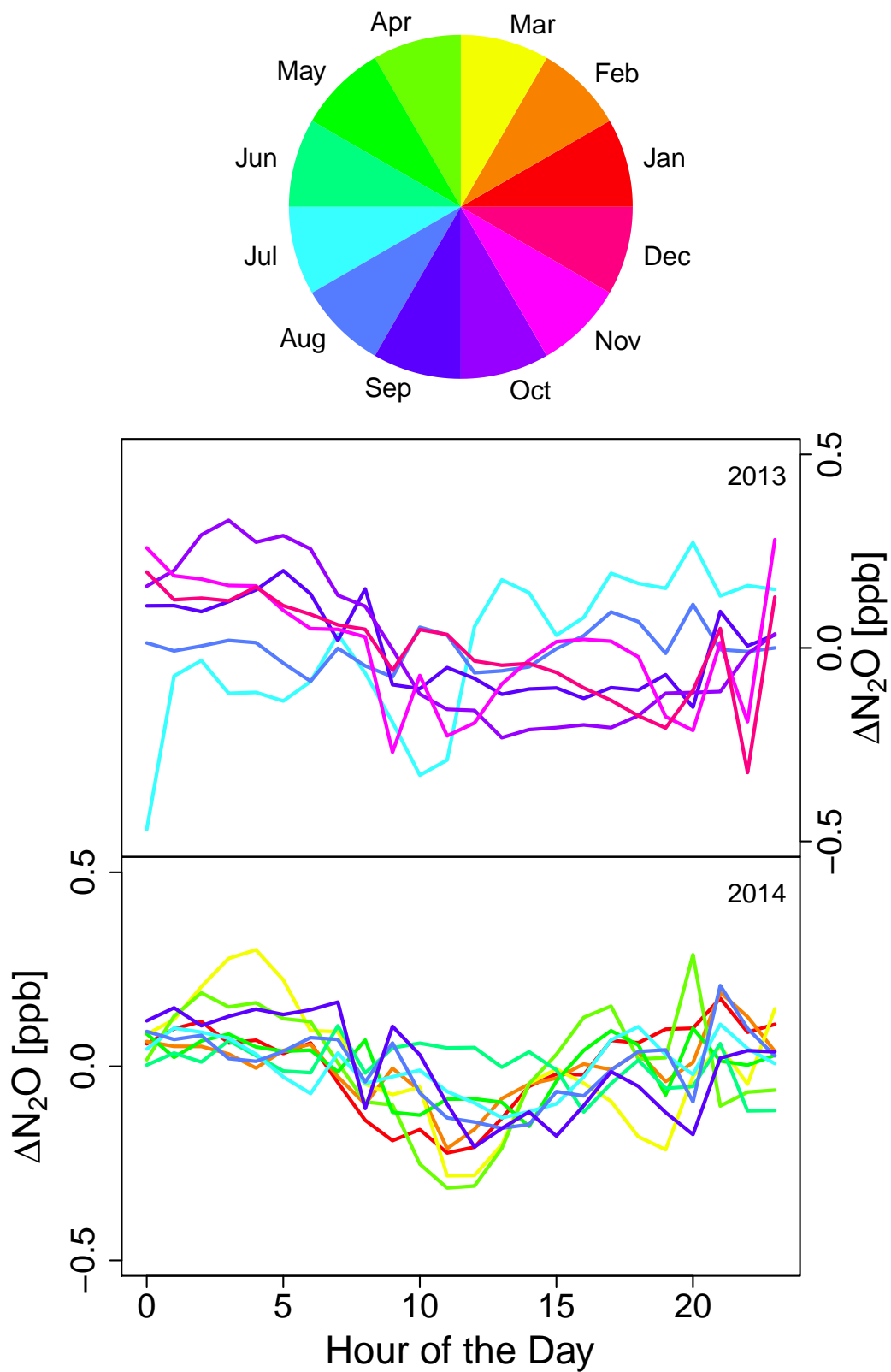


Figure A.22: The diurnal cycle of N<sub>2</sub>O, averaged for each month.

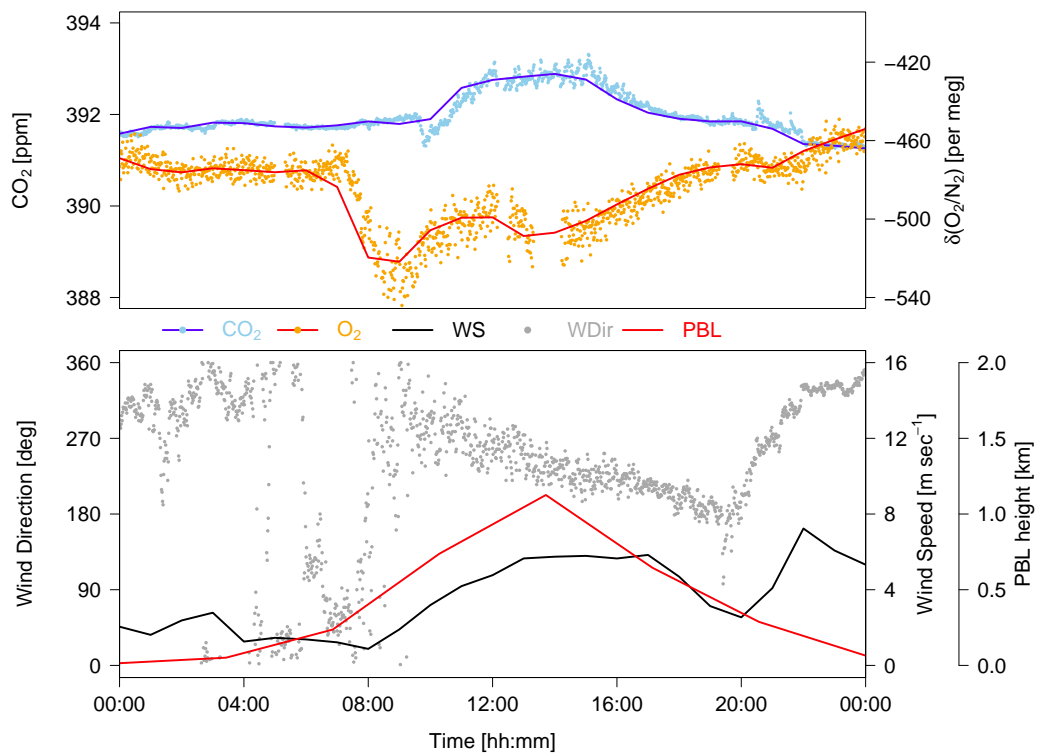


Figure A.23:  $\text{CO}_2$ ,  $\delta(\text{O}_2/\text{N}_2)$ , wind direction, wind speed, and planetary boundary layer height on November 3<sup>rd</sup>, 2012.

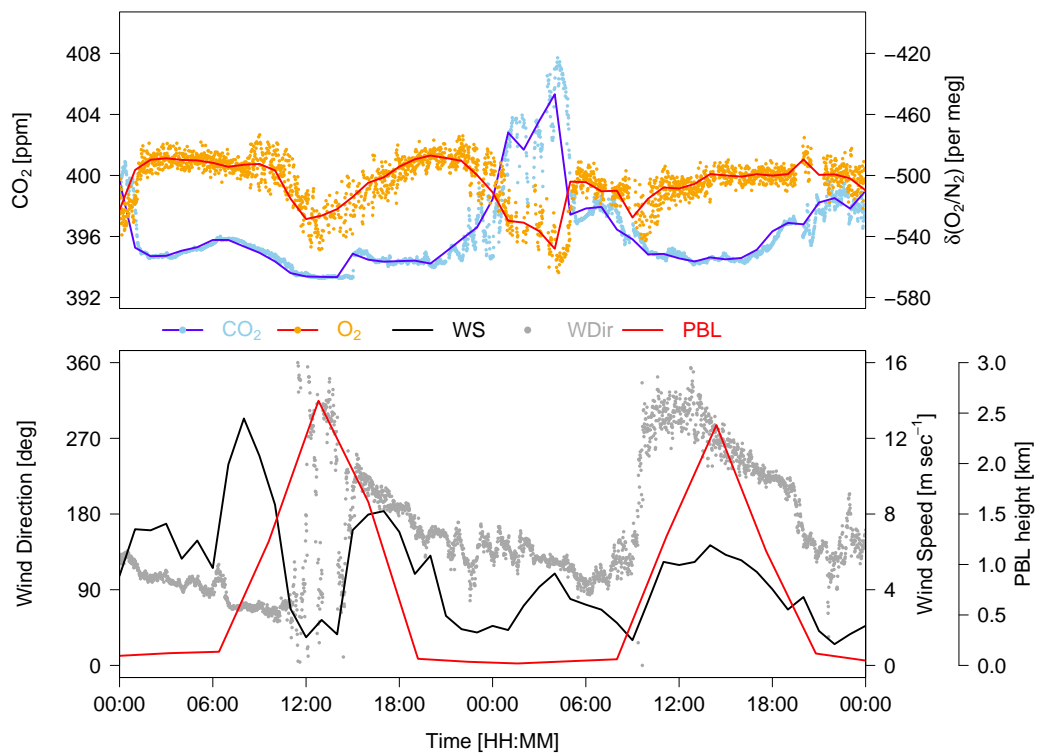


Figure A.24: CO<sub>2</sub>, δ(O<sub>2</sub>/N<sub>2</sub>), wind direction, wind speed, and planetary boundary layer height on April 5<sup>th</sup> and 6<sup>th</sup>, 2013.

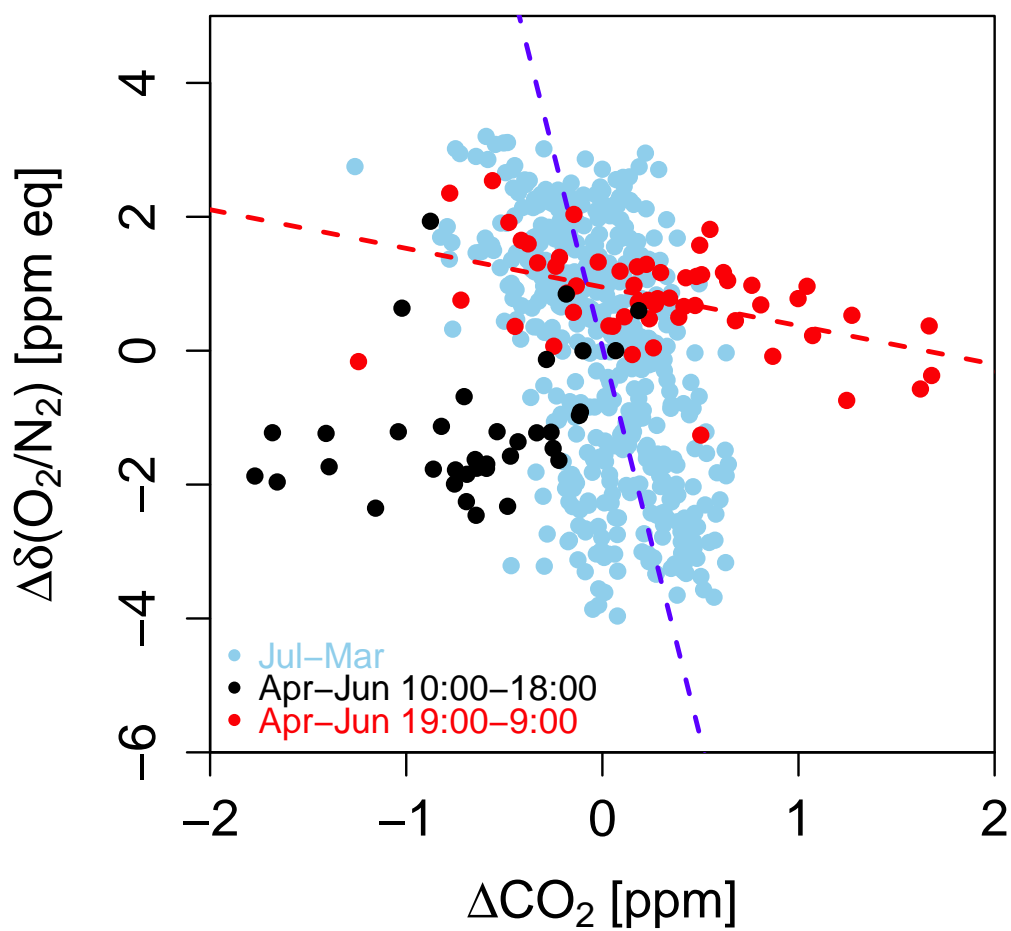


Figure A.25: The  $\text{O}_2:\text{O}_2$  molar exchange ratio of the combined average monthly diurnal cycles shown in Figure A.18 and Figure A.19. Data for July through March is shown together (blue points), while the April–June data is plotted in black for hours falling between 10:00 and 18:00, and red for hours falling between 19:00 and 9:00. Note that the black dots correspond roughly to the hours of the sea breeze, while the red dots correspond to the MPW.

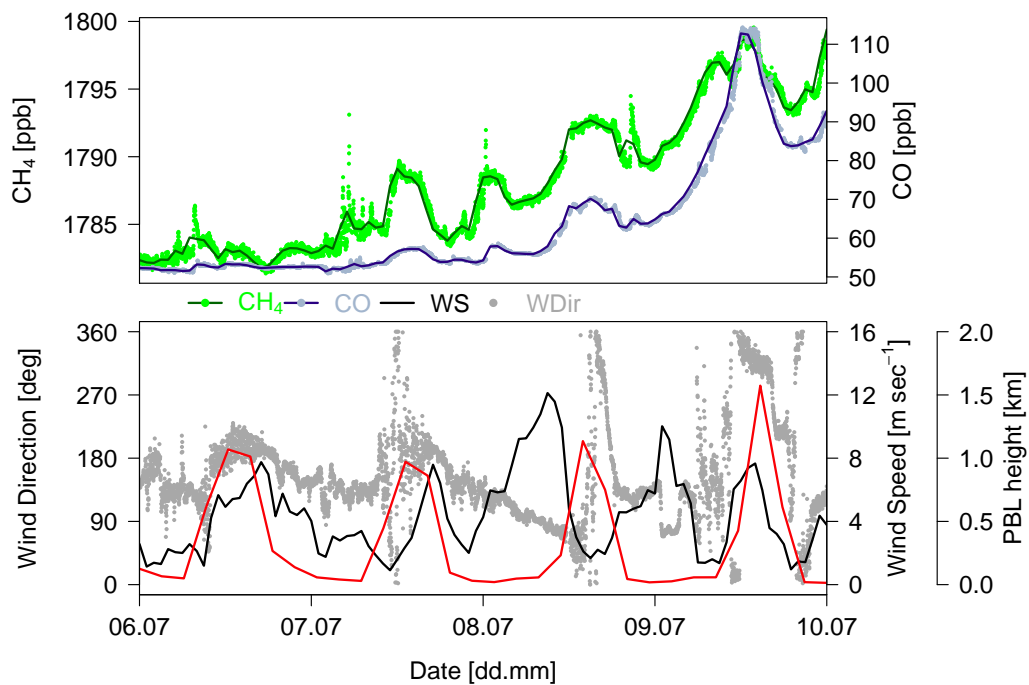


Figure A.26: CH<sub>4</sub>, CO, wind direction, and planetary boundary layer height over four days in July 2014. Winds were generally southerly or easterly, but both species follow the PBL height more closely than the wind sector. The time period selected shows an increase in CH<sub>4</sub> and CO due to a synoptic event.



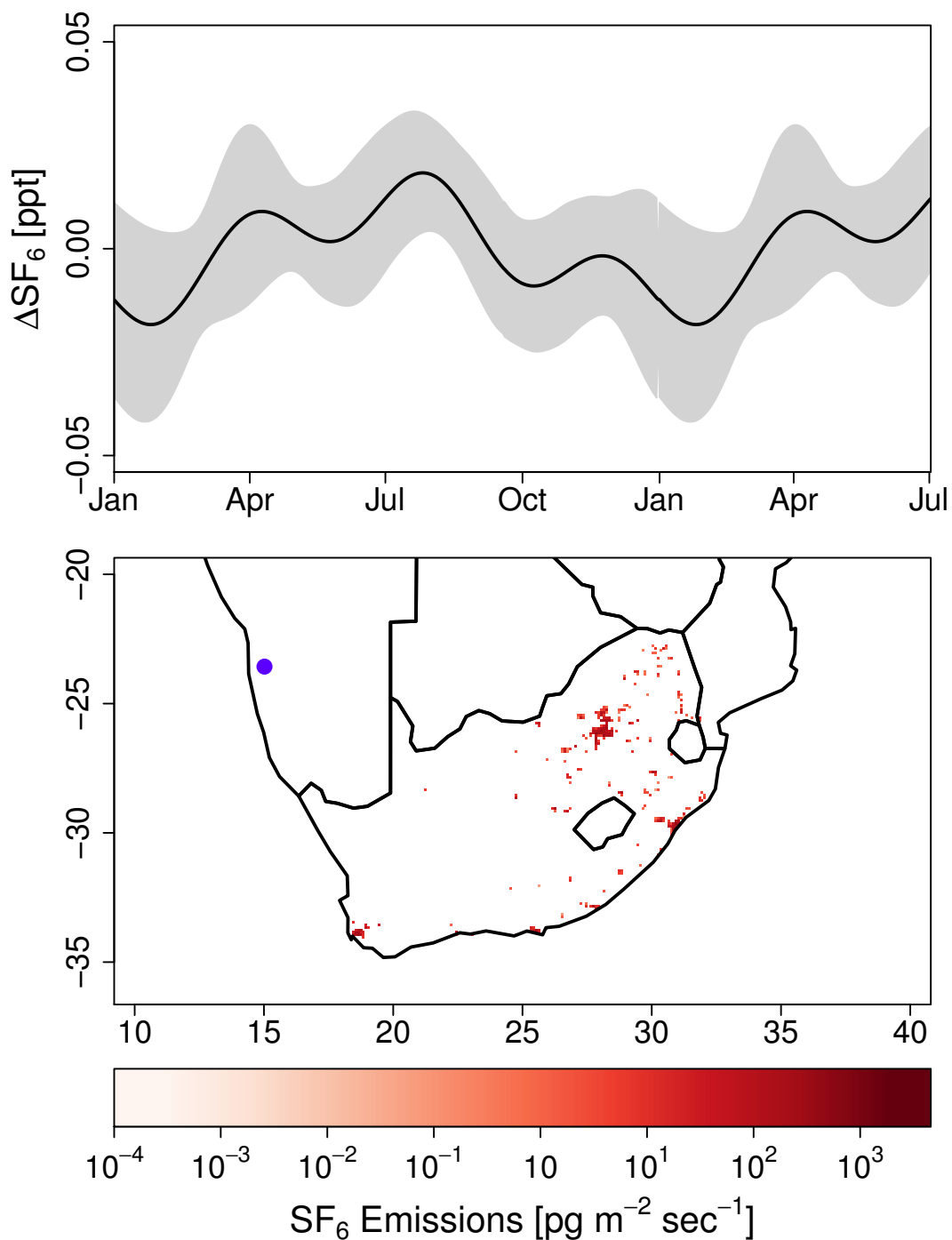


Figure A.27: The seasonal cycle of  $\text{SF}_6$  from the NMB flask record, with a gray envelope showing one standard deviation of the residuals (*top panel*), and the location of known industrial emissions of  $\text{SF}_6$  in 2010 (*bottom panel*). Emission data is from the Emission Database for Global Atmospheric Research (EC-JRC/PBL, EDGAR version 4.0, <http://edgar.jrc.ec.europa.eu/>, 2009). Location of NDAO is given by a blue dot.

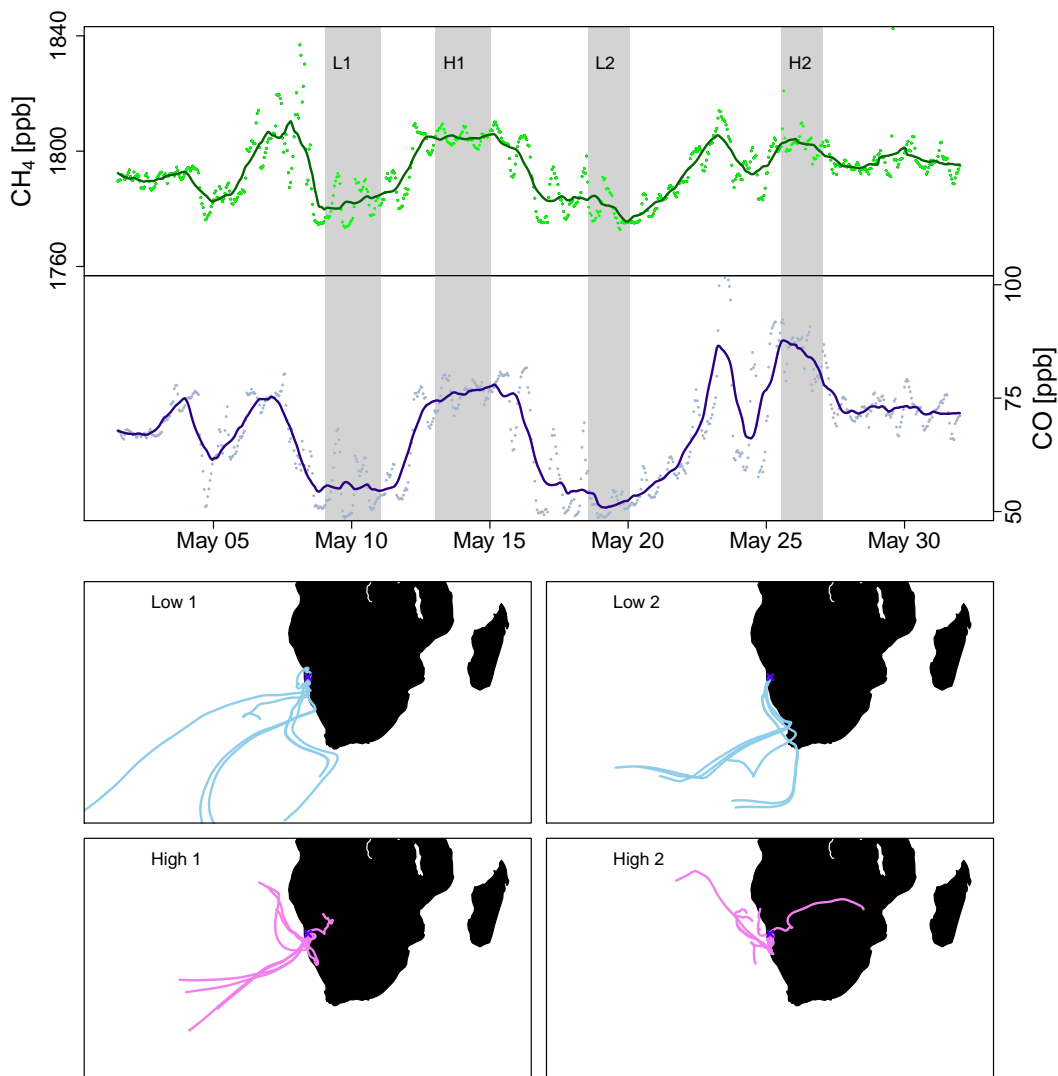


Figure A.28: Hourly CO and  $\text{CH}_4$  (points) and a running 24-hour mean of the same (lines) during a portion of May 2014. The gray rectangles indicate the time periods for the four back-trajectory plots in the bottom four panels. “Low” or “High” refers to a baseline period or enhanced period, with L1 short for low 1, etc.

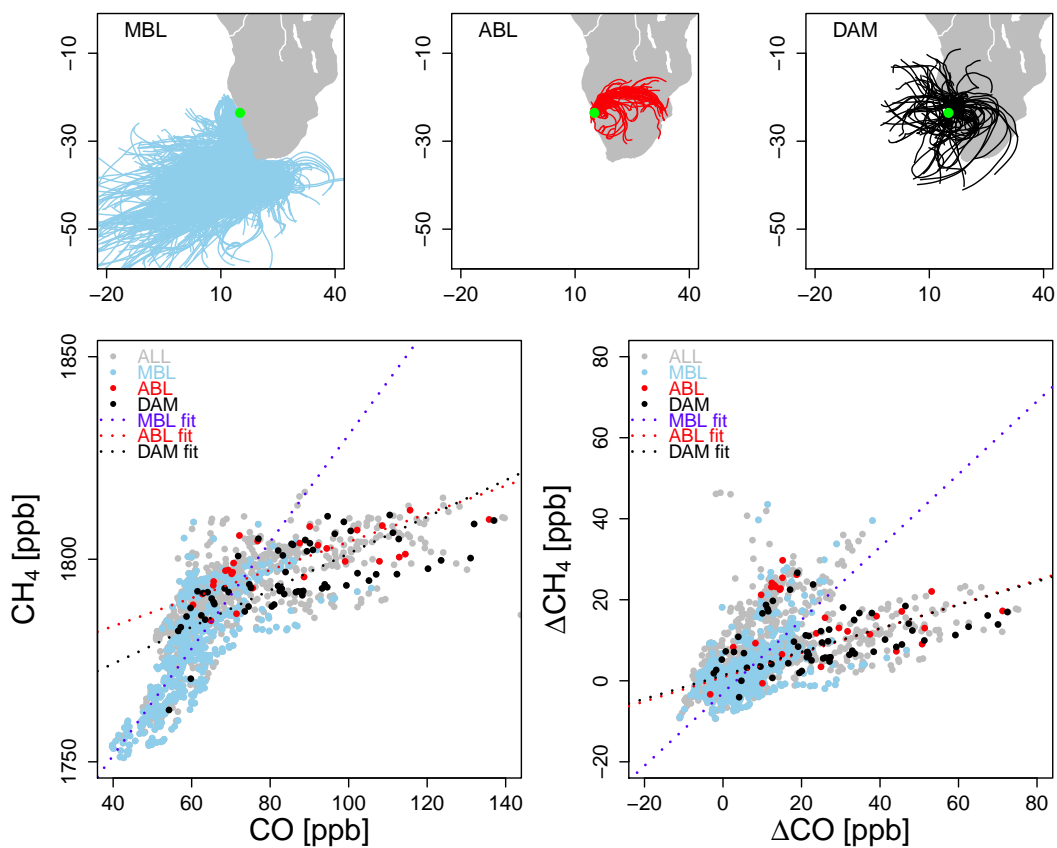


Figure A.29: The three categories of selected back-trajectories (*top panels*). MBL are surface marine trajectories, ABL are surface anticyclone-associated trajectories, and DAM are descending air masses without long-range transport. In the bottom left panel, CH<sub>4</sub> is plotted as a function of CO. Both have been smoothed with a 24-hour running mean to remove diurnal variations. In the bottom right panel, ΔCH<sub>4</sub> is plotted as a function of ΔCO. The Δ indicates that these two species have been deseasonalized in addition to the smoothing applied in the bottom left panel, so that only intraseasonal-scale variations are shown.

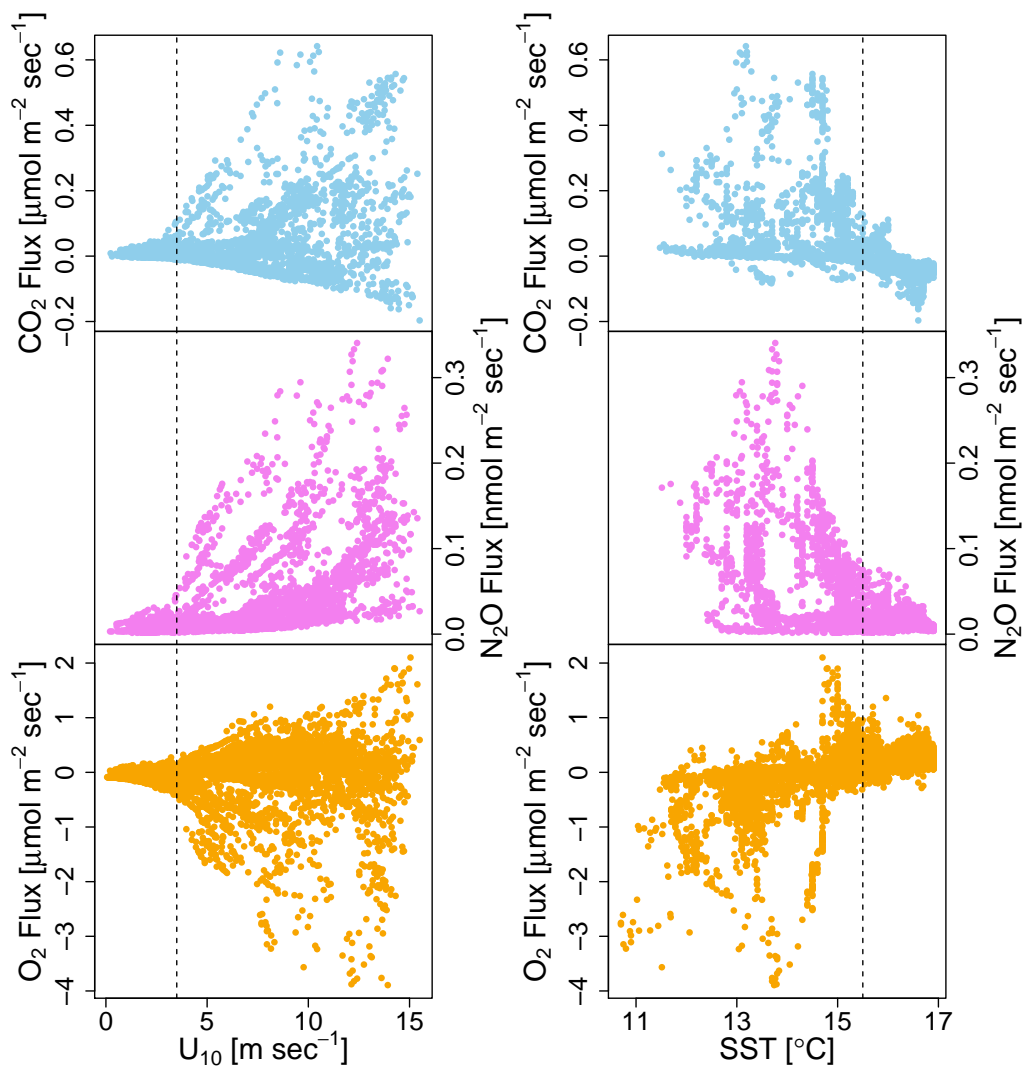


Figure A.30: Justification for the sea surface temperature (SST) and wind speed thresholds for identifying the area of upwelled water for each event. In each case, the threshold is identified by the dotted vertical line. All data is from M99.

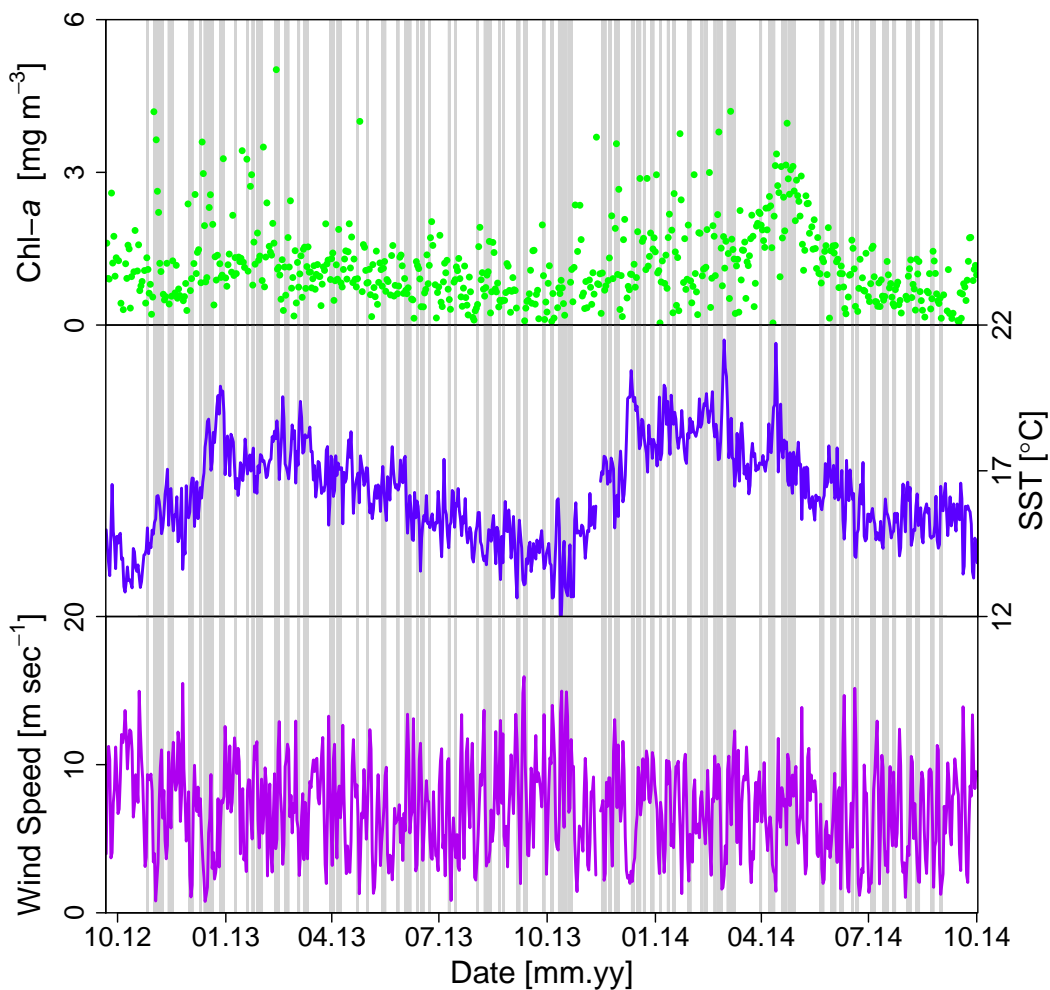


Figure A.31: Surface chlorophyll *a*, temperature, and 10-m wind speed for the Lüderitz domain over the course of the two-year study period. Days which have been flagged as containing an upwelling event have been shaded.

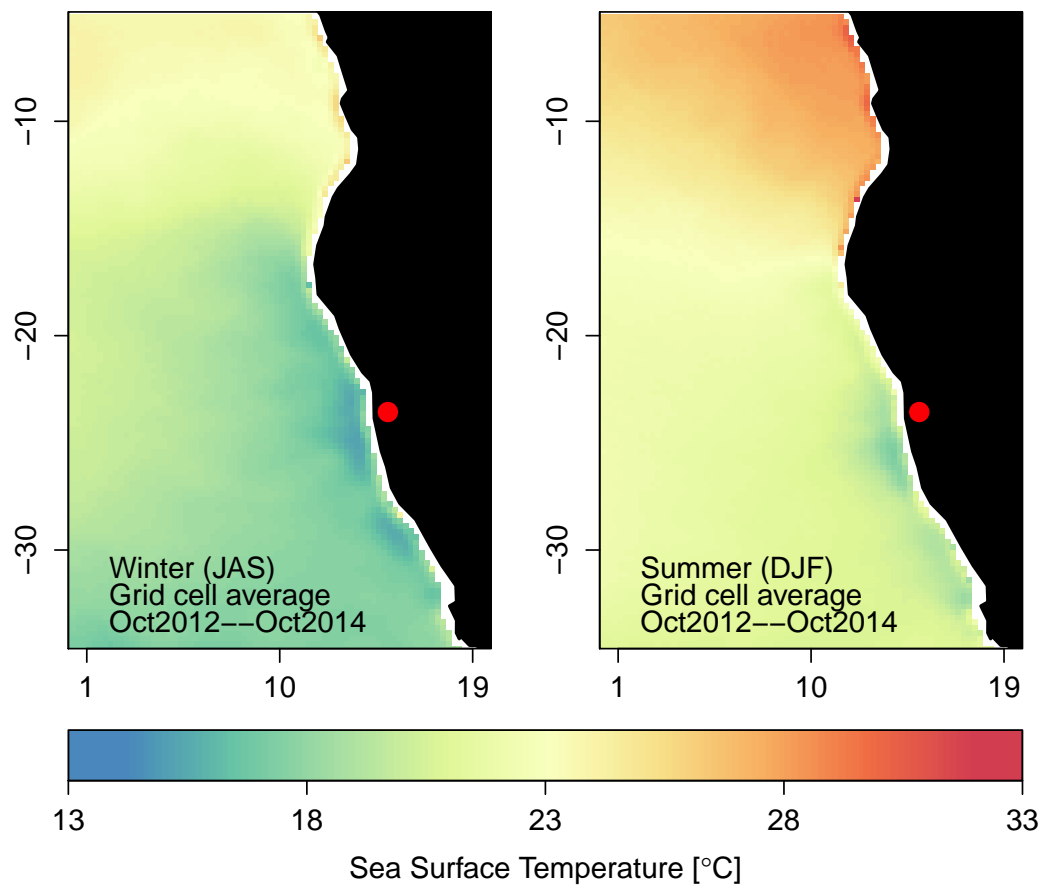


Figure A.32: Comparison of the seasonal average sea surface temperature (SST) for the Benguela Current region. Location of NDAO is given by a red dot.

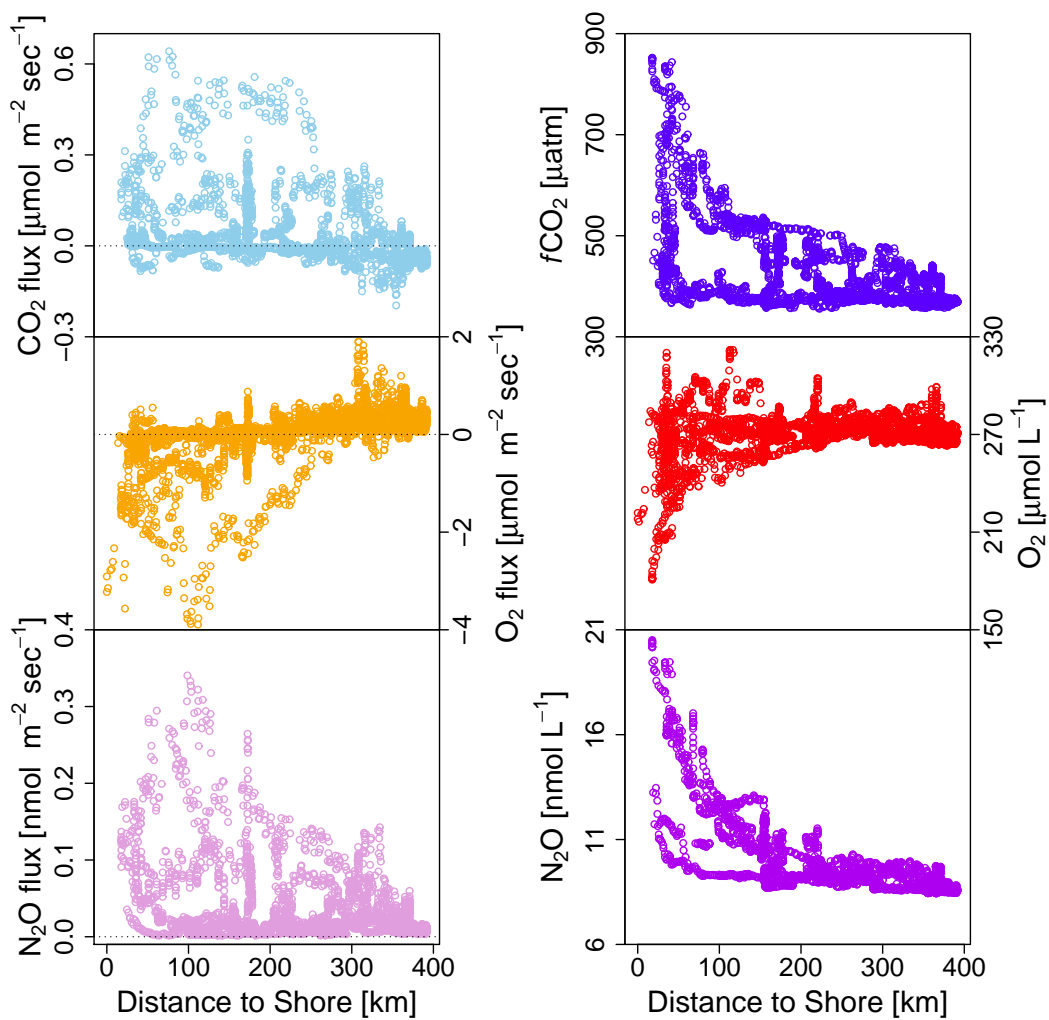


Figure A.33: Air-sea flux densities for CO<sub>2</sub>, O<sub>2</sub>, and N<sub>2</sub>O during M99 as a function of distance from shore (*left panel*), and the dissolved concentrations of the same species in surface water, ca. 6 m depth, also as a function of distance from shore (*right panel*).

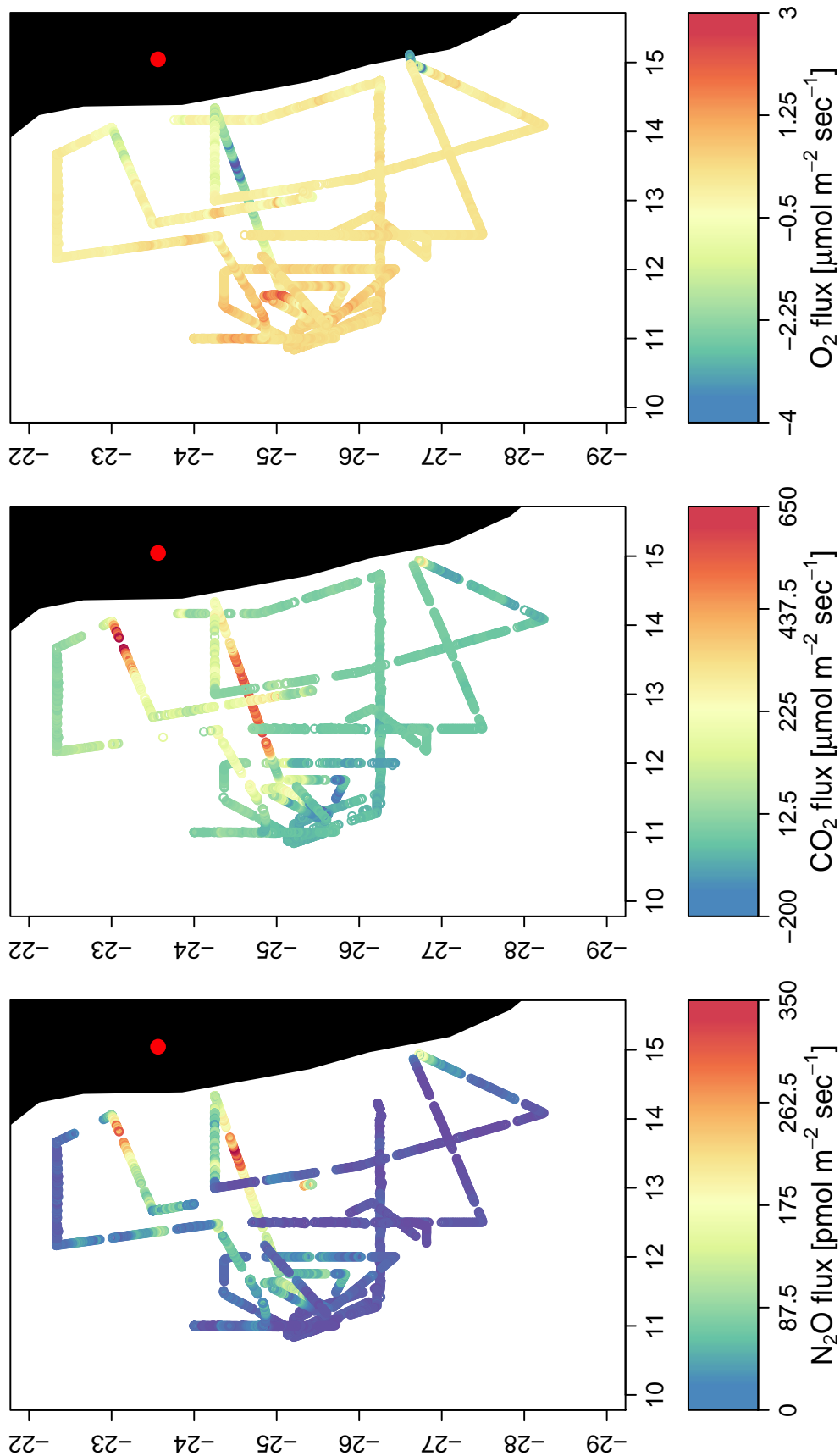


Figure A.34: Flux Densities estimated from shipboard measurements during M99. Location of NDAO is given by a red dot.



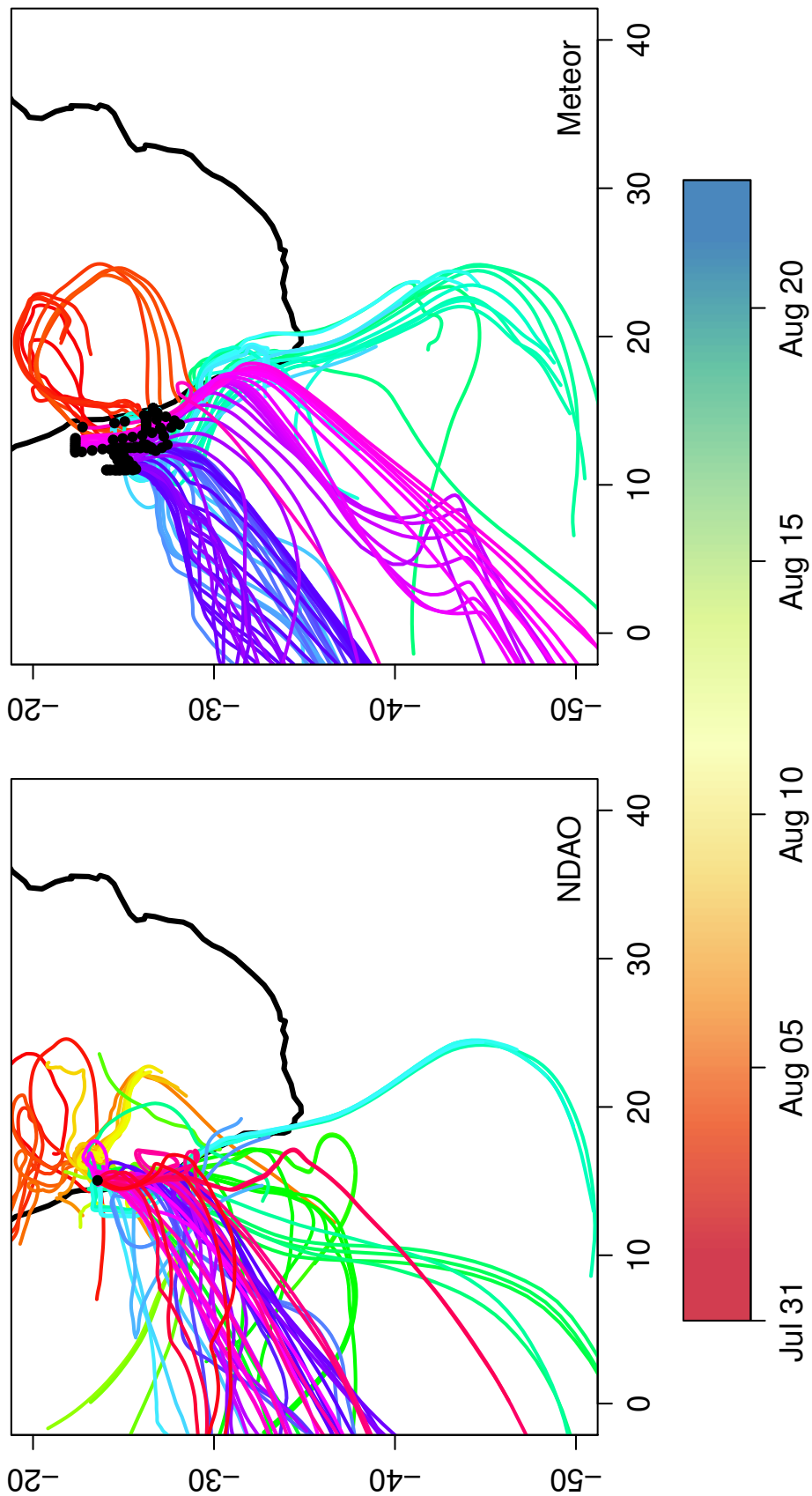


Figure A.35: Five-day back-trajectories (BTs) calculated with HYSPLIT for the duration of M99, every 6 hours. For each BT the location of the start point is given by a black dot. The left panel shows BTs calculated from NDAO, and the right panel shows BTs calculated from the Meteor. BTs are colored by date of the starting time.

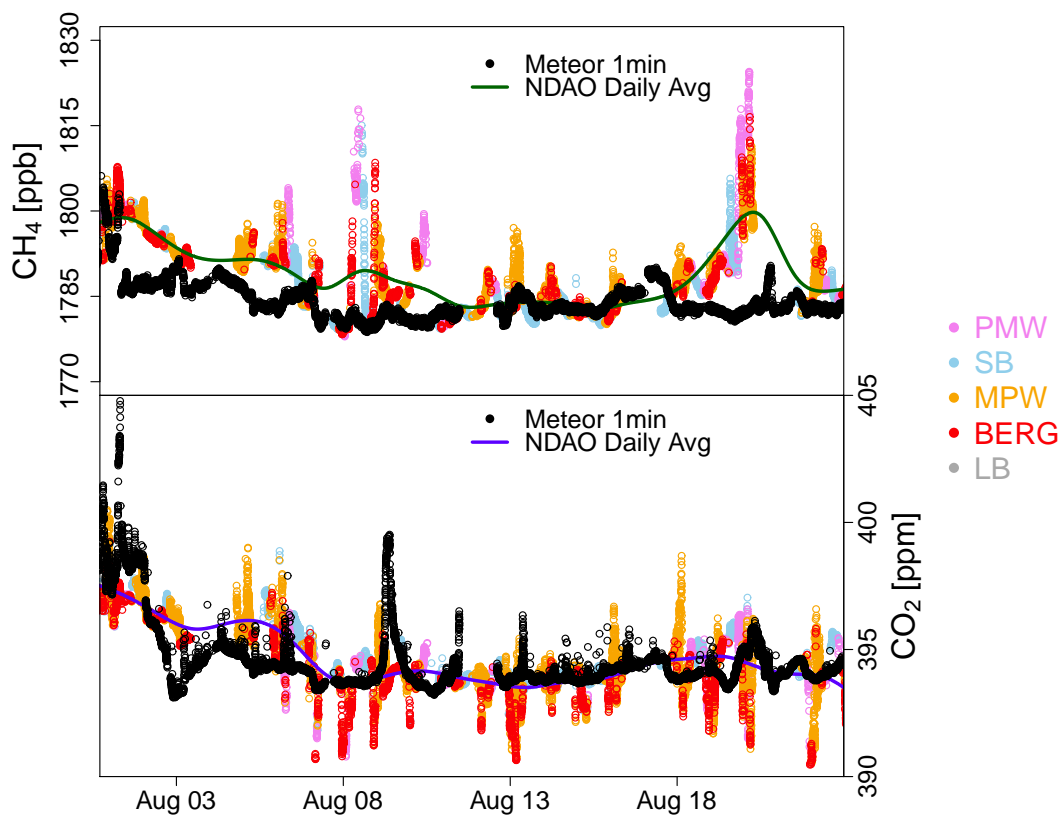


Figure A.36: Atmospheric observations of  $\text{CO}_2$  and  $\text{CH}_4$ , expressed as a dry air mole fraction, during the M99 cruise. Black points are the shipboard measurements and colored points are the NDAO measurements. NDAO measurements are colored by wind sector. Also shown for both species is a smooth fit to a rolling daily average (lines).

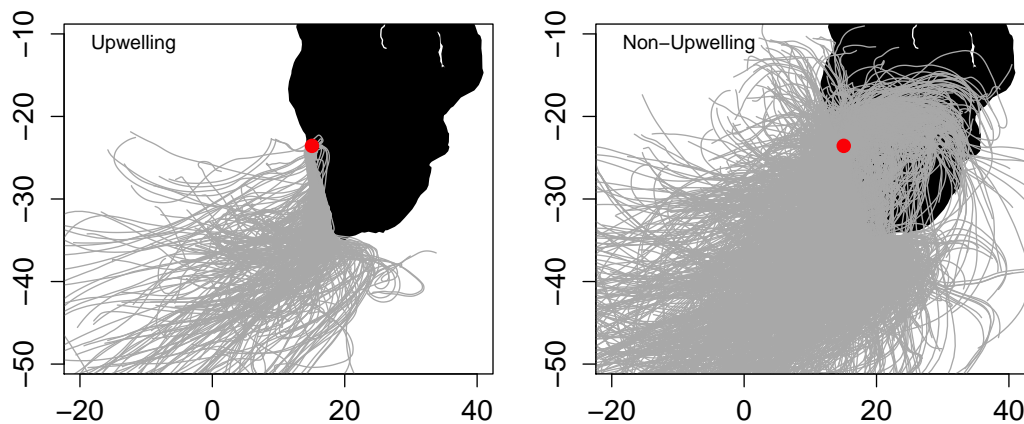


Figure A.37: Back-trajectories associated with days with upwelling events (*left panel*) and days without upwelling events (*right panel*). Location of NDAO is given by a red dot.

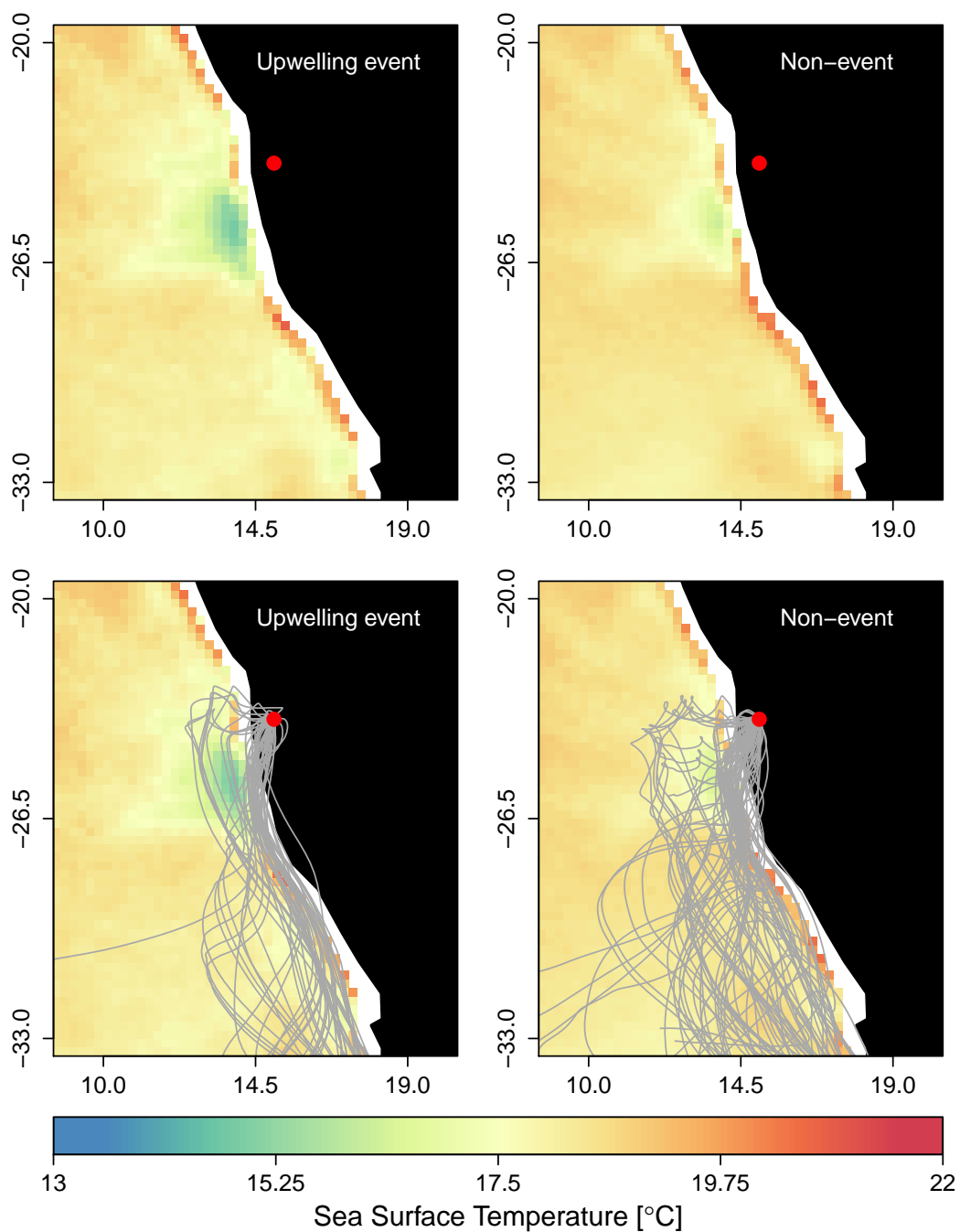


Figure A.38: SST during (*left panels*) and preceding and after (*right panels*) the upwelling event described in Figure 6.2. In the bottom two panels, the back-trajectories calculated for the respective periods are overlain. Location of NDAO given by a red dot.

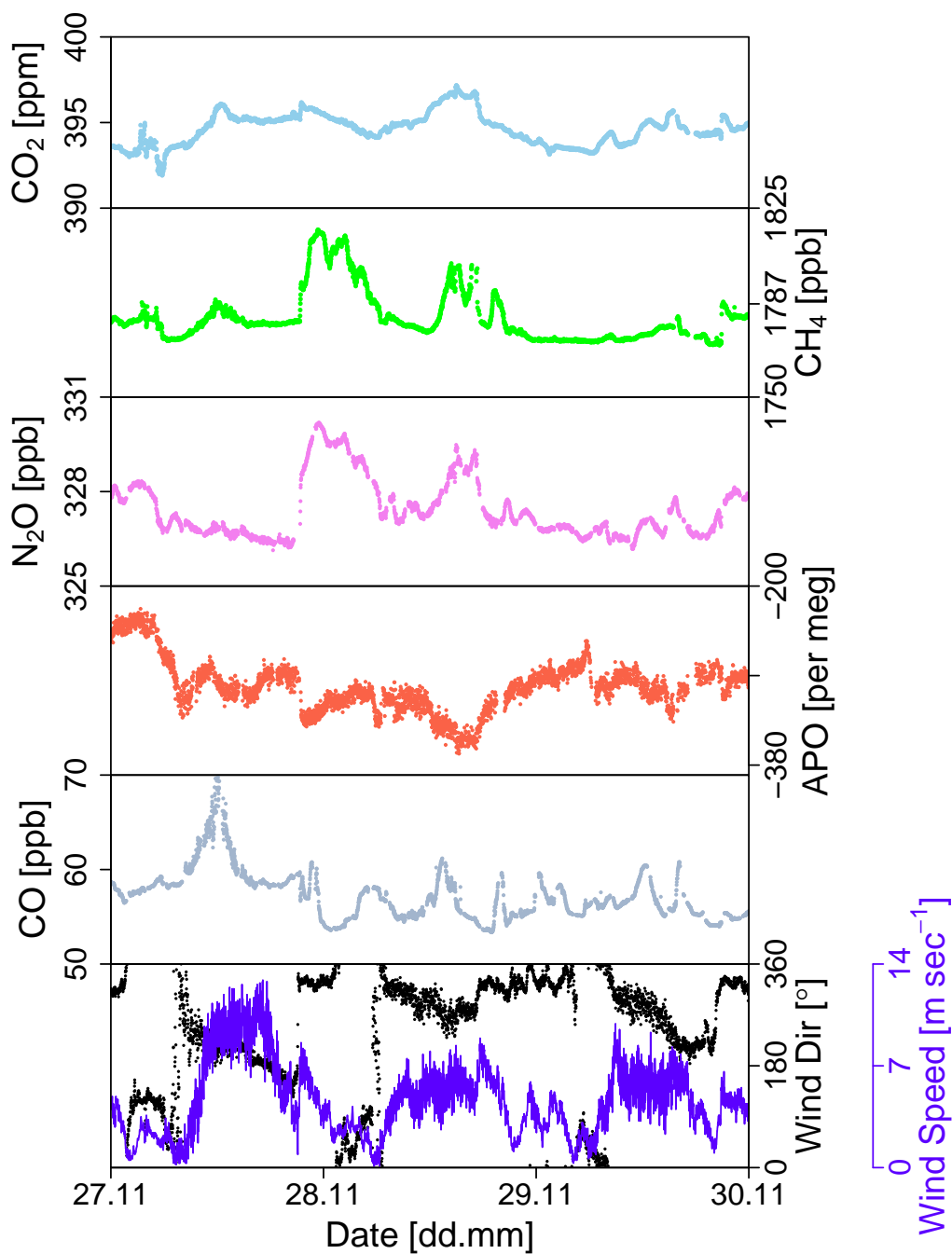


Figure A.39: NDAO measurands and meteorology during an upwelling event at the end of 2013. In the bottom panel, wind direction is abbreviated as “Wind Dir”, and is plotted as black dots, while wind speed is a blue line. See Figure 6.3 for a longer time period encompassing the same event.

# B

## Supplementary Tables

Table B.1: Flask Sampling Site Locations

Site	ID	Latitude	Longitude	Height (m.a.s.l.)	Organization
Cape Grim	CGO	40.68°S	144.68°E	94	NOAA
Easter Island	EIC	27.13°S	109.45°W	50	NOAA
Cape Point	CPT	34.35S	18.48E	230	SAWS
Cape Ferguson	CFA	19.28°S	147.05°E	2	CSIRO
Pacific Ocean 20S	20S	20.00°S	174.00°W	10	NOAA
Pacific Ocean 25S	25S	25.00°S	171.00°W	10	NOAA
Gobabeb	NMB	23.57°S	15.02°E	461	NOAA

Table B.2: Variability of NDAO Measurands at Proximal Flask Sites, 1997–2014

Site	Amplitude <sup>a</sup>	Day Max. <sup>b</sup>	Day Min. <sup>c</sup>	Growth Rate <sup>d</sup>
CO <sub>2</sub> (ppm or ppm yr <sup>-1</sup> )				
Gobabeb (NMB)	2.52	Jul. 29	Feb. 27	2.0 ± 0.3
Cape Ferguson (CFA)	1.35	Dec. 13	Jul. 3	1.9 ± 0.6
Cape Point (CPT)	0.64	Aug. 15	Mar. 6	2.0 ± 0.4
Easter Island (EIC)	1.05	Dec. 24	Apr. 22	2.0 ± 0.4
Pacific Ocean 20°S (20S)	0.86	Dec. 30	Apr. 25	1.9 ± 0.4
Pacific Ocean 25°S (25S)	0.92	Dec. 25	Apr. 24	1.9 ± 0.3
Ascension Island (ASC)	1.80	Jul. 20	Apr. 1	2.0 ± 0.4
CH <sub>4</sub> (ppb or ppb yr <sup>-1</sup> )				
Gobabeb (NMB)	29.5	Jul. 29	Feb. 4	3.6 ± 4.0
Cape Ferguson (CFA)	28.9	Aug. 17	Feb. 14	3.6 ± 4.1
Cape Point (CPT)	31.8	Aug. 28	Feb. 20	3.6 ± 3.0
Easter Island (EIC)	31.5	Sep. 7	Feb. 12	3.6 ± 4.0
Pacific Ocean 20°S (20S)	20.0	Aug. 10	Feb. 9	3.3 ± 3.5
Pacific Ocean 25°S (25S)	26.2	Aug. 13	Feb. 11	3.3 ± 3.8
Ascension Island (ASC)	22.8	Aug. 5	Feb. 1	3.6 ± 3.6
N <sub>2</sub> O (ppb or ppb yr <sup>-1</sup> )				
Gobabeb (NMB)	0.4	Feb. 29	Aug. 31	0.81 ± 0.2
Cape Ferguson (CFA)	0.3	Dec. 30	Jul. 29	0.60 ± 0.2
Cape Point (CPT)	—	—	—	—
Easter Island (EIC)	—	—	—	—
Pacific Ocean 20°S (20S)	—	—	—	—
Pacific Ocean 25°S (25S)	—	—	—	—
Ascension Island (ASC)	—	—	—	—
CO (ppb or ppb yr <sup>-1</sup> )				
Gobabeb (NMB)	27.3	Jul. 20	Jan. 19	-0.49 ± 2.5
Cape Ferguson (CFA)	33.2	Oct. 3	Feb. 21	-1.3 ± 4.4
Cape Point (CPT)	24.1	Sep. 14	Feb. 7	-0.03 ± 2.3
Easter Island (EIC)	23.1	Sep. 27	Feb. 14	-0.02 ± 2.0
Pacific Ocean 20°S (20S)	24.2	Sep. 20	Jan. 28	-0.32 ± 2.2
Pacific Ocean 25°S (25S)	24.2	Sep. 20	Jan. 29	-0.32 ± 2.2
Ascension Island (ASC)	30.8	Sep. 28	Jan. 31	0.22 ± 3.9

<sup>a</sup> Average amplitude of the seasonal cycle, calculated as peak minus following trough.

<sup>b</sup> Average day during which the maximum value for the year is reached. Note that this is approximate since flask sampling is not continuous

<sup>c</sup> Average day during which the minimum value for the year is reached.

<sup>d</sup> Average annual growth rate, plus or minus the standard deviation.

Table B.3: Variability of Additional Measurands at Proximal Flask Sites, 1998–2014

Site	Amplitude <sup>a</sup>	Day Max. <sup>b</sup>	Day Min. <sup>c</sup>	Growth Rate <sup>d</sup>
	H <sub>2</sub> (ppb or ppb yr <sup>-1</sup> )			
Gobabeb (NMB)	24.1	Dec. 30	Jun. 29	-0.98 ± 5.5
Cape Ferguson (CFA)	23.5	Feb. 1	Jul. 3	0.35 ± 3.6
Cape Point (CPT)	—	—	—	—
Easter Island (EIC)	18.0	Jan. 23	Aug. 16	i.d.
Pacific Ocean 20°S (20S)	20.0	Nov. 21	Jul. 19	i.d.
Pacific Ocean 25°S (25S)	20.2	Jan. 13	Jul. 14	i.d.
Ascension Island (ASC)	15.3	Dec. 9	May 16	i.d.
	SF <sub>6</sub> (ppt or ppt yr <sup>-1</sup> )			
Gobabeb (NMB)	0.04	Jul. 27	Feb. 9	0.25 ± 0.04
Cape Ferguson (CFA)	—	—	—	—
Cape Point (CPT)	—	—	—	—
Easter Island (EIC)	—	—	—	—
Pacific Ocean 20°S (20S)	—	—	—	—
Pacific Ocean 25°S (25S)	—	—	—	—
Ascension Island (ASC)	—	—	—	—
	δ <sup>13</sup> C–CO <sub>2</sub> (‰ or ‰ yr <sup>-1</sup> )			
Gobabeb (NMB)	0.08	Mar. 24	Jul. 26	-0.03 ± 0.02
Cape Ferguson (CFA)	0.06	Mar. 23	Nov. 27	-0.02 ± 0.02
Cape Point (CPT)	—	—	—	—
Easter Island (EIC)	0.05	Apr. 18	Dec. 4	-0.02 ± 0.02
Pacific Ocean 20°S (20S)	0.03	May 2	Dec. 3	-0.03 ± 0.01
Pacific Ocean 25°S (25S)	0.03	Mar. 31	Sep. 30	-0.02 ± 0.03
Ascension Island (ASC)	0.09	Apr. 19	Nov. 4	-0.02 ± 0.01
	δ <sup>18</sup> O–CO <sub>2</sub> (‰ or ‰ yr <sup>-1</sup> )			
Gobabeb (NMB)	0.073	Sep. 30	Mar. 31	-0.002 ± 0.05
Cape Ferguson (CFA)	—	—	—	—
Cape Point (CPT)	—	—	—	—
Easter Island (EIC)	0.28	Sep. 23	May 24	-0.002 ± 0.08
Pacific Ocean 20°S (20S)	0.20	Sep. 30	Mar. 31	-0.006 ± 0.1
Pacific Ocean 25°S (25S)	0.23	Oct. 25	Apr. 25	-0.006 ± 0.07
Ascension Island (ASC)	0.26	Nov. 2	Jun. 1	-0.015 ± 0.08

<sup>a</sup> Average amplitude of the seasonal cycle, calculated as peak minus following trough.

<sup>b</sup> Average day during which the maximum value for the year is reached. Note that this is approximate since flask sampling is not continuous

<sup>c</sup> Average day during which the minimum value for the year is reached.

<sup>d</sup> Average annual growth rate, plus or minus the standard deviation.

Table B.4: Part List of Gas Handling Equipment

Item	Manufacturer / Brand	Part Number
Membrane Pump	KNF Neuberger GmbH (Germany)	N828KNE
Membrane Pump (CRDS external)	Vacuubrand GmbH (Germany)	MD1
Membrane Pump (flask sampler)	KNF Neuberger GmbH (Germany)	PM226199-814
Microturbine flow meter	Aalborg Instruments and Controls, Inc. (USA)	P11A2-Ba0A
Pressure sensor	Sensortronics GmbH (Germany)	CTE7N01GMO
Electronic pressure regulator	MKS Instruments, Inc. (USA)	223BD-00010AAB
Mass flow controller	MKS Instruments, Inc. (USA)	1179A12CS1AV
12-port valve	Valco Instruments Company Inc (USA)	EMT2SD12MWEE
Three-way valve	Numatics, Inc (USA)	HSN2C6HOOV
Four-way valve	Bürkert Fluid Control Systems (Germany)	0330
Pressure regulators (working tanks)	Scott Specialty Gases, Inc (USA)	085C4115
Pressure regulators (reference tanks)	TESCOM (USA)	64-3440KA412
Peristaltic Pump	Masterflex (USA)	7542-01
Cryo-cooler	FTS Systems (Germany)	VT490D



Table B.5: Measurand Total System Residence ( $\tau_{calc}$ ) and Response ( $\tau_{app}$ ) Times

Measurand	$\tau_{calc}$ [sec]	$\tau_{app}$ [sec]
CO <sub>2</sub>	16	137
CH <sub>4</sub>	16	45
N <sub>2</sub> O	15	48
CO	15	115
$\delta(\text{O}_2/\text{N}_2)$	200	234
Flask	53	—

Table B.6: Comparison of Fit Parameters

Reference	Model	N <sub>2</sub> O		CO	
		$a \times 10^{-2}$	$b \times 10^{-4}$	$a \times 10^{-2}$	$b \times 10^{-4}$
This Work	N <sub>2</sub> O/CO-23d	-1.142	-6.723	-1.114	0.885
		CO <sub>2</sub>		CH <sub>4</sub>	
		$a \times 10^{-2}$	$b \times 10^{-4}$	$a \times 10^{-2}$	$b \times 10^{-4}$
This Work	ESP-1000	-1.17	-3.08	-0.96	-0.78
<a href="#">Winderlich et al. [2010]</a>	EnviroSense 3000i	-1.21	-2.03	-1.01	-1.45
<a href="#">Chen et al. [2010]</a>	G1301	-1.20	-2.67	-0.98	-2.39
<a href="#">Rella et al. [2013]</a>	Various	-1.21	-2.48	-1.02	-1.40

Table B.7: Target Tank Biases (Mean of NDAO Target Measurements - Assigned Value from MPI-BGC)

Tank	CO <sub>2</sub> [ppm]	CH <sub>4</sub> [ppb]	N <sub>2</sub> O [ppb]	CO [ppb]	$\delta(\text{O}_2/\text{N}_2)$ [per meg]
D417492	-0.38	-0.20	-0.61	-0.91	-6.4
D417437	-0.01	-0.70	0.26	-0.06	-9.8
D417479	0.01	-0.96	-0.03	-1.37	3.7
D417471	0.04	-0.19	0.07	0.44	-7.5
D417455	0.04	0.05	0.08	0.74	-3.0

Table B.8: Definition of Wind Sectors

Wind Sector	ID	Lower Bound [°]	Upper Bound [°]
Bergwind <sup>a</sup>	BERG	55	105
Land Breeze	LB	55	105
Mountain-Plain Wind	MPW	112	140
Sea Breeze (All)	SB	185	225
Sea Breeze 1	SB1	187	197
Sea Breeze 2	SB2	210	225
Plain-Mountain Wind	PMW	305	340

<sup>a</sup> Bergwinds are defined as being distinct from land breezes by having an air temperature over 20°C and relative humidity under 20%.

Table B.9: Growth Rates of Selected Measurands for the Period October 2012–December 2013

Site <sup>a</sup>	CO <sub>2</sub> [ppm yr <sup>-1</sup> ]	δ(O <sub>2</sub> /N <sub>2</sub> ) [per meg yr <sup>-1</sup> ]	APO [per meg yr <sup>-1</sup> ]	CH <sub>4</sub> [ppb yr <sup>-1</sup> ]	N <sub>2</sub> O [ppb yr <sup>-1</sup> ]
NDAO	2.80 ± 0.1	-33.4 ± 1.4	-16.4 ± 1.3	4.4 ± 0.3	1.3 ± 0.1
NMB	2.79 ± 0.01	—	—	6.8 ± 1.5	1.3 ± 0.06
CPT	2.63 ± 0.1	—	—	4.1 ± 0.1	—
ASC	2.80 ± 0.1	—	—	3.4 ± 0.5	—
EIC	2.58 ± 0.1	—	—	4.9 ± 0.5	—
CFA	2.69 ± 0.4	—	—	5.1 ± 1.7	—
CGO	2.65 ± 0.03	-26.9 ± 1.5	-14.6 ± 3.6	4.9 ± 0.4	1.4 ± 0.2

<sup>a</sup> Sites are given by their short ID, see Section 2.2.2 for a map and locations.

# Bibliography

- AFREA. (African Evaluation Association) Wood-Based Biomass Energy Development for Sub-Saharan Africa: Issues and Approaches. Technical report, Africa Renewable Energy Access Program, 2011.
- J.J. Agenbag and L.V. Shannon. A suggested physical explanation for the existence of a biological boundary at 24°30'S in the Benguela system. *South African Journal of Marine Science*, 6:119–132, 1988.
- S.K. Akagi, R.J. Yokelson, C. Wiedinmeyer, M.J. Alvarado, J.S. Reid, T. Karl, J.D. Crouse, and P.O. Wennberg. Emission factors for open and domestic biomass burning for use in atmospheric models. *Atmospheric Chemistry and Physics*, 11:4039–4072, 2011.
- C.E. Allison and R.J. Francey. Verifying Southern Hemisphere trends in atmospheric carbon dioxide stable isotopes. *Journal of Geophysical Research*, 112:D21304, 2007.
- C. Amante and B.W. Eakins. ETOPO1 1 Arc-Minute Global Relief Model: Procedures, Data Sources and Analysis. NOAA Technical Memorandum NESDIS NGDC-24. National Geophysical Data Center, NOAA. DOI:10.7289/V5C8276M, 2009.
- D. Amouroux, G. Roberts, S. Rapsomanikis, and M.O. Andreae. Biogenic Gas (CH<sub>4</sub>, N<sub>2</sub>O, DMS) Emission to the Atmosphere from Near-shore and Shelf Waters of the North-western Black Sea. *Estuarine, Coastal and Shelf Science*, 54:575–587, 2002.
- M. Amraoui, C.C. DaCamara, and J.M.C. Pereira. Detection and monitoring of African vegetation fires using MSG-SEVIRI imagery. *Remote Sensing of Environment*, 114:1038–1052, 2010.
- N. Andela and G.R. van der Werf. Recent trends in African fires driven by cropland expansion and El Niño to La Niña transition. *Nature Climate Change*, 4:791–795, 2014.
- M.O. Andreae and P. Merlet. Emission of trace gases and aerosols from biomass burning. *Global Biogeochemical Cycles*, 15(4):955–966, 2001.
- A.E. Andrews, J.D. Kofler, M.E. Trudeau, J.C. Williams, D.H. Neff, K.A. Masarie, D.Y. Chao, D.R. Kitzis, P.C. Novelli, C.L. Zhao, E.J. Dlugokencky, P.M. Lang, M.J. Croswell, M.L. Fischer, M.J. Parker, J.T. Lee, D.D. Baumann, A.R. Desai, C.O. Stanier, S.F.J. De Wekker, D.E. Wolfe, J.W. Munger, and P.P. Tans. CO<sub>2</sub>, CO, and CH<sub>4</sub> measurements from tall towers in the NOAA Earth System Research Laboratory’s Global Greenhouse Gas Reference Network: instrumentation, uncertainty analysis, and recommendations for future high-accuracy greenhouse gas monitoring efforts. *Atmospheric Measurement Techniques*, 7:647–687, 2014.
- A. Angert, D. Yakir, M. Rodeghiero, Y. Preisler, E.A. Davidson, and T. Weiner. Using O<sub>2</sub> to study the relationships between soil CO<sub>2</sub> efflux and soil respiration. *Biogeosciences*, 12(7):2089–2099, 2015. doi: 10.5194/bg-12-2089-2015.

- H.J. Annegarn, L. Otter, R.J. Swap, and R.J. Scholes. Southern Africa's ecosystem in a test tube: A perspective on the Southern African Regional Science Initiative (SAFARI 2000). *South African Journal of Science*, 98:111–113, 2002.
- S. Archibald, D.P. Roy, B.W. van Wilgen, and R.J. Scholes. What limits fire? An examination of drivers of burnt area in Southern Africa. *Global Change Biology*, 15:613–630, 2009.
- D. L. Arévalo-Martínez, M. Beyer, M. Krumbholz, I. Piller, A. Kock, T. Steinhoff, A. Körtzinger, and H. W. Bange. A new method for continuous measurements of oceanic and atmospheric  $\text{N}_2\text{O}$ ,  $\text{CO}$  and  $\text{CO}_2$ : performance of off-axis integrated cavity output spectroscopy (OA-ICOS) coupled to non-dispersive infrared detection (NDIR). *Ocean Science*, 9(4):1071–1087, 2013. doi: 10.5194/os-9-1071-2013.
- F. Aspetsberger, M. Zabel, T. Ferdelman, U. Struck, A. Mackensen, A. Ahke, and U. Witte. Instantaneous benthic response to different organic matter quality: in situ experiments in the Benguela Upwelling System. *Marine Biology Research*, 3:342–356, 2007.
- M. Aubinet, T. Vesala, and D. Papale. *Eddy Covariance: A Practical Guide to Measurement and Data Analysis*. Springer, 2012.
- M. Aydin, K.R. Verhulst, E.S. Saltzman, M.O. Battle, S.A. Montzka, D.R. Blake, Q. Tang, and M.J. Prather. Recent decreases in fossil-fuel emissions of ethane and methane derived from firn air. *Nature*, 476:198–201, 2011.
- D.S. Baer, J.B. Paul, M. Gupta, and A. O'Keefe. Sensitive absorption measurements in the near-infrared region using off-axis integrated-cavity-output spectroscopy. *Applied Physics B*, 75:261–265, 2002. doi: 10.1007/s00340-002-0971-z.
- D.C.E. Bakker, H.W. Bange, N. Gruber, T. Johannessen, R.C. Upstill-Goddard, A.V. Borges, B. Delille, C.R. Löscher, W.A. Naqvi, A.M. Omar, and J.M. Santana-Casiano. Air–Sea Interactions of Natural Long-Lived Greenhouse Gases ( $\text{CO}_2$ ,  $\text{N}_2\text{O}$ ,  $\text{CH}_4$ ). In P.S. Liss and M.T. Johnson, editors, *Ocean-Atmosphere Interactions of Gases and Particles*, pages 113–169. Springer, 2014.
- A. Bakun. Global Climate Change and Intensification of Coastal Ocean Upwelling. *Science*, 247(4939):198–201, 1990.
- A. Bakun and S.J. Weeks. Greenhouse gas buildup, sardines, submarine eruptions and the possibility of abrupt degradation of intense marine upwelling systems. *Ecology Letters*, 7: 1015–1023, 2004.
- P.S. Bakwin, P.P. Tans, C. Zhao, W. III Ussler, and E. Quesnell. Measurements of carbon dioxide on a very tall tower. *Tellus*, 47B:535–549, 1995.
- P.S. Bakwin, K.J. Davis, C. Yi, S.C. Wofsy, J.W. Munger, and L. Haszpra. Regional carbon dioxide fluxes from mixing ratio data. *Tellus*, 56B:301–311, 2004.
- H.W. Bange, U.H. Bartell, S. Rapsomanikis, and M.O. Andreae. Methane in the Baltic and North Seas and a reassessment of the marine emissions of methane. *Global Biogeochemical Cycles*, 8(4):465–480, 1994.
- H.W. Bange, S. Rapsomanikis, and M.O. Andreae. Nitrous oxide in coastal waters. *Global Biogeochemical Cycles*, 10(1):197–207, 1996a.
- H.W. Bange, S. Rapsomanikis, and M.O. Andreae. Nitrous oxide emissions from the Arabian Sea. *Geophysical Research Letters*, 23(22):3175–3178, 1996b.

- H.W. Bange, R. Ramesh, S. Rapsomanikis, and M.O. Andreae. Methane in surface waters of the Arabian Sea. *Geophysical Research Letters*, 25(19):3547–3550, 1998.
- H.W. Bange, M.O. Andreae, S. Lal, C.S. Law, S.W.A. Naqvi, P.K. Patra, T. Rixen, and R.C. Upstill-Goddard. Nitrous oxide emissions from the Arabian Sea: A synthesis. *Atmospheric Chemistry and Physics*, 1(1):61–71, 2001. doi: 10.5194/acp-1-61-2001.
- H.W. Bange, T.G. Bell, M. Cornejo, A. Freing, G. Uher, R.C. Upstill-Goddard, and G. Zhang. MEMENTO: a proposal to develop a database of marine nitrous oxide and methane measurements. *Environmental Chemistry*, 6:195–197, 2009. doi: 10.1071/EN09033.
- H.W. Bange, A. Freing, A. Kock, and C.R. Löscher. Marine Pathways to Nitrous Oxide. In K. Smith, editor, *Nitrous Oxide and Climate Change*. Earthscan, London, U.K., 2010.
- K.B. Bartlett, G.W. Sachse, J.E. Jr. Collins, and R.C. Harriss. Methane in the tropical South Atlantic: Sources and distribution during the late dry season. *Journal of Geophysical Research*, 101(D19):24,139–24,150, 1996.
- T.S. Bates, K.C. Kelly, J.E. Johnson, and R.H. Gammon. Regional and seasonal variations in the flux of oceanic carbon monoxide to the atmosphere. *Journal of Geophysical Research*, 100(D11):23,093–23,101, 1995.
- T.S. Bates, K.C. Kelly, J.E. Johnson, and R.H. Gammon. A reevaluation of the open ocean source of methane to the atmosphere. *Journal of Geophysical Research*, 101(D3):6953–6961, 1996.
- M.J. Bender, P.P. Tans, J.T. Ellis, J. Orchardo, and K. Habfast. A high precision isotope ratio mass spectrometry method for measuring the  $O_2/N_2$  ratio of air. *Geochimica et Cosmochimica Acta*, 58:4751–4758, 1994.
- P. Bergamaschi, S. Houweling, A. Segers, M. Krol, C. Frankenberg, R.A. Scheepmaker, E. Dlugokencky, S.C. Wofsy, E.A. Kort, C. Sweeney, T. Schuck, C. Brenninkmeijer, H. Chen, V. Beck, and C. Gerbig. Atmospheric  $CH_4$  in the first decade of the 21<sup>st</sup> century: Inverse modeling analysis using SCHIAMACHY satellite retrievals and NOAA surface measurements. *Journal of Geophysical Research: Atmospheres*, 118:1–20, 2013. doi: 10.1002/jgrd.50480.
- I.T. Bertschi, R.J. Yokelson, D.E. Ward, T.J. Christian, and W. M. Hao. Trace gas emissions from the production and use of domestic biofuels in Zambia measured by open-path Fourier transform infrared spectroscopy. *Journal of Geophysical Research*, 108(D13):8469, 2003.
- D. Bianchi, J.P. Dunne, J. Sarmiento, and E. Galbraith. Data-based estimates of suboxia, denitrification, and  $N_2O$  production in the ocean and their sensitivities to dissolved  $O_2$ . *Global Biogeochemical Cycles*, 26:GB2009, 2012.
- B. Blanke, S. Speich, A. Bentamy, C. Roy, and B. Sow. Modeling the structure and variability of the southern Benguela upwelling using QuikSCAT wind forcing. *Journal of Geophysical Research: Oceans*, 110(C7):C07018, 2005. doi: 10.1029/2004JC002529.
- B.W. Blomquist, C.W. Fairall, B.J. Huebert, and S.T. Wilson. Direct measurement of the oceanic carbon monoxide flux by eddy correlation. *Atmospheric Measurement Techniques*, 5:3069–3075, 2012. doi: 10.5194/amt-5-3069-2012.
- T.A. Boden, G. Marland, and R.J. Andres. Global, Regional and National  $CO_2$  emissions. Carbon Dioxide Information Analysis Center, 2009.

- A. Bombelli, M. Henry, S. Castaldi, S. Adu-Bredu, A. Arneth, A. de Grandcourt, E. Grieco, W. L. Kutsch, V. Lehsten, A. Rasile, M. Reichstein, K. Tansey, U. Weber, and R. Valentini. An outlook on the Sub-Saharan Africa carbon balance. *Biogeosciences*, 6(10):2193–2205, 2009. doi: 10.5194/bg-6-2193-2009.
- W.J. Bond, F.I. Woodward, and G.F. Midgley. The global distribution of ecosystems in a world without fire. *New Phytologist*, 165:525–538, 2005.
- L. Bopp, C. Le Quéré, M. Heimann, A.C. Manning, and P. Monfray. Strong CO<sub>2</sub> emissions from the Arabian Sea during South-West Monsoon. *Global Biogeochemical Cycles*, 16(2):1022, 2002. doi: 10.1029/2001GB001445.
- P. Bousquet, P. Ciais, J.B. Miller, E.J. Dlugokencky, D.A. Hauglustaine, C. Prigent, G.R. van der Werf, P. Peylin, E.-G. Brunke, C. Carouge, R.L. Langenfelds, J. Lathière, F. Papa, M. Ramonet, M. Schmidt, L.P. Steele, S.C. Tyler, and J. White. Contribution of anthropogenic and natural sources to atmospheric methane variability. *Nature*, 443:439–443, 2006.
- D.M.J.S. Bowman, J.K. Balch, P. Artaxo, W.J. Bond, J.M. Carlson, M.A. Cochrane, C.M. D’Antonio, R.S. DeFries, J.C. Doyle, S.P. Harrison, F.H. Johnston, J.E. Keeley, M.A. Krawchuk, C.A. Kull, J.B. Marston, M.A. Moritz, I.C. Prentice, C.I. Roos, A.W. Scott, T.W. Swetnam, G. van der Werf, and S.J. Pyne. Fire in the Earth System. *Science*, 324:481–484, 2009.
- D. Boyer. Stock dynamics and ecology of pilchard in the northern Benguela. In M.J. O’Toole, editor, *The Benguela Current and Comparable Eastern Boundary Upwelling Ecosystems*, pages 79–82. GTZ GmbH, Eschborn, Germany, 1996.
- D. Boyer, J. Cole, and C. Bartholomae. Southwestern Africa: Northern Benguela Current Region. *Marine Pollution Bulletin*, 41(1–6):123–140, 2000.
- C.A.M. Brenninkmeijer, C. Koepfel, T. Röckmann, D.S. Scharffe, M. Braünlich, and V. Gros. Absolute measurements of the abundance of atmospheric carbon monoxide. *Journal of Geophysical Research*, 106(D9):10,003–10,010, 2001. doi: 10.5194/amt-5-3069-2012.
- J.C. Brimelow and J. van Heerden. Surface temperature and wind fields over the Skeleton Coast (Namibia) and adjacent interior during SAFARI-92. *Journal of Geophysical Research*, 101(D19):23,767–23,775, 1996.
- D. Brocard and J.-P. Lacaux. Domestic biomass combustion and associated atmospheric emissions in West Africa. *Global Biogeochemical Cycles*, 12(1):127–139, 1998.
- I.J. Brown, R. Torres, and A.P. Rees. The origin of sub-surface source waters define the sea-air flux of methane in the Mauritanian Upwelling, NW Africa. *Dynamics of Atmosphere and Oceans*, 67:39–46, 2014.
- V. Brüchert, M.E. Pérez, and C.B. Lange. Coupled primary production, benthic foraminiferal assemblage, and sulfur diagenesis in organic-rich sediments of the Benguela upwelling system. *Marine Geology*, 163:27–40, 2000.
- V. Brüchert, B.B. Jørgensen, K. Neumann, D. Riechmann, M. Schlösser, and H. Schulz. Regulation of bacterial sulfate reduction and hydrogen sulfide fluxes in the central Namibian coastal upwelling zone. *Geochimica et Cosmochimica Acta*, 67(23):4505–4518, 2003.



- V. Brüchert, B. Currie, K.R. Peard, U. Lass, R. Endler, A. Dübecke, E. Julies, T. Leipe, and S. Zitzmann. Biogeochemical and Physical Control on Shelf Anoxia and Water Column Hydrogen Sulphide in the Benguela Coastal Upwelling System Off Namibia. In L.N. Neretin, editor, *Past and Present Water Column Anoxia*, pages 161–193. Springer, the Netherlands, 2006.
- V. Brüchert, B. Currie, and K.R. Peard. Hydrogen sulphide and methane emissions on the central Namibian shelf. *Progress in Oceanography*, 83:169–179, 2009.
- E.-G. Brunke, C. Labuschagne, B. Parker, H.E. Scheel, and S. Whittlestone. Baseline air mass selection at Cape Point, South Africa: application of  $^{222}\text{Rn}$  and other filter criteria to  $\text{CO}_2$ . *Atmospheric Environment*, 38:5693–5702, 2004.
- R.P. Burger and S.J. Piketh. Re-evaluating the conceptual model describing the thermodynamic structure of the troposphere in the mid-latitudes. 29th Annual Conference of South African Society for Atmospheric Sciences, 26–27 September, Durban, South Africa, 2013.
- M.L. Calleja, C.M. Duarte, M. Álvarez, R. Vaquer-Sunyer, S. Augustí, and G.J. Herndl. Prevalence of strong vertical  $\text{CO}_2$  and  $\text{O}_2$  variability in the top meters of the ocean. *Global Biogeochemical Cycles*, 27:1–9, 2013. doi: 10.1002/gbc.20081.
- C. Campillo-Campbell and A. Gordoá. Physical and biological variability in the Namibian upwelling system: October 1997–October 2001. *Deep-Sea Research II*, 51:147–158, 2004.
- J.G. Canadell, M.R. Raupach, and R.A. Houghton. Anthropogenic  $\text{CO}_2$  emissions in Africa. *Biogeosciences*, 6:463–468, 2009.
- Z. Cao, M. Dai, W. Evans, J. Gan, and R. Feely. Diagnosing  $\text{CO}_2$  fluxes in the upwelling system off the Oregon–California coast. *Biogeosciences*, 11(22):6341–6354, 2014. doi: 10.5194/bg-11-6341-2014.
- D.G. Capone and D.A. Hutchins. Microbial biogeochemistry of coastal upwelling regimes in a changing ocean. *Nature Geoscience*, 6:711–717, 2013.
- M-E. Carr. Estimation of potential productivity in Eastern Boundary Currents using remote sensing. *Deep-Sea Research II*, 49:59–80, 2002.
- M-E. Carr and E.J. Kearns. Production regimes in four Eastern Boundary Current systems. *Deep-Sea Research II*, 50:3199–3221, 2003.
- F.P. Chavez and M. Messié. A comparison of Eastern Boundary Upwelling Ecosystems. *Progress in Oceanography*, 83:80–96, 2009.
- H. Chen, J. Winderlich, C. Gerbig, A. Hofer, C.W. Rella, E.R. Crosson, A.D. Van Pelt, J. Steinbach, O. Kolle, V. Beck, B.C. Daube, E.W. Gottlieb, V.Y. Chow, G.W. Santoni, and S.C. Wofsy. High-accuracy continuous airborne measurements of greenhouse gases ( $\text{CO}_2$  and  $\text{CH}_4$ ) using the cavity ring-down spectroscopy (CRDS) technique. *Atmospheric Measurement Techniques*, 3:375–386, 2010.
- H. Chen, A. Karion, C.W. Rella, J. Winderlich, C. Gerbig, A. Filges, T. Newberger, C. Sweeney, and P.P. Tans. Accurate measurements of carbon monoxide in humid air using the cavity ring-down spectroscopy (crds) technique. *Atmospheric Measurement Techniques*, 6:1031–1040, 2013.

- F. Chevallier, A. Fortems, P. Bousquet, I. Pison, S. Szopa, M. Devaux, and D. A. Hauglustaine. African CO emissions between years 2000 and 2006 as estimated from MOPITT observations. *Biogeosciences*, 6:103–111, 2009.
- P. Ciais, S.-L. Piao, P. Cadule, P. Friedlingstein, and A. Chédin. Variability and recent trends in the African terrestrial carbon balance. *Biogeosciences*, 6:1935–1948, 2009.
- P. Ciais, A. Bombelli, M. Williams, S.L. Piao, J. Chave, C.M. Ryan, M. Henry, P. Brender, and R. Valentini. The carbon balance of Africa: synthesis of recent research studies. *Philosophical Transactions of the Royal Society A*, 369:2038–2057, 2011.
- P. Ciais, C. Sabine, G. Bala, L. Bopp, V. Brovkin, J. Canadell, A. Chhabra, R. DeFries, J. Galloway, M. Heimann, C. Jones, R.B. Le Quéré, C. Myneni, S. Piao, and P. Thornton. Carbon and Other Biogeochemical Cycles. In T.F. Stocker, D. Qin, G.-K. Plattner, M. Tignor, S.K. Allen, J. Boschung, A. Nauels, Y. Xia, V. Bex, and P.M. Midgley, editors, *Climate Change 2013: The Physical Science Basis. Contribution of Working Group I to the Fifth Assessment Report of the Intergovernmental Panel on Climate Change*. Cambridge University Press, Cambridge, United Kingdom and New York, NY, USA, 2013.
- CIESIN. Center for International Earth Science Information Network (CIESIN), the Centro Internacional de Agricultura Tropical and Socioeconomic Data and Applications Center (SEDAC), and Columbia University. Gridded Population of the World, Verison 3 (GPWv3): Population Density Grid, 2005.
- J. Cihlar, S. Denning, F. Ahern, O. Arino, A. Belward, F. Bretherton, W. Cramer, G. Dedieu, C. Field, R.J. Francey, R. Gommes, J. Gosz, K. Hibbard, T. Igarashi, P. Kabat, D. Olson, S. Plummer, I. Rasool, M.R. Raupach, R.J. Scholes, J. Townshend, R. Valentini, and D. Wickland. Initiative to quantify terrestrial carbon sources and sinks. *Eos*, 83(1):6–7, 2002.
- P.G. Coble, C.E. Del Castillo, and B. Avril. Distribution and optical properties of CDOM in the Arabian Sea during the 1995 Southwest Monsoon. *Deep-Sea Research II*, 45:2195–2223, 1998.
- Y. Cohen and L.I. Gordon. Nitrous Oxide Production in the Ocean. *Journal of Geophysical Research*, 84(C1):347–353, 1979.
- T.J. Conway, P.M. Lang, and K.A. Masarie. Atmospheric Carbon Dioxide Dry Air Mole Fractions from the NOAA ESRL Carbon Cycle Cooperative Global Air Sampling Network, 1968-2010, Version: 2011-10-04. <ftp://ftp.cmdl.noaa.gov/ccg/co2/flask/event>, 2011.
- K.H. Cook. Role of Continents in Driving the Hadley Cells. *Journal of the Atmospheric Sciences*, 60:957–976, 2003.
- M. Cornejo, L. Fariás, and A. Paulmier. Temporal variability in N<sub>2</sub>O water content and its air–sea exchange in an upwelling area off central Chile (36°S). *Marine Chemistry*, 101: 85–94, 2006.
- C. Cosijn and P.D. Tyson. Stable discontinuities in the atmosphere over South Africa. *South African Journal of Science*, 92:381–386, 1996.
- E.R. Crosson. A cavity ring-down analyzer for measuring atmospheric levels of methane, carbon dioxide and water vapor. *Applied Physics B*, 92:403–408, 2008.

- P. Crutzen. A Discussion of the Chemistry of Some Minor Constituents in the Stratosphere and Troposphere. *Pure and Applied Geophysics*, 106–108:1385–1399, 1973.
- P.J. Crutzen and M.O. Andreae. Biomass Burning in the Tropics: Impact on Atmospheric Chemistry and Biogeochemical Cycles. *Science*, 250:1669–1678, 1990.
- D.A. Day and I. Faloona. Carbon monoxide and chromophoric dissolved organic matter cycles in the shelf water of the northern California upwelling system. *Journal of Geophysical Research*, 114:C01006, 2009. doi: 10.1029/2007JC004590.
- M.A. de Angelis and C. Lee. Methane production during zooplankton grazing on marine phytoplankton. *Limnology and Oceanography*, 39:1298–1308, 1994.
- A.T. de Laat. On the origin of tropospheric O<sub>3</sub> over the Indian Ocean during the winter monsoon: African biomass burning vs. stratosphere-troposphere exchange. *Atmospheric Chemistry and Physics*, 2:325–341, 2002.
- H.P.J. de Wilde and W. Helder. Nitrous oxide in the Somali Basin: the role of upwelling. *Deep-Sea Research II*, 44(6–7):1319–1340, 1997.
- D.P. Dee, S.M. Uppala, A.J. Simmons, P. Berrisford, P. Poli, S. Kobayashi, U. Andrea, A. Balmaseda, G. Balsamo, P. Bauer, P. Bechtold, A.C.M. Beljaars, L. van de Berg, J. Bidlot, N. Bormann, C. Delsol, R. Dragani, M. Fuentes, A.J. Geer, L. Haimberger, S.B. Healy, H. Hersbach, E.V. Hólm, L. Isaksen, P. Kållberg, M. Köhler, M. Matricardi, A.P. McNally, B.M. Monge-Sanz, J.-J. Morcrette, B.-K. Park, C. Peubey, P. de Rosnay, C. Tavolato, J.-N. Thépaut, and F. Vitart. The ERA-Interim reanalysis: configuration and performance of the data assimilation system. *Quarterly Journal of the Royal Meteorological Society*, 137(A):553–597, 2011.
- H. Demarcq. Trends in primary production, sea surface temperature and wind in upwelling systems (1998–2007). *Progress in Oceanography*, 83:376–385, 2009.
- H. Demarcq, R. Barlow, and L. Hutchings. Climatology and Variability of Sea Surface Temperature and Surface Chlorophyll in the Benguela and Agulhas Ecosystems As Observed by Satellite Imagery. *African Journal of Marine Science*, 25(1):363–372, 2003.
- H. Demarcq, R. Barlow, and L. Hutchings. Application of a chlorophyll index derived from satellite data to investigate the variability of phytoplankton in the Benguela system. *African Journal of Marine Science*, 29(2):271–282, 2007.
- F. Desbiolles, B. Blanke, A. Bentamy, and N. Grima. Origin of fine-scale wind stress curl structures in the Benguela and Canary upwelling systems. *Journal of Geophysical Research: Oceans*, 119:7931–7948, 2005. doi: 10.1002/2014JC010015.
- F. Desbiolles, B. Blanke, and A. Bentamy. Short-term upwelling events at the western African coast related to synoptic atmospheric structures as derived from satellite observations. *Journal of Geophysical Research: Oceans*, 119:1–23, 2014. doi: 10.1002/2013JC009278.
- P.A. Dirmeyer and J. Shukla. The effect on regional and global climate of expansion of the world’s deserts. *Quarterly Journal of the Royal Meteorological Society*, 122:451–482, 1996.
- E. Dlugokencky, L. Bruhwiler, J.W.C. White, L.K. Emmons, P.C. Novelli, S.A. Montzka, K.A. Masarie, P.M. Lang, A.M. Crotwell, J.B. Miller, and L.V. Gatti. Observational constraints on recent increases in the atmospheric CH<sub>4</sub> burden. *Geophysical Research Letters*, 36:L18803, 2009.

- E.J. Dlugokencky, L.P. Steele, P.M. Lang, and K.A. Masarie. The growth rate and distribution of atmospheric methane. *Journal of Geophysical Research*, 99(D8):17,021–17,043, 1994.
- E.J. Dlugokencky, P.M. Lang, and K.A. Masarie. Atmospheric Methane Dry Air Mole Fractions from the NOAA ESRL Carbon Cycle Cooperative Global Air Sampling Network, 1983-2009, Version: 2011-10-04. <ftp://ftp.cmdl.noaa.gov/ccg/ch4/flask/event/>, 2010.
- E.J. Dlugokencky, E.G. Nisbet, R. Fisher, and D. Lowry. Global atmospheric methane: budget, changes, and dangers. *Philosophical Transactions of the Royal Society A*, 369: 2058–2072, 2011. doi: 10.1098/rsta.2010.0341.
- R.R. Draxler. HYSPLIT4 User’s Guide. Technical report, NOAA Tech. Memo. ERL ARL-230, NOAA Air Resources Laboratory, Silver Spring, MD, USA., 1999.
- R.R. Draxler and G.D. Hess. Description of the HYSPLIT4 modeling system. Technical report, NOAA Tech. Memo. ERL ARL-224, NOAA Air Resources Laboratory, Silver Spring, MD, USA., 1997.
- R.R. Draxler and G.D. Hess. An overview of the HYSPLIT4 modelling system for trajectories, dispersion and deposition. *Australian Meteorological Magazine*, 47:295–308, 1998.
- B.N. Duncan, J.A. Logan, I. Bey, I.A. Megretskaia, R.M. Yantosca, P.C. Novelli, N.B. Jones, and C.P. Rinsland. Global budget of CO, 1988–1997: Source estimates and validation with a global model. *Journal of Geophysical Research - Atmospheres*, 112:D22301, 2007.
- C.M. Duncombe Rae. A demonstration of the hydrographic partition of the Benguela upwelling ecosystem at 26°40’S. *African Journal of Marine Science*, 27(3):617–628, 2005.
- F.D. Eckardt, K. Soderberg, L.J. Coop, A.A. Muller, K.J. Vickery, R.D. Grandin, C. Jack, T.S. Kapalanga, and J. Henschel. The nature of moisture at Gobabeb, in the central Namib Desert. *Journal of Arid Environments*, 93:7–19, 2013.
- D. Edwards. Fire Regimes in the Biomes of South Africa. In N.M. de V. Booyse, P. ad Tainton, editor, *Ecological Effects of Fire in South African Ecosystems*, volume 48, *Ecological Studies*, chapter 2. Springer-Verlag, 1984.
- D.H. Ehhalt. The atmospheric cycle of methane. *Tellus*, 26(1-2):58–70, 1974.
- K.-C. Emeis, V Brüchert, B. Currie, R. Endler, T. Ferdelman, A. Kiessling, T. Leipe, K. Noli-Peard, U. Struck, and T. Vogt. Shallow gas in shelf sediments of the Namibian coastal upwelling ecosystem. *Continental Shelf Research*, 24:627–642, 2004.
- W. Evans, B. Hales, and P.G. Stratton. Seasonal cycle of surface ocean  $p\text{CO}_2$  on the Oregon shelf. *Journal of Geophysical Research*, 116:C05012, 2011. doi: 10.1029/2010JC006625.
- W. Evans, B. Hales, P.G. Stratton, R.K. Shearman, and J.A. Barth. Failure to bloom: Intense upwelling results in negligible phytoplankton response and prolonged  $\text{CO}_2$  outgassing over the Oregon shelf. *Journal of Geophysical Research: Oceans*, 120, 2015. doi: 10.1002/2014JC010580.
- FAO. The role of Wood Energy in Africa. Technical Report FOPW/99/3, Food and Agriculture Organization, 1999.

- L. Farías, A. Paulmier, and M. Gallegos. Nitrous oxide and N-nutrient cycling in the oxygen minimum zone off northern Chile. *Deep-Sea Research I*, 54:164–180, 2007.
- L. Farías, C. Fernández, J. Faúndez, M. Cornejo, and M.E. Alcaman. Chemolithoautotrophic production mediating the cycling of the greenhouse gases  $\text{N}_2\text{O}$  and  $\text{CH}_4$  in an upwelling ecosystem. *Biogeosciences*, 6(12):3053–3069, 2009. doi: 10.5194/bg-6-3053-2009.
- W. Fennel. Theory of the Benguela Upwelling System. *Journal of Physical Oceanography*, 29:177–190, 1999.
- B.A. Flowers, H.H. Powers, M.K. Dubey, and N.G. McDowell. Inter-comparison of two high-accuracy fast-response spectroscopic sensors of carbon dioxide: a case study. *Atmospheric Measurement Techniques*, 5:991–997, 2012.
- P. Forster, V. Ramaswamy, P. Artaxo, T. Berntsen, R. Betts, D.W. Fahey, J. Haywood, J. Lean, D.C. Lowe, G. Myhre, D. Nganga, R. Prinn, G. Raga, M. Schulz, and R. Van Doorland. Changes in Atmospheric Constituents in Radiative Forcing. In S. Solomon, D. Qin, M. Manning, Z. Chen, M. Marquis, K.B. Averyt, M. Tignor, and H.L. Miller, editors, *Climate Change 2007: The Physical Science Basis. Contribution of Working Group I to the Fourth Assessment Report of the Intergovernmental Panel on Climate Change*. Cambridge University Press, Cambridge, UK and New York NY, USA, 2007.
- C.H. Frame, E. Deal, C.D. Nevison, and K.L. Casciotti.  $\text{N}_2\text{O}$  production in the eastern South Atlantic: Analysis of  $\text{N}_2\text{O}$  stable isotopic and concentration data. *Global Biogeochemical Cycles*, 28, 2014. doi: 10.1002/2013GB004790.
- R.J. Francey, C.M. Trudinger, M. van der Schoot, P.B. Krummel, L.P. Steele, and R.L. Langenfelds. Differences between trends in atmospheric  $\text{CO}_2$  and the reported trends in anthropogenic  $\text{CO}_2$  emissions. *Tellus*, 62B:316–328, 2010.
- A.C. Franco, J.M. Hernández-Ayón, E. Beier, V. Garçon, H. Maske, A. Paulmier, J. Färber-Lorda, R. Castro, and Sosa-Ávalos, R. Air-sea  $\text{CO}_2$  fluxes above the stratified oxygen minimum zone in the coastal region off Mexico. *Journal of Geophysical Research: Oceans*, 119:1161–1179, 2014. doi: 10.1002/2013JC009337.
- M.T. Freiman and P.D. Tyson. The thermodynamic structure of the atmosphere over South Africa: Implications for water vapour transport. *Water SA*, 26(2):153–158, 2000.
- C.S. Garbe, A. Rutgersson, J. Boutin, G. de Leeuw, B. Delille, C.W. Fairall, N. Gruber, J. Hare, D.T. Ho, M.T. Johnson, P.D. Nightingale, H. Pettersson, J. Piskozub, E. Sahlée, W.-T. Tsai, B. Ward, D.K. Woolf, and C.J. Zappa. Transfer Across the Air–Sea Interface. In P. Liss and M.T. Johnson, editors, *Ocean–Atmosphere Interactions of Gases and Particles*, pages 55–112. Springer, Heidelberg, Germany, 2014.
- H.E. García and L.I. Gordon. Oxygen solubility in seawater: Better fitting equations. *Limnology and Oceanography*, 37(6):1307–1312, 1992.
- M. Garstang, P.D. Tyson, R. Swap, M. Edwards, P. Kållberg, and J.A. Lindesay. Horizontal and vertical transport of air over southern africa. *Journal of Geophysical Research*, 101 (D19):23,721–23,736, 1996.
- GCP. The Human Perturbation of the Carbon Cycle. Report of the Global Carbon Project, 2011.

- C. Geels, S.C. Doney, R. Dargaville, J. Brandt, and J.H. Christensen. Investigating the sources of synoptic variability in atmospheric CO<sub>2</sub> measurements over the Northern Hemisphere continents: a regional model study. *Tellus*, 56B:35–50, 2004.
- M. Ghil, M.R. Allen, M.D. Dettinger, K. Ide, D. Kondrashov, M.E. Mann, A.W. Robertson, A. Saunders, Y. Tian, F. Varadi, and P. Yiou. Advanced Spectral Methods for Climatic Time Series. *Reviews of Geophysics*, 40(1):1–1–41, 2002. doi: 10.1029/2001RG000092.
- A. Ghosh, P. K. Patra, K. Ishijima, T. Umezawa, A. Ito, D.M. Etheridge, S. Sugawara, K. Kawamura, J.B. Miller, E.J. Dlugokencky, P.B. Krummel, P.J. Fraser, L.P. Steele, R.L. Langenfelds, C.M. Trudinger, J.W.C. White, B. Vaughn, T. Saeki, S. Aoki, and T. Nakazawa. Variations in global methane sources and sinks during 1910-2010. *Atmospheric Chemistry and Physics*, 15(5):2595–2612, 2015. doi: 10.5194/acp-15-2595-2015.
- L. Giglio, J.T. Randerson, and G.R. van der Werf. Analysis of daily, monthly, and annual burned area using the fourth generation Global Fire Emissions Database (GFED4). *Journal of Geophysical Research: Biogeosciences*, 2013. doi: 10.1002/jgrg.20042.
- M. Gloor, S.-M. Fan, S. Pacala, and J. Sarmiento. Optimal sampling of the atmosphere for purpose of inverse modeling: A model study. *Global Biogeochemical Cycles*, 14(1):407–428, 2000.
- M. Gloor, P. Bakwin, D. Hurst, L. Lock, R. Draxler, and P. Tans. What is the concentration footprint of a tall tower? *Journal of Geophysical Research*, 106(D16):17,831–17,840, 2001.
- Y. Goldreich and P.D. Tyson. Diurnal and Inter-diurnal Variations in Large-Scale Atmospheric Turbulence Over Southern Africa. *South African Geographical Journal*, 70(1): 48–56, 1988.
- M. González-Dávila, J.M. Santana-Casiano, and I.R. Ucha. Seasonal variability of  $f\text{CO}_2$  in the Angola-Benguela region. *Progress in Oceanography*, 83:124–133, 2009.
- K.S. Goubanova, S. Illig, E. Machu, V. Garçon, and B. Dewitte. SST subseasonal variability in the central Benguela upwelling system as inferred from satellite observations (1999–2009). *Journal of Geophysical Research: Oceans*, 118, 2013. doi: 10.1002/jgrc.20287.
- L. Gregor and P.M.S. Monteiro. Is the southern Benguela a significant regional sink of CO<sub>2</sub>? *South African Journal of Science*, 109(5/6):0094, 2013a. doi: 10.1590/sajs.2013/20120094.
- L. Gregor and P.M.S. Monteiro. Seasonal cycle of N:P:TA stoichiometry as a modulator of CO<sub>2</sub> buffering in eastern boundary upwelling systems. *Geophysical Research Letters*, 40: 1–6, 2013b. doi: 10.1002/2013GL058036.
- N. Gruber, M. Gloor, S.-M. Fan, and J.L. Sarmiento. Air-sea flux of oxygen estimated from bulk data: Implications for the marine and atmospheric oxygen cycles. *Global Biogeochemical Cycles*, 15(4):783–803, 2001.
- K.R. Gurney, R.M. Law, S. Denning, P.J. Rayner, D. Baker, P. Bousquet, L. Bruhwiler, Y.-H. Chen, P. Ciais, S.-M. Fan, I.Y. Fung, M. Gloor, M. Heimann, K. Higuchi, J. John, T. Maki, S. Maksyutov, K.A. Masarie, P. Peylin, M.J. Prather, B.C. Pak, J.T. Randerson, J. Sarmiento, S. Taguchi, T. Takahashi, and C.-W. Yuen. Towards robust regional estimates of CO<sub>2</sub> sources and sinks using atmospheric transport models. *Nature*, 415:626–630, 2002.

- K.R. Gurney, R.M. Law, S. Denning, P.J. Rayner, D. Baker, P. Bousquet, L. Bruhwiler, Y.-H. Chen, P. Ciais, S.-M. Fan, I.Y. Fung, M. Gloor, M. Heimann, K. Higuchi, J. John, E. Kowalczyk, T. Maki, S. Maksyutov, P. Peylin, M.J. Prather, B.C. Pak, , J. Sarmiento, S. Taguchi, T. Takahashi, and C.-W. Yuen. TransCom 3 CO<sub>2</sub> inversion intercomparison: 1. Annual mean control results and sensitivity to transport and prior flux information. *Tellus*, 55B:555–579, 2003.
- K.R. Gurney, R.M. Law, S. Denning, P.J. Rayner, B.C. Pak, D. Baker, P. Bousquet, L. Bruhwiler, Y.-H. Chen, P. Ciais, I.Y. Fung, M. Heimann, J. John, T. Maki, S. Maksyutov, P. Peylin, M.J. Prather, and S. Taguchi. TransCom 3 inversion intercomparison: Model mean results for the estimation of seasonal carbon sources and sinks. *Global Biogeochemical Cycles*, 18:GB1010, 2004. doi: 10.1029/2003GB002111.
- E. Gutknecht, I. Dadou, B. Le Vu, G. Cambon, J. Sudre, V. Garçon, E. Machu, T. Rixen, A. Kock, A. Flohr, A. Paulmier, and G. Lavik. Coupled physical/biogeochemical modeling including O<sub>2</sub>-dependent processes in the Eastern Boundary Upwelling Systems: application in the Benguela. *Biogeosciences*, 10(6):3559–3591, 2013a. doi: 10.5194/bg-10-3559-2013.
- E. Gutknecht, I. Dadou, P. Marchesiello, G. Cambon, B. Le Vu, J. Sudre, V. Garçon, E. Machu, T. Rixen, A. Kock, A. Flohr, A. Paulmier, and G. Lavik. Nitrogen transfers off Walvis Bay: a 3-D coupled physical/biogeochemical modeling approach in the Namibian upwelling system. *Biogeosciences*, 10(6):4117–4135, 2013b. doi: 10.5194/bg-10-4117-2013.
- P. Guyon, G.P. Frank, M. Welling, D. Chand, P. Artaxo, L. Rizzo, G. Nishioka, O. Kolle, H. Fritsch, M.A. F Silva Dias, L.V. Gatti, A.M. Cordova, and M.O. Andreae. Airborne measurements of trace gas and aerosol particle emissions from biomass burning in Amazonia. *Atmospheric Chemistry and Physics*, 5(11):2989–3002, 2005. doi: 10.5194/acp-5-2989-2005.
- G. Hadley. Concerning the Cause of the General Trade-Winds: By Geo. Hadley, Esq: F.R.S. *Philosophical Transactions*, 39:58–62, 1735.
- E. Hagen, R. Feistel, J.J. Aagenbag, and T. Ohde. Seasonal and interannual changes in Intense Benguela Upwelling (1982–1999). *Oceanologica Acta*, 24(6):557–568, 2001.
- M. Hall. Man’s Historical and Traditional Use of Fire in Southern Africa. In N.M. de V. Booyse, P. ad Tainton, editor, *Ecological Effects of Fire in South African Ecosystems*, volume 48, *Ecological Studies*, chapter 3. Springer-Verlag, 1984.
- R.C. Hamme and R.F. Keeling. Ocean ventilation as a driver of interannual variability in atmospheric potential oxygen. *Tellus*, 60B:706–717, 2008.
- A. Hänsler. *Impact of Climate Change on the Coastal Climate of South-Western Africa*. Ph.D. Thesis, University of Hamburg, 2011.
- W.M. Hao, D.E. Ward, G. Olbu, and S.P. Baker. Emissions of CO<sub>2</sub>, CO, and hydrocarbons from fires in diverse African savanna ecosystems. *Journal of Geophysical Research*, 101 (D19):23,577–23,584, 1996.
- N.J. Hardman-Mountford, A.J. Richardson, J.J. Aagenbag, E. Hagen, L. Nykjaer, F.A. Shillington, and C. Villacastin. Ocean climate of the South East Atlantic observed from satellite data and wind models. *Progress in Oceanography*, 59:181–221, 2003.
- N.C.G. Hart, C.J.C. Reason, and N. Fauchereau. Tropical-Extratropical Interactions over Southern Africa: Three Cases of Heavy Summer Season Rainfall. *Monthly Weather Review*, 138:2608–2623, 2010.

- L. Haszpra, M. Ramonet, M. Schmidt, Z. Barcza, Z. Pátkal, K. Tarczay, C. Yver, J. Tarniewicz, and P. Ciais. Variation of CO<sub>2</sub> mole fraction in the lower free troposphere, in the boundary layer and at the surface. *Atmospheric Chemistry and Physics*, 12: 11,539–11,566, 2012.
- J. Haywood, S.R. Osborne, P.N. Francis, A. Keil, P. Formenti, M.O. Andreae, and P.H. Kaye. The mean physical and optical properties of regional haze dominated by biomass burning aerosol measured from the C-130 aircraft during SAFARI 2000. *Journal of Geophysical Research*, 108(D13):8473, 2003.
- M. Heimann. Enigma of the recent methane budget. *Nature*, 476:157–158, 2011.
- M. Heimann, G. Esser, A. Haxeltine, J. Kaduk, D.W. Kicklighter, W. Knorr, G.H. Kohlmaier, A.D. McGuire, J. Melillo, B. Moore III, R.D. Otto, I.C. Prentice, W. Sauf, A. Schloss, S. Sitch, U. Wittenberg, and Würth, G. Evaluation of terrestrial carbon cycle models through simulations of the seasonal cycle of atmospheric CO<sub>2</sub>: First results of a model intercomparison study. *Global Biogeochemical Cycles*, 12(1):1–24, 1998.
- J.J. Heymans, L.J. Shannon, and A. Jarre. Changes in the northern Benguela ecosystem over three decades: 1970s, 1980s, and 1990s. *Ecological Modelling*, 172:175–195, 2004.
- R.C. Hills. The Structure of the Inter-Tropical Convergence Zone in Equatorial Africa and Its Relationship to East African Rainfall. *Transactions of the Institute of British Geographers*, 4(3):329–352, 1979.
- D.T. Ho, R. Wanninkhof, P. Schlosser, D.S. Ullman, D. Hebert, and K.F. Sullivan. Toward a universal relationship between wind speed and gas exchange: Gas transfer velocities measured with <sup>3</sup>He/SF<sub>6</sub> during the Southern Ocean Gas Exchange Experiment. *Journal of Geophysical Research*, 116:C00F04, 2011.
- P.V. Hobbs. Clean air slots amid dense atmospheric pollution in southern Africa. *Journal of Geophysical Research*, 108(D13):8490, 2003.
- P.V. Hobbs, P. Sinha, R.J. Yokelson, T.J. Christian, D.R. Blake, S. Gao, T.W. Kirchstetter, T. Novakov, and P. Pilewskie. Evolution of gases and particles from a savanna fire in South Africa. *Journal of Geophysical Research*, 108(D13):8485, 2003.
- W.C. Hockaday, C.A. Masiello, J.T. Randerson, R.J. Smernik, J.A. Baldock, O.A. Chadwick, and J.W. Harden. Measurement of soil carbon oxidation state and oxidative ratio by <sup>13</sup>CO<sub>2</sub> nuclear magnetic resonance. *Journal of Geophysical Research*, 114:GB02014, 2009. doi: 10.1029/2008JG000803.
- E.A. Hoffa, D.E. Ward, W.M. Hao, R.A. Susott, and R.H. Wakimoto. Seasonality of carbon emissions from biomass burning in a Zambian savanna. *Journal of Geophysical Research*, 104(D11):13,841–13,853, 1999.
- P.B. Hooghiemstra, M.C. Krol, P. Bergamaschi, A.T.J. de Laat, G.R. van der Werf, P.C. Novelli, M.N. Deeter, I. Aben, and T. Röckmann. Comparing optimized CO emission estimates using MOPITT or NOAA surface network observations. *Journal of Geophysical Research*, 117:D06309, 2012.
- T.W. Horst and J.C. Weil. How Far is Far Enough?: The Fetch Requirements for Micrometeorological Measurement of Surface Fluxes. *Journal of Atmospheric and Oceanic Technology*, 11:1018–1025, 1994.



- S. Houweling, M. Krol, P. Bergamaschi, C. Frankenberg, E.J. Dlugokencky, I. Morino, J. Notholt, V. Sherlock, D. Wunch, V. Beck, C. Gerbig, H. Chen, E. A. Kort, T. Röckmann, and I. Aben. A multi-year methane inversion using SCIAMACHY, accounting for systematic errors using TCCON measurements. *Atmospheric Chemistry and Physics*, 14(8):3991–4012, 2014. doi: 10.5194/acp-14-3991-2014.
- L. Hu, S.A. Yvon-Lewis, J.D. Kessler, and I.R. MacDonald. Methane fluxes to the atmosphere from deepwater hydrocarbon seeps in the northern Gulf of Mexico. *Journal of Geophysical Research*, 117:C01009, 2012. doi: 10.1029/2011JC007208.
- D.N. Huntzinger, S.M. Gourdj, K.L. Mueller, and A.M. Michalak. The utility of continuous atmospheric measurements for identifying biospheric CO<sub>2</sub> flux variability. *Journal of Geophysical Research*, 116:D06110, 2011. doi: 10.1029/2010JD015048.
- L. Hutchings, C.D. van der Lingen, L.J. Shannon, R.J.M. Crawford, H.M.S. Verheye, C.H. Bartholomae, A.K. van der Plas, D. Louw, A. Kreiner, M. Ostrowski, Q. Fidel, R. G. Barlow, T. Lamont, J. Coetzee, F. Shillington, J. Veitch, J. C. Currie, and P.M.S. Monteiro. The Benguela Current: An ecosystem of four components. *Progress in Oceanography*, 83:15–32, 2009.
- P. Hutchinson. The climatology of Namibia and its relevance to the drought situation. In *Coping with Aridity*, pages 17–37. NEPRU, 1995.
- A. Inness, F. Baier, A. Benedetti, I. Bouarar, S. Chabrilat, H. Clark, C. Clerbaux, P. Coheur, R.J. Engelen, Q. Errera, J. Flemming, M. George, C. Granier, J. Hadji-Lazaro, V. Huijnen, D. Hurtmans, L. Jones, J.W. Kaiser, J. Kapsomenakis, K. Lefever, J. Leitão, M. Razinger, A. Richter, M.G. Schultz, A.J. Simmons, M. Suttie, O. Stein, J.-N. Thépaut, V. Thouret, M. Vrekoussis, C. Zerefos, and the MACC team. The MACC reanalysis: an 8 yr data set of atmospheric composition. *Atmospheric Chemistry and Physics*, 13(8):4073–4109, 2013. doi: 10.5194/acp-13-4073-2013.
- M. Inthorn, T. Wagner, G. Scheeder, and M. Zabel. Lateral transport controls distribution, quality, and burial of organic matter along continental slopes in high-productivity areas. *Geology*, 34:205–208, 2006.
- S. Ishidoya, S. Murayama, C. Takamura, H. Kondo, N. Saigusa, D. Goto, S. Morimoto, N. Aoki, S. Aoki, and T. Nakazawa. O<sub>2</sub>:CO<sub>2</sub> exchange ratios observed in a cool temperate deciduous forest ecosystem of central Japan. *Tellus B*, 65:21120, 2013. doi: 10.3402/tellusb.v65i0.21120.
- K. Ishijima, T. Nakazawa, and S. Aoki. Variations of atmospheric nitrous oxide concentration in the northern and western Pacific. *Tellus*, 61B:408–415, 2009.
- S.P. Jackson. Sea Breezes in South Africa. *South African Geographical Journal*, 36:13–23, 1954.
- D.J. Jacob. *Introduction to Atmospheric Chemistry*. Princeton University Press, Princeton, NJ, 1999.
- B. Jähne, G. Heinz, and W. Dietrich. Measurement of the Diffusion Coefficients of Sparingly Soluble Gases in Water. *Journal of Geophysical Research*, 92(C10):10,767–10,776, 1987.
- X. Jiang, W.L. Ku, R-L Shia, Q. Li, J.W. Elkins, R.G. Prinn, and Y.L. Yung. Seasonal cycle of N<sub>2</sub>O: Analysis of data. *Global Biogeochemical Cycles*, 21:GB1006, 2007.

- M.T. Johnson, C. Hughes, T.G. Bell, and P.S. Liss. A Rumsfeldian analysis of uncertainties in air–sea gas exchange. In S. Komori, W. McGillis, and R. Kurose, editors, *Gas Transfer at Water Surfaces*, pages 568–587. Kyoto University Press, Kyoto, Japan, 2011.
- C. Jost, J. Trentmann, D. Sprung, M.O. Andreae, J.B. McQuaid, and H. Barjat. Trace gas chemistry in a young biomass burning plume over Namibia: Observations and model simulations. *Journal of Geophysical Research*, 108(D13):8482, 2003a.
- C. Jost, J. Trentmann, D. Sprung, M.O. Andreae, and K. Dewey. Deposition of acetonitrile to the Atlantic Ocean off Namibia and Angola and its implications for the atmospheric budget of acetonitrile. *Geophysical Research Letters*, 30(16):1837, 2003b. doi: 10.1029/2003GL017347.
- N. Juergens, J. Oldeland, B. Hachfeld, E. Erb, and C. Schultz. Ecology and spatial patterns of large-scale vegetation units within the central Namib Desert. *Journal of Arid Environments*, 93:59–79, 2013.
- C.O. Justice, J.D. Kendall, P.R. Dowty, and R.J. Scholes. Satellite remote sensing of fires during the SAFARI campaign using NOAA advanced very high resolution radiometer data. *Journal of Geophysical Research*, 101(D19):23,851–23,863, 1996.
- C.G. Justus and A. Mikhail. Height variation of wind speed and wind distributions statistics. *Geophysical Research Letters*, 3(5):261–264, 1976.
- F.M. Kai, S.C. Tyler, J.T. Randerson, and D.R. Blake. Reduced methane growth rate explained by decreased Northern Hemisphere microbial sources. *Nature*, 476:194–197, 2011.
- S.M. Kang and J. Lu. Expansion of the Hadley Cell Under Global Warming: Winter versus Summer. *Journal of Climate*, 25:8387–8394, 2012.
- D.M. Karl and B.D. Tilbrook. Production and transport of methane in oceanic particulate organic matter. *Nature*, 368:732–734, 1994.
- D.M. Karl, L. Beversdorf, K.M. Björkman, M.J. Church, A. Martinez, and E.F. DeLong. Aerobic production of methane in the sea. *Nature Geoscience*, 1:473–478, 2008.
- B. Kartal, M.M.M. Kuypers, G. Lavik, J. Schalk, H.J.M. Op den Camp, M.S.M. Jetten, and M. Strous. Anammox bacteria disguised as denitrifiers: nitrate reduction to dinitrogen gas via nitrite and ammonium. *Environmental Microbiology*, 9(3):635–642, 2007.
- C.D. Keeling. The Suess Effect:  $^{13}\text{C}$ - $^{14}\text{C}$  Interrelations. *Environment International*, 2:229–300, 1979.
- R.F. Keeling. *Development of an Interferometric Oxygen Analyzer for Precise Measurement of the Atmospheric  $\text{O}_2$  Mole Fraction*. Ph.D. Thesis, Harvard University, 1988.
- R.F. Keeling and A.C. Manning. Studies of Recent Changes in Atmospheric  $\text{O}_2$  Content. In H.D. Holland and K.K. Turekian, editors, *Treatise on Geochemistry*, volume 5.15, pages 385–405. Elsevier, 2014.
- R.F. Keeling and S.R. Shertz. Seasonal and interannual variations in atmospheric oxygen and implications for the global carbon cycle. *Nature*, 358:723–727, 1992.
- R.F. Keeling, R.P. Najjar, M.L. Bender, and P.P. Tans. What Atmospheric Oxygen Measurements Can Tell Us About the Global Carbon Cycle. *Geophysical Research Letter*, 7(1):37–67, 1993.

- R.F. Keeling, S.C. Piper, and M. Heimann. Global and hemispheric CO<sub>2</sub> sinks deduced from changes in atmospheric O<sub>2</sub> concentration. *Nature*, 381:218–221, 1996.
- R.F. Keeling, A.C. Manning, E.M. McEvoy, and S.R. Shertz. Methods for measuring changes in atmospheric O<sub>2</sub> concentration and their application in southern hemisphere air. *Journal of Geophysical Research*, 103(D3):3381–3397, 1998a.
- R.F. Keeling, B.B. Stephens, R.G. Najjar, S.C. Doney, D. Archer, and M. Heimann. Seasonal variations in the atmospheric O<sub>2</sub>/N<sub>2</sub> ratio in relation to the kinetics of air-sea gas exchange. *Global Biogeochemical Cycles*, 12(1):141–163, 1998b.
- W.C. Keene, J.M. Lobert, P.J. Crutzen, J.R. Maben, D.H. Scharffe, T. Landmann, C. Hély, and C. Brain. Emissions of major gaseous and particulate species during experimental burns of southern African biomass. *Journal of Geophysical Research*, 111(11):D04301, 2006.
- C.A. Kelley and W.H. Jeffrey. Dissolved methane concentration profiles and air-sea fluxes from 41°S to 27°N. *Global Biogeochemical Cycles*, 16(3):1040, 2002.
- G.A. Kirkman, S.J. Piketh, M.O. Andreae, H.J. Annegarn, and G. Helas. Distribution of aerosols, ozone and carbon monoxide over southern Africa. *South African Journal of Science*, 96:423–431, 2000.
- S. Kirschke, P. Bousquet, P. Ciais, M. Saunois, J.G. Canadell, E.J. Dlugokencky, P. Bergamaschi, D. Bergmann, D.R. Blake, L. Bruhwiler, P. Cameron-Smith, S. Castaldi, F. Chevallier, L. Feng, A. Fraser, M. Heimann, E.L. Hodson, S. Houweling, B. Josse, P.J. Fraser, P.B. Krummel, J.-F. Lamarque, R.L. Langenfelds, C. Le Quéré, V. Naik, S. O’Doherty, P.I. Palmer, I. Pison, D. Plummer, B. Poulter, R.G. Prinn, M. Rigby, B. Ringeval, M. Santini, M. Schmidt, D.T. Shindell, I.J. Simpson, R. Spahni, L. P. Steele, S.A. Strode, Ke. Sudo, S. Szopa, G.R. van der Werf, A. Voulgarakis, M. van Weele, R.F. Weiss, J.E. Williams, and G. Zeng. Three decades of global methane sources and sinks. *Nature Geoscience*, 6(10):813–823, 2013.
- V. Kitidis, G.H. Tilstone, T.J. Smyth, R. Torres, and C.S. Law. Carbon monoxide emission from a Mauritanian upwelling filament. *Marine Chemistry*, 127:123–133, 2011.
- A. Kock, S. Gebhardt, and H.W. Bange. Methane emissions from the upwelling area off Mauritania (NW Africa). *Biogeosciences*, 5:1119–1125, 2008.
- A. Kock, J. Schafstall, M. Dengler, P. Brandt, and H.W. Bange. Sea-to-air and diapycnal nitrous oxide fluxes in the eastern tropical North Atlantic Ocean. *Biogeosciences*, 9:957–964, 2012.
- M. Kopacz, D.J. Jacob, J.A. Fisher, J.A. Logan, L. Zhang, I.A. Megretskaja, R.M. Yantosca, K. Singh, D.K. Henze, J.P. Burrows, M. Buchwitz, I. Khlystova, W.W. McMillan, J.C. Gille, D.P. Edwards, A. Eldering, V. Thouret, and P. Nedelec. Global estimates of CO sources with high resolution by adjoint inversion of multiple satellite datasets (MOPITT, AIRS, SCIAMACHY, TES). *Atmospheric Chemistry and Physics*, 10(3):855–876, 2010. doi: 10.5194/acp-10-855-2010.
- E.A. Kort, P.K. Patra, K. Ishijima, B.C. Daube, J.L. Jiménez, J.W. Elkins, D. Hurst, F.L. Moore, C. Sweeney, and S.C. Wofsy. Tropospheric distribution and variability of N<sub>2</sub>O: Evidence for strong tropical emissions. *Geophysical Research Letters*, 38:L15806, 2011.

- A. Körtzinger, J.C. Duinker, and L. Mintrop. Strong CO<sub>2</sub> emissions from the Arabian Sea during South-West Monsoon. *Geophysical Research Letters*, 24(14):1763–1766, 1997.
- M. Kottek, J. Grieser, C. Beck, B. Rudolf, and F. Rubel. World Map of the Köppen-Geiger climate classification updated. *Meteorologische Zeitschrift*, 15(3):259–263, 2006.
- E.A. Kozlova and A.C. Manning. Methodology and calibration for continuous measurements of biogeochemical trace gas and O<sub>2</sub> concentrations from a 300-m tall tower in central Siberia. *Atmospheric Measurement Techniques*, 2:205–220, 2009.
- E.A. Kozlova, A.C. Manning, Y. Kisilyakhov, T. Seifert, and M. Heimann. Seasonal, synoptic, and diurnal-scale variability of biogeochemical trace gases and O<sub>2</sub> from a 300-m tall tower in central Siberia. *Global Biogeochemical Cycles*, 22:GB4020, 2008.
- Andrew Ku. Investigation: Is your ssd more reliable than a hard drive?, July 2011. URL <http://www.tomshardware.com/reviews/ssd-reliability-failure-rate,2923.html>.
- I. Kuhnel. Tropical-extratropical cloudband climatology. *International Journal of Climatology*, 9:441–463, 1989.
- W.L. Kutsch, L. Merbold, W. Ziegler, M.M. Mukelabai, M. Muchinda, O. Kolle, and R.J. Scholes. The charcoal trap: Miombo forests and the energy needs of people. *Carbon Balance and Management*, 6(5), 2011.
- M.M.M. Kuypers, G. Lavik, D. Woebken, M. Schmid, B.M. Fuchs, R. Amann, and B.B. Jørgensen. Massive nitrogen loss from the Benguela upwelling system through anaerobic ammonium oxidation. *Proceedings of the National Academy of Sciences*, 102(18):6478–6483, 2005.
- G. Lambert and S. Schmidt. Reevaluation of the Oceanic Flux of Methane: Uncertainties and Long Term Variations. *Chemosphere*, 26(1–4):579–589, 1993.
- J. Lancaster, N. Lancaster, and M.K. Seely. Climate of the central Namib desert. *Madoqua*, 14:5–61, 1984.
- N. Lancaster. Winds and Sand Movements in the Namib Sand Sea. *Earth Surface Processes and Landforms*, 10:607–619, 1985.
- D.V. Land, A.P. Levick, and J.W. Hand. The use of the Allan deviation for the measurement of the noise and drift performance of microwave radiometers. *Measurement Science and Technology*, 18:1917–1928, 2007.
- R.L. Langenfelds, R.J. Francey, B.C. Pak, L.P. Steele, J. Lloyd, C.M. Trudinger, and C.E. Allison. Interannual growth rate variations of atmospheric CO<sub>2</sub> and its  $\delta^{13}\text{C}$ , H<sub>2</sub>, CH<sub>4</sub>, and CO between 1992 and 1999 linked to biomass burning. *Global Biogeochemical Cycles*, 16(3):1048, 2002.
- B. Langmann, B. Duncan, C. Textor, J. Trentmann, and G.R. van der Werf. Vegetation fire emissions and their impact on air pollution and climate. *Atmospheric Environment*, 43: 107–116, 2009.
- G.G. Laruelle, R. Lauerwald, B. Pfeil, and P. Regnier. Regionalized global budget of the CO<sub>2</sub> exchange at the air-water interface in continental shelf seas. *Geophysical Research Letters*, 28(11):1199–1214, 2014. doi: 10.1002/2014GB004832.

- C. Lauk and K.-H. Erb. Biomass consumed in anthropogenic vegetation fires: Global patterns and processes. *Ecologic Economics*, 69:301–309, 2009.
- R.M. Law, P.J. Rayner, L.P. Steele, and I.G. Enting. Using high temporal frequency data for CO<sub>2</sub> inversions. *Global Biogeochemical Cycles*, 16(4):1053, 2002.
- K. Lee, L.T. Tong, F.J. Millero, C.L. Sabine, A.G. Dickson, C. Goyet, G.-H. Park, R. Wanninkhof, R.A. Feely, and R.M. Key. Global relationships of total alkalinity with salinity and temperature in surface waters of the world’s oceans. *Geophysical Research Letters*, 33:L19605, 2006. doi: 10.1029/2006GL027207.
- V. Lehsten, K. Tansey, H. Balzter, K. Thonicke, A. Spessa, U. Weber, B. Smith, and A. Arneeth. Estimating carbon emissions from African wildfires. *Biogeosciences*, 6:349–360, 2009.
- J. Lelieveld, P. Crutzen, and F.J. Dentener. Changing concentrations, lifetime and climate forcing of atmospheric methane. *Tellus*, 50B:128–150, 1998.
- J.R. Lengoasa, J.A. Lindesay, and A.M. van Nierop. The influence of a synoptic-scale disturbance on topographically induced boundary layer circulations over the central Namib Desert. *Madoqua*, 18(2):71–78, 1993.
- L.A. Levin, K.K. Liu, K.-C. Emeis, D.L. Breitburg, J. Cloern, C. Deutsch, M. Giani, A. Goffart, E.E. Hofmann, Z. Lachkar, K. Limburg, S.-M. Liu, E. Montes, W. Naqvi, O. Ragueneau, C. Rabouille, S.K. Sarkar, D.P. Swaney, P. Wassman, and K.F. Wishner. Comparative biogeochemistry-ecosystem-human interactions on dynamic continental margins. *Journal of Marine Systems*, 141(0):3–17, 2015. doi: 10.1016/j.jmarsys.2014.04.016.
- J.C. Lin, C. Gerbig, S.C. Wofsy, A.E. Andrews, B.C. Daube, K.J. Davis, and C.A. Grainger. A near-field tool for simulating the upstream influence of atmospheric observations: The Stochastic Time-Inverted Lagrangian Transport (STILT) model. *Journal of Geophysical Research*, 108(D16):4493, 2003. doi: 10.1029/2002JD003161.
- J.A. Lindesay and P.D. Tyson. Thermo-topographically Induced Boundary Layer Oscillations Over the Central Namib, Southern Africa. *International Journal of Climatology*, 101: 63–77, 1990.
- C. Liousse, E. Assamoi, P. Criqui, C. Granier, and R. Rosset. Explosive growth in African combustion emissions from 2005 to 2030. *Environmental Research Letters*, 9(14):035003, 2014. doi: 10.5194/acp-11-6787-2011.
- P.S. Liss and L. Merlivat. Air-Sea Gas Exchange Rates: Introduction and Synthesis. In P. Buat-Ménard, editor, *The Role of Air-Sea Exchange in Geochemical Cycling*, pages 113–127. Reidel Publishing Company, Dordrecht, the Netherlands, 1986.
- E.N. Lorenz. The Nature and Theory of the General Circulation of the Atmosphere. World Meteorological Organization. No. 218, TP 115, 1967.
- S. Loucaides, T. Tyrrell, E.P. Achterberg, R. Torres, P.D. Nightingale, V. Kitidis, P. Serret, M. Woodward, and C. Robinson. Biological and physical forcing of carbonate chemistry in an upwelling filament off northwest Africa: Results from a Lagrangian study. *Global Biogeochemical Cycles*, 26:GB3008, 2012. doi: 10.1029/2011GB004216.
- J. Ludwig, L. Marufu, B. Huber, M.O. Andreae, and G. Helas. Domestic Combustion of Biomass Fuels in Developing Countries: A Major Source of Atmospheric Pollutants. *Journal of Atmospheric Chemistry*, 44:23–37, 2003.

- T.J. Lueker. Coastal upwelling fluxes of O<sub>2</sub>, N<sub>2</sub>O, and CO<sub>2</sub> assessed from continuous atmospheric observations at Trinidad, California. *Biogeosciences*, 1:101–111, 2004.
- T.J. Lueker, R.F. Keeling, and M.K. Dubey. The Oxygen to Carbon Dioxide Ratios observed in Emissions from a Wildfire in Northern California. *Geophysical Research Letters*, 28(12): 2413–2416, 2001.
- T.J. Lueker, S.J. Walker, M.K. Vollmer, R.F. Keeling, C.D. Nevison, and R.F. Weiss. Coastal Upwelling air-sea fluxes revealed in atmospheric observations of O<sub>2</sub>/N<sub>2</sub>, CO<sub>2</sub> and N<sub>2</sub>O. *Geophysical Research Letters*, 30(6):1292, 2003.
- D. Lüthi, M. Le Floch, B. Bereiter, T. Blunier, J.-M. Barnola, U. Siegenthaler, D. Raynaud, J. Jouzel, H. Fischer, K. Kawamura, and T. F. Stocker. High-resolution carbon dioxide concentration record 650,000–800,000 years before present. *Nature*, 453:379–382, 2008.
- J.R.E. Lutjeharms and J.M. Meeuwis. The extent and variability of South-East Atlantic upwelling. *South African Journal of Marine Science*, 5:51–62, 1987.
- J.R.E. Lutjeharms and P.L. Stockton. Kinematics of the Upwelling Front Off Southern Africa. *South African Journal of Marine Science*, 5:35–49, 1987.
- J.R.E. Lutjeharms, F. Shillington, and C.M. Duncombe Rae. Observations of Extreme Upwelling Filaments in the Southeast Atlantic Ocean. *Science*, 253:774–776, 1991.
- C.P. Lynam, M.J. Gibbons, B.E. Axelsen, C.A. Sparks, J. Coetzee, B.G. Heywood, and A.S. Brierley. Jellyfish overtake fish in a heavily fished ecosystem. *Current Biology*, 16(13): R492–R493, 2006.
- B. Lyon and S.J. Mason. The 1997–98 Summer Rainfall Season in Southern Africa. Part I: Observations. *Journal of Climate*, 20:5134–5148, 2007.
- J. Ma, R. Liu, L.-S. Tang, Z.-D. Lan, and Y. Li. A downward CO<sub>2</sub> flux seems to have nowhere to go. *Biogeosciences*, 11(22):6251–6262, 2014. doi: 10.5194/bg-11-6251-2014.
- D. Mackay and W.Y. Shiu. A Critical Review of Henry’s Law Constants for Chemicals of Environmental Interest. *Journal of Physical and Chemical Reference Data*, 10(4):1175–1199, 1981.
- C. Macron, B. Pohl, Y. Richard, and M. Bessafi. How do Tropical Temperate Troughs Form and Develop over Southern Africa? *Journal of Climate*, 27:1633–1647, 2014.
- M.D. Mahecha, M. Reichstein, M. Jung, S.I. Seneviratne, S. Zaehle, C. Beer, M.C. Braakhekke, N. Carvalhais, H. Lange, G. Le Maire, and E. Moors. Comparing observations and process-based simulations of biosphere-atmosphere exchanges on multiple timescales. *Journal of Geophysical Research*, 115:G02003, 2010.
- D. Manatsa, Y. Morioka, S.K. Behera, T. Yamagata, and C.H. Matarira. Link between Antarctic ozone depletion and summer warming over southern Africa. *Nature Geoscience*, 6:934–939, 2013.
- M. Manizza, R.F. Keeling, and C.D. Nevison. On the processes controlling the seasonal cycles of the air–sea fluxes of O<sub>2</sub> and N<sub>2</sub>O: A modelling study. *Tellus B*, 64:18429, 2012. doi: 10.3402/tellusb.v64i0.18429.
- K.H. Mann and J.R. Lazier. *Dynamics of Marine Ecosystems: Biological-Physical Interactions in the Ocean*. Blackwell Publishing, Malden, MA, 1996.

- A.C. Manning. *Temporal variability of atmospheric oxygen from both continuous measurements and a flask sampling network: Tools for studying the global carbon cycle*. Ph.D. Thesis, University of California, San Diego, 2001.
- A.C. Manning and R.F. Keeling. Global oceanic and land biotic carbon sinks from the scripps atmospheric oxygen flask sampling network. *Tellus*, 58B:95–116, 2006.
- A.C. Manning, R.F. Keeling, and J.P. Severinghaus. Precise atmospheric oxygen measurements with a paramagnetic oxygen analyzer. *Global Biogeochemical Cycles*, 13(4):1107–1115, 1999.
- S. Maritorena and D.A. Siegel. Consistent merging of satellite ocean color data sets using a bio-optical model. *Remote Sensing of Environment*, 94:429–440, 2005.
- L. Marufu, J. Ludwig, M.O. Andreae, F.X. Meixner, and G. Helas. Domestic Biomass Burning in Rural and Urban Zimbabwe – Part A. *Biomass and Bioenergy*, 12(1):53–68, 1997.
- L. Marufu, J. Ludwig, M.O. Andreae, J. Lelieveld, and G. Helas. Spatial and temporal variation in domestic biofuel consumption rates and patterns in Zimbabwe: implications for atmospheric trace gas emission. *Biomass and Bioenergy*, 16:311–332, 1999.
- C.A. Masiello, M.E. Gallaghe, J.T. Randerson, R.M. Deco, and O.A. Chadwick. Evaluating two experimental approaches for measuring ecosystem carbon oxidation state and oxidative ratio. *Journal of Geophysical Research*, 113:G03010, 2008. doi: 10.1029/2007JG000534.
- D.L. Mauzerall, J.A. Logan, D.J. Jacob, B.E. Anderson, D.R. Blake, J.D. Bradshaw, B. Heikes, G.W. Sachse, H. Singh, and B. Talbot. Photochemistry in biomass burning plumes and implications for tropospheric ozone over the tropical South Atlantic. *Journal of Geophysical Research*, 103(D7):8401–8423, 1998.
- W.R. McGillis, J.B. Edson, J.D. Ware, J.W.H. Dacey, J.E. Hare, C.W. Fairall, and R. Wanninkhof. Carbon dioxide flux techniques performed during GasEx-98. *Marine Chemistry*, 75:267–280, 2001.
- S.A. McKeen and S.C. Liu. Hydrocarbon Ratios and Photochemical History of Air Masses. *Geophysical Research Letters*, 20(21):2362–2366, 1993.
- D.J. McKenney, C.F. Drury, W.I. Findlay, B. Mutus, T. McDonnell, and C. Gajda. Sources of nitrous oxide in soils. *Nutrient Cycling in Agroecosystems*, 49:7–16, 1997.
- L. Merbold, A. Ardö, R.J. Scholes, Y. Nouvellon, A. de Grandcourt, S. Archibald, J.M. Bonnefond, N. Boulain, N. Brueggemann, C. Bruemmer, B. Cappelaere, E. Ceschia, H.A.M. El-Khidir, B.A. El-Tahir, U. Falk, J. Lloyd, L. Kergoat, V. Le Dantec, E. Mougin, M. Muchinda, M.M. Mukelabai, D. Ramier, O. Roupsard, F. Timouk, E.M. Veenendaal, and W.L. Kutsch. Precipitation as driver of carbon fluxes in 11 African ecosystems. *Biogeosciences*, 6:1027–1041, 2009.
- F.J. Millero, T.B. Graham, F. Huang, H. Bustos-Serrano, and D. Pierrot. Dissociation constants of carbonic acid in seawater as a function of salinity and temperature. *Marine Chemistry*, 100:80–94, 2006. doi: 10.1016/j.marchem.2005.12.001.
- C. Minejima, M. Kubo, Y. Tohjima, H. Yamagishi, Y. Koyama, S. Maksyutov, K. Kita, and H. Mukai. Analysis of  $\Delta\text{O}_2/\Delta\text{CO}_2$  ratios for the pollution events observed at Hateruma Island, Japan. *Atmospheric Chemistry and Physics*, 12:2713–2723, 2012.

- V. Mohrholz, C.H. Bartholomae, A.K. van der Plas, and H.U. Lass. The seasonal variability of the northern Benguela undercurrent and its relation to the oxygen budget on the shelf. *Continental Shelf Research*, 28:424–441, 2008.
- V. Mohrholz, A. Eggert, T. Junker, G. Nausch, T. Ohde, and M. Schmidt. Cross shelf hydrographic and hydrochemical conditions and their short term variability at the northern Benguela during a normal upwelling season. *Journal of Marine Systems*, 140:92–110, 2014.
- G. Monteil, S. Houweling, E. Dlugokencky, G. Maenhout, B.H. Vaughn, J.W.C. White, and T. Rockmann. Interpreting methane variations in the past two decades using measurements of CH<sub>4</sub> mixing ratio and isotopic composition. *Atmospheric Chemistry and Physics*, 11:9141–9153, 2011.
- P.M. Monteiro and A. van der Plas. Low Oxygen Water (LOW) variability in the Benguela System: Key processes and forcing scales relevant to forecasting. In V. Shannon, G. Hempel, P. Malanotte-Rizzoli, C. Moloney, and J. Woods, editors, *Large Marine Ecosystems*, volume 14, chapter 5. Elsevier, 2006.
- P.M. Monteiro, A. van der Plas, V. Mohrholz, E. Mabile, A. Pascall, and W. Joubert. Variability of natural hypoxia and methane in a coastal upwelling system: Oceanic physics or shelf biology? *Geophysical Research Letters*, 33:L16614, 2006.
- P.M. Monteiro, A. van der Plas, J-L. Mélice, and P. Florenchie. Interannual hypoxia variability in a coastal upwelling system: Ocean-shelf exchange, climate and ecosystem-state implications. *Deep-Sea Research I*, 55:435–450, 2008.
- J Mühle, C.A.M. Brenninkmeijer, T.S. Rhee, F. Slemr, D.E. Oram, S.A. Penkett, and A. Zahn. Biomass burning and fossil fuel signatures in the upper troposphere observed during a CARIBIC flight from Namibia to Germany. *Geophysical Research Letters*, 29 (19):1910, 2002.
- S.K. Mulaudzi. *An Estimation of Emissions from Domestic Biofuel Combustion over Southern Africa*. M.S. Thesis, University of Witwaterstrand, 2006.
- A. Muller, C.J.C. Reason, and Faucherau. Extreme rainfall in the Namib Desert during late summer 2006 and influences of regional ocean variability. *International Journal of Climatology*, 28:1061–1070, 2008.
- G. Myhre, D. Shindell, F.-M. Bréon, W. Collins, J. Fuglestedt, J. Huang, D. Koch, J.-F. Lamarque, D. Lee, B. Mendoza, T. Nakajima, A. Robock, G. Stephens, T. Takemura, and H. Zhang. Anthropogenic and Natural Radiative Forcing. In T.F. Stocker, D. Qin, G.-K. Plattner, M. Tignor, S.K. Allen, J. Boschung, A. Nauels, Y. Xia, V. Bex, and P.M. Midgley, editors, *Climate Change 2013: The Physical Science Basis. Contribution of Working Group I to the Fifth Assessment Report of the Intergovernmental Panel on Climate Change*. Cambridge University Press, Cambridge, United Kingdom and New York, NY, USA, 2013.
- S.W.A. Naqvi, D.A. Jayakumar, P.V. Narvekar, H. Naik, V.V.S.S. Sarma, W. D’Souza, S. Joseph, and M.D. George. Increased marine production of N<sub>2</sub>O due to intensifying anoxia on the Indian continental shelf. *Nature*, 408(6810):346–349, 2000.
- S.W.A. Naqvi, H.W. Bange, L. Fariás, P.M.S. Monteiro, M.I. Scranton, and J. Zhang. Marine hypoxia/anoxia as a source of CH<sub>4</sub> and N<sub>2</sub>O. *Biogeosciences*, 7(7):2159–2190, 2010. doi: 10.5194/bg-7-2159-2010.



- H. Nara, H. Tanimoto, Y. Tohjima, H. Mukai, Y. Nojiri, K. Katsumata, and C. W. Rella. Effect of air composition ( $\text{N}_2$ ,  $\text{O}_2$ , Ar, and  $\text{H}_2\text{O}$ ) on  $\text{CO}_2$  and  $\text{CH}_4$  measurement by wavelength-scanned cavity ring-down spectroscopy: calibration and measurement strategy. *Atmospheric Measurement Techniques*, 5(11):2689–2701, 2012.
- N. Narayan, A. Paul, S. Mulitza, and M. Schulz. Trends in coastal upwelling intensity during the late 20th century. *Ocean Science*, 6(3):815–823, 2010. doi: 10.5194/os-6-815-2010.
- C. Nevison, J.H. Butler, and J.W. Elkins. Global distribution of  $\text{N}_2\text{O}$  and the  $\Delta\text{N}_2\text{O}$ -AOU yield in the subsurface ocean. *Global Biogeochemical Cycles*, 17(4):1119, 2003.
- C.D. Nevison, R.F. Weiss, and D.J. Erickson. Global oceanic emissions of nitrous oxide. *Journal of Geophysical Research*, 100(C8):15,809–15,820, 1995.
- C.D. Nevison, D.E. Kinnison, and R.F. Weiss. Stratospheric influences on the tropospheric seasonal cycles of nitrous oxide and chlorofluorocarbons. *Geophysical Research Letters*, 31:L20103, 2004a.
- C.D. Nevison, T.J. Lueker, and R.F. Weiss. Quantifying the nitrous oxide source from coastal upwelling. *Global Biogeochemical Cycles*, 18:GB1018, 2004b. doi: 10.1029/2003GB002110.
- C.D. Nevison, R.F. Keeling, R.F. Weiss, B.N. Popp, X. Jin, P.J. Fraser, L.W. Porter, and P.G. Hess. Southern Ocean ventilation inferred from seasonal cycles of atmospheric  $\text{N}_2\text{O}$  and  $\text{O}_2/\text{N}_2$  at Cape Grim, Tasmania. *Tellus*, 57B:218–229, 2005.
- C.D. Nevison, E. Dlugokencky, G. Dutton, J.W. Elkins, P.J. Fraser, B. Hall, P.B. Krummel, R.L. Langenfelds, S. O’Doherty, R. Prinn, L.P. Steele, and R.F. Weiss. Exploring causes of interannual variability in the seasonal cycles of tropospheric nitrous oxide. *Atmospheric Chemistry and Physics*, 11:3713–3730, 2011.
- R.E. Newell, J.W. Kidson, D.G. Vincent, and G.J. Boer. *The General Circulation of the Tropical Atmosphere and Interactions with Extratropical Latitudes, Vol 1*. MIT Press, Cambridge, MA, 1972.
- S.E. Nicholson. A low-level jet along the Benguela coast, an integral part of the Benguela current system. *Climatic Change*, 99:613–624, 2010.
- P.D. Nightingale, G. Malin, C.S. Law, A.J. Watson, P.S. Liss, M.I. Liddicoat, J. Boutin, and R.C. Upstill-Goddard. In situ evaluation of air-sea gas exchange parameterizations using novel conservative volatile tracers. *Global Biogeochemical Cycles*, 14(1):373–387, 2000.
- E. Nisbet and R.F. Weiss. Top-down versus bottom-up. *Science*, 328:1241–1243, 2010.
- S.W. Nixon. Coastal Marine Eutrophication: A Definition, Social Causes and Future Concerns. *Ophelia*, 41:199–219, 1995.
- NOAA/ESRL. Nitrous Oxide—Combined Data Set. Available <http://www.esrl.noaa.gov/gmd/hats/combined/N2O.html>, 2012.
- P. Novelli. Personal communication, October 29 2014.
- P.C. Novelli and K.A. Masarie. Atmospheric Carbon Monoxide Dry Air Mole Fractions from the NOAA ESRL Carbon Cycle Cooperative Global Air Sampling Network, 1988-2009, Version: 2011-10-04. <ftp://ftp.cmdl.noaa.gov/ccg/co/flask/event/>, 2010.

- P.C. Novelli, K.A. Masarie, and P.M. Lang. Distributions and recent changes of carbon monoxide in the lower troposphere. *Journal of Geophysical Research*, 103(D15):19,015–19,033, 1998.
- P.C. Novelli, K.A. Masarie, P.M. Lang, B.D. Hall, R.C. Myers, and J.W. Elkins. Reanalysis of tropospheric CO trends: Effects of the 1997–1998 wildfires. *Journal of Geophysical Research*, 108(D15):4464–4874, 2003.
- P.C. Novelli, P.M. Lang, and K.A. Masarie. Atmospheric Hydrogen Dry Air Mole Fractions from the NOAA ESRL Carbon Cycle Cooperative Global Air Sampling Network, 1988–2009, Version: 2011-10-04. <ftp://ftp.cmdl.noaa.gov/ccg/h2/flask/event/>, 2010.
- K. Ohta. Diurnal Variations of Carbon Monoxide Concentration in the Equatorial Pacific Upwelling Region. *Journal of Oceanography*, 53:173–178, 1997.
- J. Olivier and P.L. Stockton. The influence of upwelling extent upon fog incidence at Lüderitz, southern Africa. *International Journal of Climatology*, 9:69–75, 1989.
- D.M. Olson, E. Dinerstein, E.D. Wikramanayake, N.D. Burgess, G.V.N. Powell, E.C. Underwood, J.A. D’amico, I. Itoua, H.E. Strand, J.C. Morrison, C.J. Loucks, T.F. Allnutt, T.H. Ricketts, Y. Kura, J.F. Lamoreux, W.W. Wettengel, P. Hedao, and K.R. Kassem. Terrestrial Ecoregions of the World: A New Map of Life on Earth. *BioScience*, 51(11):933–938, 2001.
- S.J. O’Shea, S.J.-B. Bauguitte, M.W. Gallagher, D. Lowry, and C.J. Percival. Development of a cavity-enhanced absorption spectrometer for airborne measurements of  $\text{CH}_4$  and  $\text{CO}_2$ . *Atmospheric Measurement Techniques*, 6:1095–1109, 2013.
- P. Otero, X.A. Padin, M. Ruiz-Villarreal, L. M. García-García, A.F. Ríos, and F.F. Pérez. Net sea–air  $\text{CO}_2$  flux uncertainties in the Bay of Biscay based on the choice of wind speed products and gas transfer parameterizations. *Biogeosciences*, 10(5):2993–3005, 2013. doi: 10.5194/bg-10-2993-2013.
- P.J.-B. Oudot, E. Fourré, C. Mormiche, M. Guevel, J.-F. TERNON, and P. Le Corre. Transatlantic equatorial distribution of nitrous oxide. *Deep-Sea Research I*, 49:1175–1193, 2002.
- N.J. Owens, C.S. Law, R.F. Mantoura, P.H. Burkill, and C.A. Llewellyn. Methane flux to the atmosphere from the Arabian Sea. *Nature*, 354:293–296, 1991.
- H. Paeth and J. Feichter. Greenhouse-gas versus aerosol forcing and African climate response. *Climate Dynamics*, 26:35–54, 2006.
- B.A. Paldus and A.A. Kachanov. An historical overview of cavity-enhanced methods. *Canadian Journal of Physics*, 83:975–999, 2005.
- J.C. Pales and C.D. Keeling. The Concentration of Atmospheric Carbon Dioxide in Hawaii. *Journal of Geophysical Research*, 70(24):6053–6076, 1965.
- T.R. Parish. Forcing of the Summertime Low-Level Jet along the California Coast. *Journal of Applied Meteorology*, 39:2421–2433, 2000.
- S. Park, P. Croteau, K.A. Boering, D.M. Etheridge, D. Ferretti, P.J. Fraser, K-R Kim, P.B. Krummel, R.L. Langenfelds, T.D. van Ommen, L.P. Steele, and C.M. Trudinger. Trends and seasonal cycles in the isotopic composition of nitrous oxide since 1940. *Nature Geoscience*, 5:261–265, 2012.

- P.K. Patra, M. Takigawa, G.S. Dutton, K. Uhse, K. Ishijima, B.R. Lintner, K. Miyazaki, and J.W. Elkins. Transport mechanisms for synoptic, seasonal and interannual SF<sub>6</sub> variations and "age" of air in troposphere. *Atmospheric Chemistry and Physics*, 9(4):1209–1225, 2009. doi: 10.5194/acp-9-1209-2009.
- J.B. Paul, L. Lapson, and J.G. Anderson. Ultrasensitive absorption spectroscopy with a high-finesse optical cavity and off-axis alignment. *Applied Optics*, 40:4904–4910, 2001. doi: 10.1007/s00340-002-0971-z.
- A.R. Paulino, P.P. Batista, and I.S. Batista. A global view of the atmospheric lunar semi-diurnal tide. *Journal of Geophysical Research: Atmospheres*, 118, 2013.
- A. Paulmier, D. Ruiz-Pino, and V. Garçon. The oxygen minimum zone (OMZ) off Chile as intense source of CO<sub>2</sub> and N<sub>2</sub>O. *Continental Shelf Research*, 28:2746–2756, 2008.
- K.R. Peard. Seasonal and Interannual Variability of Wind-Driven Upwelling at Lüderitz, Namibia. Master's thesis, University of Cape Town, 2007.
- J. Peltola, M. Vainio, M. Siltanen, M. Metsälä, and L. Halonen. Off-axis re-entrant cavity ring-down spectroscopy with a mid-infrared continuous-wave optical parameter oscillator. *Applied Physics B*, 107:839–847, 2012. doi: 10.1007/s00340-012-5074-x.
- J.R. Petit, J. Jouzel, D. Raynaud, N.I. Barkov, J.-M. Barnola, I. Basile, M. Bender, J. Chappellaz, M. Davis, G. Delaygue, M. Delmotte, V.M. Kotlyakov, M. Legrand, V.Y. Lipenkov, C. Lorius, L. Pépin, C. Ritz, E. Saltzman, and M. Stievenard. Climate and atmospheric history of the past 420,000 years from the Vostok ice core, Antarctica. *Nature*, 399:429–436, 1999.
- V. V. Petrenko, P. Martinerie, P. Novelli, D. M. Etheridge, I. Levin, Z. Wang, T. Blunier, J. Chappellaz, J. Kaiser, P. Lang, L. P. Steele, S. Hammer, J. Mak, R. L. Langenfelds, J. Schwander, J. P. Severinghaus, E. Witrant, G. Petron, M. O. Battle, G. Forster, W. T. Sturges, J.-F. Lamarque, K. Steffen, and J. W. C. White. A 60 yr record of atmospheric carbon monoxide reconstructed from Greenland firn air. *Atmospheric Chemistry and Physics*, 13:7567–7585, 2013.
- K.E. Pickering, A.M. Thompson, D.P. McNamara, and M.R. Schoeberl. An Intercomparison of Isentropic Trajectories over the South Atlantic. *Monthly Weather Review*, 122:864–879, 1994.
- P.A. Pickers and A.C. Manning. Investigating bias in the application of curve fitting programs to atmospheric time series. *Atmospheric Measurement Techniques*, 8(3):1469–1489, 2015. doi: 10.5194/amt-8-1469-2015.
- S.J. Piketh and N.M. Walton. Characteristics of Atmospheric Transport of Air Pollution for Africa. *The Handbook of Environmental Chemistry*, 4(Part G):173–195, 2004.
- S.J. Piketh, R.J. Swap, W. Maenhaut, H.J. Annegarn, and P. Formenti. Chemical evidence of long-range atmospheric transport over southern Africa. *Journal of Geophysical Research*, 107(D24):ACH 7–1, 2002.
- D. Pino, V.-G.d. Arellano, W. Peter, J. Schröter, C.C. van Heerwaarden, and M.C. Krol. A conceptual framework to quantify the influence of convective boundary layer development on carbon dioxide mixing ratios. *Atmospheric Chemistry and Physics*, 12:2969–2985, 2012.
- R. Poole and M. Tomczak. Optimum multiparameter analysis of the water mass structure in the Atlantic Ocean thermocline. *Deep-Sea Research I*, 46:1895–1921, 1999.

- M.J. Prather, C.D. Holmes, and J. Hsu. Reactive greenhouse gas scenarios: Systematic exploration of uncertainties and the role of atmospheric chemistry. *Geophysical Research Letters*, 39:L09803, 2012.
- H.U. Price, D.A. Jaffe, O.R. Cooper, and P.V. Doskey. Photochemistry, ozone production, and dilution during long-range transport episodes from Eurasia to the northwest United States. *Journal of Geophysical Research*, 109:D23S13, 2004.
- X.-W. Quan, H.F. Diaz, and M.P. Hoerling. Changes in the Tropical Hadley Cell Since 1950. In H.F. Diaz and R.S. Bradley, editors, *The Hadley Circulation: Present, Past and Future*. Kluwer Academic Publishers, Dordrecht, The Netherlands, 2004.
- Z. Rácz and R.K. Smith. The dynamics of heat lows. *Quarterly Journal of the Royal Meteorological Society*, 125:225–252, 1999.
- J.T. Randerson, C.A. Masiello, C.J. Still, T. Rahn, H. Poorter, and C.B. Field. Is carbon within the global terrestrial biosphere becoming more oxidized? Implications for trends in atmospheric O<sub>2</sub>. *Global Change Biology*, 12:260–271, 2006. doi: 10.1111/j.1365-2486.2006.01099.x.
- C.A. Randles and V. Ramaswamy. Direct and semi-direct impacts of absorbing biomass burning aerosol on the climate of southern Africa: a Geophysical Fluid Dynamics Laboratory GCM sensitivity study. *Atmospheric Chemistry and Physics*, 10:9819–9831, 2010.
- S.B. Ratna, S. Behera, J.V. Ratnam, K. Takahashi, and T. Yamagata. An index for tropical temperate troughs over southern Africa. *Climate Dynamics*, 41:421–441, 2013.
- J.V. Ratnam, S.K. Behera, Y. Masumoto, and T. Yamagata. Remote Effects of El Niño and Modoki Events on the Austral Summer Precipitation of Southern Africa. *Journal of Climate*, 27:3802–3815, 2014.
- M.R. Raupach, J.G. Canadell, and C. Le Quéré. Anthropogenic and biophysical contributions to increasing atmospheric CO<sub>2</sub> growth rate and airborne fraction. *Biogeosciences*, 5:1601–1613, 2008.
- A.R. Ravishankara, S. Solomon, A.A. Turnipseed, and R.F. Warren. Atmospheric lifetimes of long-lived halogenated species. *Science*, 259(5092):194–199, 1993. doi: 10.1126/science.259.5092.194.
- A.R. Ravishankara, J.S. Daniel, and R.W. Portmann. Nitrous Oxide (N<sub>2</sub>O): The Dominant Ozone-Depleting Substance Emitted in the 21st Century. *Science*, 326:123–125, 2009.
- P.J. Rayner, I.G. Enting, and C.M. Trudinger. Optimizing the CO<sub>2</sub> observing network for constraining sources and sinks. *Tellus*, 48B:433–444, 1996.
- C.J.C. Reason and H. Mulenga. Relationships between South African rainfall and SST anomalies in the southwest Indian Ocean. *International Journal of Climatology*, 19:1651–1673, 1999.
- C.J.C. Reason and M. Rouault. ENSO-like decadal variability and South African rainfall. *Geophysical Research Letters*, 29(13):1638, 2002.
- C.J.C. Reason, W. Landman, and W. Tennant. Seasonal to Decadal Prediction of Southern African Climate and Its Links with Variability of the Atlantic Ocean. *Bulletin of the American Meteorological Society*, 87:941–955, 2006.

- D.S. Reay, E.A. Davidson, K.A. Smith, P. Smith, J.M. Melillo, F.J. Dentener, and P. Crutzen. Global agriculture and nitrous oxide emissions. *Nature Climate Change*, 2:410–416, 2012.
- W.S. Reeburgh. Oceanic methane biogeochemistry. *Chemical Reviews*, 107:486–513, 2007a.
- W.S. Reeburgh. Global methane biogeochemistry. In H.D. Holland and K.K. Turekian, editors, *Treatise on Geochemistry: The Atmosphere*, volume 4.03, chapter 3, pages 1–32. Elsevier, 2007b.
- A.P. Rees, I.J. Brown, D.R. Clark, and R. Torres. The Lagrangian progression of nitrous oxide within filaments formed in the Mauritanian upwelling. *Geophysical Research Letters*, 38:L21606, 2011. doi: 10.1029/2011GL049322.
- C.E. Reeves, P. Formenti, C. Afif, G. Ancellet, J.-L. Attié, J. Bechara, A. Borbon, F. Cairo, H. Coe, S. Crumeyrolle, F. Fierli, C. Flamant, L. Gomes, T. Hamburger, C. Jambert, K.S. Law, C. Mari, R.L. Jones, A. Matsuki, M.I. Mead, J. Methven, G.P. Mills, A. Minikin, J.G. Murphy, J.K. Nielsen, D.E. Oram, D.J. Parker, A. Richter, H. Schlager, A. Schwarzenboeck, and V. Thouret. Chemical and aerosol characterisation of the troposphere over West Africa during the monsoon period as part of AMMA. *Atmospheric Chemistry and Physics*, 10(16):7575–7601, 2010. doi: 10.5194/acp-10-7575-2010.
- G. Rehder, R.W. Collier, K. Heeschen, P.M. Kosro, J. Barth, and E. Suess. Enhanced marine CH<sub>4</sub> emissions to the atmosphere off Oregon caused by coastal upwelling. *Global Biogeochemical Cycles*, 16(3):1081, 2002. doi: 10.1029/2000GB001391.
- J.J. Reimer, R. Vargas, S.V. Smith, R. Lara-Lara, G. Gaxiola-Castro, J.M. Hernández-Ayón, A. Castro, M. Escoto-Rodriguez, and J. Martínez-Osuna. Air–sea CO<sub>2</sub> fluxes in the near-shore and intertidal zones influenced by the California Current. *Journal of Geophysical Research: Oceans*, 118:1–16, 2013.
- C.W. Rella, H. Chen, A.E. Andrews, A. Filges, C. Gerbig, J. Hatakka, A. Karion, N.L. Miles, S.J. Richardson, M. Steinbacher, C. Sweeney, B. Wastine, and C. Zellweger. High accuracy measurements of dry mole fractions of carbon dioxide and methane in humid air. *Atmospheric Measurement Techniques*, 6:837–860, 2013.
- G.I. Reygondeau, A. Longhurst, E. Martinez, G. Beaugrand, D. Antoine, and O. Maury. Dynamic biogeochemical provinces in the global ocean. *Global Biogeochemical Cycles*, 27:1–13, 2013. ISSN 1944-9224. doi: 10.1002/gbc.20089.
- T.S. Rhee, A.J. Kettle, and M.O. Andreae. Methane and nitrous oxide emissions from the ocean: A reassessment using basin-wide observations in the Atlantic. *Journal of Geophysical Research*, 114:D12304, 2009.
- I. Richter, C.R. Mechoso, and A.W. Robertson. What Determines the Position and Intensity of the South Atlantic Anticyclone in Austral Winter?—An AGCM Study. *Journal of Climate*, 21:214–229, 2008.
- M. Rigby, R. Prinn, P.J. Fraser, P.G. Simmonds, R.L. Langenfelds, J. Huang, D.M. Cunnold, L.P. Steele, P.B. Krummel, R.F. Weiss, S. O’Doherty, P.K. Salameh, H.J. Wan, C.M. Harth, J. Mühle, and L.W. Porter. Renewed growth of atmospheric methane. *Geophysical Research Letters*, 35:L22805, 2008.
- C.M. Risien, C.J.C. Reason, F.A. Shillington, and D.B. Chelton. Variability in satellite winds over the Benguela upwelling system during 1999–2000. *Journal of Geophysical Research*, 109:C03010, 2004.

- C. Rödenbeck, Le Quéré, M. Heimann, and R.F. Keeling. Interannual variability in oceanic biogeochemical processes inferred by inversion of atmospheric  $O_2/N_2$  and  $CO_2$  data. *Tellus*, 60B:685–705, 2008.
- E. Roeckner, P. Stier, J. Feichter, S. Kloster, M. Esch, and I. Fischer-Bruns. Impact of carbonaceous aerosol emissions on regional climate change. *Climate Dynamics*, 27:553–571, 2006.
- A.C.L. Sá, J.M.C. Pereira, M.E. Charlton, B. Mota, P.M. Barbosa, and A.S. Fotheringham. The pyrogeography of sub-Saharan Africa: a study of the spatial non-stationarity of fire-environment relationships using GWR. *Journal of Geographic Systems*, 13:227–248, 2011.
- C.F. Saamak. A shift from natural to human-driven fire regime: implications for trace-gas emissions. *The Holocene*, 11(3):373–375, 2001.
- J.M. Santana-Casiano, M. González-Dávila, and I.R. Ucha. Carbon dioxide fluxes in the Benguela upwelling system during winter and spring: A comparison between 2005 and 2006. *Deep-Sea Research II*, 56:533–541, 2009.
- F. Santos, M. Gomez-Gesteira, M. deCastro, and I. Alvarez. Differences in coastal and oceanic SST trends due to the strengthening of coastal upwelling along the Benguela current system. *Continental Shelf Research*, 34:79–86, 2012.
- J. Sarmiento, M. Gloor, N. Gruber, C. Beaulieu, A.P. Jacobson, S.E.M. Fletcher, S. Pacala, and K. Rodgers. Trends and regional distributions of land and ocean carbon sinks. *Biogeosciences*, 7:2351–2367, 2010.
- W.H. Schlesinger. *Biogeochemistry: An Analysis of Global Change*. Academic Press, San Diego, CA, 1997.
- W.H. Schlesinger, J. Belnap, and G. Marion. On carbon sequestration in desert ecosystems. *Global Change Biology*, 15:1488–1490, 2009. doi: 10.1111/j.1365-2486.2008.01763.x.
- B. Schmid, J. Redemann, P.B. Russell, P.V. Hobbs, D.L. Hlavka, M.J. McGill, B.N. Holben, E.J. Welton, J.R. Campbell, O. Torres, R.A. Kahn, D.J. Diner, M.C. Helmlinger, D.A. Chu, C. Robles-Gonzalez, and G. de Leeuw. Coordinated airborne, spaceborne, and ground-based measurements of massive thick aerosol layers during the dry season in southern Africa. *Journal of Geophysical Research*, 108(D13):8496, 2003.
- H.P. Schmid. Footprint modeling for vegetation atmosphere exchange studies: a review and perspective. *Agricultural and Forest Meteorology*, 113:159–183, 2002.
- T. Schneider, T. Bischoff, and G.H. Haug. Migrations and dynamics of the intertropical convergence zone. *Nature*, 513:45–53, 2014.
- D.H. Schoellhamer. Singular spectrum analysis for time series with missing data. *Geophysical Research Letters*, 28(16):3187–3190, 2001.
- R.J. Scholes, D.E. Ward, and C.O. Justice. Emissions of trace gases and aerosol particules due to vegetation burning in southern hemisphere Africa. *Journal of Geophysical Research*, 101(D19):23,677–23,682, 1996.
- B.R. Schulze. The Climate of Gobabeb. *Scientific Papers of the Namib Desert Research Station*, 38, 1969.

- M.I. Scranton and J.W. Farrington. Methane Production in the Waters off Walvis Bay. *Journal of Geophysical Research*, 82(31):4947–4953, 1977.
- U. Seibt, W.A. Brand, M. Heimann, J. Lloyd, J.P. Severinghaus, and L. Wingate. Observations of  $O_2:CO_2$  exchange ratios during ecosystem gas exchange. *Global Biogeochemical Cycles*, 18:GB4024, 2004. doi: 10.1029/2004GB002242.
- W. Seiler. The cycle of atmospheric CO. *Tellus*, 26(1–2):116–135, 1974.
- W. Seiler, H. Giehl, E.-G. Brunke, and E. Halliday. The seasonality of CO abundance in the Southern Hemisphere. *Tellus*, 36B:219–231, 1984.
- P.K. Sen. Estimates of the regression coefficient based on Kendall’s tau. *Journal of the American Statistical Association*, 63:1379–1389, 1968.
- P. Serrano-Ortiz, M. Roland, S. Sanchez-Moral, I.A. Janssens, F. Domingo, Y. Godd eris, and A. Kowalski. Hidden, abiotic  $CO_2$  flows and gaseous reservoirs in the terrestrial carbon cycle: Review and perspectives. *Agricultural and Forest Meteorology*, 150:321–329, 2010.
- J P Severinghaus. *Studies of the terrestrial  $O_2$  and carbon cycles in sand dune gases and in Biosphere 2*. Ph.D. Thesis, Columbia University, 1995.
- L.J. Shaffer. Indigenous Fire Use to Manage Savanna Landscapes in Southern Mozambique. *Fire Ecology*, 6(2):43–59, 2010.
- L.V. Shannon and G. Nelson. The Benguela: large scale features and processes and system variability. In G. Wefer, W.H. Berger, G. Siedler, and D.J. Webb, editors, *The South Atlantic: Present and Past Circulation*, pages 163–210. Springer, 1996.
- E.S. Shanyengana, J.R. Henschel, M.K. Seely, and R.D. Sanderson. Exploring fog as a supplementary water source in Namibia. *Atmospheric Research*, 64:251–259, 2002.
- A. Sheuyange, G. Oba, and R.B. Weladji. Effects of anthropogenic fire history on savanna vegetation in northeastern Namibia. *Journal of Environmental Management*, 75:189–198, 2005.
- H. Siegel, T. Ohde, and M. Gerth. The Upwelling Area Off Namibia, the Northern Part of the Benguela Current System. In V. Barale and M. Gade, editors, *Remote Sensing of the African Seas*, pages 167–183. Springer, New York, U.S.A., 2014.
- J.M.N. Silva, J.M.C. Pereira, A.I. Cabral, A.C.L. S a, M.J.P. Vasconcelos, B. Mota, and J.-M. Gr egoire. An estimate of the area burned in southern Africa during the 2000 dry season using SPOT-VEGETATION satellite data. *Journal of Geophysical Research*, 108(D13): 8498, 2003.
- I.J. Simpson, M.P.S. Anderson, S. Meinardi, L. Bruhwiler, N.J. Blake, D. Helmig, F.S. Rowland, and D.R. Blake. Long-term decline of global atmospheric ethane concentrations and implications for methane. *Nature*, 488:490–494, 2012.
- H.B. Singh, D. Herlth, R. Kolyer, R. Chatfield, W. Viezee, L.J. Salas, Y. Chen, J.D. Bradshaw, S.T. Sandholm, R. Talbot, G.L. Gregory, B. Anderson, G.W. Sachse, E.V. Browell, A.S. Bachmeier, D.R. Blake, B. Heikes, D. Jacob, and H.E. Fuelberg. Impact of biomass burning emissions on the composition of the South Atlantic troposphere: Reactive nitrogen and ozone. *Journal of Geophysical Research*, 101(D19):24,203–24,219, 1996.

- A.T. Singleton and C.J.C. Reason. Variability in the characteristics of cut-off low pressure systems over subtropical southern Africa. *International Journal of Climatology*, 27:295–310, 2007.
- P. Sinha, P.V. Hobbs, R.J. Yokelson, D.R. Blake, S. Gao, and T.W. Kirchstetter. Distributions of trace gases and aerosols during the dry biomass burning season in southern africa. *Journal of Geophysical Research*, 108(D17):4536, 2003.
- P. Sinha, L. Jaegle, P.V. Hobbs, and Q. Liang. Transport of biomass burning emissions from southern Africa. *Journal of Geophysical Research*, 109:D20204, 2004.
- T.N. Siraya. Comparison of uncertainty estimates: Allan variance and sample variance. *Measurement Science Review*, 1(1):25–28, 2001.
- M. Sjöskog. Plants Around Gobabeb. Technical report, Gobabeb Training and Research Centre, 2008.
- M. Sjöström, M. Zhao, S. Archibald, A. Arneth, B. Cappelaere, U. Falk, A. de Grandcourt, N. Hanan, L. Kergoat, W. Kutsch, L. Merbold, E. Mougin, A. Nickless, Y. Nouvellon, R.J. Scholes, E.M. Veenendaal, and J. Ardö. Evaluation of MODIS gross primary productivity for Africa using eddy covariance data. *Remote Sensing of Environment*, 131:275–286, 2013.
- E.A. Solomon, M. Kastner, I.R. MacDonald, and I. Leifer. Considerable methane fluxes to the atmosphere from hydrocarbon seeps in the gulf of mexico. *Nature Geoscience*, 2: 561–565, 2009.
- Staff Reporter. “Lüderitz renaming misunderstood: Shanghala”. *Namibian Sun*, August 27, 2013.
- J. Steinbach, C. Gerbig, C. Rödenbeck, U. Karstens, C. Minejima, and H. Mukai. The CO<sub>2</sub> release and Oxygen uptake from Fossil Fuel Emission Estimate (COFFEE) dataset: effects from varying oxidative ratios. *Atmospheric Chemistry and Physics*, 11:6855–6870, 2011.
- B.B. Stephens, R.F. Keeling, M. Heimann, K.D. Six, R. Murnane, and K. Caldeira. Testing global ocean carbon cycle models using measurements of atmospheric O<sub>2</sub> and CO<sub>2</sub> concentration. *Global Biogeochemical Cycles*, 12(2):213–230, 1998.
- B.B. Stephens, R.F. Keeling, and W.J. Paplawsky. Shipboard measurements of atmospheric oxygen using a vacuum-ultraviolet absorption technique. *Tellus*, 55B:857–878, 2003.
- B.B. Stephens, P.S. Bakwin, P.P. Tans, R.M. Teclaw, and D.D. Baumann. Application of a Differential Fuel-Cell Analyzer for Measuring Atmospheric Oxygen Variations. *Journal of Atmospheric and Oceanic Technology*, 24:82–93, 2007.
- B.B. Stephens, G.W. Brailsford, A.J. Gomez, S.E. Mikaloff Fletcher, S. Nichol, and M. Manning. Analysis of a 39-year continuous atmospheric CO<sub>2</sub> record from Baring Head, New Zealand. *Biogeosciences*, 10:2683–2697, 2013.
- A. Stohl. Computations, Accuracy, and Applications of Trajectories—A Review and Bibliography. *Atmospheric Environment*, 32(6):947–966, 1994.
- R. Stone. Have Desert Researchers Discovered a Hidden Loop in the Carbon Cycle? *Science*, 320:1409–1410, 2008. doi: 10.1126/science.320.5882.1409.
- S.A. Strode and S. Pawson. Detection of carbon monoxide trends in the presence of inter-annual variability. *Journal of Geophysical Research: Atmospheres*, 118, 2013.



- A. Stubbins, G. Uher, V. Kitidis, C.S. Law, R.C. Upstill-Goddard, and E.M.S. Woodward. The open-ocean source of atmospheric carbon monoxide. *Deep-Sea Research II*, 53:1685–1694, 2006.
- P. Sturm, M. Leuenberger, C. Sirignano, R.E.M. Neubert, H.A.J. Meijer, R. Langenfelds, W.A. Brand, and Y. Tohjima. Permeation of atmospheric gases through polymer O-rings used in flasks for air sampling. *Journal of Geophysical Research*, 109:D04309, 2004.
- P. Sturm, M. Leuenberger, and M. Schmidt. Atmospheric O<sub>2</sub>, CO<sub>2</sub>, and  $\delta^{13}\text{C}$  observations from the remote sites Jungfraujoch, Switzerland, and Puy de Dôme, France. *Geophysical Research Letters*, 32:L17811, 2005. doi: 10.1029/2005GL023304.
- P. Suntharalingam and J.L. Sarmiento. Factors governing the oceanic nitrous oxide distribution: Simulations with an ocean general circulation model. *Global Biogeochemical Cycles*, 14(1):429–454, 2000.
- H.U. Sverdrup. On the process of upwelling. *Journal of Marine Research*, 1:115–164, 1938.
- R. Swap, M. Garstang, S.A. Macko, P.D. Tyson, W. Maenhaut, P. Artaxo, P. Kålberg, and R. Talbot. The long-range transport of southern African aerosols to the tropical South Atlantic. *Journal of Geophysical Research*, 101(D19):23,777–23,791, 1996.
- R.J. Swap and P.D. Tyson. Stable discontinuities as determinants of the vertical distribution of aerosols and trace gases in the atmosphere. *South African Journal of Science*, 95:63–71, 1999.
- R.J. Swap, H.J. Annegarn, J.T. Suttles, M.D. King, S. Platnick, J.L. Privette, and R.J. Scholes. Africa burning: A thematic analysis of the Southern African Regional Science Initiative (SAFARI 2000). *Journal of Geophysical Research*, 108(D13):8465, 2003.
- W.J. Sydeman, M. García-Reyes, D.S. Schoeman, R.R. Rykaczewski, S.A. Thompson, B.A. Black, and S.J. Bograd. Climate change and wind intensification in coastal upwelling ecosystems. *Science*, 345(6192):77–80, 2014.
- S. Szopa, D.A. Hauglustaine, and P. Ciais. Relative contributions of biomass burning emissions and atmospheric transport to carbon monoxide interannual variability. *Geophysical Research Letters*, 34:L18810, 2007.
- T. Takahashi, S.C. Sutherland, R. Wanninkhof, C. Sweeney, R.A. Feely, D.W. Chipman, B. Hales, G. Friederich, F. Chavez, C. Sabine, A. Watson, D.C.E. Bakker, U. Schuster, N. Metzl, H. Yoshikawa-Inoue, M. Ishii, T. Midorikawa, Y. Nojiri, A. Körtzinger, T. Steinhoff, M. Hoppema, J. Olafsson, T. Arnason, B.D. Tilbrook, T. Johannessen, A. Olsen, R. Bellerby, C.S. Wong, B. Delille, N.R. Bates, and H.J.W. de Baar. Climatological mean and decadal change in surface ocean  $p\text{CO}_2$ , and net sea–air flux over the global oceans. *Deep-Sea Research II*, 56:554–577, 2009.
- P.P. Tans. An observational strategy for assessing the role of terrestrial ecosystems in the global carbon cycle: Scaling down to regional levels. In J.R. Ehleringer and C.B. Field, editors, *Scaling Physiological Processes: Leaf to Globe*, pages 179–190. Academic Press, San Diego, CA, 1993.
- P.P. Tans, K.W. Thoning, W.P. Elliott, and T.J. Conway. Error Estimates of Background Atmospheric CO<sub>2</sub> Patterns From Weekly Flask Samples. *Journal of Geophysical Research*, 95(D9):14,603–14,070, 1990.

- H. Theil. A rank-invariant method of linear and polynomial regression analysis. *Proceedings of the Royal Netherlands Academy of Science*, 53:386–392, 1950.
- A.M. Thompson, K.E. Pickering, D.P. McNamara, M.R. Schoeberl, R.D. Hudson, J.H. Kim, E.V. Browell, V.W. Kirchhoff, and D. Nganga. Where did tropospheric ozone over southern Africa and the tropical Atlantic come from in October 1992? Insights from TOMS, GTE, TRACE A and SAFARI 1992. *Journal of Geophysical Research*, 101(24):24,251–24,278, 1996.
- R.L. Thompson, A.C. Manning, D.C. Lowe, and D.C. Weatherburn. A ship-based methodology for high precision atmospheric oxygen measurements and its application in the Southern Ocean region. *Tellus*, 59:643–653, 2007.
- R.L. Thompson, A.C. Manning, M. Gloor, U. Schultz, T. Seifert, F. Haensel, A. Jordan, and M. Heimann. In-situ measurements of oxygen, carbon monoxide and greenhouse gases from Ochsenkopf tall tower in Germany. *Atmospheric Measurement Techniques*, 3:573–591, 2009.
- R.L. Thompson, P. Bousquet, F. Chevallier, P.J. Rayner, and P. Ciais. Impact of the atmospheric sink and vertical mixing on nitrous oxide fluxes estimated using inversion methods. *Journal of Geophysical Research*, 116:D17301, 2011.
- R.L. Thompson, K. Ishijima, E. Saikawa, M. Corazza, U. Karstens, P.K. Patra, P. Bergamaschi, F. Chevallier, E. Dlugokencky, R.G. Prinn, R.F. Weiss, S. O’Doherty, P.J. Fraser, L.P. Steele, P.B. Krummel, A. Vermeulen, Y. Tohjima, A. Jordan, L. Haszpra, M. Steinbacher, S. Van der Laan, T. Aalto, F. Meinhardt, M.E. Popa, J. Moncrieff, and P. Bousquet. TransCom N<sub>2</sub>O model inter-comparison Part 2: Atmospheric inversion estimates of N<sub>2</sub>O emissions. *Atmospheric Chemistry and Physics*, 14(12):6177–6194, 2014. doi: 10.5194/acp-14-6177-2014.
- K.W. Thoning, P.P. Tans, and W.D. Komhyr. Atmospheric Carbon Dioxide at Mauna Loa Observatory 2. Analysis of the NOAA GMCC Data, 1974–1985. *Journal of Geophysical Research*, 94(D6):8549–8564, 1989.
- Y. Tohjima. Method for measuring changes in the atmospheric O<sub>2</sub>/N<sub>2</sub> ratio by a gas chromatograph equipped with a thermal conductivity detector. *Journal of Geophysical Research*, 105(D11):14,575–14,584, 2000.
- Y. Tohjima, T. Machida, I. Watai, T. Akama, and Y. Moriwaki. Preparation of gravimetric standards for measurements of atmospheric oxygen and reevaluation of atmospheric oxygen concentration. *Journal of Geophysical Research*, 110:D11302, 2005a.
- Y. Tohjima, H. Mukai, T. Machida, Y. Nojiri, and M. Gloor. First measurements of the latitudinal atmospheric O<sub>2</sub> and CO<sub>2</sub> distributions across the western Pacific. *Geophysical Research Letters*, 32:L17805, 2005b. doi: 10.1029/2005GL023311.
- Y. Tohjima, C. Minejima, H. Mukai, T. Machida, H. Yamagishi, and Y. Nojiri. Analysis of seasonality and annual mean distribution of atmospheric potential oxygen (APO) in the Pacific region. *Global Biogeochemical Cycles*, 26:GB4008, 2012. doi: 10.1029/2011GB004110.
- R. Torres, D. Turner, N. Silva, and J. Rutllant. High short-term variability of CO<sub>2</sub> fluxes during an upwelling event off the Chilean coast at 30°S. *Deep-Sea Research I*, 46:1161–1179, 1999.

- R. Torres, D. Turner, J. Rutllant, M. Sobarzo, T. Antezana, and H.E. Gonzales. CO<sub>2</sub> outgassing off central Chile (31–30°S) and northern Chile (24–23°S) during austral summer 1997: the effect of wind intensity on the upwelling and ventilation of CO<sub>2</sub>-rich waters. *Deep-Sea Research I*, 49:1413–1429, 2002.
- C.J. Tucker, J. Pinzon, M. Brown, and GIMMS/GSFC/NASA. In Hall, Forrest G., G. Collatz, B. Meeson, S. Los, E. Brown de Colstoun, and D. Landis (eds.). ISLSCP II GIMMS Monthly NDVI, 1981-2002. ISLSCP Initiative II Collection. Data set. Technical report, 2010.
- P.D. Tyson. Berg Winds of South Africa. *Weather*, 19(1):7–11, 1964.
- P.D. Tyson. Atmospheric transport of aerosols and trace gases over southern Africa. *Progress in Physical Geography*, 21(1):79–101, 1997.
- P.D. Tyson and P.C. D’Abreton. Transport and Recirculation of Aerosols off Southern Africa—Macroscale Plume Structure. *Atmospheric Environment*, 32(9):1511–1524, 1998.
- P.D. Tyson and R.A. Preston-Whyte. *The Weather and Climate of Southern Africa*. Oxford University Press, Cape Town, South Africa, 2000.
- P.D. Tyson and M.K. Seely. Local winds over the central Namib. *South African Geographical Journal*, 62:135–150, 1980.
- P.D. Tyson, M. Garstang, and R. Swap. Large-Scale Recirculation of Air over Southern Africa. *Journal of Applied Meteorology*, 35:2218–2236, 1996a.
- P.D. Tyson, M. Garstang, R. Swap, P. Källberg, and M. Edwards. An Air Transport Climatology for Subtropical Southern Africa. *International Journal of Climatology*, 16:265–291, 1996b.
- P.D. Tyson, W. Steffen, A.P. Mitra, C. Fu, and L. Lebel. The Earth System: Regional-Global Linkages. *Regional Environmental Change*, 2:128–140, 2001.
- C. Uglietti, M. Leuenberger, and F.L. Valentino. Comparison between real time and flask measurements of atmospheric O<sub>2</sub> and CO<sub>2</sub> performed at the high altitude research station jungfraujoeh, switzerland. *Science of the Total Environment*, 391:196–202, 2008.
- R.C. Upstill-Goddard, J. Barnes, and N.J. Owens. Nitrous oxide and methane during the 1994 SW monsoon in the Arabian Sea/Northwestern Indian Ocean. *Journal of Geophysical Research*, 104(C12):30,067–30,084, 1999.
- R. Valentini, A. Arneeth, A. Bombelli, S. Castaldi, R. Cazzolla Gatti, F. Chevallier, P. Ciais, E. Grieco, J. Hartmann, M. Henry, R.A. Houghton, M. Jung, W.L. Kutsch, Y. Malhi, E. Mayorga, L. Merbold, G. Murray-Tortarolo, D. Papale, P. Peylin, B. Poulter, P.A. Raymon, M. Santini, S. Sitch, G. Vaglio Laurin, G.R. van der Werf, C.A. Williams, and R.J. Scholes. A full greenhouse gases budget of Africa: synthesis, uncertainties, and vulnerabilities. *Biogeosciences*, 11:381–407, 2014.
- S. van der Laan, I.T. van der Laan-Luijkx, C. Rödenbeck, A. Varlagin, I. Shironya, R.E.M. Neubert, M. Ramonet, and H.A.J. Meijer. Atmospheric CO<sub>2</sub>, δ(O<sub>2</sub>/N<sub>2</sub>), APO and oxidative ratios from aircraft flask samples over Fyodorovskoye, Western Russia. *Atmospheric Environment*, 97:174–181, 2014.

- A.K. van der Plas, P.M.S. Monteiro, and A. Pascall. Cross-shelf biogeochemical characteristics of sediments in the central Benguela and their relationship to overlying water column hypoxia. *African Journal of Marine Science*, 29(1):37–47, 2007.
- G.R. van der Werf, J.T. Randerson, L. Giglio, G.J. Collatz, M. Mu, P.S. Kasibhatla, D.C. Morton, R.S. DeFries, Y. Jin, and T.T. van Leeuwen. Global fire emissions and the contribution of deforestation, savanna, forest, agricultural, and peat fires (1997–2009). *Atmospheric Chemistry and Physics*, 10(23):11707–11735, 2010. doi: 10.5194/acp-10-11707-2010.
- T.T. van Leeuwen and G. van der Werf. Spatial and temporal variability in the ratio of trace gases emitted from biomass burning. *Atmospheric Chemistry and Physics*, 11:3611–3629, 2011.
- T.T. van Leeuwen, W. Peters, M.C. Krol, and G.R. van der Werf. Dynamic biomass burning emission factors and their impact on atmospheric CO mixing ratios. *Journal of Geophysical Research: Atmospheres*, 118:1–19, 2013.
- B.W. van Wilgen, C.S. Everson, and W.S.W. Trollope. *Fire Management in Southern Africa: Some Examples of Current Objectives, Practices, and Problems*. In J.G. Goldammer, editor, *Fire in the Tropical Biota*, volume 84, *Ecological Studies*, chapter 3. Springer-Verlag, 1990.
- J. Veitch, P. Penven, and F. Shillington. The Benguela: A laboratory for comparative modeling studies. *Progress in Oceanography*, 83:296–302, 2009.
- S.A. Venegas, L.A. Mysak, and D.N. Straub. Atmosphere–Ocean Coupled Variability in the South Atlantic. *Journal of Climate*, 10:2904–2920, 2000.
- A.T. Vermeulen, A. Hensen, M. Gloor, A.C. Manning, P. Ciais, R. Eisma, W.C. van den Bulk, J.J. Mols, and J.W. Erisman. Chiotto—continuous high-precision tall tower observations of greenhouse gases. In *Inverse Modelling of National and EU Greenhouse Gas Emission Inventories*, pages 49–62. Joint Research Centre, Ispra, Italy, 2004.
- N. Vigaud, Y. Richard, M. Rouault, and N. Fauchereau. Moisture transport between the South Atlantic Ocean and southern Africa: relationships with summer rainfall and associated dynamics. *Climate Dynamics*, 32:113–123, 2009.
- M. Voss, H.W. Bange, J.W. Dippner, J.J. Middelburg, J.P. Montoya, and B. Ward. The marine nitrogen cycle: recent discoveries, uncertainties and the potential relevance of climate change. *Philosophical Transactions of the Royal Society B*, 368:20130121, 2013.
- A. Wada, H. Matsueda, Y. Sawa, K. Tsuboi, and S. Okubo. Seasonal variation of the enhancement ratios of trace gases observed over 10 years in the western North Pacific. *Atmospheric Environment*, 45:2129–2137, 2011.
- K.M. Wai, S. Wu, A. Kumar, and H. Liao. Seasonal variability and long-term evolution of tropospheric composition in the tropics and Southern Hemisphere. *Atmospheric Chemistry and Physics*, 14:4859–4874, 2014.
- J.M. Wallace and P.V. Hobbs. *Atmospheric Science: An Introductory Survey*. Academic Press, 2nd edition, 2006.
- S. Walter, H.W. Bange, U. Breitenbach, and D.W.R. Wallace. Nitrous oxide in the North Atlantic Ocean. *Biogeosciences*, 3(4):607–619, 2006. doi: 10.5194/bg-3-607-2006.

- D. Wang, T.C. Gouhier, B.A. Menge, and A.R. Ganguly. Intensification and spatial homogenization of coastal upwelling under climate change. *Nature*, 518:390–394, 2015. doi: 10.1038/nature14235.
- Z. Wang, J. Chappellaz, P. Martinerie, K. Park, V. Petrenko, E. Witraut, L.K. Emmons, T. Blunier, C.A.M. Brenninkmeijer, and J.E. Mak. The isotopic record of Northern Hemisphere atmospheric carbon monoxide since 1950: implications for the CO budget. *Atmospheric Chemistry and Physics*, 12:4365–4377, 2012.
- R. Wanninkhof. Relationship Between Wind Speed and Gas Exchange Over the Ocean. *Journal of Geophysical Research*, 92(C5):7373–7382, 1992.
- R. Wanninkhof, W.E. Asher, D.T. Ho, C. Sweeney, and W.R. McGillis. Advances in Quantifying Air–Sea Gas Exchange and Environmental Forcing. *Annual Review of Marine Science*, 1:213–244, 2009.
- D.E. Ward, W.M. Hao, R.A. Susott, R.E. Babbit, R.W. Shea, J.B. Kauffman, and C.O. Justice. Effect of fuel composition on combustion efficiency and emission factors for African savanna ecosystems. *Journal of Geophysical Research*, 101(D19):23,569–23,576, 1996.
- P.J. Webster. The Elementary Hadley Circulation. In H.F. Diaz and R.S. Bradley, editors, *The Hadley Circulation: Present, Past and Future*. Kluwer Academic Publishers, Dordrecht, The Netherlands, 2004.
- S.J. Weeks, B. Currie, A. Bakun, and K.R. Peard. Hydrogen sulphide eruptions in the Atlantic Ocean off southern Africa: implications of a new view based on SeaWiFS satellite imagery. *Deep-Sea Research I*, 51:153–172, 2004.
- R.F. Weiss. Carbon Dioxide in Water and Seawater: The Solubility of a Non-Ideal Gas. *Marine Chemistry*, 2:203–215, 1974.
- R.F. Weiss and B.A. Price. Nitrous Oxide Solubility in Water and Seawater. *Marine Chemistry*, 8:347–359, 1980.
- J.W.C. White and B.H. Vaughn. University of Colorado, Institute of Arctic and Alpine Research (INSTAAR), Stable Isotopic Composition of Atmospheric Carbon Dioxide ( $^{13}\text{C}$  and  $^{18}\text{O}$ ) from the NOAA ESRL Carbon Cycle Cooperative Global Air Sampling Network, 1990-2008 Version: 2011-10-04. <ftp://ftp.cmdl.noaa.gov/ccg/co2o18/flask/event/>, 2009.
- J.W.C. White and B.H. Vaughn. University of Colorado, Institute of Arctic and Alpine Research (INSTAAR), Stable Isotopic Composition of Atmospheric Carbon Dioxide ( $^{13}\text{C}$  and  $^{18}\text{O}$ ) from the NOAA ESRL Carbon Cycle Cooperative Global Air Sampling Network, 1990-2008 Version: 2011-10-04. <ftp://ftp.cmdl.noaa.gov/ccg/co2c13/flask/event/>, 2011.
- C.A. Williams, N.P. Hanan, J.C. Neff, R.J. Scholes, J.A. Berry, S.A. Denning, and D.F. Baker. Africa and the global carbon cycle. *Carbon Balance and Management*, 2(3), 2007.
- J. Winderlich, H. Chen, C. Gerbig, T. Seifert, O. Kolle, J.V. Lavrič, C. Kaiser, A. Höfer, and M. Heimann. Continuous low-maintenance  $\text{CO}_2/\text{CH}_4/\text{H}_2\text{O}$  measurements at the Zotino Tall Tower Observatory (ZOTTO) in Central Siberia. *Atmospheric Measurement Techniques*, 3:1113–1128, 2010.

- U. Wittenberg, M. Heimann, G. Esser, A.D. McGuire, and W. Sauf. On the influence of biomass burning on the seasonal CO<sub>2</sub> signal as observed at monitoring stations. *Global Biogeochemical Cycles*, 12(3):531–544, 1998.
- F. Wittke, A. Kock, and H.W. Bange. Nitrous oxide emissions from the upwelling area off Mauritania (NW Africa). *Geophysical Research Letters*, 37:L12601, 2010. doi: 10.1029/2010GL042442.
- WMO/GAW. GAW Report No. 213. 17<sup>th</sup> WMO/IAEA Meeting on Carbon Dioxide, Other Greenhouse Gases and Related Tracers Measurement Techniques (GGMT-2013), Beijing, China, 10–13 June. 2013.
- WMO/GAW. WMO Greenhouse Gas Bulletin: The State of Greenhouse Gases in the Atmosphere Based on Global Observations through 2013, 9 September. No 10, 2014.
- S.C. Wofsy, G.W. Sachse, G.L. Gregory, D.R. Blake, J.D. Bradshaw, S.T. Sandholm, H.B. Singh, J.A. Barrick, R.C. Harriss, R.W. Talbot, M.A. Shipham, E.V. Browell, D.J. Jacob, and J.A. Logan. Atmospheric Chemistry in the Arctic and Subarctic: Influence of Natural Fires, Industrial Emissions, and Stratospheric Inputs. *Journal of Geophysical Research*, 97(D15):16,731–16,746, 1992.
- G. Wohlfahrt, L.F. Fenstermaker, and J.A. Arnone. Large annual net ecosystem CO<sub>2</sub> uptake of a Mojave Desert ecosystem. *Global Change Biology*, 14:1475–1487, 2008. doi: 10.1111/j.1365-2486.2008.01593.x.
- M.J. Wooster, P.H. Freeborn, S. Archibald, C. Oppenheimer, G.J. Roberts, T.E.L. Smith, N. Govender, M. Burton, and I. Palumbo. Field determination of biomass burning emission ratios and factors via open path FTIR spectroscopy and fire radiative power assessment: headfire, backfire and residual smouldering combustion in African savannahs. *Atmospheric Chemistry and Physics*, 11:11591–11615, 2011.
- H.M. Worden, M.N. Deeter, C. Frankenberg, M. George, F. Nichitiu, J. Worden, K.W. Aben, I. ad Bowman, C. Clerbaux, P.F. Coheur, A.T.J. de Laat, R. Detweiler, J.R. Drummond, D.P. Edwards, J.C. Gille, D. Hurtmans, M. Luo, S. Martínez-Alonso, S. Massie, G. Pfister, and J.X. Warner. Decadal record of satellite carbon monoxide observations. *Atmospheric Chemistry and Physics*, 13:837–850, 2013.
- D.J. Wuebbles and K. Hayhoe. Atmospheric Methane: Trends and Impacts. In J. van Ham, A.P. Baede, L.A. Meyer, and R. Ybema, editors, *Non-CO<sub>2</sub> Greenhouse Gases: Scientific Understanding, Control and Implementation*, pages 425–432. 2000.
- J. Xie, Y. Li, C. Zhai, C. Li, and Z. Lan. CO<sub>2</sub> absorption by alkaline soils and its implication to the global carbon cycle. *Environmental Geology*, 56(5):953–961, 2009. doi: 10.1007/s00254-008-1197-0.
- H. Yamagishi, Y. Tohjima, H. Mukai, and K. Sasaoka. Detection of regional scale sea-to-air oxygen emission related to spring bloom near Japan by using in-situ measurements of the atmospheric oxygen/nitrogen ratio. *Atmospheric Chemistry and Physics*, 8(12):3325–3335, 2008. doi: 10.5194/acp-8-3325-2008.
- R.J. Yokelson, J.G. Goode, D.E. Ward, R.A. Susott, R.E. Babbitt, D.D. Wade, I. Bertschi, D.W.T. Griffith, and W.M. Hao. Emissions of formaldehyde, acetic acid, methanol, and other trace gases from biomass fires in North Carolina measured by airborne Fourier transform infrared spectroscopy. *Journal of Geophysical Research*, 104(D23):30,109–30,125, 1999.

- R.J. Yokelson, I.T. Bertschi, T.J. Christian, P.V. Hobbs, D.E. Ward, and W.M. Hao. Trace gas measurements in nascent, aged, and cloud-processed smoke from African savanna fires by airborne Fourier transform infrared spectroscopy (AFTIR). *Journal of Geophysical Research*, 108(D13):8478, 2003.
- R.J. Yokelson, I.R. Burling, S.P. Urbanski, E.L. Atlas, K. Adachi, P.R. Buseck, C. Wiedinmyer, S.K. Akagi, D.W. Toohey, and C.E. Wold. Trace gas and particle emissions from open biomass burning in Mexico. *Atmospheric Chemistry and Physics*, 11(14):6787–6808, 2011. doi: 10.5194/acp-11-6787-2011.
- J. Yoon and A. Pozzer. Model-simulated trend of surface carbon monoxide for the 2001–2010 decade. *Atmospheric Chemistry and Physics*, 14:10465–10482, 2014.
- L.M. Zamora, A. Oschlies, H.W. Bange, K.B. Huebert, J.D. Craig, A. Kock, and C.R. Löscher. Nitrous oxide dynamics in low oxygen regions of the Pacific: insights from the MEMENTO database. *Biogeosciences*, 9(12):5007–5022, 2012. doi: 10.5194/bg-9-5007-2012.
- C. Zellweger, M. Steinbacher, and B. Buchmann. Evaluation of new laser spectrometer techniques for in-situ carbon monoxide measurements. *Atmospheric Measurement Techniques*, 5:2555–2567, 2012. doi: 10.5194/amt-5-2555-2012.
- G. Zeng, S. W. Wood, O. Morgenstern, N. B. Jones, J. Robinson, and D. Smale. Trends and variations in CO, C<sub>2</sub>H<sub>6</sub>, and HCN in the Southern Hemisphere point to the declining anthropogenic emissions of CO and C<sub>2</sub>H<sub>6</sub>. *Atmospheric Chemistry and Physics*, 12(16):7543–7555, 2012.
- M. Zhang, J.M. Chen, T. Wang, T.T. Cheng, L. Lin, R.S. Bhatia, and M. Hanvey. Chemical characterization of aerosols over the Atlantic Ocean and the Pacific Ocean during two cruises in 2007 and 2008. *Journal of Geophysical Research*, 115:D22302, 2010.